DOCTOR OF PHILOSOPHY

Studies of reversal processes in particulate recording media using pulsed field magnetometry

Prichard, Leslie Stephen

Award date:
2000

Awarding institution:
Bangor University

Studies of Reversal Processes in Particulate Recording Media using Pulsed Field Magnetometry

by

Leslie Stephen Prichard

A thesis submitted to the University of Wales
in candidature for the degree of
Doctor of Philosophy

School of Electronic Engineering and Computer Systems
University of Wales
Bangor
Gwynedd

March 2000

To Helen

Summary

This investigation details the development of two pulsed field magnetometers which allow novel measurements of particulate recording media to be performed. The samples studied are indicative of advanced metal particle recording media which are currently utilised for high density data storage applications, such as Imation Travan™ linear tape.

In the first part of this investigation, a magnetometer has been developed to study reversal processes in metal particle dispersions. The instrument consists of a MOSFET pulse generator which produces well-defined current pulses of over 125A, with selectable pulse widths between 25μs and 130μs. The current pulse is driven into a small field coil assembly, the geometry of which is such that a magnetic field of over 4.7kOe is generated, with symmetrical rise and fall times of around 15μs. Extensive proving studies are presented, which reveal that differences in chemical formulation and dispersion quality may be monitored through pulsed remanence curves.

The second part of this investigation concerns the highly topical issue of high speed reversal in particulate media. A 50Ω pressurised nitrogen spark gap switch has been developed, capable of producing well-defined single-shot voltage pulses of over 3kV. The pulse width is adjustable from 7ns to 56ns, with rise times of under 3ns. The magnetometer consists of a charged coaxial line connected through the spark gap to an improved 50Ω microstrip structure, the geometry of which allows pulsed magnetic fields to be produced with a maximum amplitude of 1.8kOe. Again, extensive proving studies have been performed and the results are compared with recent models of thermally activated reversal.

These pulsed field studies have revealed a correlation between the degree of particle orientation in the tape and high speed reversal properties. The origins of this effect are complex, and are related at different timescales to the crystallite or activation volume, particle interactions and phenomena influenced by gyromagnetic effects. The implications of this are that larger head fields are required to write high frequency transitions on increasingly textured systems. Clearly, this promotes conflicting requirements in terms of recording performance and media durability.

Acknowledgements

I would like to express my sincerest gratitude to Prof. Kevin O'Grady for his excellent guidance, encouragement and supervision throughout this PhD study. I am also most grateful for the additional financial support which he kindly arranged.

A separate thanks must also go to Prof. Kevin O'Grady and Dr. Chris Hancock for their help and encouragement during the preparation of this manuscript. For proofreading the entire text, I am also most grateful to my now deranged aunty, Mrs. Linda Burgham.

I am also deeply grateful for the help, support and advice from friends and colleagues, in particular, Mr. John Cambridge, Dr. Chris Hancock, Mr. Gwyn Williams, Mr. Miles Woolfenden, Dr. Philip Mayo, Dr. Neal Nelson, Dr. Michael Sharrock, Dr. John Dolan, Dr. Matthew Jackson, Mr. Gwyn Jones, Dr. Evi Dova, Dr. John Hutchings, Dr. Helen Laidler, Dr. Andrew Goodman and Ms. Mireia Blanco.

The financial support of the EPSRC is acknowledged, together with Imation Corporation, for their support of a CASE award. I wish also to acknowledge my employers, Potts, Kerr & Co., for the use of their printing and photocopying facilities.

For not making me sleep in the rain, I would like to thank Dr. Matthew Jackson, Mr. Gywn Jones, Mr. Robin Jones and Mr. Dewi Jones for their hospitality and friendship.

For all manner of help and assistance, I would like to express my deepest gratitude to Mrs. June Cooney and Mr. Robin Caterrall. Furthermore, I would like to thank my mum, Mrs. Rhoda Prichard, for baby-sitting Oliver. As always, I am indebted to my grandad, Mr. Leslie Culverston.

Finally, I am eternally grateful to my wife, Helen, for all of her help, encouragement and understanding, and last but not least, to Oliver for ensuring that I arrived promptly in university every morning.

List of Symbols and Abbreviations

1-S*	Coercivity squareness factor
A	Cross-sectional area
a	Prolate spheroid short axis
α	Transition length
a, b	Inner and outer radii of conductors
α_1, α_2, α_3	Direction cosines
abcd	Closed integration path
α_d	Damping factor
A_e	Exchange constant
AGFM	Alternating gradient force magnetometer
B	Magnetic flux density
BJT	Bipolar junction transistor
BV_{DS}	Drain to source breakdown voltage
C	Phase velocity
c	Prolate spheroid long axis
C_0	Characteristic capacitance
CE	Counter empty signal
C_{eq}	Total equivalent capacitance
C_{gs}	Gate to source capacitance
χ_{irr}	Irreversible susceptibility
CMRR	Common mode rejection ratio
C_{ox}	Gate oxide layer capacitance
C_p	Specific heat
χ_t	Transverse susceptibly
d	Head to medium spacing
δ	Thickness of magnetic coating
DCD	DC demagnetisation
ΔE	Energy barrier to reversal
DIMAG	DIspersion by MAGnetic measurement
ΔL_f	Correction for free space
δM	Interaction parameter
D_o	Fundamental length for curling reversal mode
Δw	Width correction factor
E	Activation energy
E_a	Anisotropy energy
E_K	Crystalline anisotropy energy
ENC	Enable counter signal
ENR	Enable register signal
E_p	Magnetostatic energy
ε_r	Relative permittivity
E_s	Shape anisotropy energy
E_t	Total energy
F	Die thickness
f_0	Attempt frequency
FMR	Ferromagnetic resonance

f_o	Resonant frequency
FWHM	Full width at half maximum
G	Current sheet correction factor
γ	Gas constant
γ_0	Gyromagnetic ratio
H	Applied field
η	Carrier viscosity
H	Current sheet correction factor
h	Microstrip lime separation
H_c	Coercivity
H_{ci}	Intrinsic coercivity
h_{ci}	Reduced intrinsic coercivity
H_{cr}	Remanent coercivity obtained from the DCD curve
H_{cr}'	Remanent coercivity obtained from the IRM curve
H_d	Demagnetisation field
H_f	Fluctuation field
H_K	Anisotropy field
i_d	Drain current
i_{dump}	Steering current
i_{field}	Field current
I_{field}	Field current
IGBT	Insulated gate bipolar transistor
IRM	Isothermal remanent magnetisation
i_{source}	Constant current source
jwL_{s1}, jwL_{s2}	Inductive reactance of search coils
k	Boltzmann constant
K	Coil end factor
K_1, K_2	Anisotropy constants
K_{dc}	Integration constant
K_K	Crystalline anisotropy constant
K_s	Shape anisotropy constant
K_t	Total anisotropy constant
$K_{T\dot{H}}$	Thermal conductivity
K_u	Uniaxial anisotropy constant
K_uV/kT	Thermal stability factor
l	Coil length
L	Inversion channel length
L_0	Characteristic inductance
L_α	Overall delay line length
L_β	Effective increase in line length due to the switch
L_D	Internal drain inductance
L_{drain}	Drain inductance
L_f	Inductance of a current sheet of infinite length
L_{f1}, L_{f2}	Inductance of field coils
L_{LEAD}	Lead inductance
L_{left}, L_{right}	Effective field coil length left and right to the point of interest
l_r	Length of rod assembly
L_S	Internal source inductance

L_{TRACK}	PCB track inductance
M	Magnetisation per unit volume
m	Reduced magnetisation
μ_0	Permeability of free space
MD	Molecular dynamic model
M_d	Remanent magnetisation
m_e	Reduced equilibrium magnetisation
MFM	Magnetic force microscopy
μ_n	Electron mobility
MOSFET	Metal oxide semiconductor field effect transistor
MP	Metal particle
μ_r	Relative permeability
M_r	Remanent magnetisation
$M_r(\infty)$	Saturation remanence
M_s	Saturation magnetisation
M_{sb}	Bulk saturation magnetisation
N	Number of turns on a coil
N_a	Demagnetisation factor
N_c	Demagnetisation factor
N_d	Demagnetisation factor
NMR	Nuclear magnetic resonance
OR	Orientation ratio
PALASM	Programmable array logic assembler
P_D	Power dissipated
PZT	Piezoelectric transducer
Q	Head field constant
θ_{JA}	Junction to ambient thermal resistance
r	Coil radius
ρ	Density
R	Sweep-rate
ρ, ρ'	Reflection coefficients
R_0	Initial sweep-rate
R_{damp}	Damping resistor
$r_{ds(on)}$	On state resistance
R_{source}	Current source resistance
RT_{meas}	Measured rise time
RT_{probe}	Rise time of the probe
RT_{scope}	Inherent rise time of the oscilloscope
RT_{sig}	Actual rise time of the signal
S	Magnetic viscosity
SALS	Small angle light scattering
SFD	Switching field distribution
SQUID	Superconducting quantum interface device
τ	Relaxation time
T	Temperature
t	Time
T_1, T_2, T_3	MOSFETs
T_A	Ambient temperature

τ_α	Thermal time constant
T_B	Blocking temperature
τ_B	Brownian relaxation time
TEM	Transmission electron microscopy
τ_i	Integration time constant
T_j	Semiconductor junction temperature
t_{pulse}	Input pulse width
T_{tot}	Total pulse width
υ	Activation volume
v	Induced voltage
V	Volume
V_{amp}	Amplifier voltage
V_b	Breakdown voltage
$V_{BR(DS)}$	Rated drain to source breakdown voltage
VCM	Vibrating coil magnetometer
V_{dev}	Common deviation voltage
V_{DS}	Drain to source voltage
V_{GS}	Gate to source voltage
V_L	Load voltage
V_m	Median particle volume
V_{null}	Null voltage
V_p	Superparamagnetic transition volume
V_{phys}	Physical particle volume
VSM	Vibrating sample magnetometer
V_T	Threshold voltage
V_x, V_y	Bridge voltages
W	Inversion channel width
w	Microstrip line width
w_r	Width of rod assembly
Y	Elastic modulus
Z_0	Characteristic impedance
Z_1, Z_2, Z_3, Z_4	Bridge impedance
Z_E	Characteristic impedance of electrodes
Z_L	Load impedance

Contents

Chapter 1

Introduction

1.1 Introduction to the Thesis

This investigation details the development of two pulsed field magnetometers which allow novel measurements of particulate recording media to be performed. In the first part of this investigation, a magnetometer has been developed to study reversal processes in metal particle dispersions, and is an extension to previous studies of low coercivity media (Hancock 1995). The instrument consists of a MOSFET pulse generator which produces well-defined current pulses of over 125A, with selectable pulse widths between 25μs and 130μs. The current pulse is driven into a small field coil assembly, the geometry of which is such that a magnetic field of over 4.7kOe is generated, with symmetrical rise and fall times of around 15μs. This short duration magnetic field impulse magnetises the wet dispersion sample, while an anti-phase sense coil and integrator stage process the magnetisation of the sample under the field pulse. The output is monitored using a 500MHz digitising storage oscilloscope, allowing the dynamic magnetisation response to the applied pulsed field to be viewed in real-time. Extensive proving studies are presented, which reveal that differences in chemical formulation and dispersion quality may be monitored through pulsed remanence curves.

The second part of this investigation concerns the highly topical issue of high speed reversal in particulate media. The magnetometer developed is again an extension to previous work, in which an instrument capable of producing nanosecond duration pulsed fields of up to 450 Oe was described (Hancock 1995). Unfortunately, the field produced by this instrument is not of sufficient magnitude to switch advanced high

coercivity metal particle media. Consequently, a 50Ω pressurised nitrogen spark gap switch has been developed, capable of producing well-defined single-shot voltage pulses of over 3kV. The pulse width is adjustable from 7ns to 56ns, with rise times of under 3ns. The magnetometer consists of a charged coaxial line connected through the spark gap to an improved 50Ω microstrip structure, the geometry of which allows pulsed magnetic fields to be produced with a maximum amplitude of 1.8kOe. Again, extensive proving studies have been performed and the results are compared with recent models of magnetisation reversal (Sharrock, et al. 1981) (el-Hilo, et al. 1992).

1.2 Motivation for the Work

Presently, in a society which is driven by information technology, the role of the magnetic recording industry is fundamental. In recent years, the requirements for both data storage and transfer rates have exploded. To illustrate this, a current NASA project is collecting over 1000GB of new data every day from earth watching satellites. Furthermore, with multimedia and Internet applications still emerging, the amount of data stored by both major corporations and private individuals is sure to grow enormously. More surprisingly, these astonishing storage requirements are currently being outstripped by recent advances in rigid disk media (Li, et al. 1999). Unfortunately these improvements tend to overshadow other advanced recording technologies, and it is often the case that significant advances in particulate recording media are disregarded. However, the appeal of particulate media is simple; it provides both the lowest cost and highest storage capacity in a removable format, and as such dominates the market in reliable backup applications for both desktop and mainframe computer systems.

Historically, the development of particulate media for backup applications advanced dramatically in the early 1980s, when the accepted open reel technique was replaced by a much more convenient cartridge based system. At this time, significant improvements in media and compression techniques also occurred, which allowed up to 2GB of data to be stored on a single 4inch square cartridge. The half inch wide tape was coated using either CrO_2 (IBM 3480 standard) or cobalt modified γ-Fe_2O_3 particles having a coercivity of around 480 Oe. Perhaps more significantly, the first marketing of metal particles for applications in compact 8mm video recording followed in 1985

(Tamagawa, et al. 1983), although the dominance of the VHS system at that time restricted the commercial success.

Today, there are two main data storage formats utilising metal particle technology: linear and helical scan recording. Using helical scan, signals are recorded diagonally across the tape using a rapidly rotating head (Mee, et al. 1988), similar to that employed in a home video recorder. Accordingly, the relative speed between the tape and the head is such that the tape needs to be highly durable to withstand the heating and wear caused by repeated contact with the head (Hisano, et al. 1998). Conversely, in linear recording the tracks are recorded in the direction of the tape. In common to both formats, several technological advances have been made in recent years. These include increasing the number of data tracks using multi-channel heads to provide higher transfer rates, and utilising a tracking servo system to reduce track spacing and width, which allows improved data capacity. Of course, the introduction of smaller particles provides significant improvements in recording density by virtue of the shorter recording wavelength and track pitch (Richter, et al. 1995), which is common to both of these technologies. It is widely accepted that linear recording offers the greatest scope for future improvements to both data capacity and transfer rates, as helical recording has already had to develop each technology further, due to its limited tape area.

The reason for selecting either of these formats for backup applications is not only the low intrinsic cost, but is also dependent upon the low cost per MB of information stored. Accompanying the advances in track servo mechanisms, particle size and morphology have been significant developments in the resin systems used, which has enabled much thinner base films to be used. Consequently, a standard DDS3 helical scan cartridge consists of 125m of tape which is capable of storing 12GB of information before compression. This data is stored within a cassette measuring 5cm × 7.5cm, with a 4mm wide tape. Remarkably, this represents data storage costing less than 10 US cents per MB (O'Grady, et al. 1999). As such, the samples under investigation in this study are representative of advanced metal particle media currently utilised for high density data storage applications in either recording format, although the samples are particularly indicative of Imation Travan™ linear recording tape.

The first part of this investigation concerns the characterisation of metal particle dispersions using microsecond duration pulsed magnetic fields. It is well known that the most critical stage in the production of particulate media is the preparation of a homogenous and stable pigment dispersion (Mathur, et al. 1991). However, the magnetic characterisation of a dispersion is often difficult to interpret as the application of a DC magnetic field alters the microstructure (O'Grady, et al. 1991). Conversely, if the dispersion is rapidly changed using a pulsed field of short duration, this may be used to give an indication of the state of the microstructure without having to make allowances for field induced aggregation of particles, and is the basis for this study.

Pulsed field measurements of low coercivity oxide dispersions have been reported previously (Hancock 1995), using a novel pulsed field magnetometer capable of generating fields up to 1270 Oe. These studies have shown that pulsed field techniques are a useful tool for assessing the quality of dispersions, allowing the dispersion to be characterised non-destructively. This work has now been extended and a completely new magnetometer which generates pulsed magnetic fields over a 4.7kOe range has been developed to characterise the latest metal particle pigment dispersions. Proving studies of a series of advanced metal particle pigment formulations are presented. Differences in chemical formulation and dispersion quality may be monitored through pulsed remanence curves, and real-time imaging of the dynamic magnetisation. These findings are substantiated from further diverse magnetic and non-magnetic studies of the dispersion samples and their coatings.

The second part of this investigation concerns the highly topical issue of high speed reversal in particulate media. In recent years, the need for both higher storage densities and data transfer rates has led to the development of metal particle pigment formulations with a small physical size, where thermal activation is significant. For example, a modern linear tape drive running at $20ms^{-1}$ and recording $4kfcmm^{-1}$ would have a bit length of around 15ns and a write head flux rise time of 6ns. Correspondingly, over these short timescales, substantial increases in remanent coercivity have been observed (Doyle, et al. 1993) (Hancock, et al. 1996). As a result, the characterisation of these advanced particulate materials to find their switching speed limits is of fundamental scientific and commercial interest. With future recording systems requiring data to be written at near nanosecond duration, this raises an

interesting question: how fast can the magnetisation in magnetic recording media be switched? Since conventional laboratory methods cannot easily resolve switching behaviour in this time regime, novel pulsed field techniques have been developed to probe nanosecond reversal.

The switching characteristics of a series of metal particle tape samples are examined over a wide range of timescales. Pulsed field measurements are performed as DC demagnetisation curves which closely resemble the digital recording process. As the behaviour of recording media is strongly dependent on the timescale of the reversal process (Néel 1949), the coercivity relevant to writing may be considerably higher than that required for archival storage. Of course, in practical recording systems, the capabilities of available recording transducers limit the writing coercivity, whereas the signal intensity recovered from the media is constrained by the storage coercivity.

The high speed experimental data obtained are compared with the widely recognised thermal switching models of (Sharrock, et al. 1981) (el-Hilo, et al. 1992), in order to relate thermal activation to fundamental media parameters associated with high speed coercivity. However, at high frequencies, the limitations of these models to map the reversal of samples which are dominated by precessional switching, represents an important limitation in terms of recording speed which is attributable to the breakdown of the Arrhenius-Néel formalism. Over extremely short timescales, the behaviour of the moments is governed by the dynamics of the atomic spins, which is effectively described by the Landau-Lifshitz-Gilbert gyromagnetic equation (Gilbert 1955). Consequently, an attempt to validate switching models has been made, the implications of which suggest that further theoretical models accounting for both gyromagnetic precession and thermal switching are required.

References

Doyle, W. D., He, L., Flanders, P. J., *IEEE Trans. Magn.* **29**, 3634-3636 (1993).

el-Hilo, M., de Witte, A. M., O'Grady, K., Chantrell, R. W., *J. Magn. Magn. Mater.* **117**, L307-L310 (1992).

Gilbert, T. L., *Phys. Rev.* **100**, 1243 (1955).

Hancock, C. P., PhD, University of Wales (1995).

Hancock, C. P., O'Grady, K., el-Hilo, M., *J. Phys. D: Appl. Phys.* **29**, 2343-2351 (1996).

Hisano, S., Saito, K., *J. Magn. Magn. Mater.* **190**, 371-381 (1998).

Li, J. S., et al., *J. Appl. Phys.* **85**, 4286-4291 (1999).

Mathur, M. C. A., Raghavan, S., Jung, C., *Adv. Info. Storage Syst.* **1**, 337-351 (1991).

Mee, C. D., Daniel, E. D., *Magnetic recording* (McGraw-Hill, Inc., 1988), vol. 2: Computer data storage.

Néel, L., *Ann. Géophys.* **5**, 99-136 (1949).

O'Grady, K., Gilson, R. G., Hobby, P. C., *J. Magn. Magn. Mater.* **95**, 341-355 (1991).

O'Grady, K., Laidler, H., *J. Magn. Magn. Mater.* **200**, 616-633 (1999).

Richter, H. J., Veitch, R. J., *IEEE Trans. Magn.* **31**, 2883-2888 (1995).

Sharrock, M. P., McKinney, J. T., *IEEE Trans. Magn.* **17**, 3020-3022 (1981).

Tamagawa, N., Chubachi, R., *J. Magn. Soc. Japan* **7**, 202 (1983).

Chapter
2

Magnetism of Particulate Recording Media

2.1 Introduction

All atomic matter consists of electrons orbiting a nucleus containing one or more protons and neutrons. The electrons in the atom experience two separate motions which are responsible for the net magnetic moment: specifically the orbital moment as the electron orbits the nucleus and the spin moment as the electron spins on its own axis. The atomic nucleus is also found to have a very small magnetic moment due to its spin angular momentum, but is insignificant when compared to the moments due to the electrons. The total magnetic moment for an atom may be considered as the vector addition of all components of orbital and spin angular momentum.

The electrons exist in prescribed orbits which are determined by the laws of quantum mechanics (French, et al. 1979). In an atom that contains several electrons, the orbits exist in opposite directions so that the total orbital moment is small or zero. In the solid state, the orbits from neighbouring atoms tend to further diminish the orbital angular momentum. Moreover, as the spin of an electron exists in one of two directions, the spin moment is again reduced by neighbouring interactions. Consequently, in the majority of elements the total magnetic moment is small. However, in certain materials such as the transition elements, the ordering of the electrons is irregular and the outer electron orbits are occupied before the inner ones are completely filled. Since the partially filled orbits can have a large spin moment, whilst the interactions from neighbouring atoms are partially screened by electrons in the outer orbits, there are two possibilities for the vector sum of the magnetic moments. In the

first instance, the magnetic moments of all the electrons cancel out, resulting in an atom with no net moment, a condition classed as diamagnetism. In the second instance, the magnetic moments of all the electrons only partially cancel, resulting in an atom with a net magnetic moment. Depending upon how the moments align, these elements are classified as either paramagnetic, ferromagnetic, antiferromagnetic or ferrimagnetic.

The magnetic properties of materials may be characterised by the manner in which the magnetisation varies with the applied field, with the ratio of these quantities termed the susceptibility. Atoms or ions with a large net moment exhibit large positive values of susceptibility if the materials order as in ferro or ferrimagnets, and non-linear magnetisation curves result that retain some magnetisation when the applied field is removed. It is the properties of this particular class of materials which are exploited for use as particulate recording media.

2.2 Single Domain Particles

In zero field, ferromagnetic and ferrimagnetic materials have a structure which consists of regions or domains, each of which is spontaneously magnetised to saturation. The magnetisation vector of each domain is oriented in a direction to minimise the magnetostatic energy. The section between neighbouring domains consists of a gradual rotation of spin orientations, which is termed a domain wall. In these bulk materials, the magnetisation process is achieved by domain wall motion.

(Frenkel, et al. 1930) predicted that below a critical size, a ferromagnetic or ferrimagnetic particle will be single domain, as the magnetostatic energy is insufficient to allow the formation of domain walls. A single domain particle aligns with an applied field by rotation of the magnetisation vector, and so remains saturated along the direction of the vector. The spontaneous magnetisation is primarily governed by anisotropy effects (§2.3), thermal fluctuations (§2.5) and particle interactions (§2.5.6). Particles selected for particulate recording media are predominately single domain.

The critical size at which the transition from multi-domain to single domain behaviour occurs is typically 150Å (Kittel 1946) to 600Å (Kittel, et al. 1956), for the common ferromagnetic elements. However, the size of a single domain particle strongly depends on the particle shape and saturation magnetisation (Sato, et al. 1982). For example, in spherical iron particles the critical size is around 500Å, whereas

elongated rod shaped particles with much lower demagnetising fields and hence lower magnetostatic energy have a much larger maximum volume. According to (Stoner and Wohlfarth 1948), a rod with an aspect ratio of 10:1 has a critical length of at least five times that of a sphere.

The existence of single domain particles was proved experimentally by (Morrish, et al. 1956). These workers observed an approximately square hysteresis loop for a single domain γ-Fe_2O_3 particle, as shown in figure 2.1(a). The double step in the loop was due to the fact that they were actually measuring two particles stuck together, each of which being a single domain. More recently, (Richter, et al. 1989) measured the hysteresis curve of a single domain barium ferrite particle using a vibrating reed magnetometer, as shown in figure 2.1(b). The characteristic rectangular magnetisation curve is clearly observed.

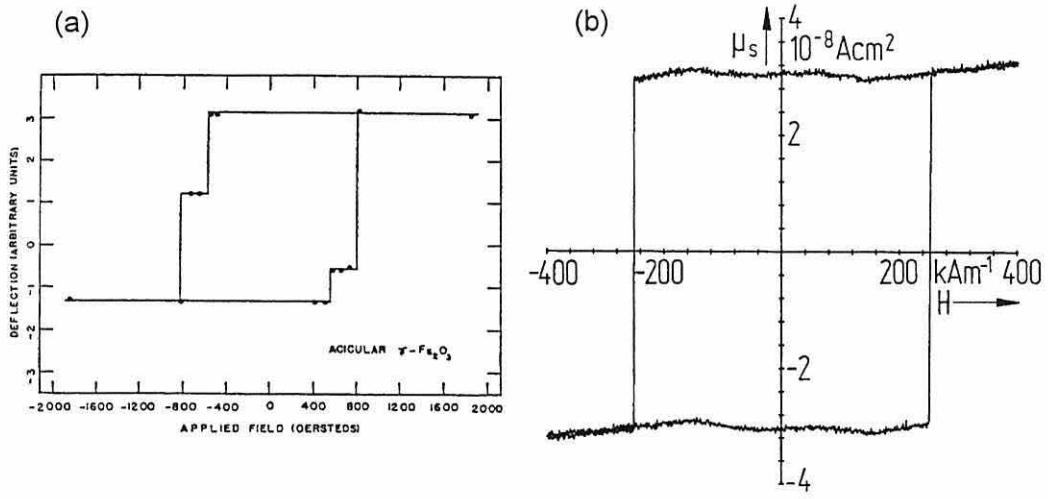

Figure 2.1 Measured hysteresis loops for (a) two single domain γ-Fe_2O_3 particles (b) single domain BaFe particle.

2.3 Magnetic Anisotropy

A magnetically anisotropic material has preferred directions of magnetisation. These directional preferences correspond to a set of energy minima within the particle, which in turn, are the basis for irreversible magnetisation and remanence. The anisotropy has a powerful influence on the shape of the hysteresis loop when measuring in different directions, and hence also on parameters which characterise the media, such as coercivity, squareness and time dependence. Of the different anisotropies described in

the following sections, only crystalline is intrinsic to the material. The other anisotropies are extrinsic properties, influenced by the shape of the material or outside forces which may be mechanical or thermal. For recording media, it is the crystalline and shape anisotropy contributions that are most relevant to the material, and are therefore discussed in the greatest detail.

2.3.1 Crystalline Anisotropy

Crystalline anisotropy is a result of the spin-orbit coupling of electrons. If an external field is applied to a material, it tries to align the spin and orbit of an electron. However, as the orbits are strongly coupled to the lattice, moments in certain directions are more difficult to rotate. Consequently, the crystalline anisotropy energy is the energy required to overcome the spin-orbit coupling, which leads to energetically preferred orientations, or easy directions, in the crystal lattice. Therefore, to magnetise a crystal away from the preferred easy direction requires additional crystalline energy density E_K. For a crystal with multiaxial cubic anisotropy, as is the case for γ-Fe_2O_3 and metal particles, the expression for E_K is given by equation 2.1 (Cullity 1972).

$$E_K = K_1(\alpha_1^2\alpha_2^2 + \alpha_2^2\alpha_3^2 + \alpha_3^2\alpha_1^2) + K_2(\alpha_1^2\alpha_2^2\alpha_3^2) + \ldots \qquad (2.1)$$

K_1 and K_2 are the material specific anisotropy constants, and α_1, α_2 and α_3 are the directional cosines of the magnetisation vector with respect to the easy axes.

For materials such as cobalt and hexagonal barium ferrite with uniaxial anisotropy, the crystallographic c-axis is the easy axis. The crystalline anisotropy energy density is expressed in terms of the angle ϕ between the magnetisation vector and the easy axis.

$$E_K = K_1 \sin^2\phi + K_2 \sin^4\phi + \ldots \qquad (2.2)$$

The value of E_K is a minimum for $\phi = 0$ and π, i.e. the preferred easy axis. For materials which have a small value of K_2 with their easy axes aligned parallel to the field, the anisotropy field H_K, which is the field required to rotate the magnetisation vector over an anisotropic energy barrier in the absence of thermal fluctuations, is given by

$$H_K = \frac{2K_1}{M_{sb}} \tag{2.3}$$

where M_{sb} is the bulk saturation magnetisation. A more generalised expression is given by (Luborsky 1961).

$$H_K = \frac{\alpha_K K_1}{M_{sb}} \tag{2.4}$$

The constant α_K depends on the crystal structure and the degree of particle orientation. For cubic crystals α_K varies between 0.64 and 2.0, and between 0.96 and 2.0 for uniaxial systems as the system goes from a random to aligned state.

2.3.2 Shape Anisotropy

If a material retained a spherical shape with no preferred crystallographic orientations, then the magnetic properties would be isotropic. Clearly, this is not the case for elongated particles, as it is easier to magnetise the crystal along its long axis, since the demagnetising field along the long axis is a minimum (Néel 1947). For the case of ellipsoidal ferromagnetic particles, the shape anisotropy may be described from the internal demagnetising field H_d,

$$H_d = -N_d M \tag{2.5}$$

where N_d is the demagnetising factor which depends on particle geometry. A prolate spheroid with geometry illustrated in figure 2.2, has a weak demagnetising field along the c-axis, which results in uniaxial anisotropy with the c-axis as the easy direction.

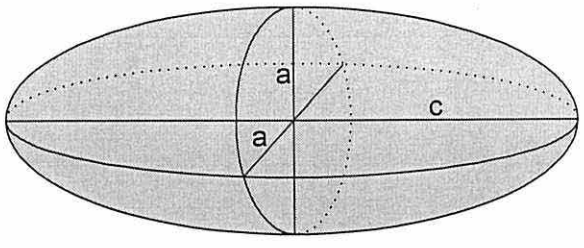

Figure 2.2 The prolate spheroid.

The shape anisotropy energy E_s varies with angle ϕ between the c-axis and the magnetisation vector, such that (Cullity 1972)

$$E_s = 0.5M_s^2(N_a - N_c)\sin^2\phi \tag{2.6}$$

where N_a and N_c are the demagnetising factors along the semi-axes, and M_s is the saturation magnetisation. This expression is of the same form as the second term of equation 2.2, and may be written as

$$E_s = K_s \sin^2\phi \tag{2.7}$$

where K_s is the shape anisotropy constant. The total anisotropy constant K_t for a prolate spheroid can then given by the equation:

$$K_t = K_K + K_s \quad \text{where} \quad K_s = 0.5M_s^2(N_a - N_c) \tag{2.8}$$

The value of K_s for a material may be increased by utilising particles with a larger aspect ratio. The majority of particles used in particulate recording media are acicular, and the contribution of the shape anisotropy is dominant over the crystalline anisotropy. The exception to this is barium ferrite, which is controlled almost exclusively by crystalline anisotropy, hence K_s is negative.

2.3.3 Other Anisotropies

Exchange anisotropy is a form of surface anisotropy which is attributed to exchange coupling between an antiferromagnetic surface layer and a ferromagnetic or ferrimagnetic core. Exchange anisotropy is observed as a displaced hysteresis loop with finite anhysteretic magnetisation in zero applied field (Meiklejohn and Bean 1956).

Stress anisotropy due to deformation of the crystal lattice by either mechanical forces or thermal gradients causes additional uniaxial anisotropy, which may create a new easy direction of magnetisation. However, in a collection of particles the overall effect is isotropic, and can usually be ignored.

Surface anisotropy is a further class of anisotropy which originates when surface spins on a material are aligned by bonded species or inclusions at the surface which change the localised crystallographic distribution, and hence create a localised easy axis.

2.4 Reversal Modes

The process of magnetisation reversal in single domain particles is achieved through rotation of the magnetisation vector under the application of a reversing field. These processes have been extensively studied in order to explain inconsistent experimental observations (Luborsky 1961), and separate into models where the magnetisation rotates coherently and those that reverse incoherently. Coherent rotation of the magnetisation may be explained using the Stoner and Wohlfarth model, as described in §2.4.1, whereas incoherent modes of reversal are explained from the fanning and curling models, as discussed in §2.4.2. A schematic representation of the various processes of magnetisation reversal is shown in figure 2.3.

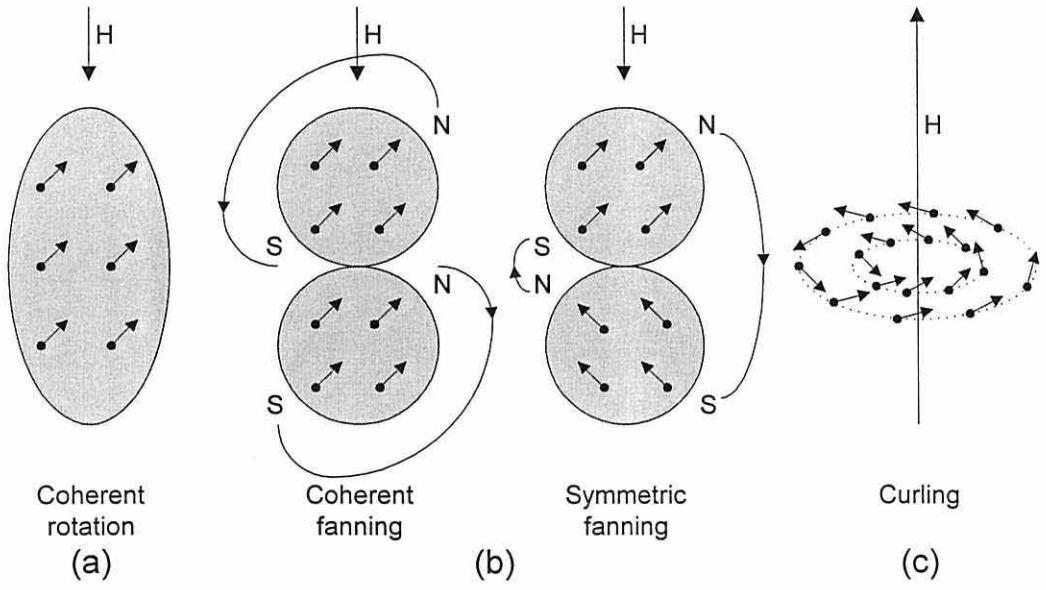

Figure 2.3 Schematic illustration of the various modes of magnetisation reversal.

2.4.1 Stoner-Wohlfarth Theory

The basic mode of magnetisation reversal for uniaxial single domain particles is uniform rotation of the magnetisation (Stoner and Wohlfarth 1948). This model of magnetisation reversal assumes that the spins of all the atoms in the particle remain parallel during rotation, as shown in figure 2.3(a). As the applied field rotates the

magnetisation vector out of the easy axis direction, it does so against the restoration force of the particle anisotropy, as described in §2.3. For a prolate spheroid with uniaxial anisotropy K_u, the total energy density E_t is the sum of the anisotropy energy E_a and the magnetostatic energy E_p as a result of applying a field H, such that

$$E_t = E_a + E_p = K_u \sin^2 \phi - HM_s \cos(\theta - \phi) \tag{2.9}$$

The angles θ and ϕ are defined in figure 2.4 for a particle of long axis c and short axis a.

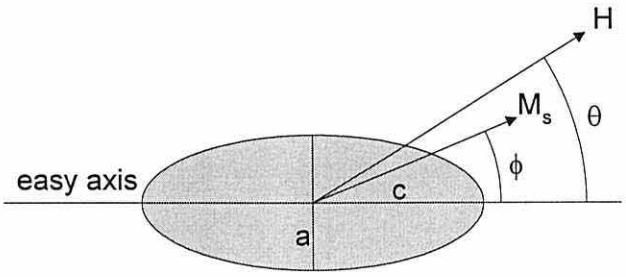

Figure 2.4 Axis system for the Stoner-Wohlfarth prolate spheroid.

Solutions to the equilibrium position of M_s are found on differentiating equation 2.9

$$\frac{dE_t}{d\phi} = 2K_u \sin\phi \cos\phi - HM_s \sin(\theta - \phi) = 0 \tag{2.10}$$

with the magnetisation in the field direction resolved by

$$M = M_s \cos(\theta - \phi) \tag{2.11}$$

When the applied field is zero the magnetisation vector lies either parallel or antiparallel to the easy axis, depending upon the earlier magnetic field history. Figure 2.5(a) shows calculated hysteresis loops for various orientations of the applied field. It is clearly seen that the shape of the magnetisation curve is strongly influenced by the particle orientation. In general, these loops consist of both reversible and irreversible components of magnetisation. For the case when the applied field is perpendicular to the easy axis ($\theta = 90°$), equations 2.10 and 2.11 then become

$$2K_u \sin\phi\cos\phi = HM_s\cos\phi \tag{2.12}$$

$$M = M_s \sin\phi \tag{2.13}$$

Hence, in terms of the reduced magnetisation m ($m = M/M_s$), then

$$m = H\left(\frac{M_s}{2K_u}\right) \tag{2.14}$$

Equation 2.14 indicates that the moment rotates out of the easy direction as a linear function, with respect to the applied field, until saturation at $H = H_K = 2K_u/M_s$. When the field is removed the magnetisation is able to relax back into its easy axis with no hysteresis observed, a completely reversible process.

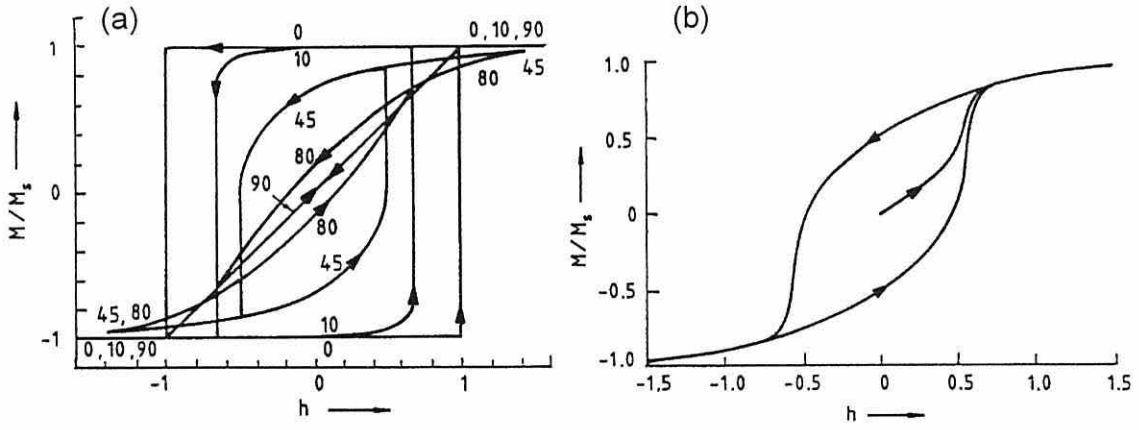

Figure 2.5 Calculated hysteresis loops for (a) various orientations of applied field for a uniaxial single domain particle (b) a random distribution of easy axes orientations.

For the case when the applied field is along the easy axis but in the opposite direction to the moment, such that $\theta = 180°$; as the field is increased the anisotropy retains the position of the magnetisation vector until at a certain applied field the magnetisation becomes unstable at $\phi = 0°$, and processes such as thermal activation reverse the magnetisation to $\theta = 180°$. This reversal at $h = H/H_K = -1$, as shown in figure 2.5(a), is an irreversible change and produces a magnetisation curve which now contains hysteresis. For an assembly of randomly orientated particles, Stoner and Wohlfarth found that

$$H_c = 0.479 H_K \tag{2.15}$$

as indicated in figure 2.5(b). For aligned elongated particles the coercivity due to the shape anisotropy is given by

$$H_c = (N_a - N_c) M_s \tag{2.16}$$

where N_a and N_c are the demagnetising factors along the short and long axes. The maximum coercivity for infinite elongation obtained from the shape anisotropy is $2\pi M_s$. Hence, for iron particles with an axial ratio of 10, the predicted coercivity from equation 2.16 is over 10kOe (Stoner and Wohlfarth 1948). However, (Luborsky 1961) found that the coercivity of aligned elongated iron particles did not exceed 1.8kOe.

This discrepancy between theoretical and experimental observations has led to the development of new models of rotation, such as fanning and curling, in which the individual spins of the atoms do not remain parallel during rotation, as discussed in §2.4.2.

2.4.2 Incoherent Modes

Early electron micrograph studies of elongated iron particles found that the edges of particles were not regular, but consisted of a series of bulges with a periodic nature (Mendelsohn, et al. 1955). The fanning model was proposed by (Jacobs and Bean 1955) from observations of elongated particles approximated by the 'chain of spheres'. This model considers each sphere as a single domain particle with no anisotropy of its own, and suggests two possible reversal mechanisms: symmetric fanning and coherent fanning, as shown in figure 2.3(b). The symmetric fanning model implies that the magnetisation vectors of successive spheres rotate in opposite directions, whilst for coherent fanning the moments of all the spheres remain parallel. For calculations of the intrinsic coercivity H_{ci} of more than two particles, the magnetostatic coupling between the spheres produces uniaxial anisotropy with the easy axis along the length of the chain, such that

$$H_{ci} = \frac{\pi M_s}{6} \quad \text{for symmetric fanning} \tag{2.17}$$

$$H_{ci} = \frac{\pi M_s}{2} \quad \text{for coherent fanning} \tag{2.18}$$

Using axial ratios equivalent to the length of the chain of spheres, (Jacobs and Bean 1955) found the symmetric and coherent fanning models produced coercivities of 2.3kOe and 5.6kOe respectively, in closer agreement with experimental observations.

The curling mode of incoherent rotation was developed by (Frei, et al. 1957) using micromagnetic techniques. For a single domain prolate spheroid particle initially magnetised along its +z direction parallel to the long axis, the application of a field in the -z direction causes a rotation of the magnetic moments parallel to the x-y plane, as shown in figure 2.3(c). An elongated particle with an aspect ratio approaching infinity may be approximated by a infinite cylinder. As a result, the spins are always parallel to the surface during reversal, so no free poles are formed and no magnetostatic energy is involved. Accordingly, the curling reversal process is completely dependent on the exchange energy from neighbouring spins within the material. Calculations of the coercivity in the curling mode show a significant size dependence, unlike the coherent and fanning mechanisms. In terms of a fundamental length D_o and exchange constant A_e, the reduced intrinsic coercivity h_{ci} for a infinite cylinder, as a function of the reduced diameter D/D_o is given by

$$D_o = \frac{2A_e^{1/2}}{M_s} \tag{2.19}$$

$$h_{ci} = \frac{H_{ci}}{2\pi M_S} = \frac{1.08}{(D/D_o)^2} \tag{2.20}$$

Hence, the intrinsic coercivity is proportional to $1/D^2$. Figure 2.6 shows the variation of coercivity with particle size for an infinite cylinder, along with a comparison of the values obtained for the other reversal modes, using iron whiskers (Luborsky, et al. 1964).

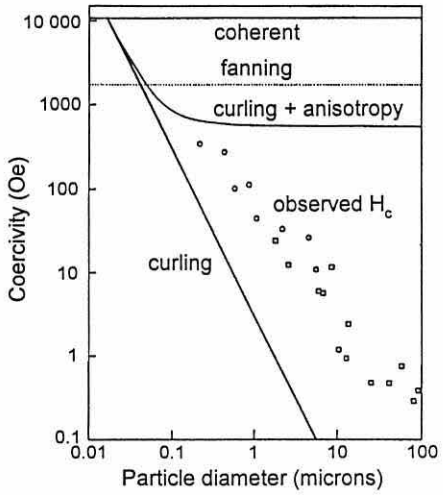

Figure 2.6 Size dependent coercivity for coherent, fanning and curling modes.

2.5 Thermal Activation

Magnetisation reversal in recording media is governed by the Stoner-Wohlfarth theory which describes the behaviour of the magnetisation vector of a single domain particle at absolute zero. However, at finite temperatures (Néel 1949) proposed the thermal activation model for a system of fine particles undergoing coherent reversal. Essentially, at H = 0, a uniaxial single domain particle has two energetically preferred orientations of opposing magnetisation separated by an energy barrier. On applying an external magnetic field, the barrier is reduced and if the field is large enough, thermal fluctuations are sufficient to overcome the barrier, and the magnetisation is reversed. Moreover, if a single domain particle is sufficiently small, thermal fluctuations may overcome the anisotropy forces and spontaneously reverse the magnetisation of the particle, an effect termed superparamagnetism (Bean and Livingston 1959). Numerical expressions for the energy barrier to reversal have been formulated for coherent reversal, as described in §2.5.1.

In recent years, the mechanism of thermally activated switching has been of considerable interest to the magnetic storage industry because of the large difference between the timescales of the recording process and the required storage stability (Sharrock 1994). In particular, the dependence of the remanent coercivity upon the timescale of the reversal process, as the value of the field required to reduce the magnetisation from saturation to zero decreases, as the time that it is allowed to act increases, as discussed in §2.5.3 and §2.5.4. Likewise, other magnetic time effects such

as the observation of magnetisation changes during exposure to a constant field, termed thermal decay or magnetic viscosity, is a consequence of thermal agitation which leads to the concept of the activation volume, as described in §2.5.2.2.

2.5.1 Energy Barrier to Reversal

From the theories of (Néel 1953) (Brown 1959) (Brown 1963), the total energy of a uniaxial single domain particle with volume V, with its easy axis aligned parallel to the applied field H, is given by

$$E_t = K_u V \sin^2 \phi - HVM_s \cos(\theta - \phi) \tag{2.21}$$

where K_u is the anisotropy constant, and the angles ϕ and θ are defined in figure 2.4. At equilibrium, the magnetisation vector M_s will point in a direction such that the total energy is minimised, given by

$$\frac{dE_t}{d\theta} = \sin\phi\cos\phi - h\sin(\theta - \phi) = 0 \tag{2.22}$$

where the reduced field $h = H/H_K$ and $H_K = 2K_u/M_s$ is the anisotropy field. In applied fields $H < H_K$ for a particle with its easy axis aligned in the direction of H ($\theta = 0$), equation 2.22 yields minima at $\phi_{min} = 0$ and 180°, and a maximum at $\phi_{max} = \cos^{-1}(-h)$. The energy barrier to reversal ΔE is then given by the difference between the maximum and minimum values of equation 2.22, such that

$$\Delta E = K_u V(1 - H/H_K)^2 \tag{2.23}$$

Hence the application of a magnetic field will reduce the energy barrier for rotation. In zero applied field $\Delta E = K_u V$ as the magnetisation vector experiences the same energy barrier regardless of the particle orientation. The effect of an applied field on the energy barrier is illustrated in figure 2.7, after (Bean and Livingston 1959).

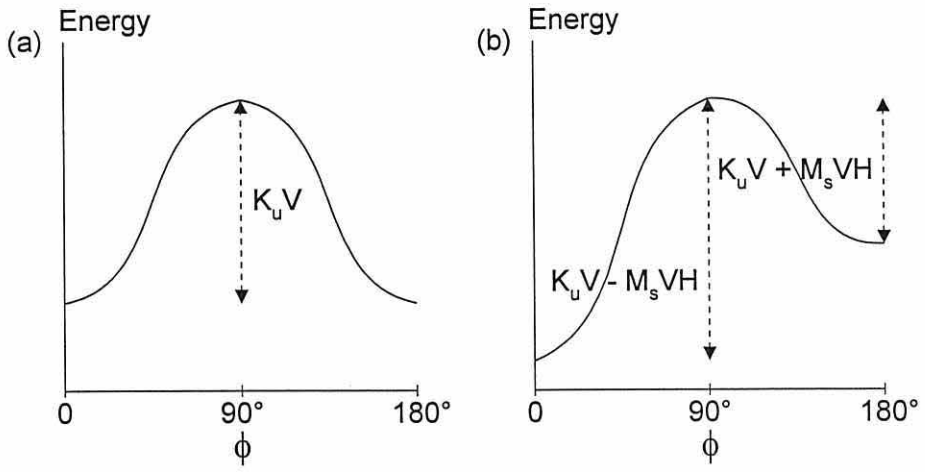

Figure 2.7 The dependence of the energy barrier ΔE on the angle θ between the moment and the easy axis for a particle with its easy axis aligned in the direction of the field H in (a) zero field and (b) an applied field.

From equation 2.23 it is apparent that when $H = H_K$ the energy barrier disappears and the magnetisation vector may make the transition between minima. Consequently, the anisotropy field H_K corresponds to the coercivity at 0 K. However, at finite temperatures the coercivity is somewhat lower as there is a finite possibility of a thermally activated transition over the energy barrier (Néel 1949). In addition, the coercivity of an assembly of particles is further reduced for several reasons:

Primarily, particles in actual media always exhibit an angular distribution of easy axes, despite efforts to orient them during coating. For instance, recording media with a squareness approaching 0.8 display mean deviations of roughly $\cos^{-1}(0.8)$, or 35° from the intended direction (Sharrock 1994). This deviation away from the easy axis strongly influences the shape of the hysteresis loop, as shown in figure 2.5(a).

Furthermore, the value of the coercivity is compounded by the variety of interparticle interactions which occur in media, as described in §2.5.6. The importance of these interactions is demonstrated by the packing fraction dependence of the coercivity, first proposed by (Néel 1947) and subsequently observed in several investigations (Luborsky 1961) (Knowles 1981) (Bertram 1986a). These studies found that for particles where the shape anisotropy dominates, the coercivity decreases as the packing density increases.

Likewise, the coercivity of an assembly of particles is strongly influenced by the mode of magnetisation reversal, as discussed previously in §2.4.2. Studies of iron,

cobalt and iron-cobalt particles (Luborsky, et al. 1960) confirmed that small particles reverse coherently whilst larger particles reverse incoherently, as shown in figure 2.8. The particle diameter which corresponds to the maximum value of coercivity is the critical diameter for the transition between coherent and incoherent behaviour.

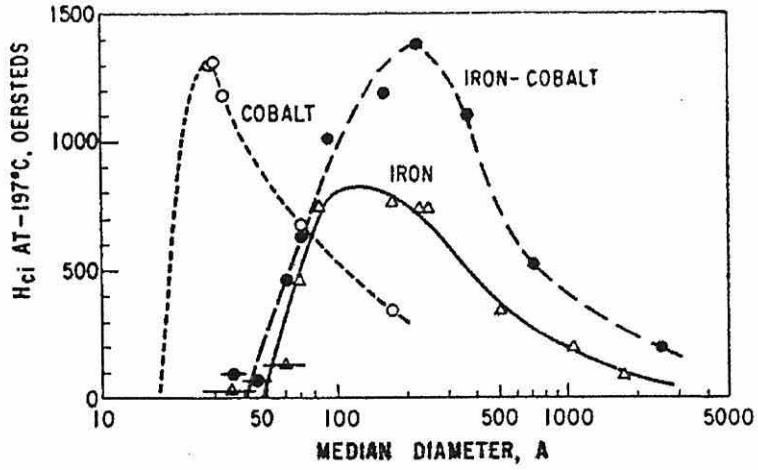

Figure 2.8 Variation of coercivity with particle size at 76 K.

Finally, particles in practical recording media invariably exhibit distributions of particle size, shape and possibly composition (Sharrock 1990). This distribution of physical properties leads to a subsequent distribution of magnetic properties such as V, K_u and ΔE (O'Grady, et al. 1981) resulting in a spread of particle coercivities, again illustrated in figure 2.8.

2.5.2 Time Dependence Effects

At any finite temperature, an irreversible change in magnetisation of a uniaxial single domain particle occurs when an applied field reduces the effective height of an energy barrier under the assistance of thermal energy. Hence, magnetisation reversal depends not only on the strength of the magnetic field, but also the length of time the field is applied; the phenomenon termed 'time dependence'. Time dependent behaviour in magnetic materials arises due to thermal activation of magnetic vectors over localised energy barriers ΔE. The time dependent decay for a system of particles after the removal of a saturating field is expressed by equation 2.24, where m(t) is the reduced magnetisation relative to saturation (Chantrell, et al. 1985)

$$m(t) = 2\exp\left(\frac{-t}{\tau}\right) - 1 \tag{2.24}$$

For the case of a uniaxial single domain particle having an anisotropic energy barrier described by equation 2.23, the relaxation time τ for magnetisation reversal is given by the Arrhenius-Néel law, such that (Néel 1949)

$$\tau^{-1} = f_0 \exp\left(-K_u V / kT\right) \tag{2.25}$$

In fact, the exponential behaviour would only be observed for a system of non-interacting particles having identical magnetic properties. In actual recording media, there is a distribution of particle sizes (§4.6.1.5) and anisotropy constants, which gives rise to a distribution of relaxation times. In most materials the magnetisation is observed to decay linearly with the logarithm of time (Street, et al. 1949), as discussed in §2.5.2.1. The parameter f_0 is termed an 'attempt frequency' of the order of 10^9Hz (Brown 1959) to 10^{12}Hz (Gaunt 1986), and represents the number of fluctuations per second of the magnetisation vector around its mean position. The product kT is the thermal energy. In his classic work, (Néel 1949) suggested that in the absence of thermal agitation, the natural response of the magnetisation vector is to precess around the easy axis of the particle. Thus, the relaxation time τ is influenced by random torques acting on the magnetic moment, the origins of which are due to thermal fluctuations.

Clearly, as both particle volume and temperature occur in the exponent of equation 2.25, these parameters strongly influence the relaxation time, which is the time taken for the magnetisation to fall to 37% of its original value. To illustrate, a 68Å spherical cobalt particle has a relaxation time of 10^{-1} seconds at room temperature, whereas a 90Å particle has a relaxation time of 100 years (Cullity 1972). Clearly, using standard measurements (§2.6) an assembly of 68Å particles would display zero remanence and appear to be superparamagnetic. Conversely, 90Å particles would seem to be thermally stable, with M_r essentially fixed at its initial value. From equation 2.25, it is possible to define a critical volume V_p for superparamagnetic behaviour. Substituting a value of τ = 100 seconds, typical of a DC measurement, into equation 2.25 gives the condition (Bean and Livingston 1959).

$$\ln\left(10^2 \cdot 10^9\right) kT = K_u V_p \tag{2.26}$$

Consequently, the transition to stable behaviour occurs when the energy barrier becomes equal to 25kT, so that the expression for V_p is given by equation 2.27.

$$V_p = \frac{25kT}{K_u} \tag{2.27}$$

Similarly, for an assembly of uniaxial particles of constant size, there exists a 'blocking temperature' T_B above which the magnetisation will be unstable.

$$T_B = \frac{K_u V}{25k} \tag{2.28}$$

2.5.2.1 Magnetic Viscosity

Pioneering studies of magnetic viscosity in Alnico permanent magnets were performed by (Street and Woolley 1949). These workers observed that the magnetisation decayed linearly with the logarithm of time over several decades in the presence of a constant field. This arises due to the summation of the exponential relaxation times over the distribution of energy barriers present in actual magnetic materials. For a measurement time $f_0 t >> 1$, the variation of the magnetisation M with time is given by

$$M(t) = M(0) \pm S \ln(t) \quad \text{and} \tag{2.29}$$

$$S = -dM / d[\ln(t)] \tag{2.30}$$

where M(0) is the magnetisation at t = 0, and the coefficient S is termed the 'magnetic viscosity'. The assumption of a ln(t) dependence has been criticised on the grounds that equation 2.30 is only applicable over limited time intervals and for a special distribution of energy barriers (Aharoni 1985). However, for materials with a wide distribution of energy barriers, a linear variation of M with ln(t) is observed, e.g. fine cobalt particles (O'Grady, et al. 1981), γ-Fe_2O_3, Co-doped and Co-Cr particles (Oseroff, et al. 1987), NdFeB magnets (Givord, et al. 1987), γ-Fe_2O_3 media (Flanders and Sharrock 1987),

CrO_2 tapes (Uren, et al. 1988) and metal particles (Stinnett, et al. 1998a). Similarly, a ln(t) dependence was observed for the series of metal particle samples examined in this study, as detailed in §4.6.1.4 and §6.2.4.

(Néel 1951) suggested that the effect of thermal agitation may be characterised by an internal 'fluctuation field' H_f. As time dependence effects are related to the distribution of energy barriers in the system, it follows that they are related in some way to the irreversible susceptibility $\chi_{irr}(H)$. The irreversible susceptibility occurs since the thermal relaxation process is one of irreversible magnetisation changes, and is obtained from the differential of the appropriate remanence curve (Uren, et al. 1988), as discussed in §2.6.2.3. Measurements of the time dependence of magnetisation are made using the method detailed by (Gaunt 1986). Specifically, data is obtained in the second and third quadrants of the hysteresis loop by first saturating the sample in first quadrant, and then applying a constant negative field to the sample. The fluctuation field H_f is then given by equation 2.31 (Néel 1951) (Street, et al. 1952).

$$H_f(H) = S(H) / \chi_{irr}(H) \tag{2.31}$$

H_f is typically several oersted, as shown in figure 2.9, and may be thought of in terms of thermal energy acting on the magnetic moment as would a fluctuating magnetic field.

For the case of a fully aligned system of uniaxial single domain particles, the fluctuation field can be shown for fields below H_K to be (Chantrell, et al. 1986)

$$S(H) = \chi_{irr}(H)\left(1 - \frac{H}{H_K}\right)H_K / 50 \tag{2.32}$$

The numerical factor of 50 arises from the appearance of $2\ln(tf_0)$. This relationship is particularly useful as $\chi_{irr}(H)$ can be readily obtained from the differential of the DC demagnetisation curve, as detailed in §2.6.2.2. Experimental studies have found that although equation 2.32 produces the correct variation of S with H for a partially aligned γ-Fe_2O_3 tape, the magnitude of S is incorrect (Uren, et al. 1989). On comparing equations 2.31 and 2.32, these workers found that the best fit to the experimental data was obtained with the factor 50 replaced with 203 for a tape with a squareness of 0.8.

Interestingly, studies by (Barbier 1954) have shown a near liner relationship between the fluctuation field and the coercivity for a range of materials, as shown in figure 2.9. This phenomenological plot has been the focus of further theoretical studies, which effectively describe the relationship between the magnetic viscosity and coercivity for a wide range of interacting systems (Liu, et al. 1990) (Liu, et al. 1991).

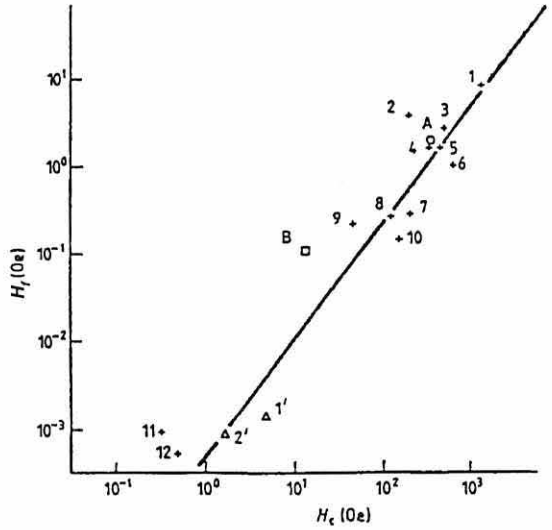

Figure 2.9 Plot of H_f against H_c for 1. Co ferrite 2. magnetite 3. Alnico 4. Alnico 5. iron powder 6. Alnico 7. Alnico (annealed) 8. nickel powder 9. iron-cobalt 10. iron-cobalt 11. Ni-Zn ferrite 12. soft iron A. Alnico B. hard steel 1'. semi-hard steel 2'. soft steel.

2.5.2.2 Activation Volumes

The concept of the activation volume υ was introduced by (Wohlfarth 1984). Arguing on dimensional grounds he outlined two definitions of the activation energy E, such that

$$E = kT = \upsilon M_s H_f \quad \text{and} \tag{2.33}$$

$$H_f = \frac{kT}{\upsilon M_s} \tag{2.34}$$

The activation volume describes the volume of magnetic material which reverses coherently, and "will be the actual particle volume for an isolated single-domain particle and the effective volume of the material covered by a single jump between pinning centres for a domain-wall motion process" (Wohlfarth 1984). In his pioneering work

(Wohlfarth 1984) also extended the (Barbier 1954) plot of figure 2.9. From the slope of this empirical study, the coercivity as a function of activation volume is given

$$H_c \approx \upsilon^{-x} \quad x = 0.73 \tag{2.35}$$

in agreement with several theoretical models (Hilzinger, et al. 1976) (Zijlstra 1982).

(Gaunt 1986) extended equation 2.34 and considered the effect of a distribution of activation energies. Consequently, the fluctuation field is related to the dependence of the energy barrier ΔE on the applied field H, so that

$$H_f = \left.\frac{kT}{\left(-\partial\Delta E / \partial H\right)}\right|_T \tag{2.36}$$

Using equations 2.3, 2.23 and 2.31, along with equation 2.36, solving for υ gives

$$H_f = \frac{kT}{\upsilon M_s\left(1 - H / H_K\right)} \tag{2.37}$$

Generally, υ obtained from equation 2.37 will be larger than that obtained from 2.34. (Gaunt 1986) interpreted υ in terms of the change in magnetic moment, such that the activation volume may be defined as "the volume associated with the magnetisation change between maximum and minimum energy positions of a domain wall or maximum and minimum orientations for the case of a single domain". The interpretation of the activation volume has been investigated by a host of workers, with υ referred to as the Barkhausen volume (Bruno, et al. 1990), the switching unit (Corradi, et al. 1990), the switching volume (Malhotra, et al. 1996) and the critical volume (O'Grady, et al. 1998).

However, studies involving the switching model of (Sharrock, et al. 1981) (Flanders and Sharrock 1987) (Sharrock 1990) (Sharrock 1994) also use the terms 'switching volume' and 'switching unit' in their investigations of the time dependence of coercivity, as described presently in §2.5.3. In order to avoid confusion, these workers have determined that this switching volume V cannot be identified with the

explicitly field-dependent activation volume υ. An activation volume reversal is considered as an essentially simultaneous event involving a single energy barrier, likewise for switching by coherent rotation, V would be considered to be the entire particle volume. In more complex reversal modes, the switching unit V may be a fraction of the particle volume. However, if the reversal mechanism is incoherent but simultaneous, as in fanning (§2.4.2), V is the entire particle volume (Sharrock 1994).

2.5.3 Thermal Switching Model

The mechanism of thermally activated reversal is of considerable interest to the magnetic storage industry because of the large difference between the timescales of the recording process and the required storage stability. High density recording media must have a sufficient coercivity to resist demagnetisation effects for archival storage stability, within the practical capabilities of available recording transducers. However, it is well known that the coercivity is dependent on the timescale of the reversal process (Néel 1949) which provokes conflicting requirements for writing and storage coercivities. Historically, coercivity measurements of particulate media over short timescales have been reported as early as 1974 (Thornley, et al. 1974). However, these measurements are somewhat difficult to perform, which has led to the development of the thermal switching model of (Sharrock, et al. 1981). With this model, the coercivity may be measured over two appreciably different and convenient timescales, using standard techniques (§2.6.1), to predict the coercivity over many orders of magnitude. This is shown schematically in figure 2.10, after (Sharrock 1990).

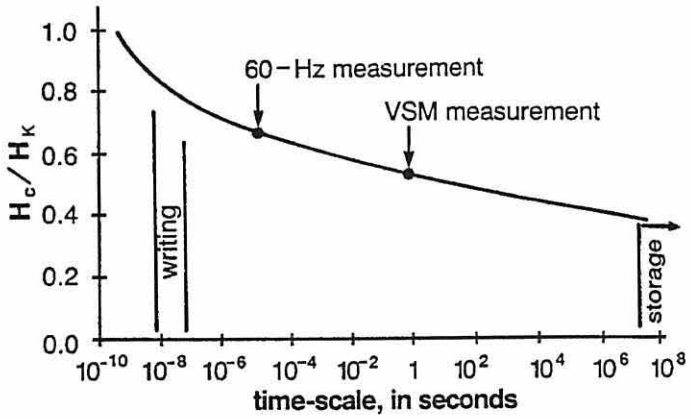

Figure 2.10 Typical variation of the effective coercivity $H_c(t)$ upon the timescale of the measurement process, according to equation 2.40.

For simplicity, the model assumes an assembly of identical, non-interacting uniaxial single domain particles having their easy axes aligned parallel to the applied field. Undertaking an Arrhenius-Néel relaxation, the time dependence of the reduced magnetisation m(t) can be represented using equations 2.24 and 2.25, such that

$$m(t) = 2\exp\left[-f_0 t \exp\left(\frac{-\Delta E}{kT}\right)\right] - 1 \tag{2.38}$$

The energy barrier height ΔE for a single particle with its easy axis aligned parallel to the applied field is given by equation 2.23, and reproduced

$$\Delta E = K_u V\left(1 - H / H_K\right)^2 \tag{2.39}$$

Using the criterion m = 0 at the coercivity, equations 2.38 and 2.39 yield an expression for the time variation of the coercivity $H_c(t)$, often referred to as Sharrock's Law.

$$H_c(t) = H_K\left(1 - \left[\frac{kT}{K_u V}\ln\left(\frac{f_0 t}{0.693}\right)\right]^{1/2}\right) \tag{2.40}$$

However, in common with the model described presently in §2.5.4, equation 2.40 artificially limits $H_c \leq H_K$ which is not meaningful when the timescale approaches $1/f_0$. In a further modification of equation 2.40, (Sharrock 1994) incorporated the theoretical argument of (Victora 1989), who suggested that for case of the applied field not aligned with the preferred axis, the exponent in equation 2.39 is predicted to be 3/2. Consequently, recent investigations by Doyle and his co-workers, e.g. (He, et al. 1996) (Stinnett, et al. 1998b), varied the exponent in equation 2.40 between 1/2 and 1.

Equation 2.40 contains only two unknowns: H_K and the product $K_u V$. These may be determined if the coercivity is measured over at least two considerably different timescales, i.e. hysteresis loop tracer and slowly swept vibrating sample magnetometer (VSM). Furthermore, if the saturation magnetisation M_s is known, K_u and V can be individually resolved using equation 2.3. The effectiveness of this approach was

demonstrated by (Sharrock, et al. 1981) from studies of γ-Fe_2O_3 tape media. The two coercivity measurements were 322 Oe from the 60Hz loop tracer, and 288 Oe from the VSM, with M_s found to be 330 emu cm^{-3}. Fitting equation 2.40 to the experimental data gives H_K = 386 Oe, $K_u = 6.37 \times 10^4$ erg cm^{-3} and $V = 2.38 \times 10^{-16}$ cm^3. The attempt frequency f_0 was set at 2×10^9 Hz from the studies of (McNab, et al. 1968). Subsequently, equation 2.40 predicts the coercivity over a wide timescale, as calculated and shown as curve (a) in figure 2.11.

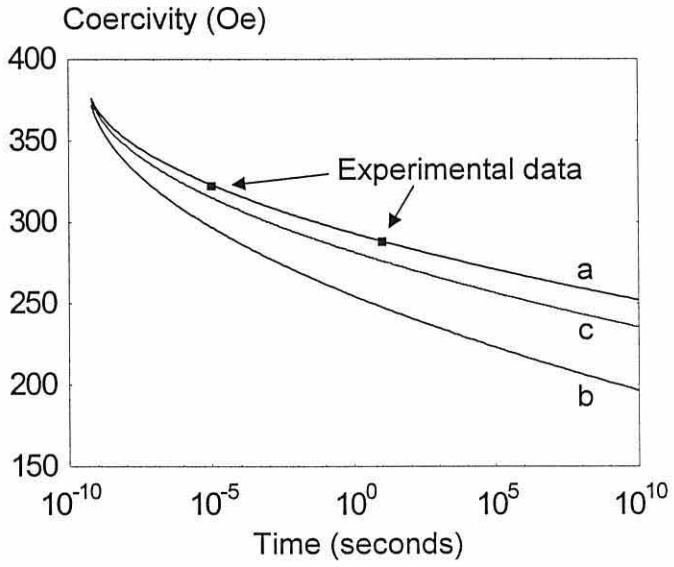

Figure 2.11 Dependence of the coercivity upon the timescale of the measurement process for γ-Fe_2O_3 recording media.

The predicted result of reducing the particle volume by a factor of two is illustrated in curve (b); likewise, curve (c) shows the expected coercivity for the original system with the temperature raised from 21°C (298K) to 100°C (377K).

The model has also been recognised as applicable for the study of print-through, which is the unintentional transfer of the recording on one layer of magnetic tape to the adjacent layers during storage on a reel (Bertram, et al. 1980). Print-through increases with time and temperature, and as such, is a consequence of thermal activation, although the fields responsible are considerably less than the required coercivity. In a classic study, (Flanders and Sharrock 1987) observed a relationship between print-through and the thermal stability factor (K_uV/kT). Therefore, for a constant value of K_u, print-through is associated with the particle size distribution.

Specifically, print-through effects particles toward the lower end of the size distribution, as very small particles are unable to retain a printed signal and large particles are too stable, in broad agreement with (Berkowitz, et al. 1985). Consequently, a useful estimation of the level of print-through in a final coated product may be obtained from time dependent coercivity measurements of the magnetic pigment prior to the manufacturing process.

2.5.4 Sweep-rate Model

A model describing the time dependence of magnetisation explicitly in terms of the sweep-rate dependence of coercivity $H_c(R)$ was derived by (el-Hilo, et al. 1992a). For an uniaxial particle with its easy axis aligned parallel to the applied field, the inverse of the relaxation time is given by (Brown 1963)

$$\tau_{\pm}^{-1} \cong f_0(1 \pm h)\exp\left[-\alpha(1 \pm h^2)\right] \tag{2.41}$$

where $\tau_{\pm}$ describes the relaxation time in and out of the field direction, h is the reduced field H/H_K and $\alpha = K_uV/kT$. Upon the application of a field, the time variation of the magnetisation is described using the rate equation of (Muller-Krumbhaar, et al. 1973)

$$\frac{dm(t)}{dt} = \left[m_e(h) - m(t)\right]\tau^{-1}(h) \tag{2.42}$$

where m_e is the reduced equilibrium magnetisation of the particle, and h is the reduced time dependent field $H(t)/H_K$. In equation 2.41, the probability of a transition into the field direction is dominant and consequently only the relaxation of $\exp[-\alpha(1-h)^2]$ is considered. Accordingly, for a system previously saturated in a positive direction, the time variation of the magnetisation during the application of a negative field may be determined on substituting equation 2.41 into 2.42, and performing the integration

$$m(t_s) = 2\exp\left(-\frac{f_0 H_K}{2\alpha R}\left[\exp^{-\alpha(1-h)^2} - \exp^{-\alpha}\right]\right) - 1 \tag{2.43}$$

where R is the sweep-rate dH/dt and t_s is the time that elapses during the field sweep. In equation 2.43, at fields approaching the coercivity, the contribution of $\exp(-\alpha)$ is negligible compared to that of $\exp[-\alpha(1-h)^2]$. Therefore, on specifying a distribution of particle volumes and using the criterion m = 0 at coercivity, equation 2.44 yields a relationship for the coercivity as a function of sweep-rate R

$$H_c(R) = H_K\left(1-\left[\frac{1}{\alpha_m}\ln\frac{f_0 H_K}{2\alpha_m}\frac{1}{R}\right]^{1/2}\right) \tag{2.44}$$

where $\alpha_m = K_u V_m/kT$ and V_m is the median particle volume, such that

$$H_c(R) = H_K\left(1-\left[\frac{kT}{K_u V_m}\ln\left(\frac{f_0 H_K kT}{2K_u V_m}\frac{1}{R}\right)\right]^{1/2}\right) \tag{2.45}$$

This variation which depends on physical parameters, produces a well defined behaviour of coercivity with sweep-rate. In a similar approach to that described in §2.5.3, fitting the relation to experimental data may be used to determine H_K, K_u and V_m. However, in previous studies of particulate media, V_m has been substituted by the activation volume υ for an optimum fit (de Witte, et al. 1993), as discussed in §6.

2.5.5 Gyromagnetic Switching

Upon the application of a magnetic field, the dynamic response of the magnetisation is to precess around the field axis at the Larmor frequency (Doyle, et al. 1998). After some time, which depends on the rate at which the magnetic energy can be dissipated to the lattice, static equilibrium is reached. Over moderate timescales, these dynamic processes may be ignored, and as such, the coercivity may be effectively described by either Sharrock's Law or the el-Hilo relation, as discussed in §2.5.3 and §2.5.4. However, with modern rigid disk systems recording 200kbpi whilst revolving at 15000 rpm (Sharrock 1999), the corresponding bit cell length of only 2ns is on the margin of these models' applicability.

Over these very short timescales, the reversal of the magnetic moment is described by the Landau-Lifshitz-Gilbert gyromagnetic equation (Gilbert 1955)

$$\frac{dM}{dt} = -\gamma_0 (M \times H) - \frac{\alpha_d}{M_s}\left(M \times \frac{dM}{dt}\right) \qquad (2.46)$$

where the gyromagnetic ratio γ_0 is -1.76×10^7 s^{-1} Oe^{-1} and α_d is a damping factor. The Gilbert modified Landau-Lifshitz equation appears more representative of a physical system as, unlike the Landau-Lifshitz formalism, d**M**/dt does not tend to infinity as the damping goes to infinity. In the absence of damping, the first term of equation 2.46 leads to infinite precession. The effect of the second term is to produce a damped precessional motion which eventually leads to an equilibrium position in which the magnetisation is collinear with the applied field. However, since this expression is only applicable at absolute zero, there have been recent attempts to model the effects of thermal agitation on the reversal process (Chantrell, et al. 1998). This was achieved by adding an effective field to equation 2.46, which also included terms for the exchange, magnetostatic, anisotropy and applied fields. A random field component was also added to reproduce the effect of thermal energy, following the work of (Brown 1979).

Utilising this approach, a series of simulations have concentrated on fast switching in longitudinal thin film media (Chantrell, et al. 1997) (Chantrell, et al. 1998) (Hannay, et al. 1999a) and (Hannay, et al. 1999b). These workers modelled a physically realistic microstructure with a lognormal grain size distribution and a random distribution of easy axes. As expected, the introduction of exchange coupling has the effect of increasing the remanence and reducing the coercivity, which leads to a very square hysteresis loop, as discussed in §2.6.2.4. The inclusion of exchange coupling tends to speed up the overall switching process, as the exchange helps realign the moments into the negative direction. However, over very short timescales, strongly exchange coupled media is found to exhibit a large rate of increase in coercivity which is not predicted by the Arrhenius-Néel law. This work in agreement with experimental observations of CoCrPtTa media over longer timescales (Richter, et al. 1999).

Likewise, very recent simulations of advanced metal particle media have revealed a rapid increase in dynamic coercivity in the nanosecond regime, which is made steeper

both by increased texture and dipolar interactions (Coverdale, et al. 2000), similar to that observed in §6.4.2. This represents an important limitation in terms of recording speed which is attributable to the breakdown of the Arrhenius-Néel formalism. Of course, the field dependence of the attempt frequency predicted by (Brown 1959) is a further complication, and further theoretical models accounting for both gyromagnetic precession and thermal switching are required (Doyle, et al. 1998).

2.5.6 Particle Interactions

The properties of magnetic materials are strongly influenced by interactions between magnetic domains. In the case of particulate recording media, which consists of densely packed particles, interactions often play a critical role in determining the magnetic and recording performance (Chantrell, et al. 1986). The nature of these interparticle interactions may be considered using figure 2.12, after (Cullity 1972).

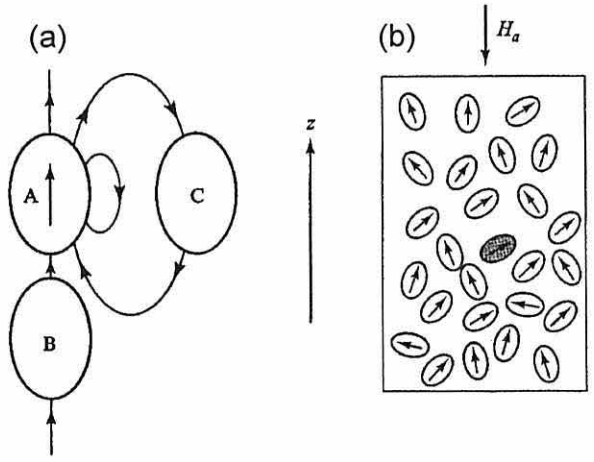

Figure 2.12 Particle interactions of (a) a simple three particle system (b) a complicated many-body problem.

It is clear from figure 2.12(a), that the external demagnetising field attributed to particle A acts to enhance the +z field direction of particle B, and opposes in the -z direction the field acting on particle C. Consequently, with respect to the applied field direction +z, the magnetostatic interaction field has the effect of magnetising particle B, along with a demagnetising effect on particle C. If the field is now reversed in the -z direction, the magnetostatic field of particle A now aids the reverse field acting on

particle C, thus resulting in a local reduction of the coercivity of particle C. Conversely, particle B tends to reverse at a higher field due to the interaction with particle A. Therefore, the field at which a particle reverses depends on both the relative position and separation of neighbouring particles.

If a similar approach is considered to the many-bodied problem of figure 2.12(b), it is evident that the field acting on the shaded particle is virtually impossible to determine quantitatively. Moreover, as the volume fraction of the magnetic particles in the assembly increases, the particles come closer together, the interactions become stronger, and the effective coercivity is reduced (Néel 1947), as discussed in §2.5.1.

With acicular metal particle media, the interactions tend to be predominately dipolar in nature (Mayo, et al. 1990a) and are characterised by a negative δM parameter, as described in §2.6.2.4. Physically, the demagnetising effect of dipolar coupled interactions tend to lead to long-range flux closure configurations, thereby stabilising the demagnetised state, with the vast majority of particles reversed in lower than expected fields (Spratt, et al. 1988). This is in agreement with Monte Carlo simulations of fine particles (Chantrell, et al. 1996), which found that dipolar interactions decrease both the coercivity and remanence, and increase the temperature above which the magnetisation will become superparamagnetic.

Recently, the effects of interactions on thermally activated magnetisation reversal at high frequencies has been simulated by a number of workers using a model based on the Landau-Lifshitz-Gilbert equation of motion (Gilbert 1955). Simulations of thin film media by (Greaves, et al. 1999) have found that the most stable medium, in terms of resistance to thermal demagnetisation, is one in which the overall interactions are close to zero. In terms of recording properties, the introduction of positive exchange coupling was also found to increase the minimum transition width, as discussed in §2.6.2.3. The effect of changing dipolar interactions on the switching properties of metal particle media at both DC and high frequencies has also been studied in this investigation, and described in §6.

2.6 Characterisation of Media

With the advent of magnetic recording media, various types of measurement techniques have developed to characterise these materials. These techniques provide an

understanding of the underlying physical processes of magnetisation and how this relates to media performance and stability. With the need for higher storage densities and faster access times demanded by the information storage industry, a reliable measure of the magnetic properties of recording media is essential to ensure their continued successful development and manufacture. The characterisation of recording media may be achieved through the series of magnetic measurements described in §2.6.2, using a variety of instruments and techniques discussed in §2.6.1.

2.6.1 Magnetometry

"There appear to be more methods and modifications of magnetic measuring techniques than there are magneticians" (Foner 1981). Although this rather perceptive observation maybe somewhat derisory, there has indeed been a wide variety of instruments developed over the years to measure the properties of magnetic materials.

Many measurements rely on detecting the motion of the sample in response to an externally applied field or field gradient, e.g. torque magnetometry (Miller 1950), alternating gradient force magnetometry (AGFM) (Zijlstra 1970), various Faraday methods discussed by (Cheetham, et al. 1987) and techniques such as cantilever magnetometry (Naughton, et al. 1997).

The measurement of magnetic induction is the basis of a wide variety of techniques, e.g. hysteresis loop tracers (Crittenden, et al. 1951), vibrating coil magnetometry (VCM) (Smith 1956), vibrating sample magnetometry (VSM) (Foner 1959), AC susceptibility, e.g. (Abel, et al. 1964) and superconducting quantum interference device magnetometry (SQUID) (Webb 1972).

Finally, there are magnetic imaging and resonance techniques, e.g. ferromagnetic resonance (FMR) (Snoek 1948), Mössbauer spectroscopy (Mössbauer 1958), nuclear magnetic resonance (NMR) (McCausland, et al. 1979), Lorentz microscopy (Hwang, et al. 1986) and magnetic force microscopy (MFM) (Binnig, et al. 1986).

The design and operation of the main instruments used to characterise the recording media samples studied in this investigation are detailed in the following sections; specifically the vibrating sample magnetometer (§2.6.1.1) and the alternating gradient force magnetometer (§2.6.1.2).

2.6.1.1 Vibrating Sample Magnetometer

The vibrating sample magnetometer (VSM) is a versatile instrument often used for the characterisation of magnetic recording media (Mee, et al. 1987). First proposed by (Foner 1959), the VSM is an induction instrument where the sample is sinusoidally vibrated perpendicular to a uniform DC field, as shown in figure 2.13.

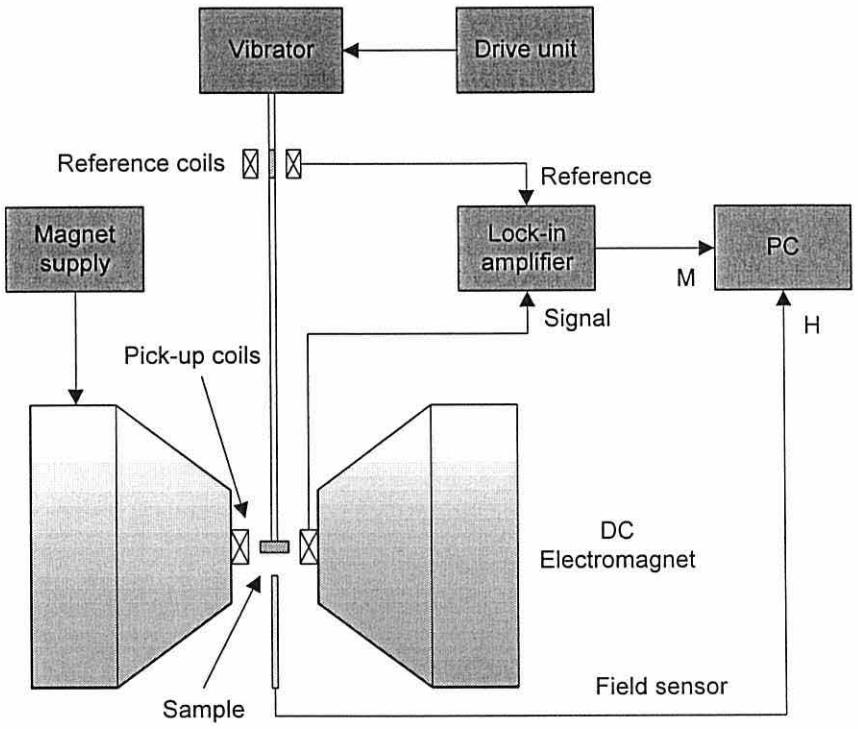

Figure 2.13 Schematic diagram of a vibrating sample magnetometer.

For the PAR 4500 vibrating sample magnetometer used in this study, the sample is vibrated at 81Hz with an amplitude of vibration of around 2mm. The sinusoidal vibration of the sample causes an analogous field distortion, and a voltage is developed in a pair of pick-up coils situated close to the sample by the changing flux Φ. The search coils are securely positioned on the pole pieces of the electromagnet for mechanical stability. Specifically, a coil having N number of turns and cross sectional area A induces a voltage which is proportional to the magnetic moment of the sample, as given by Faraday's law

$$v = -N\frac{d\Phi}{dt} = NA\frac{dM}{dt} \tag{2.47}$$

similar to that described in §3.4.1. This voltage is now passed to a phase sensitive detector, either as part of a lock-in amplifier or digital signal processor (DSP), which recovers and amplifies the required signal from the system noise. The reference signal, at the same frequency as the sample oscillation, may be provided directly from the vibrator drive or from an oscillating permanent magnet which induces a voltage in a separate search coil. The inclusion of such a reference feedback loop makes the measurement procedure insensitive to vibration and frequency changes (Cullity 1972).

Studies using a VSM only provide a relative magnetic measurement which must be calibrated against a reference of similar size and moment to that of the sample under investigation, if an absolute measure is required (Foner 1959). In recent years, careful pick-up coil design (Mallinson 1966) and detection techniques (Flanders, et al. 1993) have allowed commercial instruments to attain sensitivities better than 10^{-5} emu.

2.6.1.2 Alternating Gradient Force Magnetometer

The alternating gradient force magnetometer (AGFM) was developed from the vibrating reed magnetometer (Zijlstra 1970). Due to the continued improvement of piezoelectric sensing elements (Roos, et al. 1980), and further developments by (Flanders 1988) and (Richter, et al. 1988), commercial instruments regularly achieve sensitivities of 10^{-8} emu, making the AGFM 1000 times more sensitive than the VSM.

The principle of operation is shown schematically in figure 2.14. The sample is magnetised via a DC field from the electromagnet, whilst simultaneously subjected to a small alternating gradient field. This alternating gradient produces a periodic force on the sample which is detected, via the rod assembly, by a piezoelectric transducer (PZT). The PZT generates an appropriate output voltage as a function of force, hence magnetic moment of the sample. The alternating gradient field is supplied by a pair of stationary coils mounted on the pole pieces of the electromagnet, connected to an AC supply capable of producing a field at frequencies between 10Hz and 1kHz.

In order to obtain maximum sensitivity, the sample rod is driven at the mechanical resonant frequency f_o of the system (Flanders 1988), such that

$$f_o = \frac{w_r}{2\pi l_r^{\,2}} \sqrt{\frac{Y}{\rho}} \tag{2.48}$$

where l_r and w_r are the length and thickness of the rod respectively, Y is the elastic modulus and ρ is the density. Unlike the pick-up coils in a VSM, any noise generated by the PZT is independent of magnetic field (Flanders 1988), and the output voltage is measured using a low noise pre-amplifier and lock-in amplifier, with the frequency of the applied gradient field used as the reference signal. Alternatively, a DSP system can be employed as in the case of the commercial system used in this work.

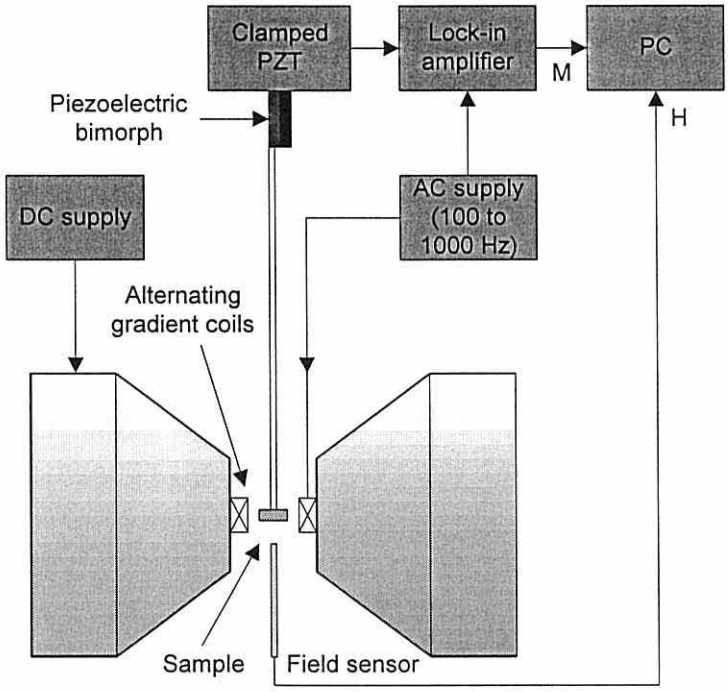

Figure 2.14 Schematic diagram of an alternating gradient force magnetometer.

Studies by (O'Grady, et al. 1993) have found that the magnitude of the AC field gradient is important when interpreting results, as the effect of the gradient is to act as an additional field to assist moment reversal. These workers examined samples of CrO_2 tape and NiFe thin film in a modified commercial AGFM capable of producing field gradients between 0.04 Oe mm^{-1} and 4 Oe mm^{-1}, and found that the most reliable results were obtained with a minimum field gradient. Typically, a 2mm sample measured with the minimum gradient experiences a maximum AC field at the sample edge of only 0.04 Oe, and zero field at the centre of symmetry.

In common with the VSM, the AGFM requires calibration with a Pauli paramagnet if an absolute measure of the moment is required. This may be achieved by

compensating for the magnetic moment of the sample using a loop current that is adjusted using a zero detection circuit (Frey, et al. 1988).

The system installed in our laboratories is a Princeton Measurement Corporation™ MicroMag™ 2900 AGFM. The instrument is equipped with an automated tuning feature to ensure operation at resonance, and software to aid positioning of the sample at the centre of symmetry of the gradient coils. This instrument has a measured sensitivity of 2×10^{-8} emu for a time constant of 1 second (O'Grady, et al. 1993).

2.6.2 Magnetic Measurements

The primary characterisation of recording media is achieved from the static properties obtained from VSM or AGFM measurements (Chantrell, et al. 1992). Magnetic measurements may be performed by plotting the magnetisation against a cyclic variation of the applied field to produce a hysteresis loop. From a measure of hysteresis, the primary characterisation parameters are obtained (§2.6.2.1). However, as irreversible magnetisation changes are the basis for remanence and coercivity, the measurement of the principal remanence curves (§2.6.2.2) provides useful information about the distribution of switching fields (§2.6.2.3) and interaction effects in particles (§2.6.2.4).

2.6.2.1 Hysteresis Loops

The measurement of hysteresis is extremely important in the characterisation of recording media. A typical hysteresis loop, along with the definition of several useful magnetic parameters is shown in figure 2.15.

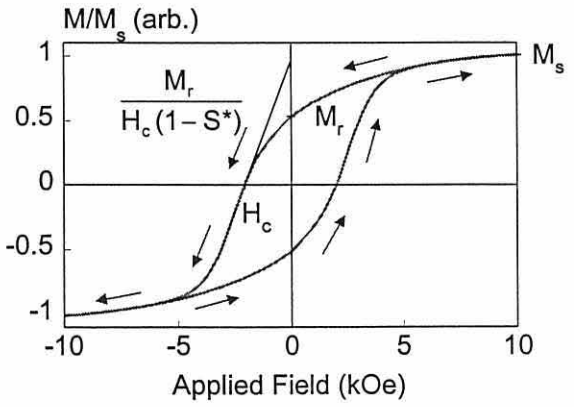

Figure 2.15 Hysteresis loop and measurement parameters.

The magnetisation curve from the demagnetised state to saturation is termed the initial magnetisation curve, whilst the hysteresis loop from positive to negative saturation is known as the major hysteresis loop. The basic parameters determined from such a hysteresis loop are specified as follows (O'Grady 1990) (Chantrell, et al. 1992).

i. Coercivity H_c, which is the reverse field necessary to reduce the previously saturated magnetisation to zero.

ii. Squareness is the ratio of the remanent magnetisation M_r to the saturation magnetisation M_s, i.e. $Sq. = M_r / M_s$. For uniaxial single domain particles, squareness is an indication of the degree of particle alignment in a tape, and a measure of the ability of the media to exhibit a sharp transition of reversal.

iii. Orientation ratio is a measure of the anisotropy of the remanent magnetisation. By rotating the sample so that it is measured perpendicular to the coating direction, the orientation ratio may be defined through $OR = Sq._{//} / Sq._{\perp}$. In terms of recording properties, the signal to noise ratio of highly oriented systems is enhanced due to the narrower switching field distribution (Köster 1984).

iv. Switching field distribution (SFD) is the measured spread of particle coercivities, as discussed in §2.5.1. The width of the SFD strongly influences the recording performance of media, and may be measured in several ways from the hysteresis loop. The SFD may be determined from the differential of the loop in the second and third quadrants, and is simply quoted as the full width at half maximum (FWHM) of the derivative Δh_c (Manly 1973). However, the most popular method to characterise the SFD width is to use the (1-S*) figure of merit determined by (Williams, et al. 1971) and endorsed by (Köster 1984). The parameter S* is the length of the line joining the magnetisation axis to a tangent to the curve at $H = H_c$, as shown in figure 2.15, and represented by equation 2.49.

$$\left(\frac{dM}{dH}\right)_{(H=H_c)} = \frac{M_r}{H_c(1-S^*)} \tag{2.49}$$

It has been suggested that (1-S*) is the best single parameter for the characterisation of recording media, mainly due to the ease of measurement (Köster 1984). Nevertheless, is should be noted that since (1-S*) and Δh_c are determined at

fields around the coercivity, these parameters will be susceptible to time dependence and sweep-rate effects. Consequently, an accurate measure of the SFD may be determined from the differential of the remanence curve, where reversible components of magnetisation do not contribute (Köster 1984), as described in §2.6.2.3.

2.6.2.2 Remanence Curves

Remanence curves, unlike hysteresis loops, measure only irreversible changes in magnetisation. There are two principal remanence curves, the isothermal remanent magnetisation (IRM) curve $M_r(H)$ and the DC demagnetisation (DCD) curve $M_d(H)$, as shown in figure 2.16.

The IRM curve is obtained by measuring the remanence of a previously demagnetised sample as the applied field is increased. Specifically, a small positive field is applied to the sample, which is then removed and the remanent magnetisation recorded. This process is then repeated for progressively larger fields until the saturation remanence $M_r(\infty)$ is reached. Obviously, in order to minimise time dependence effects, the positive field is applied for a constant period of time, typically 30 seconds, prior to each remanence measurement. The remanent coercivity H_{cr}' of the IRM curve is the field that gives rise to half of the saturation remanence.

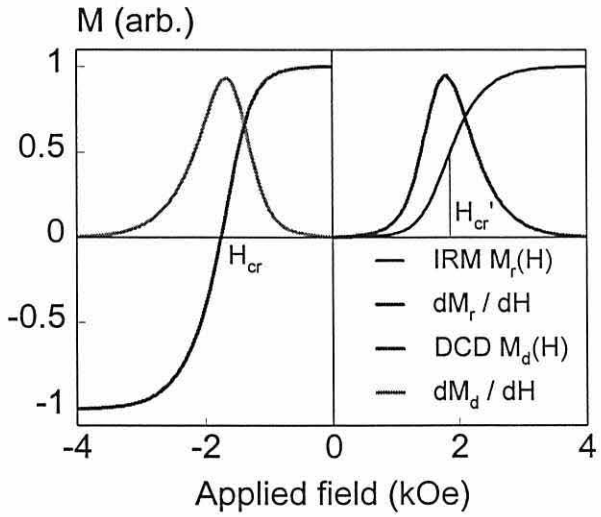

Figure 2.16 Typical isothermal and DC demagnetisation remanence curves with their appropriate switching field distributions.

The DCD curve is obtained by initially saturating the sample in a large positive field. A small reverse field is then applied in the opposite direction, which is then removed and the remanent magnetisation is measured. This process is repeated for increasingly larger negative fields until reverse saturation is reached. The remanent coercivity H_{cr} of the DCD curve is then defined as the field required to reduce M_d to zero, as shown in figure 2.16.

Pulsed field measurements of metal particle recording media, presented in §6, are performed as pulsed DCD curves, and closely resemble the digital recording process where positive saturation remanence is used to represent logic 1, and negative saturation remanence is used to represent logic 0. These measurements are similar to those described by (Doyle, et al. 1993) and (Hancock, et al. 1996). In this way, the high speed switching characteristics may be determined by measuring H_{cr} for varying short duration field pulses.

Conversely, pulsed field studies of metal particle dispersions, described in §4, are performed as pulsed IRM curves, to give an indication of the dispersion quality. Applying pulsed fields to an initially demagnetised sample provides an indication of the state of a dispersion without field induced aggregation of the particles, as discussed by (Hancock, et al. 1996) (Greaves, et al. 1997).

2.6.2.3 Switching Field Distributions

As discussed in §2.5.1, particles in recording media invariably exhibit distributions of particle size, shape and composition (Sharrock 1990) which leads to a subsequent spread of energy barriers $f(\Delta E)$ and, as a result, coercivities. In general, the fraction of particles that give rise to remanence is given by (O'Grady, et al. 1992)

$$M_r = M_r(\infty) \int_{\Delta E_c}^{\infty} f(\Delta E) d\Delta E \qquad (2.50)$$

where ΔE_c is some critical energy barrier above which a thermally activated transition is possible. To measure a remanence curve, the applied field is progressively increased, which raises the lower limit of the integral in equation 2.50 over the energy barrier

distribution. In this way the energy barrier distribution, which governs the switching field distribution, may be obtained from the differential of the remanence curve.

Clearly, the width of the SFD is an important parameter for characterising recording media, as it is known to influence the recording performance (McCary 1971) (Bertram, et al. 1978). Apart from the ability to magnetise spontaneously, the main requirement for recording media is that the remanent magnetisation is sufficiently large so that the signal amplitude may be detected during reproduction. Highly textured media with a narrow distribution of easy axes exhibits a narrow SFD, high squareness and negligible demagnetising loss. The minimum transition length α allowed by demagnetisation effects in longitudinal recording is given by the analysis due to (Williams, et al. 1971)

$$\alpha = \left(\frac{M_r \delta d}{2\pi H_c} \right)^{1/2} \tag{2.51}$$

which was later extended by (Bertram 1986b) to give

$$\alpha = \frac{d(1-S^*)}{\pi Q} + \sqrt{\left(\frac{d(1-S^*)}{\pi Q} \right)^2 + \frac{M_r \delta d}{\pi Q H_c}} \tag{2.52}$$

where δ is the thickness of the magnetic coating, d is the head to medium spacing and Q is a head field constant. At higher densities, as the transitions become shorter, the demagnetising field and the loss associated with it becomes progressively larger. However, it is clear from equation 2.52, that a narrow SFD (increasing S*) yields a shorter minimum transition length.

The differential of M with respect to H is the susceptibility, and as remanence curves are a measure of irreversible magnetisation changes, the differential of a remanence curve is termed the irreversible susceptibility $\chi_{irr}(H)$. (Néel 1951) suggested that the effect of thermal agitation may be related in some way to the irreversible susceptibility, as shown by equation 2.31; where the magnetic viscosity S is obtained in the second and third quadrants of the hysteresis loop by first saturating the sample in first quadrant, similar to the manner in which the DCD curve is measured.

Consequently, (Uren, et al. 1988) claimed that the value of the irreversible susceptibility obtained from the differential of the DCD curve is the most appropriate selection. In the absence of interactions, (Wohlfarth 1958) demonstrated that the differentials of both the IRM and DCD curves should be equal, such that

$$\overline{M}_d(H) = 1 - 2\overline{M}_r(H) \tag{2.53}$$

where the overscore indicates that the value is normalised to $M_r(\infty)$. As a result, the differential of the DCD curve requires a correction factor of two since the saturation remanence $M_d(\infty)$ changes from +1 to -1, as indicated in figure 2.16.

2.6.2.4 δM Studies

As discussed in §2.5.6, particle interactions play a critical role in determining the properties of media. The study of interactions was first demonstrated by (Henkel 1964) who plotted $M_d(H)$ against $M_r(H)$. In the absence of interactions, the so called 'Henkel plot' is linear and follows the Wohlfarth relation of equation 2.53. Deviations above and below this line indicate negative and positive interactions respectively.

(Kelly, et al. 1989) used a similar technique, in which a further term δM(H) was added to equation 2.53 in order to retain field information, given by

$$\delta M(H) = \overline{M}_d(H) - \left[1 - 2\overline{M}_r(H)\right] \tag{2.54}$$

Consequently, a δM curve is determined from a comparison of the two principal remanence curves, and shows the effective magnitude of the interactions at various fields as the magnetisation reversal occurs, as shown in figure 2.17(b). The δM parameter is generally positive where exchange coupling dominates (Kelly, et al. 1989) and negative for dipolar coupled systems (O'Grady, et al. 1992).

It is clear from figure 2.17, as with all acicular particulate media, a negative δM parameter is observed over the entire field range indicating that it is easier for the system to be demagnetised rather than magnetised (O'Grady, et al. 1992). Physically, during demagnetisation, the local magnetic field from dipolar interactions between the particles tends to promote the demagnetised state.

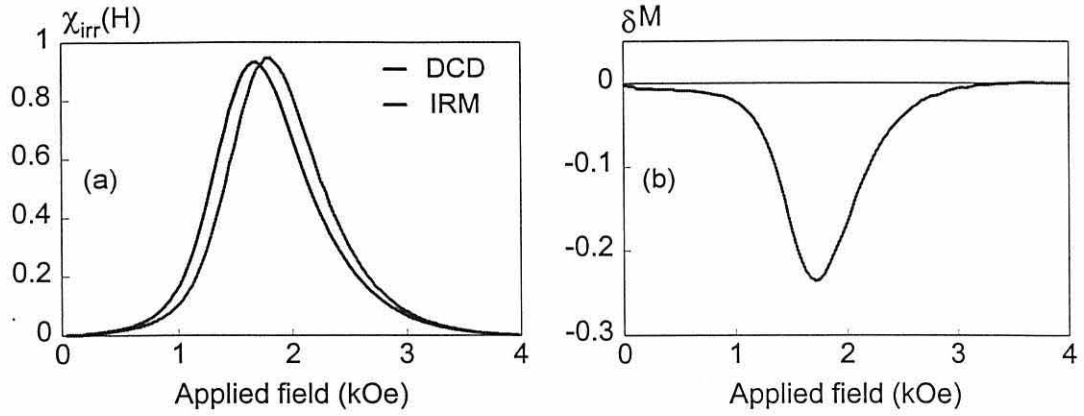

Figure 2.17 (a) Switching field distributions and obtained (b) δM curve for a metal particle tape sample.

In thin film media, the general trend for the plot is to increase to a positive peak at low fields, then decrease rapidly around the coercivity to a negative δM peak during the demagnetisation transition region (Kelly, et al. 1989). Significantly, the maximum slope of the δM curve at the region where the character of the interactions change from magnetising to demagnetising has been found to correlate well with the media noise; presently a popular approach originated by (Mayo, et al. 1991) (el-Hilo, et al. 1992b).

In a further application of this technique, (Mayo, et al. 1990b) examined the δM curves of a BaFe dispersion during the manufacturing process. A decrease in interactions was observed, resulting from the weakening in stacks of particles as the milling process continued.

References

Abel, W. R., Anderson, A. C., Wheatley, J. C., *Rev. Sci. Instrum.* **35**, 444-449 (1964).

Aharoni, A., *J. Appl. Phys.* **57**, 4702-4705 (1985).

Barbier, J. C., *Ann. Phys. Paris* **9**, 84-140 (1954).

Bean, C. P., Livingston, J. D., *J. Appl. Phys.* **30**, 120S-129S (1959).

Berkowitz, A. E., Goehner, R. P., Hall, E. L., Flanders, P. J., *J. Appl. Phys.* **57**, 3928-3930 (1985).

Bertram[b], H. N., *Proc. IEEE* **74**, 1494-1511 (1986).

Bertram[a], H. N., *IEEE Trans. Magn.* **22**, 460-465 (1986).

Bertram, H. N., Neidermeyer, R., *IEEE Trans. Magn.* **14**, 743-745 (1978).

Bertram, H. N., Stafford, M. K., Mills, D. R., *Journal of the Audio Engineering Society* **28**, 690-705 (1980).

Binnig, G., Quate, C. F., Gerber, C., *Phys. Rev. Lett.* **56**, 930-933 (1986).

Brown, W. F., *IEEE Trans. Magn.* **15**, 1196 (1979).

Brown, W. F., *J. Appl. Phys.* **30**, 130S-132S (1959).

Brown, W. F., *J. Appl. Phys.* **34**, 1319-1320 (1963).

Bruno, P., et al., *J. Appl. Phys.* **68**, 5759-5766 (1990).

Chantrell, R. W., Coverdale, G. N., el-Hilo, M., O'Grady, K., *J. Magn. Magn. Mater.* **158**, 250-255 (1996).

Chantrell, R. W., Fearon, M., Wohlfarth, E. P., *Phys. Stat. Sol. (A)* **97**, 213-221 (1986).

Chantrell, R. W., Hannay, J., *J. Magn. Soc. Japan* **21**, 283-289 (1997).

Chantrell, R. W., Hannay, J. D., Wongsam, M., Schrefl, T., Richter, H. J., *IEEE Trans. Magn.* **34**, 1839-1844 (1998).

Chantrell, R. W., O'Grady, K., *J. Phys. D: Appl. Phys.* **25**, 1-23 (1992).

Chantrell, R. W., Wohlfarth, E. P., *Phys. Stat. Sol. (A)* **91**, 619-626 (1985).

Cheetham, A. K., Day, P., *Soild state chemistry techniques* (Oxford University Press, New York, 1987).

Corradi, A. R., Dinitto, C. A., Price, T. G., Green, W. B., *IEEE Trans. Magn.* **26**, 1888-1890 (1990).

Coverdale, G. N., Chantrell, R. W., *Paper HE-10, Intermag 2000, Toronto* (2000).

Crittenden, E. C., Hudimac, A. A., Strough, R. I., *Rev. Sci. Instrum.* **22**, 872-877 (1951).

Cullity, B. D., *Introduction to magnetic materials* (Addison-Wesley Publishing Company, 1972).

de Witte, A. M., el-Hilo, M., O'Grady, K., Chantrell, R. W., *J. Magn. Magn. Mater.* **120**, 184-186 (1993).

Doyle, W. D., He, L., Flanders, P. J., *IEEE Trans. Magn.* **29**, 3634-3636 (1993).

Doyle, W. D., Stinnett, S. M., Dawson, C., He, L., *J. Magn. Soc. Japan* **22**, 91-106 (1998).

el-Hilo[a], M., de Witte, A. M., O'Grady, K., Chantrell, R. W., *J. Magn. Magn. Mater.* **117**, L307-L310 (1992).

el-Hilo[b], M., O'Grady, K., Chantrell, R. W., Sanders, I. L., Howard, J. K., *IEEE Trans. Magn.* **28**, 3282-3284 (1992).

Flanders, P. J., *J. Appl. Phys.* **63**, 3940-3945 (1988).

Flanders, P. J., Graham, C. D., *Rep. Prog. Phys.* **56**, 431-492 (1993).

Flanders, P. J., Sharrock, M. P., *J. Appl. Phys.* **62**, 2918-2928 (1987).

Foner, S., *IEEE Trans. Magn.* **17**, 3358-3363 (1981).

Foner, S., *Rev. Sci. Instrum.* **30**, 548-557 (1959).

Frei, E. H., Shtrikman, S., Treves, D., *Phys. Rev.* **106**, 446-455 (1957).

French, A. P., Taylor, E. F., *An introduction to quantum physics* (Nelson, 1979).

Frenkel, J., Dorfman, J., *Nature* **126**, 274-275 (1930).

Frey, T., Jantz, W., Stibal, R., *J. Appl. Phys.* **64**, 6002-6007 (1988).

Gaunt, P., *J. Appl. Phys.* **59**, 4129-4132 (1986).

Gilbert, T. L., *Phys. Rev.* **100**, 1243 (1955).

Givord, D., Tenaud, P., Viadieu, T., Hadjipanayis, G., *J. Appl. Phys.* **61**, 3454-3456 (1987).

Greaves, S. J., Hancock, C. P., O'Grady, K., Lane, A. M., *J. Magn. Soc. Japan* **21**, 241-244 (1997).

Greaves, S. J., Muraoka, H., Sugita, Y., Nakamura, Y., *J. Magn. Magn. Mater.* **193**, 409-411 (1999).

Hancock, C. P., Greaves, S. J., O'Grady, K., Williams, R. G., Owens, A. R., *IEEE Trans. Magn.* **32**, 4037-4039 (1996).

Hancock, C. P., O'Grady, K., el-Hilo, M., *J. Phys. D: Appl. Phys.* **29**, 2343-2351 (1996).

Hannay[a], J. D., Chantrell, R. W., Richter, H. J., *J. Appl. Phys.* **85**, 5012-5014 (1999).

Hannay[b], J. D., Walmsley, N. S., Chantrell, R. W., *J. Magn. Magn. Mater.* **193**, 245-248 (1999).

He, L., Doyle, W. D., Varga, L., Fujiwara, H., Flanders, P. J., *J. Magn. Magn. Mater.* **155**, 6-12 (1996).

Henkel, O., *Phys. Stat. Sol.* **7**, 919 (1964).

Hilzinger, H. R., Kronmüller, H., *J. Magn. Magn. Mater.* **2**, 11 (1976).

Hwang, C., et al., *J. Magn. Magn. Mater.* **54**, 1676-1678 (1986).

Jacobs, I. S., Bean, C. P., *Phys. Rev.* **100**, 1060-1067 (1955).

Kelly, P. E., O'Grady, K., Mayo, P. I., Chantrell, R. W., *IEEE Trans. Magn.* **25**, 3881-3883 (1989).

Kittel, C., *Phys. Rev.* **70**, 965-975 (1946).

Kittel, C., Galt, J. K., *J. Phys. C: Solid State Phys.* **3**, 437-564 (1956).

Knowles, J. E., *J. Magn. Magn. Mater.* **25**, 105-112 (1981).

Köster, E., *IEEE Trans. Magn.* **20**, 81-83 (1984).

Liu, J. F., Luo, H. L., *J. Magn. Magn. Mater.* **94**, 43-48 (1991).

Liu, J. F., Luo, H. L., *J. Magn. Magn. Mater.* **86**, 153-158 (1990).

Luborsky, F. E., *J. Appl. Phys.* **32**, 171S-183S (1961).

Luborsky, F. E., Morelock, C. R., *J. Appl. Phys.* **35**, 2055-2066 (1964).

Luborsky, F. E., Paine, T. O., *J. Appl. Phys.* **31**, 68S-70S (1960).

Malhotra, S. S., Shan, Z. S., Stafford, D. C., Liou, S. H., Sellmyer, D. J., *IEEE Trans. Magn.* **32**, 4019-4021 (1996).

Mallinson, J. C., *J. Appl. Phys.* **37**, 2514-2515 (1966).

Manly, W. A., *IEEE Trans. Magn.* **9**, 256-260 (1973).

Mayo[b], P. I., et al., *IEEE Trans. Magn.* **26**, 228-230 (1990).

Mayo[a], P. I., Erkkila, R. M., Bradbury, A., Chantrell, R. W., *IEEE Trans. Magn.* **26**, 1894-1896 (1990).

Mayo, P. I., et al., *J. Magn. Magn. Mater.* **95**, 109-117 (1991).

McCary, R. O., *IEEE Trans. Magn.* **7**, 4-16 (1971).

McCausland, M. A. H., MacKenzie, I. S., *Advances in Physics* **28**, 305-456 (1979).

McNab, T. K., Fox, R. A., Boyle, A. J. F., *J. Appl. Phys.* **39**, 5703-5711 (1968).

Mee, C. D., Daniel, E. D., *Magnetic recording* (McGraw-Hill, Inc., 1987), vol. 1: Technology.

Meiklejohn, W. H., Bean, C. P., *Phys. Rev.* **102**, 1413-1414 (1956).

Mendelsohn, L. I., Luborsky, F. E., Paine, T. O., *J. Appl. Phys.* **26**, 1274-1280 (1955).

Miller, D. S., *Rev. Sci. Instrum.* **21**, 605-607 (1950).

Morrish, A. H., Yu, S. P., *Phys. Rev.* **102**, 670-673 (1956).

Mössbauer, R. L., *Z. Physik* **151**, 124-143 (1958).

Muller-Krumbhaar, H., Binder, K., *J. Stat. Phys.* **8**, 1 (1973).

Naughton, M. J., et al., *Rev. Sci. Instrum.* **68**, 4061-4065 (1997).

Néel, L., *Comptes Rendus Académie des Sciences Paris* **224**, 1550-1551 (1947).

Néel, L., *J. Phys. Rad.* **12**, 339-351 (1951).

Néel, L., *Ann. Géophys.* **5**, 99-136 (1949).

Néel, L., *Rev. Mod. Phys.* **25**, 293-296 (1953).

O'Grady, K., *IEEE Trans. Magn.* **26**, 1870-1875 (1990).

O'Grady, K., Chantrell, R. W., in *Studies of magnetic properties of fine particles and their relevance to materials science* J. L. Dormann, D. Fiorani, Eds. (Elsevier Science Publishers, 1992) pp. 93-102.

O'Grady, K., Chantrell, R. W., Popplewell, J., Charles, S. W., *IEEE Trans. Magn.* **17**, 2943-2945 (1981).

O'Grady, K., Dova, P., Laidler, H., *Proc. Mat. Res. Soc. Symp.* **517**, 231-242 (1998).

O'Grady, K., Lewis, V. G., Dickson, D. P. E., *J. Appl. Phys.* **73**, 5608-5613 (1993).

Oseroff, S. B., Franks, D., Tobin, V. M., Schultz, S., *IEEE Trans. Magn.* **23**, 2871-2873 (1987).

Richter, H. J., Hempel, K. A., *IEEE Trans. Magn.* **25**, 3446-3448 (1989).

Richter, H. J., Hempel, K. A., Pfeiffer, J., *Rev. Sci. Instrum.* **59**, 1388-1393 (1988).

Richter, H. J., Ranjan, R. Y., *J. Magn. Magn. Mater.* **193**, 213-219 (1999).

Roos, W., Hempel, K. A., C., V., Dederichs, H., Schippan, R., *Rev. Sci. Instrum.* **51**, 612-613 (1980).

Sato, M., Ishii, Y., Nakae, H., *J. Appl. Phys.* **53**, 6331-6334 (1982).

Sharrock, M. P., *IEEE Trans. Magn.* **35**, 4414-4422 (1999).

Sharrock, M. P., *J. Appl. Phys.* **76**, 6413-6418 (1994).

Sharrock, M. P., *IEEE Trans. Magn.* **26**, 193-197 (1990).

Sharrock, M. P., McKinney, J. T., *IEEE Trans. Magn.* **17**, 3020-3022 (1981).

Smith, D. O., *Rev. Sci. Instrum.* **27**, 261-268 (1956).

Snoek, J. L., *Physica* **14**, 207-217 (1948).

Spratt, G. W. D., Bissell, P. R., Chantrell, R. W., Wohlfarth, E. P., *J. Magn. Magn. Mater.* **75**, 309-318 (1988).

Stinnett[a], S. M., Doyle, W. D., *IEEE Trans. Magn.* **34**, 1681-1683 (1998).

Stinnett[b], S. M., Doyle, W. D., Flanders, P. J., Dawson, C., *IEEE Trans. Magn.* **34**, 1828-1833 (1998).

Stoner, E. C., Wohlfarth, E. P., *Proc. R. Soc. (London)* **A240**, 599-642 (1948).

Street, R., Woolley, J. C., *Proc. Phys. Soc.* **A62**, 562-574 (1949).

Street, R., Woolley, J. C., Smith, P. B., *Proc. Phys. Soc.* **B65**, 679-696 (1952).

Thornley, R. F. M., Williams, J. A., *IBM J. Res. Develop.* , 576-578 (1974).

Uren, S., O'Grady, K., Chantrell, R. W., Popplewell, J., *IEEE Trans. Magn.* **25**, 3656-3658 (1989).

Uren, S., Walker, M., O'Grady, K., Chantrell, R. W., *IEEE Trans. Magn.* **24**, 1808-1810 (1988).

Victora, R. H., *Phys. Rev. Lett.* **63**, 457-460 (1989).

Webb, W. W., *IEEE Trans. Magn.* **8**, 51-60 (1972).

Williams, M. L., Comstock, R. L., *17th AIP Conf. Proc.* **5**, 738-742 (1971).

Wohlfarth, E. P., *J. Phys. F: Met. Phys.* **14**, L155-L159 (1984).

Wohlfarth, E. P., *J. Appl. Phys.* **29**, 595-596 (1958).

Zijlstra, H., *Ferromagnetic materials: a handbook on the properties of magnetically ordered substances*. E. P. Wohlfarth, Ed. (Amsterdam: North-Holland, 1982), vol. III.

Zijlstra, H., *Rev. Sci. Instrum.* **41**, 1241-1243 (1970).

Chapter
3

Dispersion Pulsed Field Magnetometer

3.1 Introduction

This chapter details the development of a pulsed field magnetometer which allows the reversal processes of metal particle dispersions to be monitored, as presented in §4. The motivation behind the instrument lies with the fact that standard magnetic measurements of dispersions, using DC magnetic fields, alter the dispersion microstructure and yield results that are difficult to interpret and often not reproducible. Conversely, if the dispersion is rapidly changed using a pulsed field of short duration, this may be used to give an indication of the state of the microstructure without having to make allowances for field induced aggregation of particles.

The magnetometer consists of a pulse generator which produces well defined current pulses of over 125A, which are free from overshoot and ringing, with selectable pulse widths between 25μs and 130μs. The current pulse is driven into a small field coil assembly, the geometry of which is such that a magnetic field of over 4.7kOe is generated, with symmetrical rise and fall times of around 15μs. This short duration magnetic field impulse magnetises the wet dispersion sample, while a pair of anti-phase sense coils and integrator stage monitor the magnetisation of the sample under the field pulse. The output is monitored using a 500MHz digitising storage oscilloscope, allowing the dynamic magnetisation response to the applied pulsed field to be viewed in real-time.

The magnetometer presented here is an extension to previous work, where an instrument capable of producing fields of up to 1270 Oe enabled γ-Fe_2O_3 and CrO_2

dispersions to be studied in a similar manner (Hancock 1995). Accordingly, particular emphasis is placed on improvements in terms of field amplitude and homogeneity.

3.2 System Outline

Pulsed magnetic field generators have been developed by a host of workers (Wheeler, et al. 1987) (Ratcliffe 1987) (Herlach 1988) (Kido, et al. 1989) (Noggle, et al. 1990) (Herlach, et al. 1995) (Nojiri, et al. 1997) (Portugall, et al. 1997) (Jones, et al. 1998). Unfortunately, each of these systems does not meet the specification required for this study, which is a portable, controllable instrument capable of generating homogenous single-shot pulsed magnetic fields of greater than 3.0kOe in a small wire wound field coil. The termination of the pulse must return to zero in order to ensure that no DC field is applied to the dispersion giving rise to misleading low field particle orientation. The pulse width should be in the microsecond region, and should be adjustable to enable the marked difference in the mechanical and Néel reversal characteristics to be tracked.

The system is based upon the design of a magnetometer capable of generating pulsed magnetic fields of up to 1270 Oe (Hancock, et al. 1998). The instrument consists of a trickle-charged bank of four 4700μF capacitors, each rated at 250V, which are discharged in a controlled manner through eight power MOSFET differential current drivers into a field coil assembly. Each of the eight current drivers uses three International Rectifier™ IRF250 power MOSFETs, which are configured to drive 20A into the field coil. The power circuits are controlled using a digital control board consisting of a synchronous state machine clocked with a quartz oscillator. This allows the eight current sources to be turned on, and be in steady state, before the pulse which controls the switching of the gates of the devices arrives.

The dispersion sample is enclosed in a plastic tube, and upon application of a pulsed field, two anti-phase search coils connected to a bridge balance circuit cancel the common field, generating a voltage which is amplified and integrated, so that the signal recovered represents the change in magnetisation due to the sample alone. This voltage is monitored using a Tektronix™ TDS640 500MHz digitising oscilloscope, allowing the dynamic magnetisation response to the pulsed field to be viewed in real-time, as described in §4.

A block diagram representing the pulsed field magnetometer as a complete system is shown in figure 3.1.

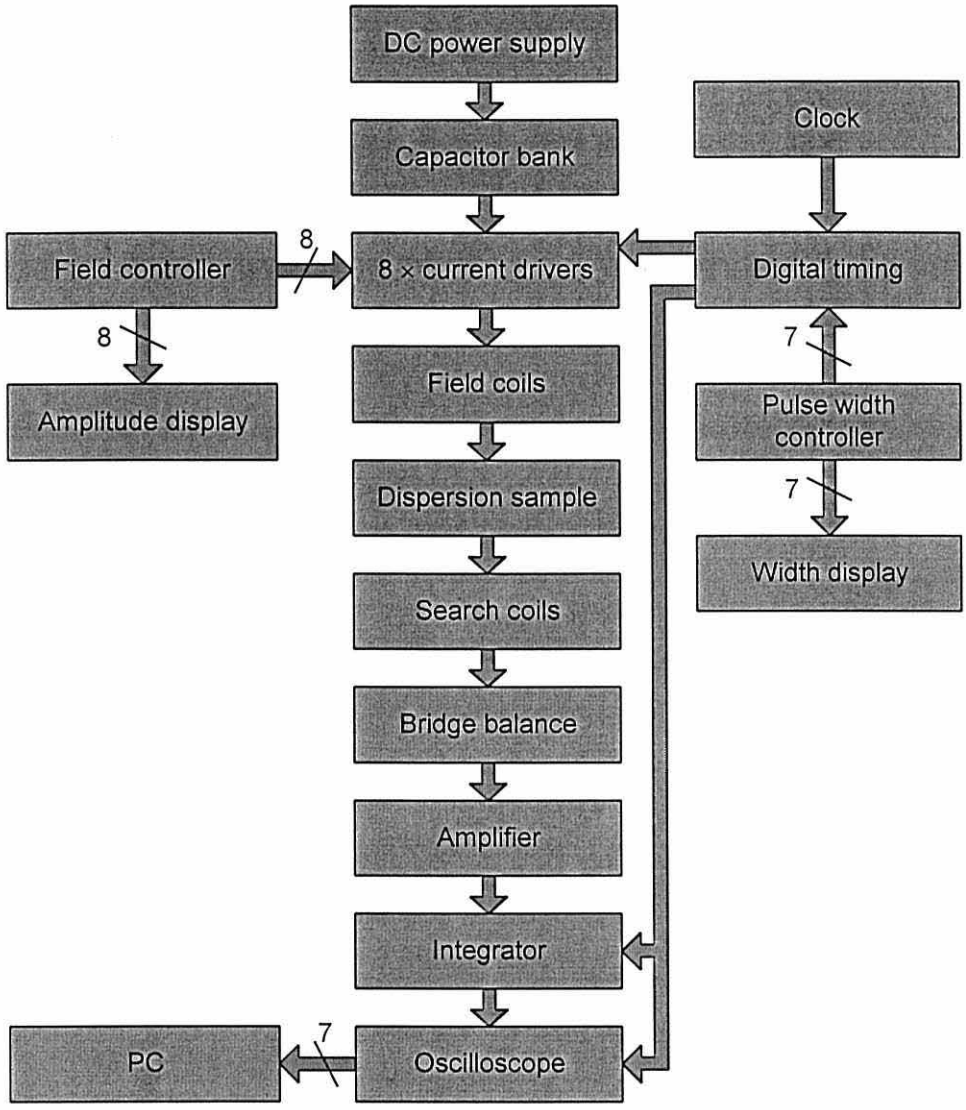

Figure 3.1 Pulsed field magnetometer system block diagram.

3.3 Pulsed Field Generation

This section outlines the techniques and circuitry used to generate short duration magnetic fields in the pulsed field magnetometer. From figure 3.1, this includes the capacitive energy source, MOSFET current drivers, pulse width controller and field coil assembly.

From the previous study of low coercivity pigment dispersions (Hancock 1995), the successful utilisation of differentially connected power MOSFETs to switch the pulsed current through small field coils via current 'steering' has also been applied to

this system. As a result, in order to produce a pulsed field of almost 5kOe, it was decided at an early stage to double the number of current drivers from four to eight. Further developments have permitted each driver to produce a peak pulse current of 20A into a modified field coil assembly, the geometry of which has increased both field magnitude and homogeneity. Of course, this is associated with increased coil inductance, and hence extended pulse rise and fall times.

As mentioned in §3.1, only improvements and modifications are presented in detail. The outline of the pulsed field system is also included for completeness.

3.3.1 Capacitive Power Supply

The DC power supply consists of a modified Kingshill™ NTM1515A linear unit configured to supply 150mA at 166V. The output of the supply is limited by R_1, a 2.2kΩ, 25W series resistor which is connected to the capacitor bank. The charged capacitor bank provides the necessary stored energy for the high current pulse, and consists of four 4700μF, 250V capacitors, C_1 to C_4, connected in parallel, which are connected to the field coils through the power MOSFET drivers. The main supply decoupling is provided by capacitors C_5 and C_6, whilst R_2 allows a discharge path for the capacitors, as indicated in figure 3.2.

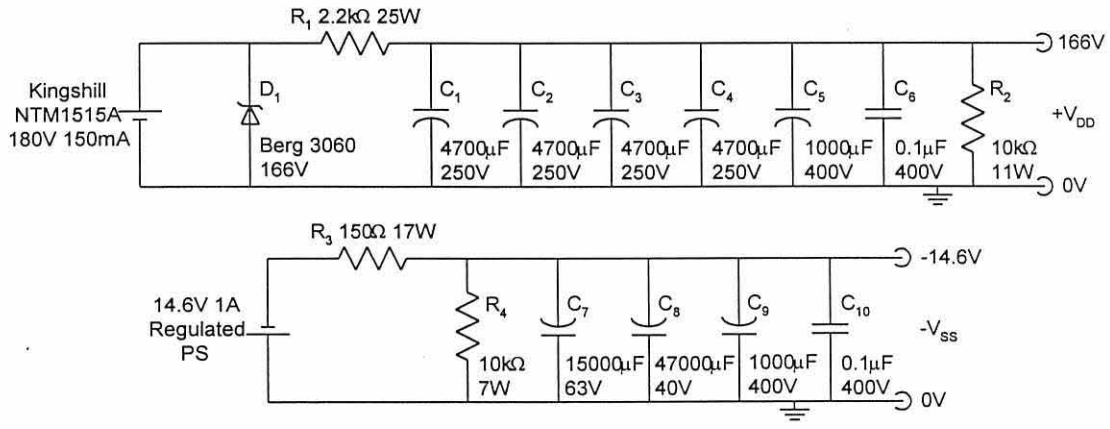

Figure 3.2 Capacitive energy source.

Figure 3.2 also shows a regulated -14.6V, 1A capacitive source that is used to supply the current source transistor T_3. The supply is provided by means of a bridge rectifier and National Semiconductor® LM337T linear voltage regulator. As with the

166V supply, capacitors C_7 and C_8 provide the capacitive charge, again decoupled through C_9 and C_{10}. Accompanying direct voltages of ±21V, 19V, -14.3V, 12V and 5V were also taken from the regulated supply with voltage levels specified from the adjustable regulators.

3.3.2 MOSFET Current Driver

A current driver incorporating power MOSFETs was chosen to switch the stored charge in the capacitor bank into the field coil assembly. Metal oxide field effect transistors (MOSFETs) were preferred to other semiconductor power devices such as power bipolar junction transistors (BJTs) and insulated gate bipolar transistors (IGBTs) as they have a large power handling capability, since there are no secondary breakdown effects which occur with fast switching transients in BJTs. This leads to a large safe operating area when used in switch mode operation, which is an important attribute when switching high levels of current into an inductive load because of the excessive levels of induced voltage generated. Power MOSFETs also exhibit a very low on-state resistance $r_{ds(on)}$, which for the International Rectifier™ IRF250 device is 0.85Ω, along with a high drain-source breakdown voltage BV_{DS} of 500V. Furthermore, the gate current requirement for power MOSFETs are significantly less than the base current of equivalently rated power transistors. Figure 3.3 shows the construction of an n-channel enhancement MOSFET, similar to the IRF250 device, together with its circuit symbol.

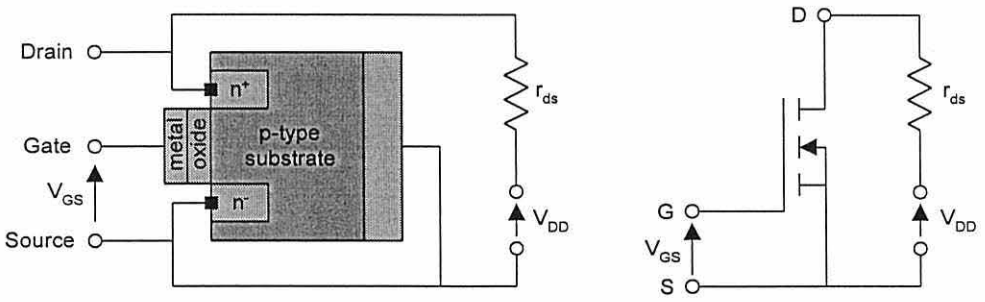

Figure 3.3 Construction of an n-channel enhancement MOSFET with its circuit symbol.

An enhancement MOSFET is a voltage-operated device requiring only a small gate current in order to turn it on and maintain it in the on state. From figure 3.3, application of a voltage which biases the gate positive with respect to the source will

convert the silicon surface beneath the gate oxide into a n-type layer or channel, thus connecting the source to the drain. Such an inversion layer is formed only if V_{GS} exceeds a threshold voltage V_T. As the voltage on the gate increases, the number of induced negative charges in the semiconductor increases, and as a result, the conductivity of the channel and the drain current i_d also increase. Thus, the drain current is enhanced by the positive gate voltage, with the on-state resistance $r_{ds(on)}$ governed primarily by the geometry of the source region (Millman, et al. 1987).

From figure 3.3, the dielectric oxide layer, the metallic contact regions and the semiconductor layers form a large gate-source capacitance C_{gs} of around 1600pF for the IRF250 device. If a single MOSFET is used to drive current through the field coil, then C_{gs} has to be charged to the gate-source threshold voltage V_T before the device can switch on, thus creating long switching times. To overcome this problem, two differentially connected MOSFETs can be arranged so that the gate capacitances are always partially charged to allow the transistor with the field coil load to be turned on quickly. This configuration is shown schematically in figure 3.4.

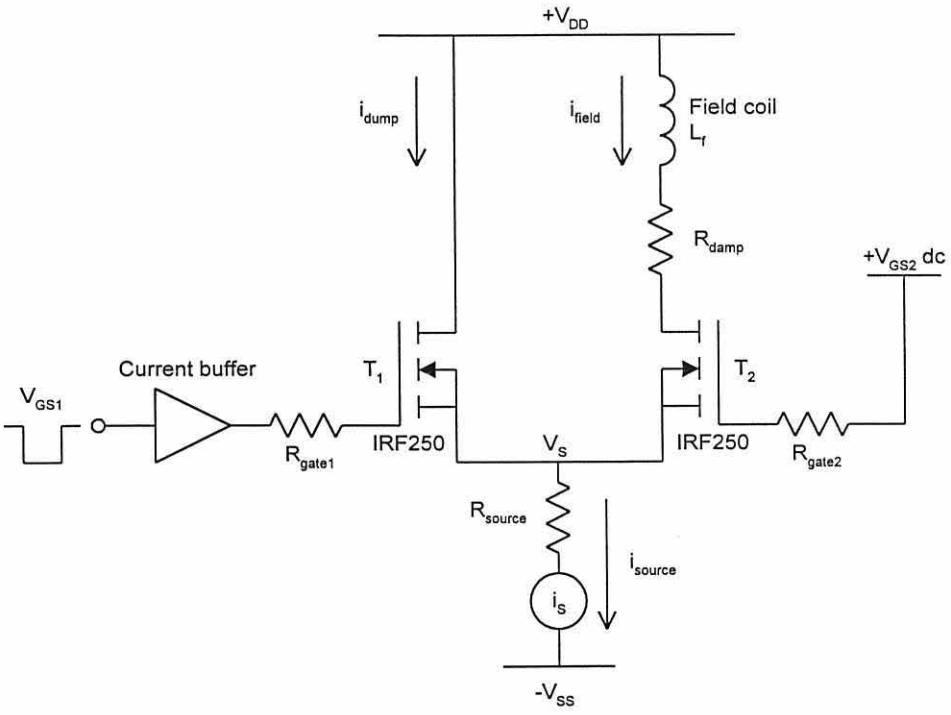

Figure 3.4 Differential driver field switching arrangement.

In this arrangement, one MOSFET is in a state of conduction, whilst the second is held at the gate-source threshold voltage V_T. Consequently, the time required to make

the second MOSFET fully conduct after the arrival of the gate pulse is comprehensively reduced. Specifically, when the gate-source voltage V_{GS1} is positive, MOSFET T_1 conducts and allows a steering current i_{dump} to flow. Accordingly, the source voltage V_S increases, and transistor T_2 is turned off since its gate-source voltage (V_{GS2}-V_S) is less than the required threshold voltage V_T. When V_{GS1} is negatively triggered, the gate-source voltage of T_2 is greater than the threshold voltage ($V_{GS2}>V_T$), T_1 is turned off and T_2 conducts, thus a current i_{field} is switched through the field coils L_f and damping resistor R_{damp}.

The response of the output current i_{field} is further determined by how rapidly charge can be injected into the gate terminal of transistor T_1. A gate pulse at T_1 activates the device in the transition region, the charge characteristics of which, are altered by the apparent increase in the gate-source capacitance C_{gs}. This Miller effect is established through the interaction of the gate-drain feedback capacitance C_{gd}, the result of which causes the gate voltage to stall with an associated loss of speed (Horowitz, et al. 1989). Accordingly, if a short turn-on time is required, a large gate current is essential to turn on the transistor rapidly. To inject a high current into the gate at switching, a Harris™ ICL7667 dual MOSFET driver was chosen to control transistor T_1. Furthermore, the driver has a low output impedance of 7Ω, with a variable output level that can be controlled by TTL inputs, as discussed in §3.3.2.1.

If the operation of transistors T_1 and T_2 is assumed to be identical, the current through the field coil i_{field} is given by equation 3.1,

$$i_{field} = \frac{i_{source}}{2} \pm \left[\frac{\sqrt{\left(\mu_n C_{ox} \frac{W}{L}\right) i_{source}}}{4} \right] V_{GS1} - V_{GS2} \qquad (3.1)$$

where μ_n is the electron mobility, C_{ox} is the gate-oxide capacitance, W is the inversion channel width and L is the channel length. Equation 3.1 indicates that the current switched through the field coils is controlled by physical device parameters, the constant current source i_{source} and the difference between the gate voltages V_{GS1}-V_{GS2}. Therefore,

in order to increase the configured field current in the practical driver to 20A, the value of R_{source} was reduced to 0.27Ω, as discussed in §3.3.2.1.

3.3.2.1 Practical Current Driver

A schematic diagram of one of the eight practical current drivers is shown in figure 3.5.

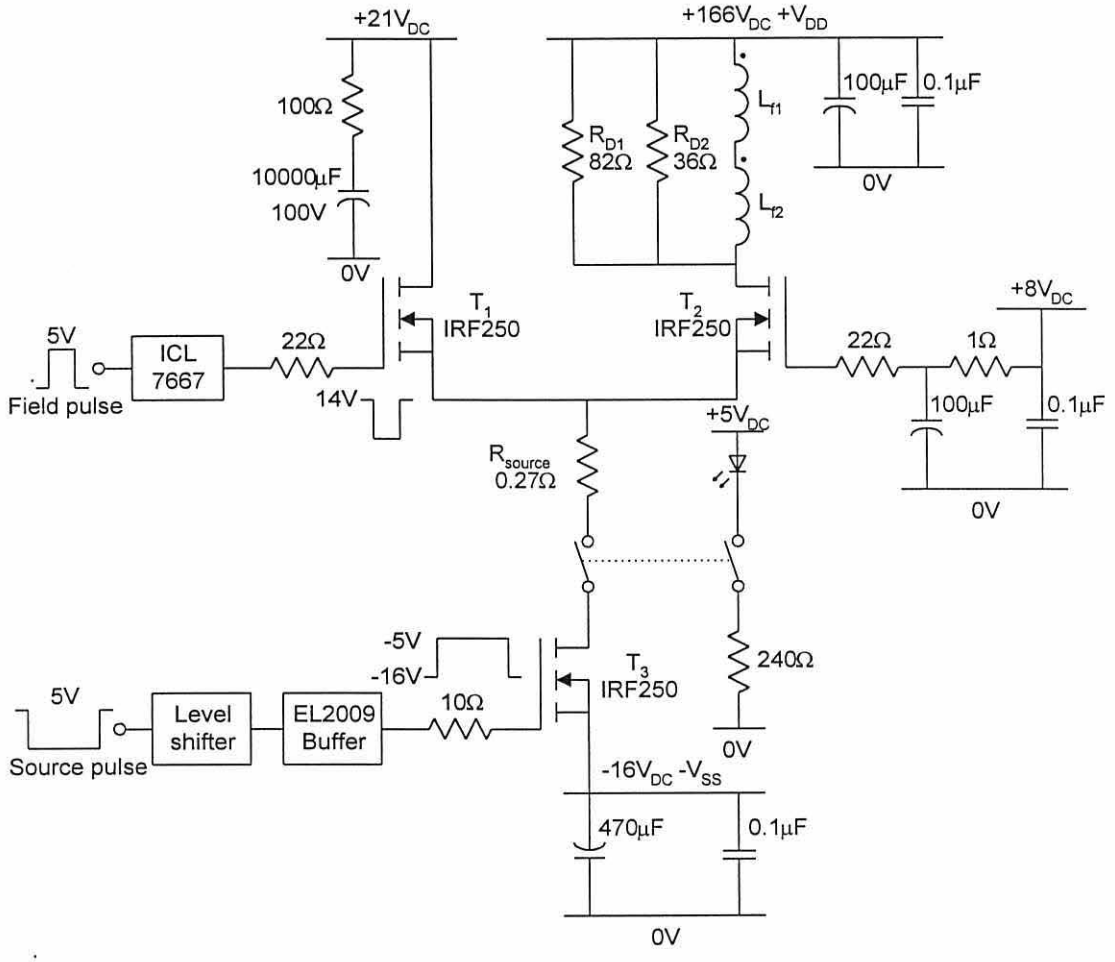

Figure 3.5 Full schematic diagram of MOSFET differential current driver.

To overcome the problem of high power dissipation, when either transistor T_1 or T_2 is in a state of conduction, a third IRF250 MOSFET T_3 was required to switch on the constant current resistor R_{source} just before the field pulse is initiated. The timing was arranged so that the current source is turned on long enough to allow the system to settle in a steady state condition ahead of the field pulse, as described in §3.5. A gate driver consisting of a level shifting network and an élantec™ EL2009 buffer amplifier provide the required current at the gate of transistor T_3. Connected to the gate of transistor T_2

was a decoupling filter consisting of a 100μF tantalum capacitor and a 0.1μF capacitor in parallel across a 1Ω resistor. This arrangement isolated voltage spikes at the gate of T_2 that were found to occur during switching, producing unacceptable pulse overshoot. Series resistors were used at the gates of all three transistors to prevent spurious high frequency oscillations which may be produced from the resonant circuit formed between the highly capacitive gate terminal and any stray circuit inductance.

In order to remove excessive overshoot and oscillations from the output current pulse, it was necessary to include some external resistive damping in the switching circuit. As indicated in figure 3.5, damping resistors R_{D1} and R_{D2} were connected in parallel with the field coil, the values of which were optimised by modelling the switching circuit as a parallel resonant circuit, as shown in figure 3.6.

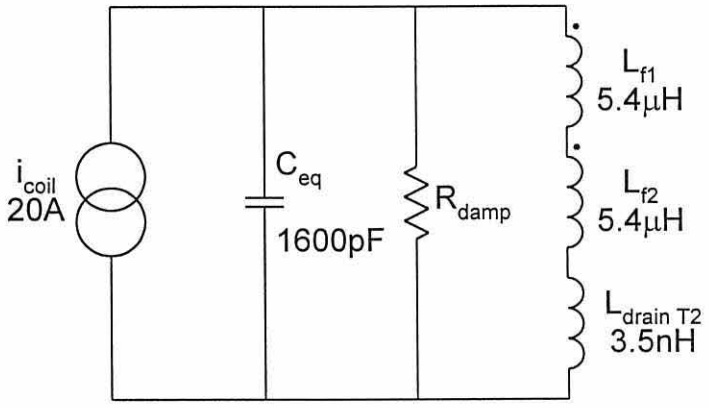

Figure 3.6 Parallel resonant model of switching circuit.

C_{eq} is the total equivalent capacitance, which for the IRF250 device is 1600pF, with the drain inductance of T_2 $L_{drain\ T2}$ quoted as 3.5nH from manufacturer's data. The field coils L_{f1} and L_{f2} each have an inductance of 5.4μH, as discussed in §3.3.3. Therefore, the value of the lumped damping resistance R_{damp} can then be calculated from equation 3.2,

$$R_{damp} = Q\sqrt{\frac{L_{f1} + L_{f2} + L_{drainT2}}{C_{eq}}} \tag{3.2}$$

where Q is the quality factor of the coil, which for a critically damped system is 0.707. The resulting value of a single damping resistor was calculated to be 58Ω. However, experimentally it was found that pulse overshoot could be optimised by placing two

resistors of 82Ω and 36Ω across the field coils, and the resulting measured current pulse is shown in figure 3.7. The pulse was monitored using a Tektronix™ TDS640 digitising oscilloscope connected to a Tektronix™ A6303 current probe and Tektronix™ AM503 current probe amplifier. From figure 3.7, it is clearly seen that the pulse is free from ringing and overshoot, whilst maintaining acceptable rise and fall times.

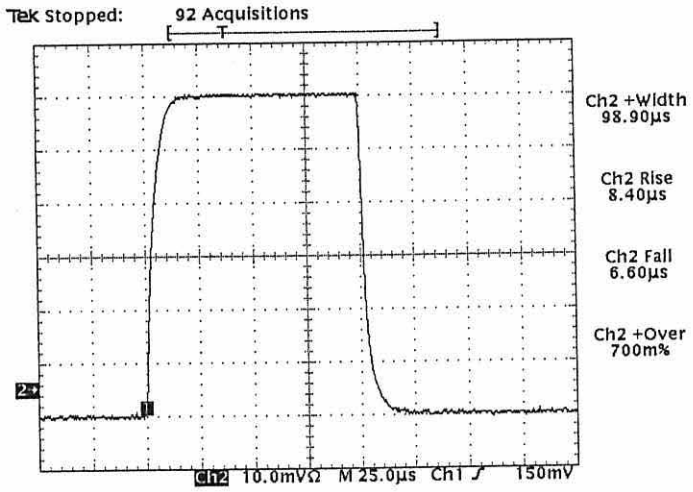

Figure 3.7 Measured current pulse for a single current driver with 82Ω and 36Ω parallel damping *(5A per vertical division)*.

Interestingly, the current switched through the field coil by a single MOSFET driver is 30A. These improvements were obtained by arranging the current drivers in pairs and grouping on individual boards with parallel supplies. Further improvements were realised by increasing the size of the interconnecting leads in the switching circuit with 1.5mm^2 PVC insulated cable. Most significantly, winding the coils using Litz wire minimises the resistance losses that occur at high frequencies due to the skin effect, and allows an increased current to extend uniformly throughout the conductor, as discussed in §3.3.3.

The design of the driver board ensured that radiated emission and supply noise were sufficiently minimised by the use of ground plane on both sides of the board. Techniques such as proper grounding, power supply decoupling, short interconnecting leads and straight PCB tracks were employed to minimise transient conditions occurring at high frequencies (Ott 1988).

Finally, in order to simplify the design of the magnetometer, the field level was determined simply by selecting the required number of drivers from a bank of eight 4A rated switches connected in series with the current source resistor. This allows eight discrete field levels to be generated, as described in §3.3.3.3.

3.3.3 Field Coils

The development of the field coils presented in this section is broadly based upon earlier investigations of distributed windings in small coils (Hancock 1995). The basic design of the field coil assembly is shown in figure 3.8.

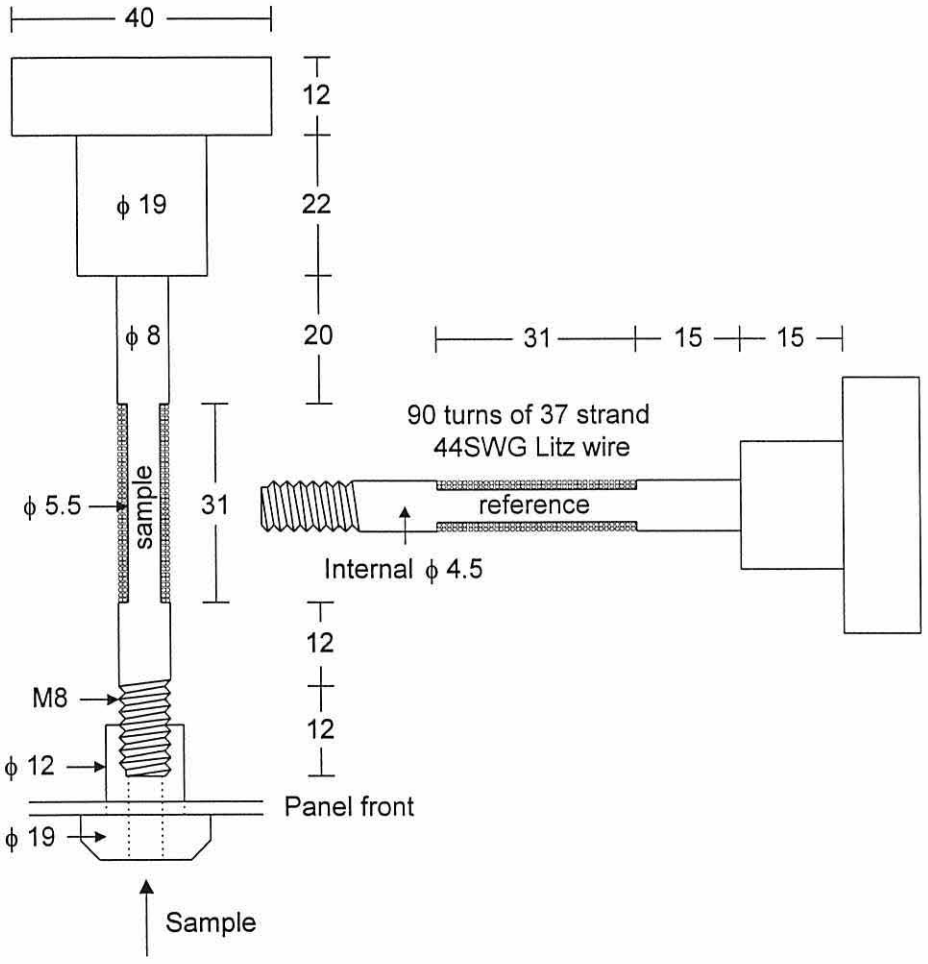

Figure 3.8 Plan view of field coil arrangement *(dimensions in mm)*.

From figure 3.8, the field coil assembly consists of two identical, series connected coils having an internal diameter of 4.5mm. One field coil is attached to the front panel of the magnetometer through a M8 threaded nylon coupling to allow access

for the dispersion sample, whilst the empty reference coil is situated orthogonally to reduce mutual inductance effects. The length of each coil is 31mm wound with 90 turns of New England Electric Wire Corporation™ 37 strand 44SWG Litz wire on a brass former. Each of the eight individual current drivers described in §3.3.2.1 supplies four separate strands of wound Litz wire. The term 'Litz' is derived from the German word 'Litzendraht' which describes a conductor consisting of a number of separately insulated strands that are twisted or braided together. As each strand tends to take all possible positions in the cross section of the entire conductor, this arrangement equalises the flux linkages and reactances of the individual strands causing the current to spread uniformly throughout the conductor, producing a larger magnetic field. Studies concerning the generation of a 10 Oe 20kHz magnetic field in larger coils have also confirmed the benefits of Litz wire (Jones, et al. 1999).

The majority of the components in the field coil former shown in figure 3.8 were manufactured from brass. This material was chosen for its good mechanical and magnetic properties, and the ease with which it could be machined. Unfortunately, as brass is a good conductor, eddy currents generated in the solenoid core will tend to oppose the main pulsed field (Cullity 1972). In order to prevent this eddy loss, a 2mm wide slot was machined down the length of both coil formers to electrically isolate the circulating current.

The calculation of the inductance of a single layer coil has been performed using the formula for a cylindrical current sheet. This analysis assumes that the coil wire is flattened to form a layer of tape of negligible thickness, with each turn of wire at the centre of each turn of tape (Grover 1946). In this approach, using look up tables and suitable formula, the value of the coil inductance can be determined to a degree of accuracy greater than can be measured in practice. The inductance of a cylindrical current sheet of infinite length L_f, with a correction to take account of end effects and differences in self and mutual inductance between the current sheet and the coil is given by equation 3.3

$$L_f = 0.002\pi^2 r\left(\frac{2r}{l}\right)N^2K \qquad (3.3)$$

where r is the coil radius, l is the coil length, N is the number of turns and K is a factor which models end effects. Values of K are tabulated as a function of the ratio of the coil diameter to its length.

The inductance of a coil of wire is rather different to that of the cylindrical current sheet. As a result, a correction for evaluating the coil winding as a conducting tape can be determined. The inductance of a coil differs from that of the equivalent current sheet, as each turn of wire has a differing self and mutual inductance from the corresponding tape. The correction for the insulating space ΔL_f may be evaluated over the length of the coil, as given by equation 3.4 (Grover 1946).

$$\Delta L_f = 0.004\pi r N(G + H) \tag{3.4}$$

In this equation, G is a function of the ratio of the enamelled wire bare diameter to the overall diameter of the winding, whilst values of H are tabulated as a function of the number of coil turns N. The calculated value of ΔL_f can then be subtracted from the inductance of the current sheet L_f to accurately obtain the inductance of the coil. Using equations 3.3 and 3.4, the field coil inductance connected to a single current driver was found to be 5.376μH.

By increasing the length and number of turns of the coil, enhanced field magnitude and homogeneity has been compromised by greater inductance and hence longer pulse rise and fall times. For a maximum current pulse of over 125A, the geometry of the field coil is such that a magnetic field of over 4.7kOe is generated, as discussed in §3.3.3.1. Accordingly, the field over the middle half of the coil is markedly uniform to 1.0%, as described in §3.3.3.2. The drawback of this, is that pulse rise and fall times are now of the order of 15μs, as discussed in §3.3.3.1. However, this is an acceptable value, as the timescale over which particles can rotate in the dispersion solution is several times greater (Prichard, et al. 1998).

3.3.3.1 Sample Field Pulses

A final optimised 50μs current pulse through the series field coils L_{f1} and L_{f2}, is shown in figure 3.9. For the vertical scale, 10mV represents 20A, i.e. 20A per division,

consequently with all eight current drivers connected, a pulse current of approximately 125A is switched.

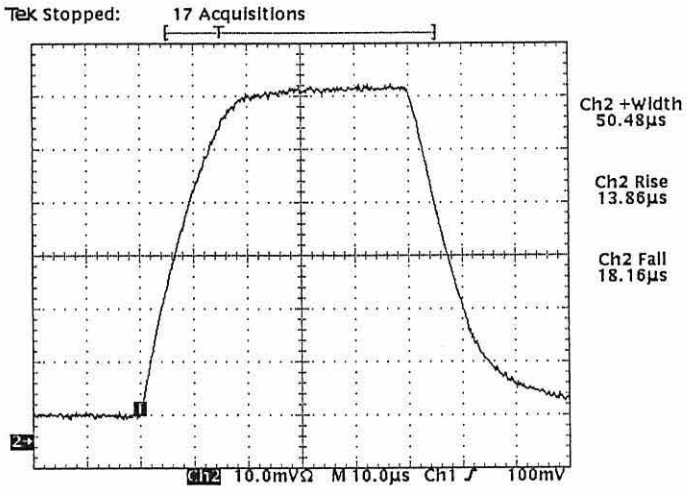

Figure 3.9 50µs current pulse for eight current drivers *(20A per vertical division)*.

From figure 3.9, it is clearly seen that the pulse is well defined, with measured rise and fall times of around 15µs. The magnetic field generated in the coils was found to be 4.7kOe, calculated using the steady state current amplitude together will a scale factor obtained from the coil geometry, as discussed in §3.3.3.2.

The pulse width is selected by switching a combination of binary weighted resistors through seven 4A rated switches on the front panel of the instrument. This data is latched through a Texas Instruments™ 74ALS574 octal flip-flop into a digital counter implemented in an AMD™ PAL22V10. To produce a pulsed field, the counter is triggered by a state machine implemented in an AMD™ MACH110 gate array which provides a TTL signal to the ICL7667 MOSFET driver connected to the gate of transistor T_1, as illustrated in figure 3.5. When the counter is empty, a signal is passed back to the state machine to end the TTL field pulse signal, as discussed in §3.5. This configuration allows $2^7 - 1 = 127$ discrete pulsed field widths to be selected.

Figure 3.10 shows a measured 100µs duration current pulse, again with all eight current drivers connected. As before, a well defined pulse with a steady state current of 125A is observed, having symmetrical rise and fall times of approximately 15µs. The majority of the pulsed field measurements presented in §4 were performed using 100µs pulsed magnetic fields.

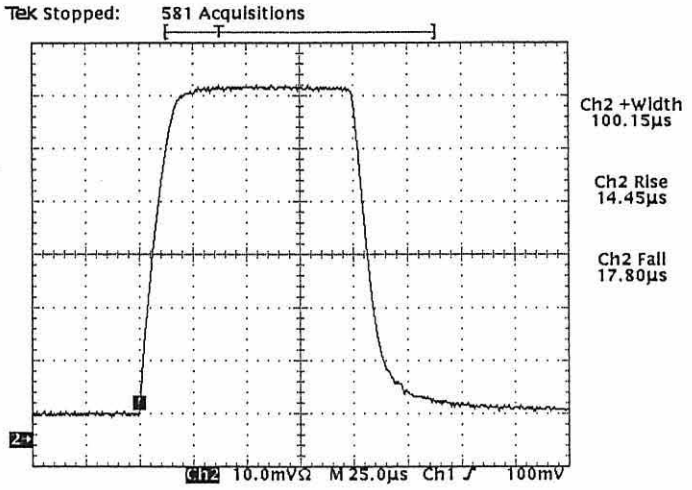

Figure 3.10 100µs current pulse for eight current drivers *(20A per vertical division)*.

An interesting feature may be observed in the longest duration 130µs pulse, as shown in figure 3.11. It is clearly seen that the trailing edge of the pulse is of lower amplitude than the leading edge, i.e. the pulse suffers from amplitude droop. There are two possible explanations for this phenomenon.

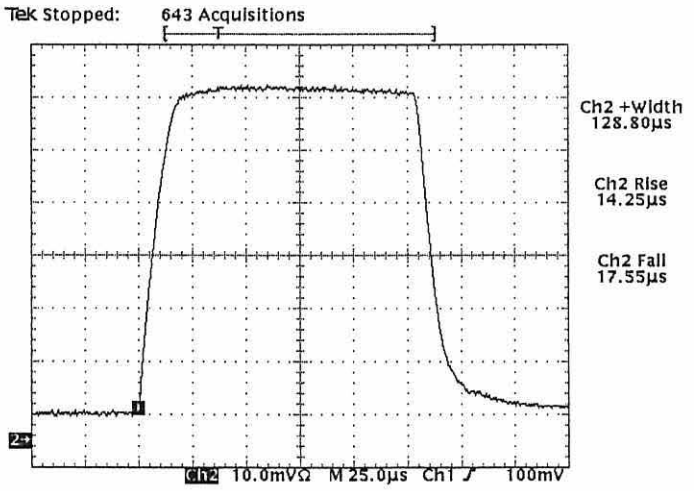

Figure 3.11 130µs current pulse for eight current drivers *(20A per vertical division)*.

Primarily, this may be due to the capacitive power supply not being able to provide enough energy over a prolonged pulse length, although this is not observed over a 125A 100µs duration pulse, as shown in figure 3.10. One further explanation may be that as a MOSFET has a positive temperature coefficient, the value of $r_{ds(on)}$ increases as the junction temperature increases (Lander 1993). Consequently, the transconductance or

FET gain parameter decreases as a function of temperature, and the drain current is reduced. The thermal characteristics of the die under a current pulse have been examined in order to explain, as least in part, the amplitude droop observed in figure 3.11.

If a pulse of energy is supplied to a semiconductor device, the temperature of the junction does not rise instantaneously, it has a thermal time constant τ_α given by (Hewlett-Packard 1998)

$$\tau_\alpha = \left[\frac{2F}{\pi}\right]^2 \left[\frac{\rho C_p}{K_{TH}}\right] \tag{3.5}$$

where ρ is the density, C_p is the specific heat and K_{TH} is the thermal conductivity of the semiconductor. The parameter F is the die thickness, which is 15 mils or 381μm for the IRF250[1]. For this device with a silicon based die[1], equation 3.5 yields a thermal time constant of 646μs. At time $t < \tau_\alpha$, the semiconductor junction temperature T_j can be determined from (Pritchard 1967)

$$T_j = P_D \theta_{JA} \left[\frac{4}{\pi^{\frac{3}{2}}}\right] \left[\frac{t}{\tau_\alpha}\right]^{1/2} + T_A \tag{3.6}$$

where P_D is the power dissipated, θ_{JA} is the junction to ambient thermal resistance and T_A is the ambient temperature.

Using manufacturer's data, substitution into equation 3.6 yields the dynamic junction temperature as a function of pulse width, as shown in figure 3.12(a). It is evident from figure 3.12(b) that the maximum rate of change of $r_{ds(on)}$ occurs at junction temperatures over 100°C, which from figure 3.12(a) is consistent with longer pulse durations over 100μs. Consequently, for extended pulse widths of over 100μs, there is a variation of gain over the pulse waveform which tends to reduce the drain current at the tail of the pulse, as shown in figure 3.11.

[1] Allen Askey, International Rectifier™, personal communication, 1999.

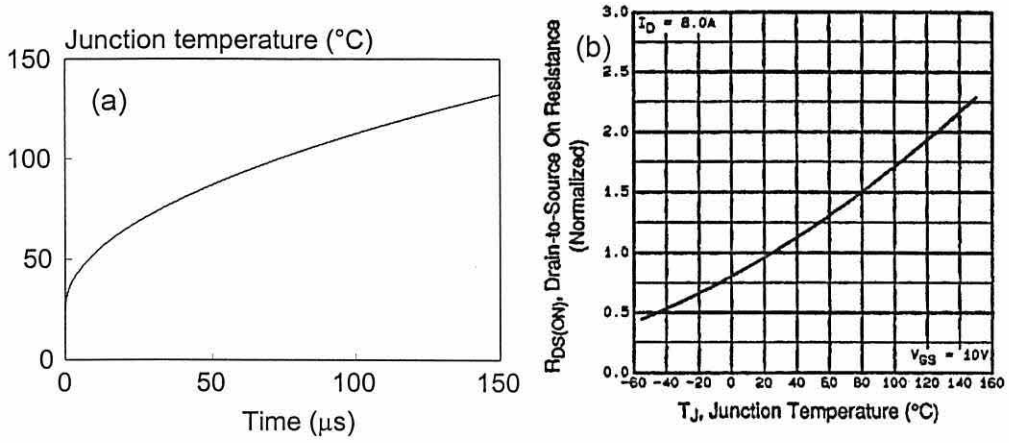

Figure 3.12 (a) Transient junction temperature (b) on-state resistance $r_{ds(on)}$ as a function of junction temperature from IRF250 datasheet.

3.3.3.2 Field Distribution Inside Coils

A current through a straight wire produces a magnetic field which is circular around the wire axis. If the wire is formed into a circular loop, a magnetic field distribution is produced similar to that shown in figure 3.13.

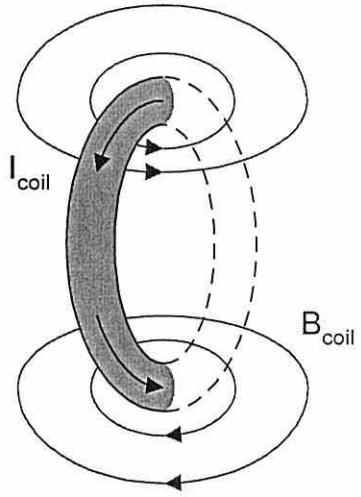

Figure 3.13 Magnetic field distribution of a circular current loop.

For a solenoid consisting of a number of wound turns, the contributions to the field from each turn tend to reinforce the resultant field inside the coil. Consequently, the subsequent field is approximately uniform and parallel to the axis of the solenoid. Outside the coil, the contributions to the field from each turn tend to cancel out, and the resultant field is relatively small. For the ideal case of a coil of effective infinite length,

the current distribution in the windings is equivalent to a cylindrical current sheet, as shown in figure 3.14. The magnetic field inside the ideal solenoid is parallel to the axis and the field outside the coil is zero (Keller, et al. 1993).

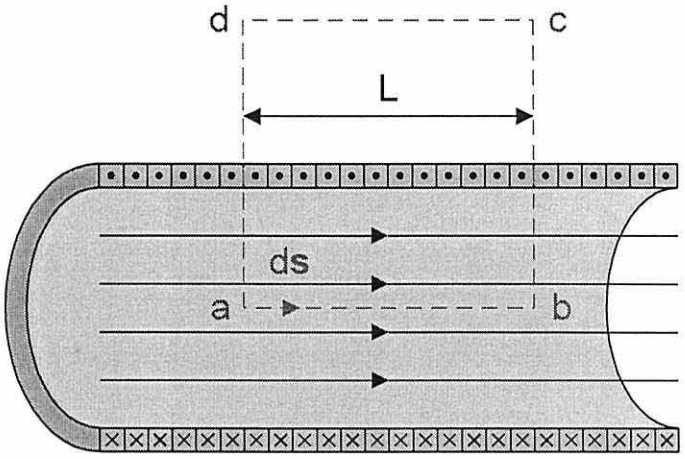

Figure 3.14 Field distribution of an ideal solenoid.

By applying Ampere's law to the closed path abcd as shown in figure 3.14, the magnetic field inside the ideal solenoid can be determined. The integral around the closed path is the sum of the integrals along each of the four line segments.

$$\oint \mathbf{B}\cdot d\mathbf{s} = \int_a^b \mathbf{B}\cdot d\mathbf{s} + \int_b^c \mathbf{B}\cdot d\mathbf{s} + \int_c^d \mathbf{B}\cdot d\mathbf{s} + \int_d^a \mathbf{B}\cdot d\mathbf{s} \tag{3.7}$$

The integrals along the lines bc and da are zero since **B** and d**s** are perpendicular, making **B**·d**s** = |B||ds| cos90° = 0. Along segment cd, which is outside the ideal solenoid, the field is negligible and so is assumed to be zero **B** = 0, hence the integral is zero. The only contribution to the closed path integral is from the line ab, with the field **B** parallel to d**s**, so **B**·d**s** = B ds. As the field is constant in the region of interest, B has the same value at each point, therefore

$$\oint \mathbf{B}\cdot d\mathbf{s} = \int_a^b \mathbf{B}\, ds = \mathbf{B}\int_a^b ds = BL \tag{3.8}$$

where L is the length of the line ab. For a solenoid with n turns per unit length, the number of turns within the closed path is nL. Since each turn carries a current I_{field}, the net current linking this closed path is nLI_{field}. This results in Ampere's law.

$$\oint B \cdot ds = BL = \mu_0 nLI_{field} \tag{3.9}$$

$$B = \mu_0 nI_{field} \quad (T) \tag{3.10}$$

$$B = \mu_0 \mu_r H \tag{3.11}$$

$$H = nI_{field} \qquad (Am^{-1}) \tag{3.12}$$

To use Ampere's law, the field must be invariable, so that B can be taken outside of the integral sign, as in equation 3.8. Of course, this is not the case for regions of a real coil where the field distribution is divergent, i.e. at either end. In this instance, the Biot-Savart law can be used to determine the axial field of a single current loop, and extended by n turns to represent the complete coil. The field at any axial position inside a real solenoid may be calculated using equation 3.13,

$$B = \frac{\mu_0 nI_{field}}{2}\left(\sin\varphi_1 - \sin\varphi_2\right) \tag{3.13}$$

$$\varphi_1 = \tan^{-1}\left(\frac{L_{left}}{r}\right) \quad \text{and} \quad \varphi_2 = \tan^{-1}\left(\frac{L_{right}}{r}\right) \tag{3.14}$$

where r is the coil radius, L_{left} and L_{right} represent the effective field coil length, left and right of the point of interest. Clearly, from equations 3.10 and 3.13, the significant factor when designing a solenoid to have a uniform field profile is the ratio of the coil length to its diameter.

Although, equations 3.13 and 3.14 calculate precisely the field at any axial position in the coil, they are qualitatively accurate over the entire cross section. The field distribution profile for the coil geometry described in §3.3.3 is shown in figure 3.15. For a maximum current pulse of 125A, the flux density at the centre of the coil is 470mT or 4.7kOe. It can be clearly seen that the field is homogeneous over a wide section of the coil. If the dispersion is held in the middle half of the coil, the field experienced by the sample is uniform to 1.0%.

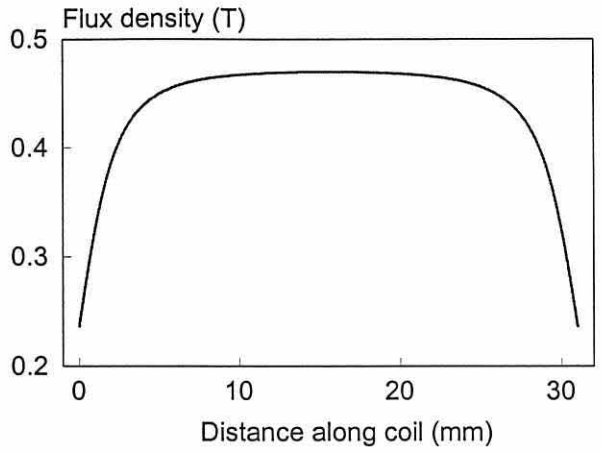

Figure 3.15 Field distribution profile of field coils.

3.3.3.3 Field Linearity

A graph showing the variation of magnetic field generated in the field coils as a function of the number of connected current drivers is shown in figure 3.16. For a constant pulse width of 100μs, the steady state current through the field coils was monitored using a Tektronix™ A6303 current probe and Tektronix™ AM503 current probe amplifier. The magnetic field was determined using the procedure described in §3.3.3.2.

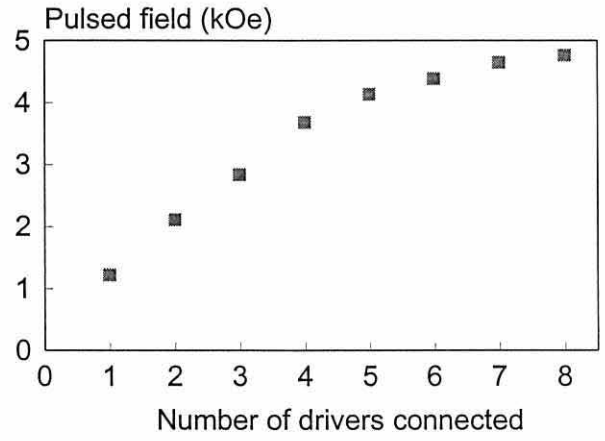

Figure 3.16 Pulsed magnetic field as a function of connected current drivers.

It is evident that the current, and hence the field, produced in the coils becomes non-linear as more of the MOSFET drivers are connected. This may be explained, at least in part, by considering the nature of the load, which consists of eight tightly coupled coils of Litz wire. Specifically, Lenz's law indicates that a considerable emf will be induced in coupled coils, which will tend to oppose the change in magnetic flux.

Further explanations for this current non-linearity, may be due to the fact that the coil inductance is now comparable with the current driver circuit inductance, hence the drain-source voltage V_{DS} of transistor T_2 is reduced through an effective voltage divider. With all eight current drivers switched on, the field coils consist of eight 5.4μH coils connected in parallel, giving a total coil inductance of approximately 675nH. The inductance of the current driver circuit, which includes the IRF250 MOSFET internal source and drain inductance[1], the current source resistor lead inductance[2], and the PCB track inductance[3] may equal the parallel coil inductance.

This, coupled with the fact that the power supply consists of a bank of severely inductive electrolytic capacitors[4] connected through long supply leads might indicate that the MOSFET driver performs as a potential divider. Consequently, as more current drivers are switched on, anything up to half of the supply voltage, $+V_{DD}$, may be dropped across the driver circuit, obviously reducing the anticipated output current. This may in part account for the saturated pulsed current, and hence the magnetic field shown in figure 3.16.

3.3.3.4 PSpice® Simulations

The current driver and field coil arrangement described in §3.3.2 and §3.3.3 was evaluated and optimised using the PC-based MicroSim™ v8.0 PSpice® circuit simulator. In order to obtain an accurate model of the circuit, the components in the driver circuit must be properly characterised. The IRF250 MOSFET was simulated using a model developed by Symmetry Design Systems, Inc. The passive components were also

---

[1] Datasheets for the International Rectifier™ IRF250, quote the internal drain inductance L_D between the lead, 6mm from the package and the centre of the die contact as 3.5nH, with the internal source inductance L_S given as 7.5nH.

[2] http://nwd2www1.analog.com/publications/magazines/Dialogue/Anniversary/10.html
Lead inductance is given by the equation

$$L_{LEAD} = 0.0002L\left[\ln\left(\frac{2L}{R}\right) - 0.75\right](\mu H)$$

EXAMPLE: 10mm of 0.5mm o.d. wire has an inductance of 7.26nH.

[3] *ibid.*
PCB track inductance is given by the equation

$$L_{TRACK} = 0.0002L\left[\ln\left(\frac{2L}{W+H}\right) + 0.2235\left(\frac{W+H}{L}\right) + 0.5\right](\mu H)$$

EXAMPLE: 10mm of 0.25mm wide track, with a thickness of 0.038mm has an inductance of 9.59nH.

[4] For capacitors with a small physical size (length less than 25mm and diameter below 15mm), parasitic inductances in the range 10 to 30nH have been reported (Whalen, et al. 1977).

accurately specified to include lead inductance and interelectrode capacitances, as described by (Whalen, et al. 1977).

Figure 3.17 shows a PSpice® simulated single MOSFET current driver with damping resistors of 82Ω and 36Ω connected in parallel across the field coils. It is clearly seen that the simulated 100μs current pulse switched through the field coils is well defined and attains a steady state value of 30A, in good agreement with the measured current pulse shown in figure 3.7.

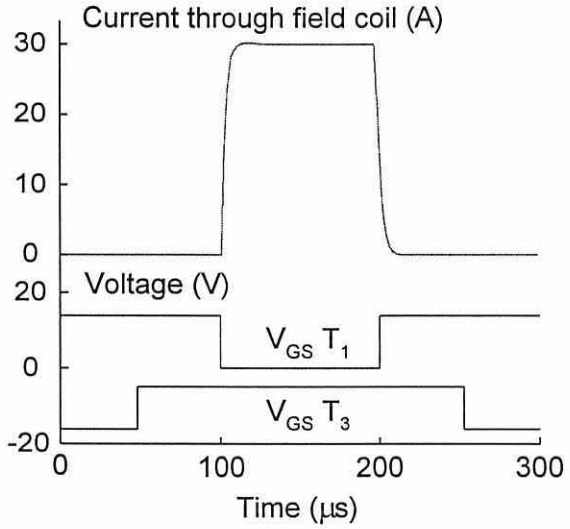

Figure 3.17 PSpice® simulated field coil current pulse for a single driver with 82Ω and 36Ω parallel damping, along with associated digital timing pulses.

From figure 3.17, in order to control the current source transistor T_3, drive levels of -5V and -16V were simulated with a 200μs pulse with rise and fall times of 100ns. The gate voltage of transistor T_1 was simulated with a 100μs drive pulse with the desired levels of 14V and 0V, as discussed in §3.5.

The corresponding induced voltage at the drain of transistor T_2 was also simulated for the 100μs current pulse, as shown in figure 3.18. As the drain of MOSFET T_2 is connected to the field coils, excessive induced voltages may be generated which may damage the device. Clearly, from figure 3.18, this is not the case as the maximum level of induced voltage is below the rated drain-source breakdown voltage $V_{(BR)DS}$ of 500V for the IRF250 device.

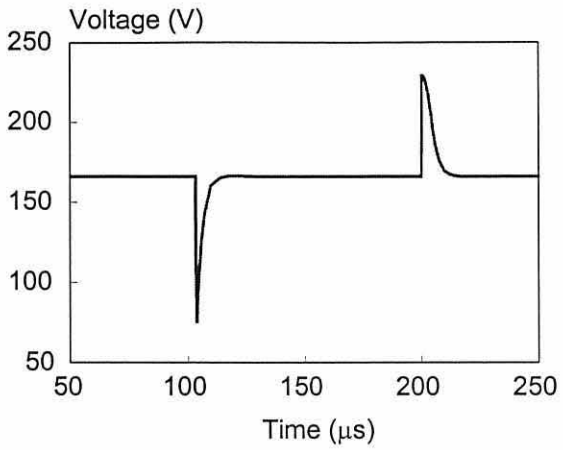

Figure 3.18 PSpice® simulated induced voltage at the drain of transistor T_2.

In order to simulate all eight current drivers connected to the field coils, PSpice® provides a facility for coupling inductors. In this way, eight individual current drivers, each configured to drive 30A as shown in figure 3.17, can be simulated simultaneously by specifying the mutual coupling between the eight distinct coils. As the degree of coupling is dependent upon the geometry and position of the individual layers, a coupling factor of 0.98 was found appropriate for tightly wound Litz coils. Using this technique, the simulated current through the field coils for all eight current drivers connected is shown in figure 3.19, in good agreement with a measured 100μs current pulse obtained in figure 3.10. The predicted steady state current amplitude is 124A, with symmetrical rise and fall times of around 17μs

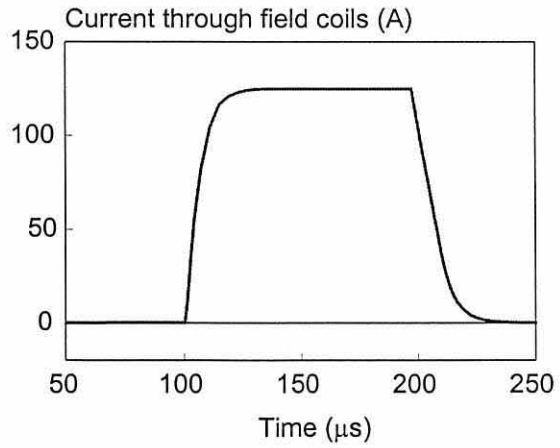

Figure 3.19 PSpice® simulated 100μs current pulse for eight current drivers.

3.4 Signal Processing

In this section, the signal processing used to detect the magnetisation change of a wet dispersion under the application of a pulsed magnetic field is described. As discussed previously in §3.3, a pulsed field is used to impulse magnetise the sample, which is held in one of two series connected field coils. Depending upon the dispersion microstructure, and the magnitude and duration of the applied field, the aligning magnetic moments will produce a flux change which is detected by two differentially connected search coils. Following the cancellation of the common field, the voltage from the search coils is passed to a bridge balancing stage and instrumentation amplifier. The scaled integral of this voltage gives the change in magnetisation due solely to the dispersion sample. As a result, dispersion magnetisation processes can be monitored in real-time using a digital storage oscilloscope, as described in §4.

As mentioned briefly in §3.1, only improvements and modifications are presented in detail. The techniques developed are based upon the earlier 1270 Oe instrument (Hancock 1995).

3.4.1 Search Coils

The search coil arrangement consists of two identical anti-phase connected coils, which are fixed axially with the field coils. The location of a single search coil around the sample field coil, is shown in figure 3.20.

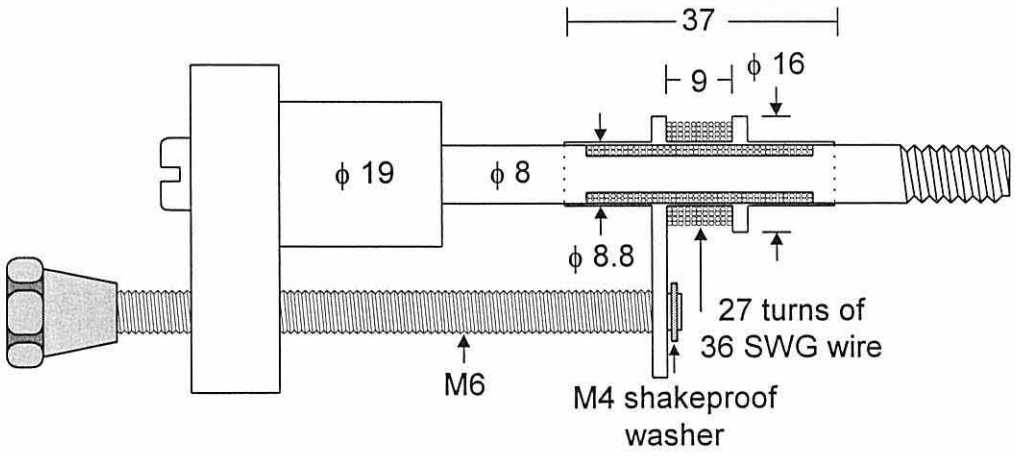

Figure 3.20 Side view of search coil arrangement *(dimensions in mm)*.

As with the field coils, the brass search coil formers were manufactured with a 2mm slot to prevent circulating eddy losses, and each wound with 27 turns of 36SWG enamelled copper wire over the coil length of 9mm. Empirically, this was found to be the optimum coil geometry considering the comprise between output sensitivity and system response time.

In order to approximately null the coils before the bridge balancing stage, the coils were positioned by turning the threaded adjuster, as shown in figure 3.20. The induced voltage in the search coils under the application of a field pulse is given by Faraday's law

$$v = -N\frac{d\Phi}{dt} \tag{3.15}$$

where Φ is the magnetic flux, and N is the number of turns of the coil. Since the magnetic field is spatially uniform and parallel to the axis of the coil, the flux linking each turn is given by

$$\Phi = BA \tag{3.16}$$

where B is the magnetic flux density and A is the cross sectional area of the coil. Hence, Faraday's law may be re-written as

$$v = -NA\frac{dB}{dt} \tag{3.17}$$

However, in the reference coil $B = \mu_0 H$, whereas in the sample coil $B = \mu_0(H + M)$. Accordingly, if the voltage in the reference coil is subtracted from the voltage generated in the sample coil, equation 3.17 becomes

$$v = NA\frac{dM}{dt} \tag{3.18}$$

It is this voltage which is amplified and integrated, so that the signal recovered represents the change in magnetisation due to the sample, scaled by a factor τ_i / NA, where τ_i is the time constant of the circuit, as described in §3.4.4.

The induced voltages from the search coils under the application of a field pulse, were found initially to suffer from excessive pulse ringing. Using the technique described in §3.3.2.1, it was necessary to include some external resistive damping by modelling the search circuit as a parallel resonant system. For a coil inductance of 3.73μH, critical damping was achieved by placing a damping resistor of 36Ω in parallel with each search coil. Figure 3.21 shows the measured induced voltage from a single damped search coil for a 125A 100μs pulse through the field coils. In order to display the response, 26dB of attenuation was provided at the input channel of the oscilloscope.

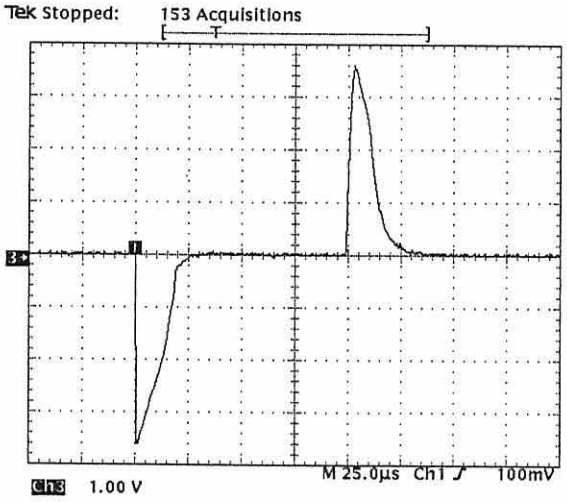

Figure 3.21 Induced voltage from a single search coil *(20V per vertical division)*.

On providing the differential connection, the measured deviation voltage from the search coils is shown in figure 3.22.

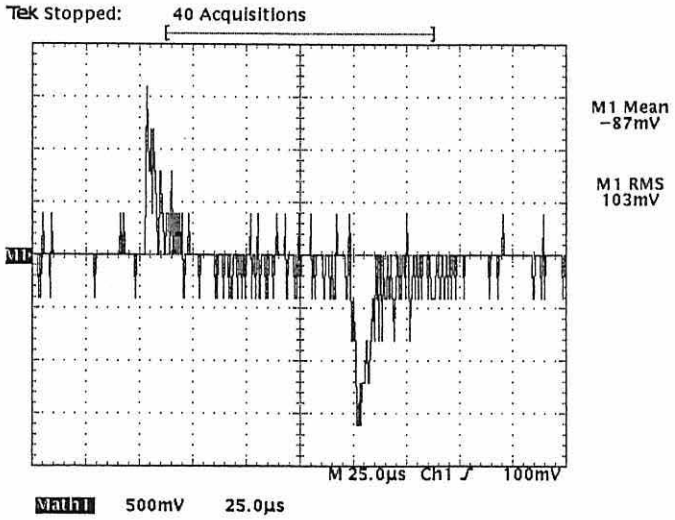

Figure 3.22 Measured deviation voltage from the differentially connected search coils.

The null signal from the search coils with no sample present has a RMS value of 103mV, indicating good common field cancellation considering the high levels of induced voltage present, as indicated in figure 3.21. Although the null deviation voltage shown in figure 3.22 is of a reasonable level, an additional balancing stage was utilised to further optimise the null value and improve the resultant signal to noise ratio, as described presently in §3.4.2.

3.4.2 Balancing Stage

The bridge balancing arrangement used to cancel the common deviation voltage V_{dev} is shown in figure 3.23.

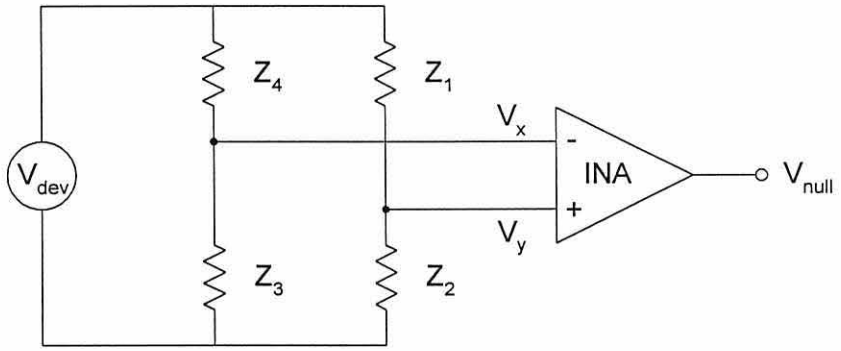

Figure 3.23 Schematic diagram of bridge balancing arrangement.

If the circuit in figure 3.23 is solved using Kirchhoff's voltage law, then the resultant null voltage V_{null} is given by equation 3.19.

$$V_{null} = V_y - V_x = \frac{\frac{Z_4}{Z_3} - \frac{Z_1}{Z_2}}{\left(\frac{Z_1}{Z_2} + 1\right)\left(\frac{Z_4}{Z_3} + 1\right)} V_{dev} \qquad (3.19)$$

For optimum sensitivity, the impedance ratios Z_1/Z_2 and Z_4/Z_3 should be balanced and as close to unity as possible. In the practical balancing circuit, a Burr-Brown® INA103 instrumentation amplifier was chosen to perform the subtraction of the two bridge voltages. The advantages of this instrumentation amplifier are that it has a wide unity gain bandwidth of 3MHz, a high common mode rejection ratio (CMRR) of 110dB and a

low input noise level of $1nV\sqrt{Hz}^{-1}$. The design of the practical balancing circuit is shown in figure 3.24.

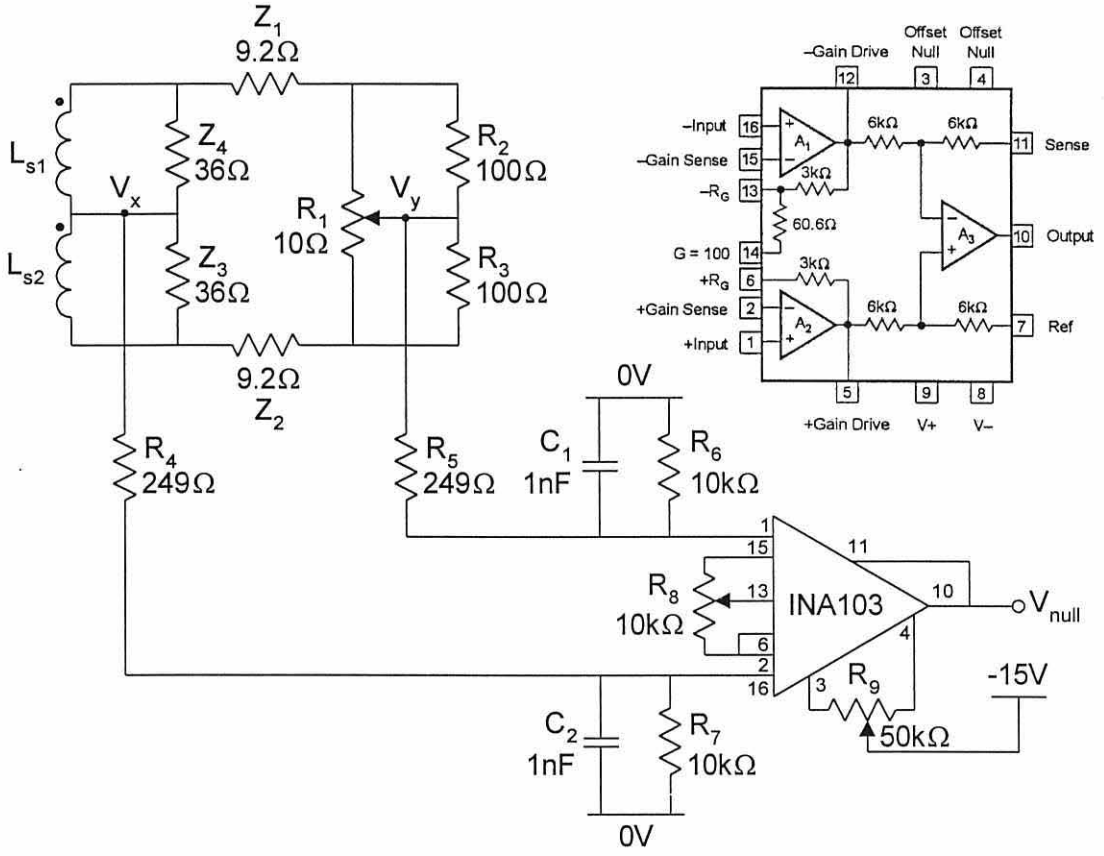

Figure 3.24 Bridge balancing stage.

As the values of the bridge impedances Z_3 and Z_4 were fixed at 36Ω for optimum damping, as described in §3.4.1, the values of the impedances Z_1 and Z_2 were chosen to match the parallel impedance of jwL_{s1} and Z_4, with jwL_{s2} and Z_3. The bridge can then be nulled by fine adjustment of the 10Ω potentiometer R_1, in parallel with resistors R_2 and R_3. The two bridge voltages V_x and V_y were then taken to the input of the instrumentation amplifier through decoupling resistors R_4 and R_5, the values of which were chosen to limit the input current to less than 10mA, and hence limit the common mode voltage. Resistors R_6 and R_7 provide a return path for the floating input signals, and are rated at 10kΩ to prevent source loading. Connected in parallel across R_6 and R_7 are 1nF capacitors C_1 and C_2 to reduce inductive ringing.

Since the bridge balancing stage attenuates the input voltage by a factor of two, the 10kΩ potentiometer R_8 was adjusted to approximately 6kΩ to compensate the gain

of the amplifier, which is given by 1 + 6kΩ/R_8[1]. The output offset voltage was then nulled through the 50kΩ potentiometer R_9. Although not shown on figure 3.24, the ±15V supplies to the INA103 were decoupled through parallel 100nF ceramic and 1μF tantalum capacitors.

Figure 3.25 shows the resultant nulled signal V_{null} from the balancing stage with no sample present. For a 125A 100μs current pulse, the RMS noise at the output of the instrumentation amplifier is 68mV, a significant improvement.

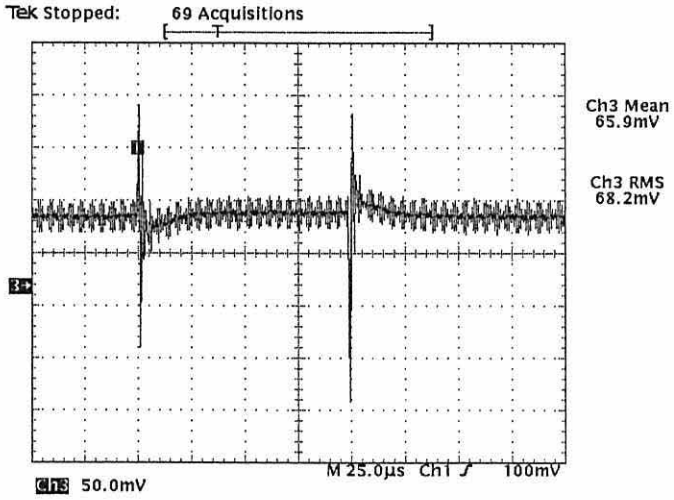

Figure 3.25 Nulled signal from the balancing stage with no sample present.

3.4.3 Amplification Stage

The voltage from the balancing stage V_{null} is passed to a Burr-Brown® OPA37 ultra low noise precision operational amplifier[2], configured as a noninverting amplifier with a voltage gain of 11. The advantages of this operational amplifier are that it has a typical input offset voltage of only 6μV, a low temperature coefficient of 0.2μV °C^{-1} and a high CMRR of 128dB. The design of the amplification stage is shown in figure 3.26, with the gain specified by resistors R_{10} and R_{11}. The offset voltage was trimmed using the 10kΩ potentiometer R_{12}. The output of the amplifier V_{amp} is then passed to the resetable integrator described presently in §3.4.4.

[1] INA103 datasheet PDS-1016H ©1990 Burr-Brown Corporation
[2] OPA37 datasheet PDS-466H ©1989 Burr-Brown Corporation

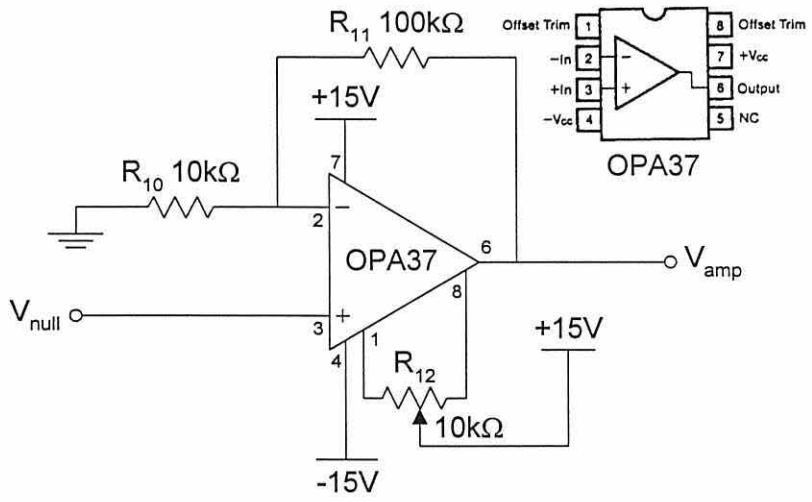

Figure 3.26 Amplification stage.

3.4.4 Resetable Integrator

In order to determine the flux change of the dispersion under the application of a pulsed magnetic field, the voltage generated in the search coil, described in equation 3.18, is integrated to give the change in magnetisation due solely to the sample. This is accomplished using a resetable integrator circuit, shown schematically in figure 3.27, where $V_{in}(t)$ is the output of the gain stage V_{amp}, as shown in figure 3.26. The integration time constant $\tau_i = R_{in}C_f$ is chosen to be at least ten times the selected pulse width to prevent the output of the operational amplifier from saturating (Hancock 1995).

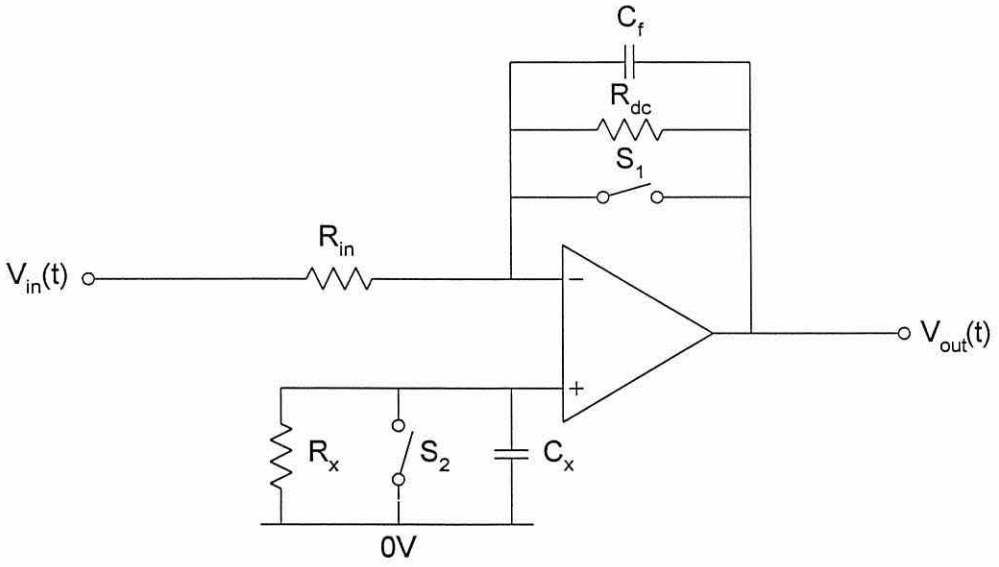

Figure 3.27 Schematic diagram of resetable integrator circuit.

A significant problem with this form of circuit is that the output tends to suffer from residual drift, consequently it is necessary to place a high value resistor R_{dc} across C_f to provide DC feedback with a gain of R_{dc}/R_{in} for stable biasing. This has the effect of discharging the feedback capacitor C_f to reduce any DC offsets at the inverting input. Furthermore, in order to minimise any input offset current, the two input bias currents must be of equal magnitude and phase. This is achieved by balancing the input impedances, so that $C_f = C_x$ and $R_{dc} = R_x$.

The output voltage of the resetable integrator shown in figure 3.27 is given by

$$V_{out}(t) = \frac{-1}{R_{in}C_f}\int_{t1}^{t2} V_{in}(t)\,dt + K_{dc} \qquad (3.20)$$

so that the output voltage is the time integral of the input voltage plus a constant offset. The constant K_{dc}, produces an output offset at the start of the integration period which may be due to charge accumulation on the feedback capacitor C_f. In order to minimise this effect, switches S_1 and S_2 are closed momentarily prior to the commencement of the integration period to discharge capacitors C_f and C_x. At the start of the integration S_1 and S_2 are then opened. In the final design, these switches are provided by CMOS analogue switches with the timing arranged from the digital control board. Motorola® 74HC4316 quad bilateral switches were selected as they exhibit a low on-state resistance of 120Ω, and may be interfaced directly with the TTL signal levels developed by the timing circuitry described in §3.5.

In the practical balancing circuit, an élantec™ EL2006 high gain fast FET input operational amplifier was configured as the resetable integrator. The advantages of this operational amplifier are that it has a maximum input bias current of only 500pA, a high open loop gain of 90dB and wide 40MHz bandwidth[1]. It is critical to use an amplifier with a very low input bias which otherwise may charge C_f and generate a large output offset voltage.

The final design of the resetable integrator is shown in figure 3.28.

[1] EL2006/EL2006A, 'High performance analog integrated circuits databook' p. 9-28, ©1994 élantec™

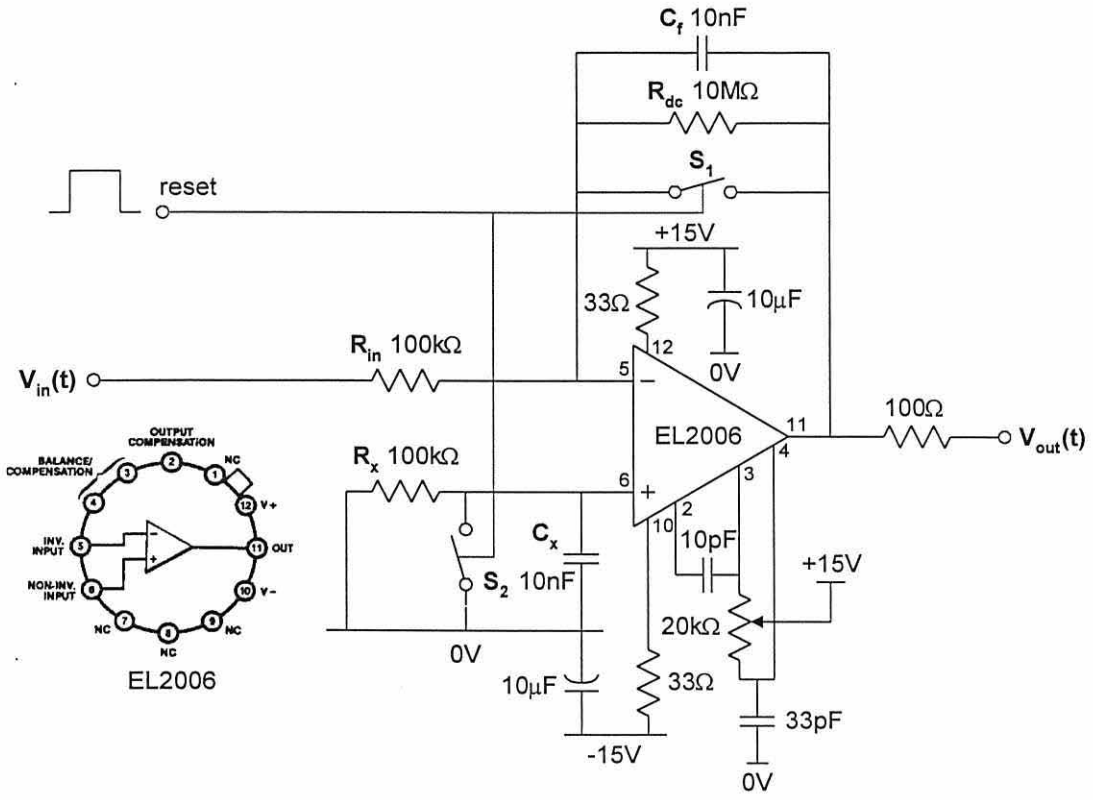

Figure 3.28 Final resetable integrator circuit.

The integrator time constant τ_i, determined by the values of R_{in} and C_f, was fixed at ten times the most prevalent field pulse width, which is 100μs. Hence, R_{in} was chosen to be 100kΩ in order to avoid excessive loading of the source, and the value of the feedback capacitor C_f fixed at 10nF, so that the time constant of the integrator is 1ms. The value of the DC feedback resistor R_{dc} was set at 10MΩ to give a DC gain of -100, which has the effect of rolling off the integrator action at low frequencies, less than $1/R_{dc}C_f$ (Horowitz, et al. 1989).

A 100Ω series resistor at the output of the EL2006 was included to remove oscillations which were subsequently found to occur. The ringing was believed to be due to coupling of the load capacitance to the inductive part of the open loop output impedance forming a resonant LC circuit. Further problems of transient conditions benefited from power supply decoupling through 10μF tantalum capacitors, and careful attention to board layout and grounding. The output offset voltage was trimmed using the 20kΩ potentiometer. Compensation components were also located close to the appropriate pins to minimise any stray reactance.

The criterion for stability against oscillation for a feedback amplifier is that the open loop phase shift must be less than 180° at the frequency of unity loop gain. Unfortunately, as the operational amplifier shown in figure 3.28 is configured as a follower, the output is 180° out of phase with the input signal. Considering the feedback capacitor C_f produces a further 90° lagging phase shift at the output, the high gain of the EL2006 will almost certainly cause the circuit to suffer instability and oscillations. The easiest way to compensate this effect, is to add additional feedback capacitance at the point in the circuit that produces the initial roll off. As the EL2006 has no internal compensation, external compensation has to be provided around the main gain stage of the amplifier. For this particular device, this is achieved between pins 2 and 3, and pin 4 and ground, as indicated in figure 3.28. Empirically, it was found that optimum compensation was obtained with a 10pF capacitor across pins 2 and 3, along with a 33pF capacitor between pin 4 and ground.

3.4.4.1 Integrator Testing

The resetable integrator detailed in figure 3.28 was initially tested using reset and integration pulses developed using a Global Specialties™ 4001 pulse generator and monostable multivibrator network, as shown in figure 3.29. The advantage of these useful integrated circuits is that when the output is forced to the other state by an input pulse, it will return to the original state after a time delay determined by the capacitor value and circuit parameters.

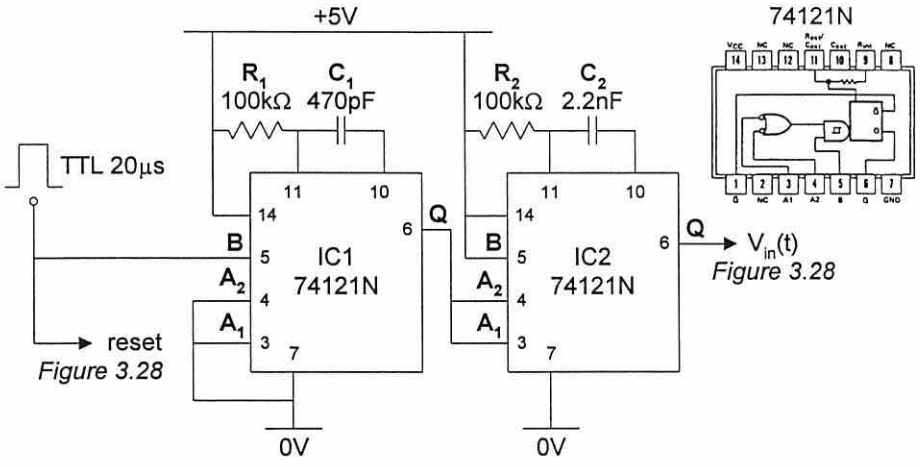

Figure 3.29 Resetable integrator test circuit.

The circuit, implemented using Texas Instruments™ 74121N precision monostable multivibrators, is triggered on the trailing edge of a 20μs duration TTL signal developed by the pulse generator. This pulse also resets the resetable integrator by closing the CMOS analogue switches across the integration capacitor C_f, as shown in figure 3.28. The output of triggered IC_1 is then held positive for a time period of 33μs, determined by $0.7R_1C_1$, before the trailing edge of this signal triggers IC_2, which produces a TTL output pulse of 126μs duration. It is this signal which is passed to the input of the resetable integrator, in a similar manner to the timing circuitry described in §3.5. The test pulses developed, and the real-time integrator output are shown in figure 3.30. The uppermost trace is the reset signal, the middle response is the data to be integrated and the bottom response is the output of the resetable integrator.

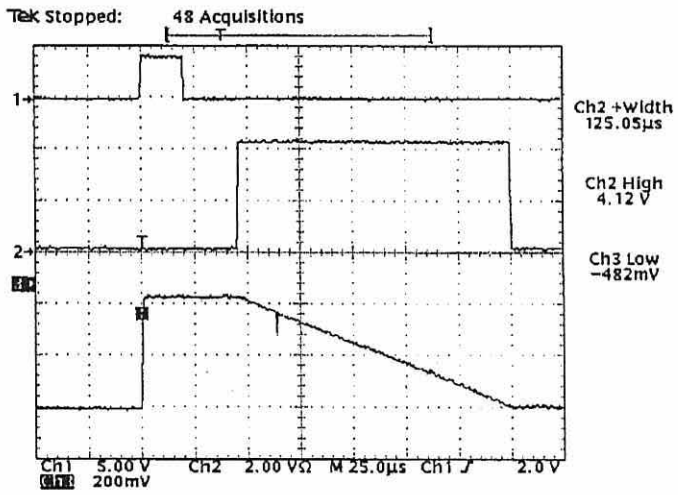

Figure 3.30 Resetable integrator test measurements.

It is clear from figure 3.30 that the output of the resetable integrator performs correctly, with the output falling with a constant slope over the duration of the pulsed input. As discussed in §3.4.4, the output offset voltage was nulled by fine adjustment of the 20kΩ potentiometer shown in figure 3.28. Consequently, at the end of the integration period, the observed integrator output voltage remains essentially constant. Further measurements were also taken over extended timescales in order to ensure that the output of the integrator did not suffer any form of residual drift. From figure 3.30, the final integrated level is found to be very close to an eighth of the magnitude of the

input signal. On solving equation 3.20, the final value of the integrated output may be calculated from equation 3.21,

$$V_{out} = V_{in}\left[\frac{-1}{R_{in}C_f}t_{pulse}\right] \tag{3.21}$$

where t_{pulse} is the input pulse width. With the integrator time constant $\tau_i = R_{in}C_f$ fixed at 1000μs, a TTL level 4.12V 126μs input pulse gives rise to a final output level of 482mV, in good agreement with figure 3.30.

To complete the detection circuitry described in §3.4, a further amplification stage was made available at the output of the resetable integrator for lower moment dispersion samples. The amplifier was configured using a Burr-Brown® OPA37 operational amplifier with a voltage gain of 16, similar to that detailed in figure 3.26.

3.5 Digital Timing

The digital timing board provides control signals for both the MOSFET current driver described in §3.3.2.1, and the resetable integrator outlined in §3.4.4. The circuit develops three single-shot TTL signal levels, as shown in figure 3.31.

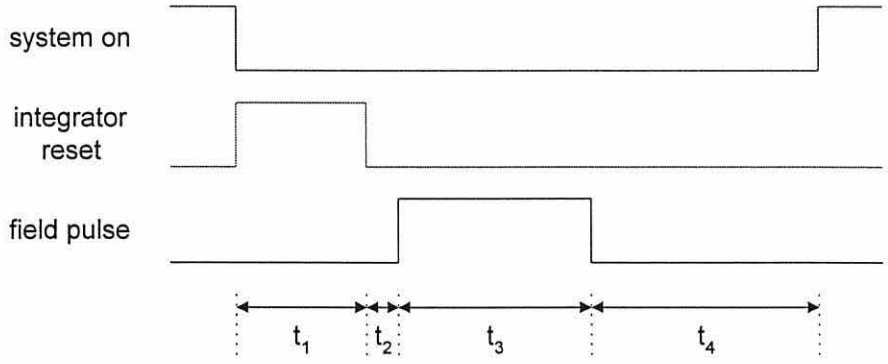

Figure 3.31 TTL signals developed by the digital control board.

When a pulsed field is required, the system activation button is pressed and the uppermost pulse initialises the system. From figure 3.5, this signal controls the constant current source transistor T_3. At the same point in time, a pulse of duration t_1 is executed to reset the resetable integrator by closing the CMOS analogue switches across the

integration capacitor C_f, as indicated in figure 3.28. After a further short delay t_2, which allows the integrator to settle into a steady state condition, the third indicated pulse t_3 is initialised which controls the duration of the field pulse, i.e. switches the gate signal of transistor T_1, as shown in figure 3.5. Finally, after time period t_4 the system activation pulse returns high, and the constant current source transistor T_3 is turned off. A system diagram of the digital timing board is shown in figure 3.32.

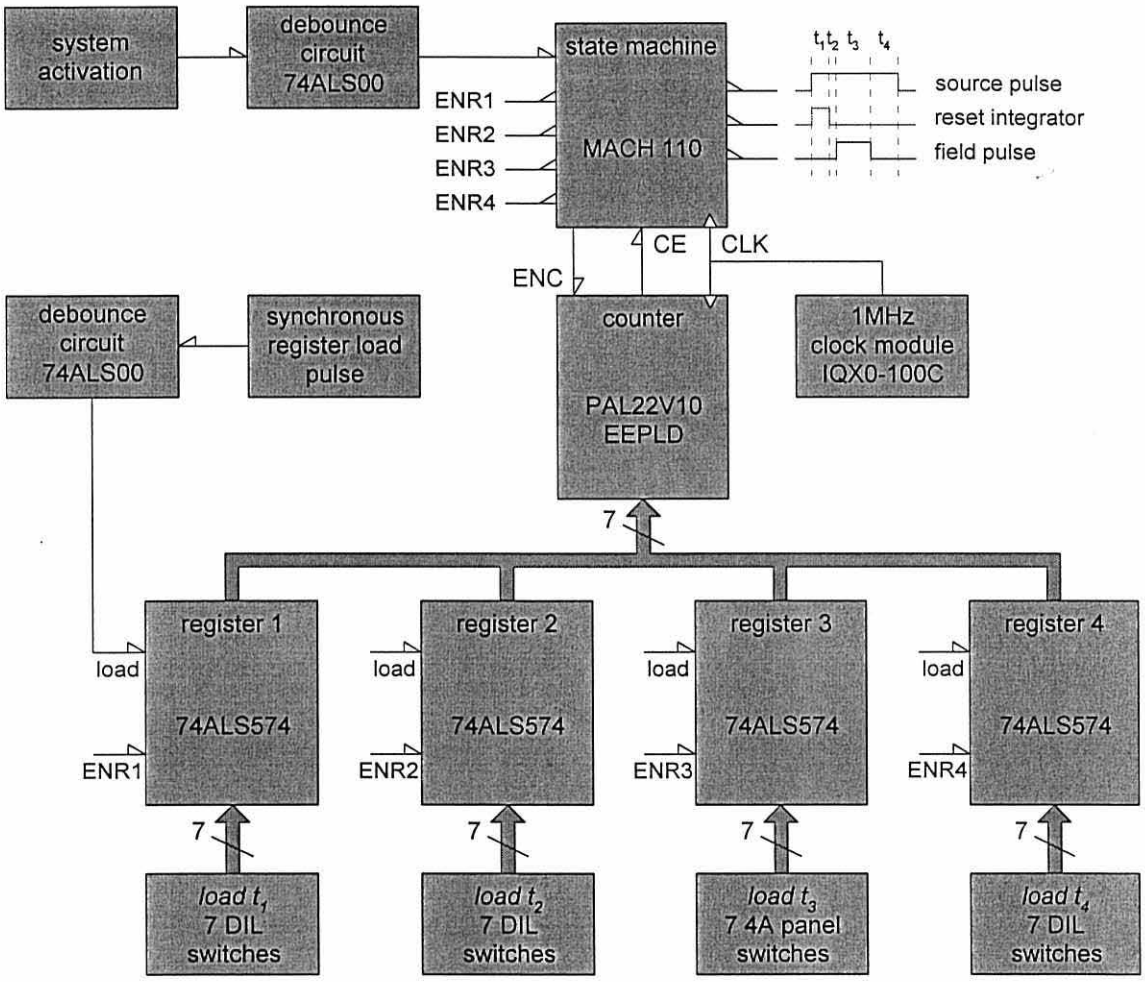

Figure 3.32 System diagram of digital control board.

The digital controller is designed as a synchronous state machine with the timing performed using a pre-loaded countdown counter implemented using a logic device programmed with PALASM™, a programmable array logic assembler, thoroughly documented for this application by (Hancock 1995). The counter is clocked at 1MHz using an IQD™ IQX0-100C quartz oscillator module, giving a system time resolution of 1μs. The numbers to be loaded into the counter determine the time segments t_1 to t_4, and

are stored in four separate Texas Instruments™ 74ALS574 octal flip-flops. Each time segment is selected by switching a combination of resistors before the data is latched through the register into an AMD™ PAL22V10 digital counter. Specifically, the contents of the appropriate register are latched into the counter after an enable register signal (ENR) from the AMD™ MACH110 state machine. The countdown counter is triggered by an enable counter signal (ENC) from the state machine, which now counts down from its pre-loaded value to zero. When the counter reaches zero, a counter empty signal (CE) is passed back to the state machine which causes a progression to the next state. Consequently, each state produces an output which constitutes part of the timing signals.

The numbers stored in the four 74ALS574 registers are loaded simultaneously on the rising edge of a debounced load pulse, which is fed into the clock input of the latches. The system activation pulse is also protected by a similar debounce circuit, implemented using 74ALS00 NAND gates, to prevent multiple triggering of the system. The time segment which controls the width of the field pulse t_3 is simply selected by setting seven 4A rated switches on the front panel of the magnetometer, thus enabling field pulses of between 25μs and 130μs to be generated. The TTL level timing pulses obtained from the digital controller, measured on the Tektronix™ TDS640 oscilloscope, are shown in figure 3.33.

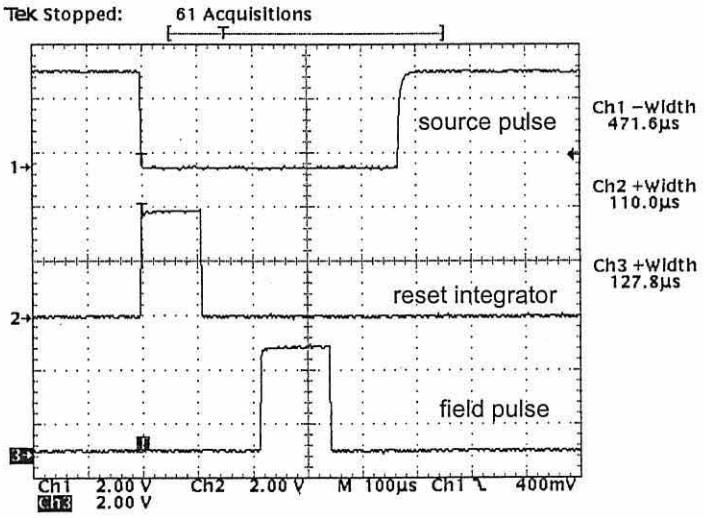

Figure 3.33 Measured TTL timing pulses obtained from the digital control board.

3.6 Concluding Remarks

This chapter has detailed the design and development of a pulsed field magnetometer used to study the reversal processes of advanced metal particle dispersions. The results obtained from the instrument are presented in §4, with publications derived from the work included in Appendix A. The majority of the pulsed field measurements were performed during two separate visits to the laboratories of the industrial collaborators in this project, Imation Research Limited, Harlow, UK. Problems concerning safety, reliability and portability were addressed by securely mounting the components in a 19inch racking enclosure. Photographs of the complete pulsed field magnetometer are shown in figures 3.34 and 3.35.

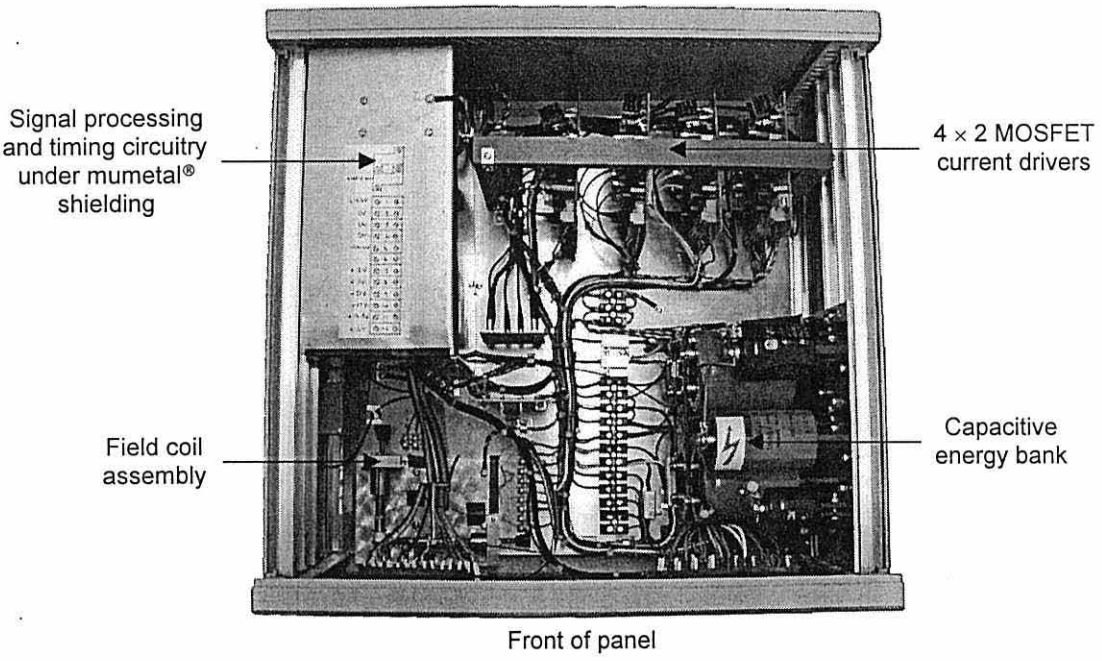

Figure 3.34 Photograph of the interior of the pulsed field magnetometer.

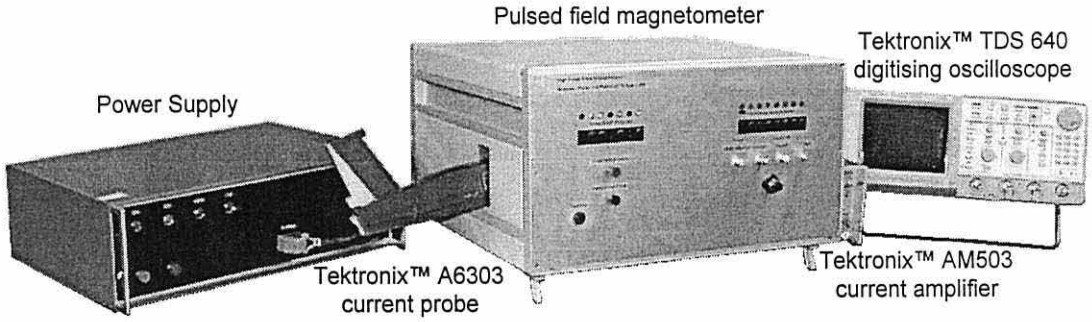

Figure 3.35 Photograph of the pulsed field magnetometer.

References

Cullity, B. D., *Introduction to magnetic materials* (Addison-Wesley Publishing Company, 1972).

Grover, F. W., *Inductance calculations working formulas and tables* (Dover Publications, Inc., 1946).

Hancock, C. P., PhD, University of Wales (1995).

Hancock, C. P., Owens, A. R., Williams, R. G., *Meas. Sci. Technol.* **9**, 365-377 (1998).

Herlach, F., *IEEE Trans. Magn.* **24**, 1049-1051 (1988).

Herlach, F., Perenboom, J. A. A. J., *Physica B* **211**, 1-16 (1995).

Hewlett-Packard, "High frequency transistor primer, Part III" *http://www.hp.com/go/rf/* (1998).

Horowitz, P., Hill, W., *The art of electronics* (Cambridge University Press, ed. 2nd, 1989).

Jones, G. R., O'Grady, K., "The development of a reversible transverse susceptometer", S. Iezekiel, Ed., PREP'99 Conference, UMIST, Manchester, 261-264 (IEEE, 1999).

Jones, H., Van Cleemput, M., Hickman, A. L., Ryan, D. T., Saleh, P. M., *Physica B* **246-247**, 337-340 (1998).

Keller, F. J., Gettys, W. E., Skove, M. J., *Physics classical and modern* (McGraw-Hill, Inc., ed. 2nd, 1993).

Kido, G., Miyakawa, T., Nakagawa, Y., *Physica B* **155**, 403-406 (1989).

Lander, C. W., *Power electronics* (McGraw-Hill, ed. 3rd, 1993).

Millman, J., Grabel, A., *Microelectronics* (McGraw-Hill, ed. 2nd, 1987).

Noggle, C., Trujillo, H., Miera, B., Adler, R., "A rep-rated pulser for generating fast-rising pulsed magnetic fields", 19th Power Modulator Symposium, San Diego, CA., 539-543 (IEEE, 1990).

Nojiri, H., et al., *Physica B* **241**, 210-212 (1997).

Ott, H. W., *Noise reduction techniques in electronic systems* (John Wiley and Sons, ed. 2nd, 1988).

Portugall, O., et al., *J. Phys. D: Appl. Phys.* **30**, 1697-1702 (1997).

Prichard, L. S., Mayo, P. I., O'Grady, K., *IEEE Trans. Magn.* **34**, 1684-1686 (1998).

Pritchard, R. L., *Electrical characteristics of transistors* (McGraw-Hill, 1967).

Ratcliffe, P. J., *Elect. Wire. World* **93**, 225-226 (1987).

Whalen, J. J., Paludi, C., *Int. J. Electronics* **43**, 501-511 (1977).

Wheeler, C. B., Mitchell, I. H., *Proc. IEE* **134-A**, 577-585 (1987).

Chapter
4

Pulsed Field Measurements of Advanced Metal Particle Dispersions

4.1 Introduction

This chapter outlines the proving studies performed using the pulsed field magnetometer developed in §3. In this investigation, pulsed field measurements of a series of advanced metal particle pigment formulations are presented. Differences in chemical formulation and dispersion quality were monitored through pulsed remanence curves, and real-time imaging of the dynamic magnetisation. These findings are substantiated from further diverse magnetic and non-magnetic studies of the dispersion samples and their coatings. These include rheological and optical measurements, as well as standard magnetic characterisation of simple hand-spread tapes. A comprehensive pigment evaluation along with time dependence studies provide a full analysis of the dispersion process.

This chapter also examines the components and preparation of particulate recording media, along with an extensive review of the variety of characterisation techniques employed to ensure the production of a coated product with good magnetic and mechanical properties.

4.2 Components of Particulate Media

The most critical stage in the production of particulate media is the preparation of a homogenous and stable pigment dispersion (Mathur, et al. 1991). In addition to the wide range of pigments that have been developed in order to satisfy the requirements of

the recording industry, the diverse components also required to produce a good quality dispersion are outlined in this section.

γ-Fe_2O_3 pigments are still widely used materials for low-cost recording applications where medium to long access time is permissible. Acicular iron oxide particles have lengths typically 0.2μm to 0.8μm, with aspect ratios between 4:1 and 12:1. The coercivity is controlled by particle elongation, and is generally between 250 Oe and 400 Oe, having a saturation magnetisation of around 75 emu g^{-1}. On coating, values of squareness up to 0.8 have been achieved providing reasonable resistance to demagnetising effects, and a useful output signal at lower densities. A full review of the preparation of γ-Fe_2O_3 particles and other pigments for use as recording media is given by (Bate 1980).

CrO_2 pigments are popular in the manufacture of high quality audio and video tapes. The ferromagnetic particles are again acicular, with lengths typically of the order 0.2μm to 0.5μm and aspect ratios between 10:1 and 15:1. The particles possess a bulk saturation magnetisation similar to that of γ-Fe_2O_3, typically 73 emu g^{-1}, with coercivities in the range 400 Oe to 650 Oe. Excellent morphology allows squareness ratios of up to 0.9 to be realised, with a resulting higher output signal recovered from the tape. CrO_2 particles are prepared from the hydrothermal reduction of CrO_3 in pressurised and heated water (Swoboda, et al. 1961).

Ferromagnetic metal particle (MP) pigments are currently used for high density data storage, where a high magnetic moment and coercivity are required. These particles consist of an iron metal core surrounded by a passivating oxide layer that prevents corrosion with the atmosphere, dispersants, and binders. Particles are obtained from iron oxyhydroxide, by reduction with hydrogen. The particles are coated with a number of anti-oxidising and anti-sintering agents and are partially oxidised to provide chemical stability. The process provides very small uniform particles which allows for the addition of cobalt, added via its hydroxide at the precipitation stage. The presence of cobalt serves to increase the magnetisation of the particles, along with improving corrosion resistance (Kisomoto, et al. 1991) and morphology (Okamoto, et al. 1996). For the latest MP technology, various oxides of aluminium and yttrium are also deposited in the passivation layer to improve their chemical stability (Morales, et al. 1998). Consequently, the passivation layer can be smaller, hence a greater volume of

the particle contributes to the recorded signal. Typical values of bulk saturation magnetisation are in the range 130 to 190 emu g^{-1}, with coercivities between 1000 Oe and 2800 Oe. Particle lengths for advanced media are typically 0.06μm to 0.1μm. Innovations such as the 100MB iomega zip™ disk, the 120MB Imation SuperDisk™, and the 200MB Sony HiFD™ disk are all based on advanced metal particle technology.

As well as the magnetic pigment, the role of the non-magnetic components in a dispersion are just as significant. Dispersants, which are also known as wetting agents are used to improve the uniformity of the dispersion. They separate particle agglomerates which are formed primarily by Van der Waals attraction between particles. The type of dispersant is chosen such that it bonds readily with the particle surface, allowing the solvent to wet the pigment.

Binders, also known as resins, are of prime importance as they ensure that a strong, durable, and well-dispersed magnetic coating is bound to the substrate. The binder must exhibit high wear resistance and flexibility, combined with long term chemical and physical stability. Formulations of polyurethane resins provide elasticity, whilst vinyls supply strength and durability.

Various solvents are used in the preparation of dispersions. The main function of the solvent is to dissolve the binder into which the magnetic pigment is dispersed, whilst the evaporation rate of the solvent is critical to both the coating and orientation processes. In a commercial dispersion, a number of solvents are used, which evaporate at rates controlled by their differing boiling points. Typical solvents include Methyl ethyl ketone, Methyl isobutyl ketone, Cyclohexanone, and Toluene.

Abrasive agents are added to clean the surface of the recording transducer. The build-up of debris and tape particles can adversely affect the performance of the recording system, and abrasives such as aluminium oxide help to prevent this. These particles are of similar size to the magnetic pigment, between 0.4μm and 0.6μm, and are added to the dispersion at the milling stage.

Anti-static agents are included to prevent the build up of large electrostatic charges which may occur during recording or playback. These electrostatic charges attract airborne particles to the tape, causing drop-outs, noise, and tape stacking problems. The most popular anti-static agent is carbon black, which also acts as a tape lubricant.

Finally, cross-linking agents are used to improve the mechanical properties of the tape, providing increased resistance to adverse thermal and humidity effects. Typical chemical cross-linking agents are poly functional isocyanates.

The substrate or web is the backing layer onto which the dispersion is coated, the properties of which are critical to the quality of the recording media. The substrate must have good mechanical properties, high wear resistance, and smooth surface characteristics. A common substrate being polyethylene terephthalate. Typically, a finished substrate will have a thickness in the region of 5μm to 30μm.

4.3 Preparation of Media

The principles of dispersing and coating particulates, which originated in the paint industry, have been borrowed heavily by the manufacturers of flexible recording media. In this section, the processing and production of particulate media is described. In order to produce a uniform and robust magnetic coating, with the desired thickness and surface properties, the magnetic particles must be well-dispersed in a binder, solvent, and dispersant formulation (Mee, et al. 1987). Other additives such as lubricants, anti-static agents and fillers are included to improve mechanical durability (O'Grady, et al. 1991). The dispersion is then coated onto a substrate, whilst allowing the particles to align and dry to an orienting field in order to improve the recording performance of the medium (McCary 1971). The preparation of dispersions can be separated into a number of stages, each of which influences the quality of the final product. Likewise, other processes after dispersion production, such as coating, orientation, and calendering have a significant effect on the quality of the media, and are equally discussed.

4.3.1 Premixing

The first stage of the dispersion process is the premix. Premixing combines together the individual components of the dispersion, allowing the dispersant to coat the surface of the pigment to prevent agglomeration. In the first stage of the process, the pigment is preworked in a water-cooled kneader or sawtooth mixer to form a high viscosity paste, thus ensuring high shear. During preworking, the mixing vessel is sealed, and the paste milled under an inert gas to prevent ignition of the pyrophoric metal particles. The

second stage of the process involves the gradual addition of solvents and binders to the vessel to maintain optimum shear. The mix is then blended for several hours, whilst carefully monitoring the solids ratio and viscosity to check solvent loss. After premixing, the dispersion may be allowed to stand for a short period to enhance pigment wetting.

4.3.2 Milling

The purpose of milling is to disperse the particles in order to produce a homogenous dispersion for coating. The high shear process is provided by rotation of the dispersion in a bead mill, as shown in figure 4.1. The mill consists of a series of pegs fixed along the length of a shaft which rotates at several thousand revolutions per minute in a chamber filled with ceramic beads. The beads generate large tear forces to break down agglomerates and structures. In large-scale production, the dispersion will pass through several different mills during the manufacturing process. For small batches, a single mill may be used with the dispersion recirculated by pumping. The milling process is highly energetic, and the chamber is water-cooled to prevent solvent evaporation.

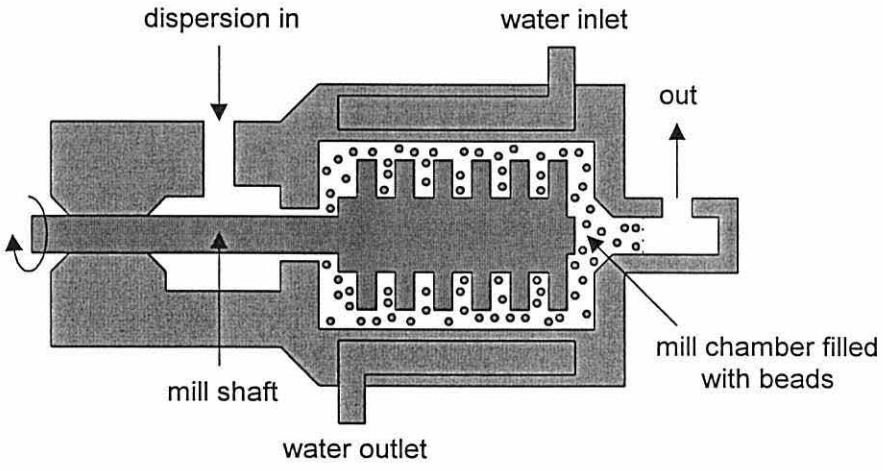

Figure 4.1 Schematic diagram of a high shear bead mill.

4.3.3 Letdown

At the end of the milling stage, the viscosity of the dispersion is too high for coating. The letdown involves the careful addition of solvents and binders to achieve a suitable coating viscosity, typically 50% of that during milling. The delicate process is

undertaken in several stages in the high shear environment of the mill in order to prevent flocculation of the particles. Despite these precautions, flocculates, agglomerates, and other debris which can be inadvertently synthesised in the dispersion, may be removed by series filtering.

4.3.4 Activation and Coating

The final process before coating is to activate the dispersion to provide cross-linking of the resin system. The cross-linking process bonds long chains of resins together, to afford a coated tape product with increased mechanical durability and enhanced resistance to temperature and humidity effects.

There are several methods of coating the dispersion onto a substrate which are described clearly by (Mee, et al. 1987). Essentially, the techniques are similar, in that a cylindrical roll is used to pick-up the dispersion from a bath or pressure-fed nozzle, before depositing a uniform coating onto the substrate passing between a knife-blade or secondary coating roll. The thickness of the coating is approximately 6 to 10 times as thick as the dry coating, and is controlled by a combination of roll separation, coating viscosity and velocity. In a production environment, automated coaters manage substrates as thin as 6μm, as wide as 1.5m, at coating speeds in excess of 5m s^{-1}.

4.3.5 Orientation and Calendering

Directly after coating, unless an isotropic media is required as is the case for flexible disks, a magnetic field parallel to the coating direction is applied to orientate the particles. The process of orientation improves the recording properties of the media, by increasing the remanent magnetisation and signal to noise ratio (Chantrell, et al. 1992). One of the most popular longitudinal orientation processes consists of a pair of opposing permanent magnets followed by a solenoid (Sumiya, et al. 1983). The orienting fields produced by the permanent magnets are of equal magnitude and opposite sign, thus cancelling any residual field outside of the orienting system. The additional solenoid is adjusted to compensate for insufficient cancellation of fields which may oppose the alignment field. This is critical, as even small fields may alter particle alignment. The web is then allowed to dry in a controlled manner inside the enclosed atmosphere of an

oven in order to recover solvent vapours. The final stage of manufacture involves slitting the tape with rotating knife blades and winding onto spools.

4.4 Characterisation of Dispersions

A magnetic suspension in its liquid form is a very complex material, with a number of different forces acting between the particles. Attractive forces within a dispersion arise from both Van der Waals attraction and dipolar interactions; the repulsive forces between particles are due to steric repulsion and electrostatic interactions. Full analytical expressions for these forces can be found in the review paper by (Mathur, et al. 1991). It has been found by the same author, that the dominating forces acting within a dispersion are the long-range dipolar attraction and the short-range steric repulsion. The stability and quality of a dispersion is therefore controlled by balancing these forces, and as a result, recent studies have been undertaken to model these interactions. A series of molecular dynamic (MD) models of acicular particles under varying shear conditions have been developed in order to study dispersion microstructure (Coverdale, et al. 1993) (Deymier, et al. 1994) (Gunal, et al. 1996). More recently, a cluster analysis algorithm based upon maximisation of the entropy of the system, has provided an alternative approach for characterisation of dispersion microstructure (Coverdale, et al. 1998).

4.4.1 Magnetisation Processes in Dispersions

In order to outline the reversal processes in dispersions, it is worth considering some of the possible states of a dispersion, which are illustrated schematically in figure 4.2.

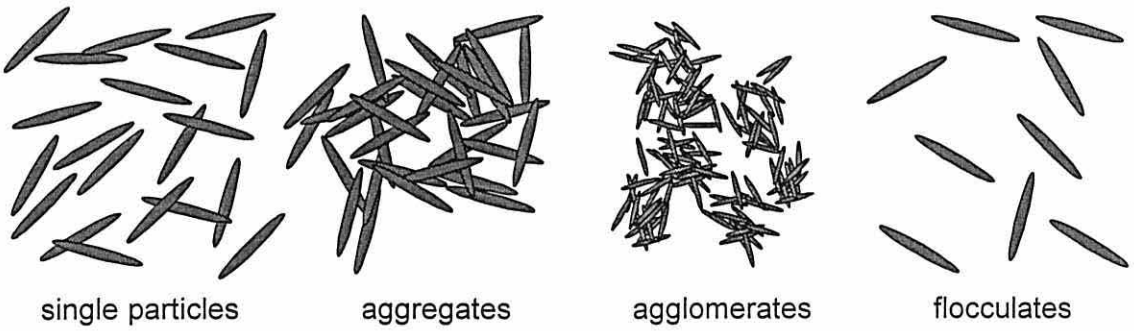

Figure 4.2 Microstructure of a dispersion.

Generally, the microstructure contains particles in four configurations. Firstly, there are dispersed single particles which can easily align to an external field, producing a tape with a maximum remanence. Secondly aggregates are formed, which are tightly bound clusters of unwetted single particles unlikely to be broken down by milling due to the large Van der Waals forces involved. Agglomerates are more loosely bound structures of wetted single particles and aggregates. These are predominately formed as networks in the dry pigment, but may be separated during milling. Finally, flocculation of the particles can sometimes occur if steric repulsive forces are sufficient.

Studies of metal particle systems have found that there are three main processes which contribute to magnetisation reversal in dispersions (Greaves, et al. 1996a). At low fields there is a localised deformation of the flocculates as they acquire a net moment. As the field increases, single particles and small aggregates are able to rotate into the applied field direction. These processes of mechanical orientation are generally reversible, with considerable relaxation effects taking place after removal of the applied field. For dispersions containing large aggregates, the couple due to the field is too small to allow them to rotate, and Néel switching of the magnetic moments is observed with increasing field. This is an irreversible process with no observed time or rate-dependent effects. In real systems there is a distribution of aggregate sizes and both processes are observed. Therefore, standard measurements of dispersions are difficult to resolve as the magnetic field alters the microstructure.

4.4.2 Magnetic Characterisation of Dispersions

The production of high quality particulate media is only possible if the suspension of magnetic particles used to coat the substrate is well-dispersed. The quality of a dispersion is assessed by the number and type of agglomerates, while the stability is measured by the formation of flocculates or agglomerates as a function of time (Mathur, et al. 1991). Several magnetic techniques have been used to study both the quality and stability of dispersions. However, the high magnetic volume fraction gives rise to a strongly interacting dynamic system, which yields results that are difficult to interpret and often not reproducible, as the application of a magnetic field alters the dispersion microstructure (O'Grady, et al. 1991).

The properties of wet, frozen, and oriented γ-Fe_2O_3 dispersions have been studied using a VSM (Fisher, et al. 1982). The effects of milling, formulation, and viscosity on the dispersion and the final coated product were compared through standard measurements of H_c, H_{cr}, M_r/M_s, and S^*. Dispersion stability was also determined by measuring time dependence as a function of DC field. Good correlation between the magnetic properties of the oriented frozen dispersion and the coating was observed, suggesting that this technique could be performed to forecast the quality of the finished product from the dispersion attributes. More recently, by using low temperature magnetometry to effectively limit particle rotation, studies of BaFe media have been undertaken (Greaves, et al. 1996b). The interactions in the dispersion were studied using the well-established δM technique (Kelly, et al. 1989), as a function of milling. Hysteresis measurements of samples cooled to 77K in a 10kOe orienting field revealed a monotonic increase in M_r/M_s with milling, resulting from the greater mobility of particles able to rotate in the DC field. From δM measurements, a decrease in interactions was noted, resulting from the weakening in stacks of particles as the milling process continued.

Studies which invoke mechanical shear to a dispersion during a magnetic measurement have been found to destroy particle networks and structures, which simplifies the interpretation of results. By using a VSM constructed with a vertical solenoid (Scholten, et al. 1990a), measurements were performed on CrO_2 samples sheared at $100s^{-1}$ between the walls of a cylindrical viscometer. Samples of dispersion were subjected to increasing DC fields to measure the initial magnetisation curves for both sheared and unsheared samples. The unsheared sample exhibits a steep increase in magnetisation at low fields which is due to particle rotation. By comparing the ratio of the two responses, the proportion of the particles that are free to rotate can be gained, and hence an indication of dispersion quality. The dynamic properties of the suspension were studied in AC magnetic fields. The most interesting aspect is the frequency dependence of the initial susceptibility in freshly prepared and aged samples. This work was extended to include Co-γ-Fe_2O_3 dispersions during stages of milling, letdown, and ageing (Balkenende 1994). The interpretation of these results led to a model of low field magnetisation processes to be developed from Langevin behaviour. This technique was further extended to cover MP dispersions (Veitch, et al. 1994). The shear cell was

improved to give a maximum shear of approximately $12000s^{-1}$ in a field of 4.8kOe. Again, results obtained from this magnetometer correlated well with the orientation of resulting tapes and revealed that metal particle formulations can be dispersed to single particles by kneading in an appropriate dispersant.

Measuring the DC magnetic field response of MP media in the form of isothermal remanence curves (Mayo, et al. 1992), and DC demagnetisation remanence curves (Mayo, et al. 1993a), as described in §2.6.2.2, again reveals information concerning the dispersion quality. Theoretical interpretation of the data using a Brownian motion relaxation model has been used to estimate the mean aggregate size of the particle networks in the dispersion. This work has been continued to clarify the magnetisation processes and microstructure in metal particle dispersions (Greaves, et al. 1996a).

The study of transverse susceptibility has been found to be a useful technique for the quality assessment of CrO_2 dispersions (Sollis, et al. 1993). The procedure involves the application of a small AC field, typically 3 Oe at 10kHz, situated perpendicular to a large DC bias field, with the transverse susceptibility χ_t measured in the AC field direction. Tape samples oriented to the AC field have been found to exhibit a strong peak around the anisotropy field H_K (Sollis, et al. 1992), however, well-dispersed suspensions are able to align to the DC field and the peak is reduced. Thus, by monitoring the linearity of a plot of $1/\chi_t$ for a field reduction from high field gives a measure of particle alignment, and hence dispersion quality. This work was extended to correlate remanence curve data, time dependence studies, shear magnetometry, and neutron depolarisation studies with transverse susceptibility measurements of CrO_2 dispersions (Mayo, et al. 1993b). An associated technique known as DIMAG (DIspersion by MAGnetic measurement) has been used successfully to assess the quality of MP dispersions (Jung, et al. 1992), and Co-γ-Fe_2O_3 dispersions (Jung, et al. 1993), by comparison with standard measurements of hand-spread coatings. In this procedure, a dispersion sample initially subjected to a 60 Oe AC field, is then exposed to a perpendicular DC bias of up to 840 Oe for a short duration. During the application and removal of DC field, the amplitude and phase response is related directly to the dispersion quality.

A major focus of study in Bangor has been the development of pulsed field magnetometry in order to study reversal mechanisms of dispersions. The technique involves precluding particle rotation by applying short duration magnetic fields to the sample. This approach was first established in 1975 to investigate the dynamic magnetisation properties of ferrofluids (Bogardus, et al. 1975). Using a Velonex™ 360 pulse generator connected to a drive coil, pulsed magnetic fields between 1μs and 3ms could be selected with a maximum field of 1kOe. The magnetisation of the sample was determined from the time integral of the signal from a pair of opposed sense coils. Over wide timescales, these workers observed both particle rotation and Néel switching in commercial ferrofluids, using the terms of 'slow' and 'fast' decay of magnetisation reversal, as described in §4.5. On fitting an exponential term to the magnetisation decay, and using a simple particle rotation model developed by (Janak 1971), an estimation of the 'particle size' could be made.

Recently this topic has been revisited for the characterisation of recording media. Studies of γ-Fe_2O_3 and CrO_2 dispersions have been performed using a purpose-built magnetometer capable of generating field pulses up to 1270 Oe, with pulse widths from 4μs to 127μs (Hancock, et al. 1996) (Greaves, et al. 1996c). These studies found that for pulsed fields of less than 100μs duration, particle rotation appeared to be eliminated to give a useful assessment of dispersion quality, in agreement with low temperature measurements and studies of simple hand-spread coatings. This work has been extended for metal particle dispersions, with the development a pulsed field system capable of producing magnetic fields of up to 4.7kOe, as described in §3. In agreement with (Greaves, et al. 1997), pulsed field studies of MP dispersions have revealed that particle rotation can occur in response to pulsed fields of less than 100μs length. By comparison with standard measurements of the coated tape, differences in chemical formulation and dispersion quality could be monitored through pulsed remanence curves.

4.4.3 Non-magnetic Techniques

Typical non-magnetic measurements of dispersions include techniques based on optical microscopy and rheological studies. Optical microscopy is a powerful qualitative tool for studying the uniformity and surface properties of coatings. One of the most widely

used optical techniques in the media industry is the measure of gloss. Gloss is a term used to describe the intensity of light specularly reflected at a fixed angle from the plane of a magnetic coating. With this simple technique, higher gloss values are obtained when particles are well-dispersed with milling, whilst a dispersion containing a large number of structures will have a reduced reflectivity (Jakusch 1987). The disadvantage of this approach is that only the surface of the media is probed, which is influenced by the uniformity and reproducibility of the coating process.

Other optical techniques have been developed using transmission electron microscopy (TEM) images of coated tapes (Scholten, et al. 1990b), and also rapidly frozen BaFe dispersions (Potanin, et al. 1997). These studies provide a representation of the dispersion microstructure at various stages of production. A completely non-invasive technique which measures the intensity of the small angle light scattering (SALS) from a suspension of sheared erythrocyte particles has been developed (Salem, et al. 1985). By relating the recorded SALS pattern to the alignment and orientation of the sheared suspension, an indication of the dispersion quality can be gained. Similar results have been obtained from static and dynamic light scattering measurements of various iron oxide particles (Chu, et al. 1987), and X-ray scattering of a series of magnetite ferrofluids (Anthore, et al. 1980). The disadvantage of these studies is that the dispersion must be highly dilute to allow transmission of light to a detector, whilst X-ray scattering is limited to small particles below 100nm.

In addition to optical microscopy, the other popular technique used to characterise dispersions is rheology. The rheological properties of a magnetic suspension are complex, yet yield valuable information concerning the state of the dispersed particles to give a measure of the dispersion quality. In fact, the behaviour of magnetic dispersions is similar to non-magnetic systems (Smith, et al. 1979).

A rheogram is a plot of shear stress against shear rate and is usually measured using a viscometer. The curve obtained provides several useful characteristics such as the yield point and viscosity which have been found to change considerably with milling (Dasgupta 1984). In this study, a measure of the viscosity of γ-Fe_2O_3 dispersions obtained from a low shear viscometer, was extrapolated to approach the high shear environment of the mill, and was found to correlate well with measurements of M_r/M_s, orientation ratio, and SFD of hand-spread coatings. A similar study from extrapolated

rheograms of γ-Fe_2O_3 and CrO_2 suspensions has yielded useful results in regard to optimum mill times and dispersion microstructure (Kuin 1987).

Recently, a novel rheomagnetic technique has been developed for studying the concentration and orientation of dispersions (Kwon, et al. 1992). This on-line measurement procedure has been used to continuously estimate the quality of γ-Fe_2O_3 and BaFe dispersions prior to coating. Essentially, the system consists of a flow cell connecting a large tube to a narrow one. In the large tube the dispersion flow is quiescent, and the orientation of the particles is random. As the flow passes to the narrow tube, the particles are oriented by the flow, and the permeability of the suspension becomes anisotropic. The change in permeability is detected by measuring the change in inductance across the cell. Consequently, a dispersion can be characterised through the interpretation of inductance against flow rate to yield useful results. Similarly, the use of such an instrument has provided an indirect measure of dispersion quality for spin-coating of particulate rigid disks (Shah, et al. 1992).

4.5 Pulsed Field Measurements

Exposing a dispersion to DC field will invoke a combination of both particle rotation and Néel switching, which is dependent upon the microstructure and suspension viscosity (O'Grady, et al. 1991). Accordingly, pulsed magnetic fields provide an indication of the state of a dispersion without field induced aggregation of the particles. Indeed, for both γ-Fe_2O_3 and CrO_2 formulations, a short duration pulse of typically 100μs has been found to effectively 'freeze' the dispersion, whilst still lasting long enough to initiate Néel switching of the magnetisation (Hancock, et al. 1996). For MP dispersions, some degree of mechanical orientation is observed due to the large torque acting upon dispersed particles with high magnetisation (Prichard, et al. 1998), as included in Appendix A.

Pulsed field studies allow the dynamic reversal properties of dispersions to be monitored, therefore, alignment and relaxation processes can be observed in real-time. The first study of this kind was initiated by (Bogardus, et al. 1975), for formulations of spherical Fe_3O_4 particles. Figure 4.3 indicates the dynamic magnetisation response of three different ferrofluid formulations to a 400 Oe pulsed field of 200μs duration. After the applied field is removed, two distinct relaxation mechanisms are observed. The

magnetisation is characterised primarily by a fast decay occurring in less than 1μs, together with a slow decline that can be as long as 1ms. From additional measurements of frozen ferrofluids, the authors concluded that the 'fast' component of reversal was due to magnetisation switching within the particle, whilst bulk particle rotation characterised the 'slow' relaxation.

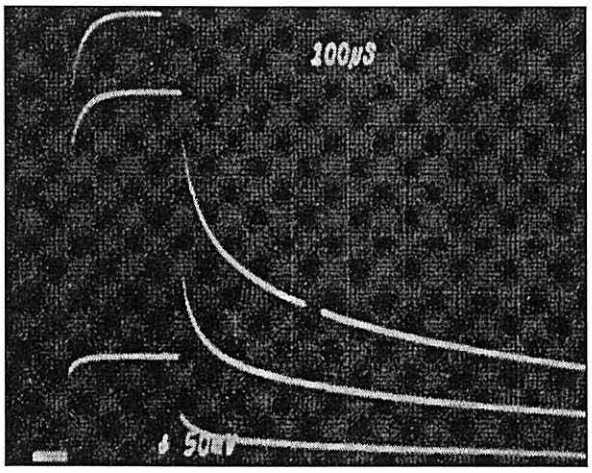

Figure 4.3 Waveforms of magnetisation against time for three water-based ferrofluids of 200, 400, and 600 gauss saturation moment, in response to a pulsed field of 400 Oe.

More recently, pulsed field studies have been used to provide an assessment of dispersion quality in the manufacture of particulate recording media (Hancock 1995). In this study, a magnetometer capable of producing pulses between 10 Oe and 1270 Oe, with selectable pulse widths from 4μs to 127μs was used to study the reversal mechanisms of γ-Fe_2O_3 and CrO_2 dispersions. Figure 4.4 shows the magnetisation response of a γ-Fe_2O_3 dispersion after one hour of milling (Hancock, et al. 1996). It is observed that the magnetisation closely follows the field pulse, consistent with the 'fast' reversal reported by (Bogardus, et al. 1975). Hancock et al concluded that over short timescales, particle rotation was precluded, providing a means of monitoring differences in chemical formulation and dispersion quality through pulsed remanence curves, as described in §4.5.1.

This work has been extended for advanced MP technology using a combination of dynamic magnetisation studies, pulsed remanence curves, optical techniques, standard measurements of hand-spread coatings, pigment characterisation and time

dependence studies. Results from this comprehensive study are presented in the remaining sections of this chapter.

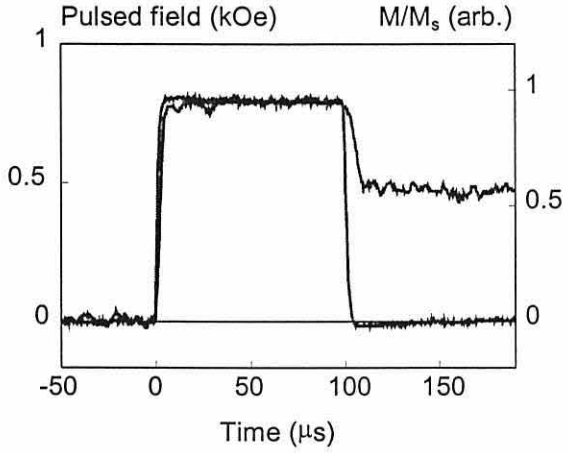

Figure 4.4 γ-Fe_2O_3 dispersion response to an applied pulsed field of 800 Oe.

4.5.1 Pulsed Remanence Curves

Fundamentally, pulsed field measurements are performed as pulsed remanence curves, which are identical to conventional IRM studies, as described in §2.6.2.2. The measurement procedure is illustrated in figure 4.5.

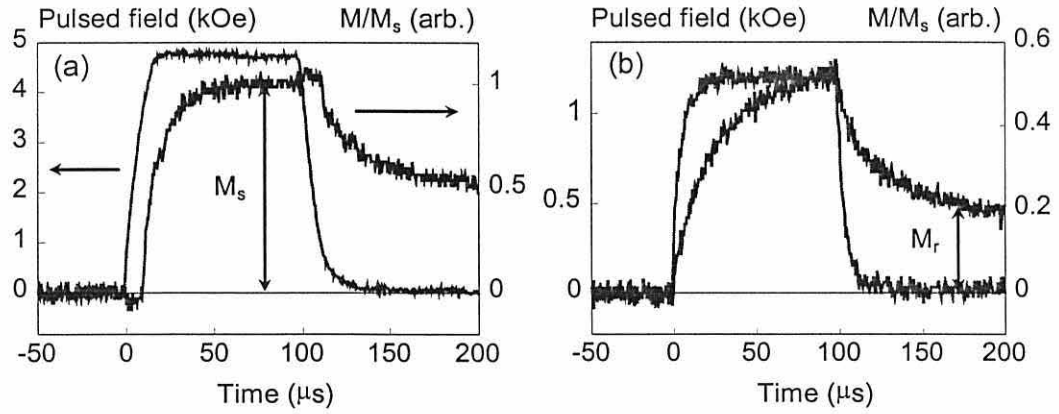

Figure 4.5 Pulsed measurement technique: (a) saturation pulse (b) remanence pulse.

For each appropriate pulsed field H, the remanence M_r can be determined directly from the oscilloscope (b). This is then compared to saturation level determined by applying a maximum pulsed field of 4.7kOe to the sample (a). The remanence ratio is given simply M_r/M_s (H). As IRM curves are measured from the demagnetised state, a fresh sample is used for each field pulse. The normalising parameter in the calculation

is the sample volume, which must be kept constant for each measurement. Also, in order to reduce demagnetising effects, the sample is enclosed in plastic tubing, with an axial ratio of around 8:1.

4.6 Dispersion and Milling Trial

In order to relate the pulsed field characteristics of dispersions to the properties of the final coated product, a dispersion and milling trial was conducted in conjunction with the industrial collaborators in this project, Imation Research Limited, Harlow, UK. Two very similar magnetic formulations, termed samples #1 and #2, containing the same advanced MP pigment were prepared to form dispersions with a solids ratio of 40% by weight. The preparation of the dispersion samples is illustrated in figure 4.6.

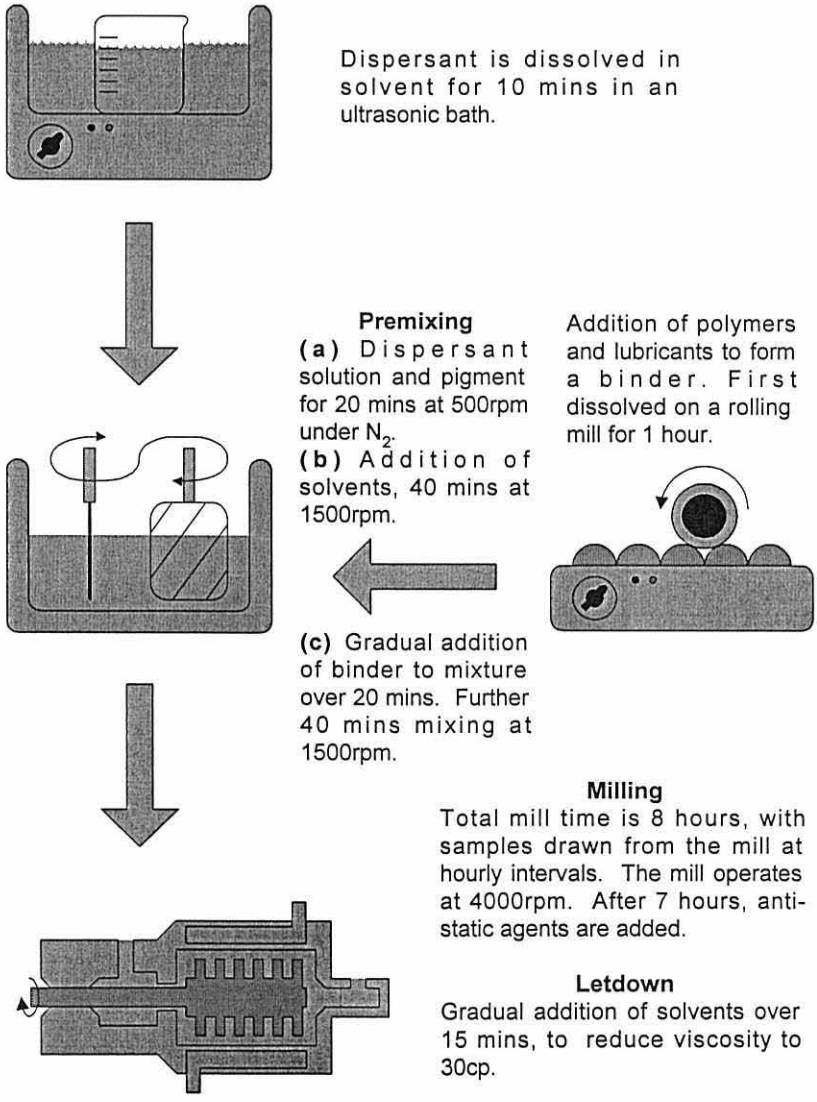

Figure 4.6 Preparation of MP dispersion samples used in this study.

The dispersions were composed of a proprietary blend of binders, solvents, dispersants, and lubricants similar to those found in any commercially available MP tape formulation. The only difference between the formulations was that one of the dispersing agents was not included in sample #2, leading to a poorer dispersion.

Using similar procedures to those described in §4.3, the dispersions were initially premixed at high solids ratio in a Ross™ LDM-1QT double planetary mixer before being transferred to a Dispermat® SL504 high shear recirculating bead mill where the dispersion was milled to completion over 8 hours. The final dispersions were subsequently letdown to approximately 30% solids ratio and coated using a simple knide-blade coater with a separation of 70μm. The tapes were oriented using a pair of 1000 Oe permanent magnets, and allowed to dry in a 400 Oe field, provided by an electromagnet, for 1 minute. During milling, wet samples drawn from the mill at hourly intervals were monitored using rheological measurements and analysis of hand-spread coating gloss, as discussed in §4.4.3. Dispersion samples were also taken for pulsed field analysis at various stages of milling and letdown, together with standard magnetic measurements of hand-spread coatings.

4.6.1 Characterisation of MP Pigment

As previously discussed in §4.6, the two dispersion samples analysed in this study were produced from the same advanced MP pigment. This section details the structure and properties of the pigment through a variety of techniques. Conventional bulk magnetic measurements including basic hysteretic information, along with studies of the switching behaviour determined by remanence curves is presented. The well-established δM technique has been used to study the nature of interactions on reversal.

Measurements of the time dependence of magnetisation were made using the method detailed in §2.5.2. The activation volume of reversal was determined and related to the physical particle volume from transmission electron microscopy (TEM) images, allowing an observation of the crystallite nature of the particles to be undertaken.

Recently, studies have focused on the distribution of grain sizes in thin film media (Jones, et al. 1999). In order to explain, at least in part, the anomalously wide

switching field distribution observed in MP recording media, a comparable investigation has been performed.

4.6.1.1 Basic Magnetic Characterisation

All the magnetic measurements reported in §4.6.1 were produced using a PAR 4500 vibrating sample magnetometer. The MP pigment sample was prepared by packing the powder into a plastic tube such that the axial ratio was greater than 5:1. In this way, the need to correct for sample shape demagnetising effects was eliminated.

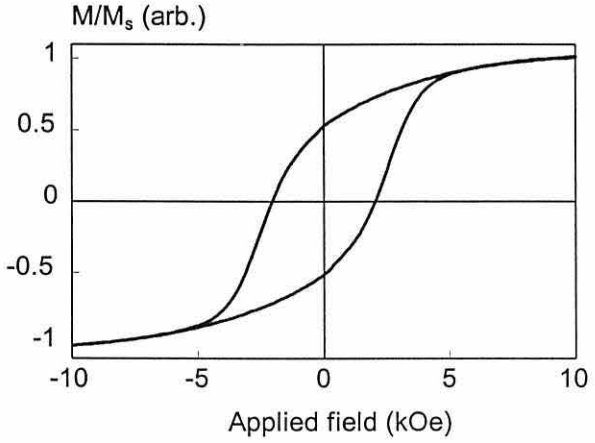

Figure 4.7 Hysteresis loop for advanced MP pigment.

The loop has a squareness of around 0.5, which is to be expected in single domain acicular particles where there is no preferential orientation of the particles, accordingly the easy axes are randomly distributed according to (Stoner and Wohlfarth 1948). The characteristics obtained from figure 4.7 are shown in table 4.1.

	MP pigment
H_c (Oe)	2040
M_r/M_s[a]	0.51
1-S*	0.589
M_s (emu g^{-1})[a]	154.2

[a] M_s = M at 10kOe

Table 4.1 Hysteresis loop properties of dry pigment.

4.6.1.2 Remanence Curves

Using the procedure described in §2.6.2.2, an IRM curve was measured as indicated in figure 4.8(a). The isothermal remanence $M_r(H)$ is obtained after the application and removal of a field H, with the sample initially demagnetised. Figure 4.8(b) shows the irreversible susceptibility $\chi_{irr}(H)$, obtained by differentiation of the IRM curve, as discussed in §2.6.2.3.

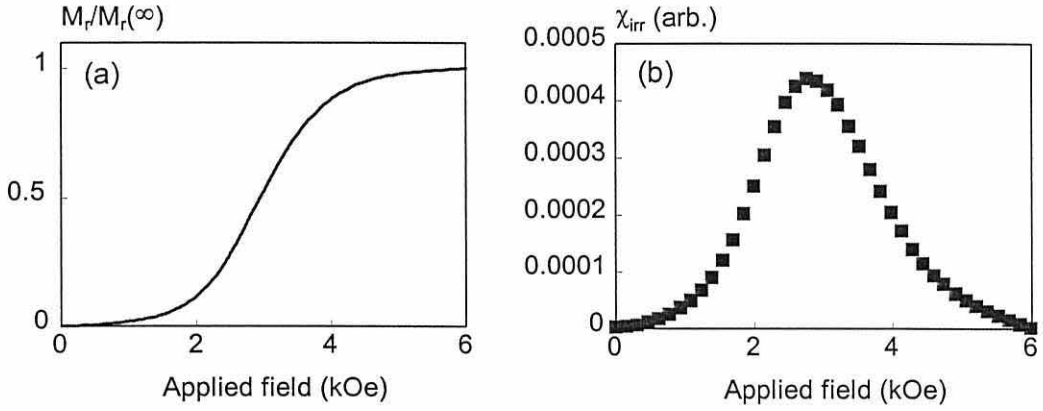

Figure 4.8 VSM measured IRM curve (a) and irreversible susceptibility (b) for pigment.

From figure 4.8, the onset of Néel reversal occurs at approximately 1300 Oe, with the remanent coercivity H_{cr}', the peak of the susceptibility curve, equal to 2780 Oe. It is also interesting to note that some particles have apparent switching fields of over 5kOe. Figure 4.9(a) indicates a DCD measurement, along with the appropriate irreversible susceptibility curve, as shown in figure 4.9(b).

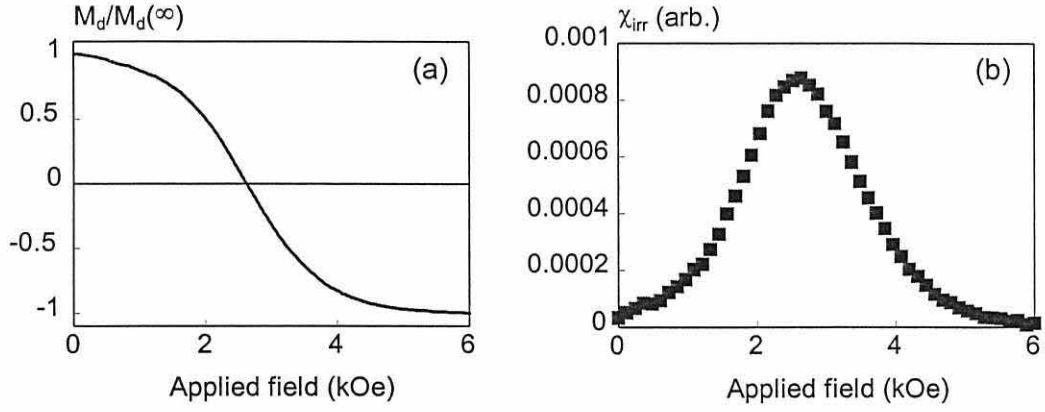

Figure 4.9 VSM measured DCD curve (a) and irreversible susceptibility (b) for pigment.

The DCD remanence $M_d(H)$ is obtained from the saturation remanent state by the application of increasing demagnetising fields. Specifically, a small negative external field is applied to the sample, and then removed. The remanent magnetisation in zero field is then recorded in terms of reversing field. As with the IRM measurement, in order to negate the effects of time dependent magnetisation, care is taken to apply the external field for a constant period of time for each remanence measurement. From figure 4.9(a), the remanent coercivity H_{cr}, at the crossover point of the DCD curve is 2620 Oe.

From figures 4.8 and 4.9, parameters obtained from the remanence curves are summarised in table 4.2. The full width at half maximum (FWHM) provides an indication of the breadth of the switching field distribution.

	H_{cr} (Oe)	FWHM (Oe)
IRM[a]	2780	2030
DCD[b]	2620	1990

[a] $M_r(H_{cr}') = 0.5 \times M_r(\infty)$ [b] $M_d(H_{cr}) = 0$

Table 4.2 Remanence curve parameters for MP pigment.

In the absence of many-body interaction effects, the switching field distributions obtained from the IRM and DCD curves would be identical (Wohlfarth 1958). Clearly, from figures 4.8(b) and 4.9(b) this is not the case. The peak of the DCD curve occurs at a lower field than in the IRM curve, indicating that it is easier for the system to be demagnetised rather than magnetised. In this case, this is termed a negative interaction, and could well be an indication of the effects of the strong dipolar interactions in the system, consistent with remanence studies of CrO_2 pigments (Spratt, et al. 1987).

It should be reiterated at this stage, that remanence measurements provide information on the irreversible Néel component of reversal only, whilst the pulsed remanence curves presented in §4.6.3 and §4.6.4 are due to a combination of reversible mechanical orientation of the particles together with Néel reversal.

4.6.1.3 δM Studies

In a densely packed system of fine particles, it is well known that interactions between the particles play a central role in determining the magnetic behaviour. To examine the

role of interactions, the δM technique, as discussed in §2.6.2.4, provides a simple quantitative approach. The δM curve obtained for the MP pigment sample in this investigation is shown in figure 4.10. It is clearly seen that a negative δM parameter is observed over the entire field range, indicating that it is easier for the system to be demagnetised rather than magnetised, a negative interaction. The δM curve is characterised by a rapid deviation at low fields continuing until a minimum is reached around the remanent coercivity. Finally, a gradual decay to linearity is noted at higher reversing fields. Qualitatively, this may be explained by considering the pigment to contain closed-loop particle configurations from dipolar interactions, which tend to stabilise the demagnetised state (Spratt, et al. 1988).

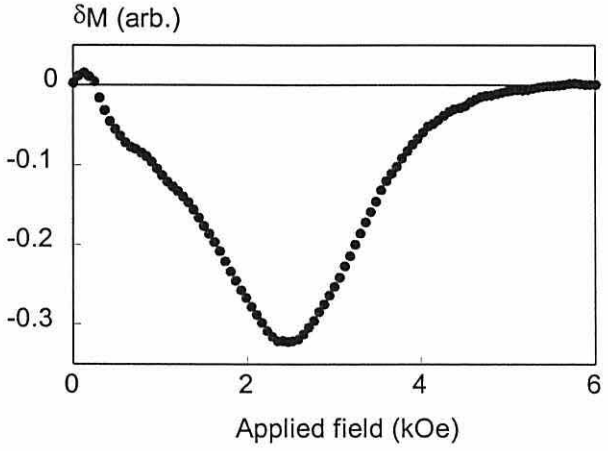

Figure 4.10 δM plot for MP pigment sample.

The existence of negative interactions suggest that the vast majority of the particles are rapidly reversed in lower than expected fields. The mechanism for reversal is probably linked to the co-operative switching of 'random agglomerated' particles (Mayo, et al. 1990). Accordingly, long-range flux closure configurations are formed which may reverse more readily.

4.6.1.4 Time Dependence Studies

Time dependent effects occur in all magnetic materials that exhibit hysteresis, and are due to thermal activation of transitions over local energy barriers, as discussed in §2.5.2. Measurements of the time dependence of magnetisation were made using the method detailed by (Street, et al. 1949) and interpreted according to the framework of (Gaunt

1986). In this technique, it is assumed that the magnetisation varies linearly with ln(t). This assumption is only correct if the width of the energy barrier distribution is large (Aharoni 1985). In the case of the pigment in this study, due to the wide variation of switching fields present and the random orientation of the anisotropy axes, a near linear variation of magnetisation with ln(t) is expected, as shown in figure 4.11. However, on careful inspection of this decay, it is evident that the magnetisation is curved slightly downwards, which would be indicative of moments at a somewhat higher energy barrier relaxing and becoming involved in the time dependence process, as suggested by the work of (el-Hilo, et al. 1993).

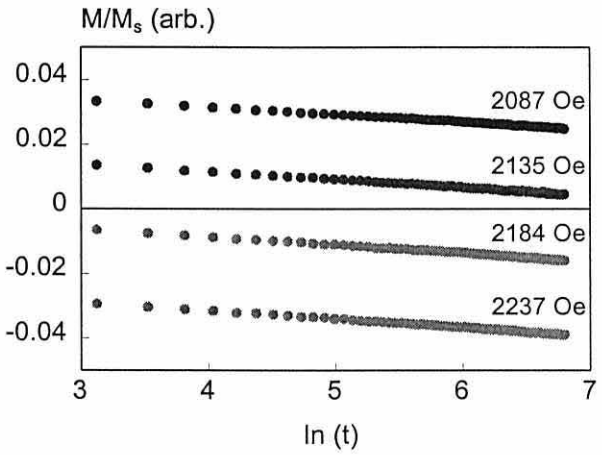

Figure 4.11 Variation of magnetisation with time at fields around the coercivity.

Specifically, data is obtained in the second and third quadrants of the hysteresis loop by first saturating the sample in the first quadrant, reducing the field to zero, and then applying a constant negative field to the sample. Measurements of the magnetisation are plotted against ln(t), as discussed in §2.5.2.1. By evaluating this data using a least squares straight line fit, the value of the magnetic viscosity S is obtained, such that

$$S = -\frac{dM}{d\ln(t)} \tag{4.1}$$

Figure 4.12 shows the variation of the magnetic viscosity with field for the MP pigment sample. It is clearly seen that the coefficient S varies with the applied field in a

well-defined manner. In agreement with (O'Grady, et al. 1981) and (Uren, et al. 1988), the magnetic viscosity experiences a broad maximum at a field slightly greater than the coercivity. Clearly, if the coercivity is defined as the field required to reduce the magnetisation to zero, its value will depend on the time at which the zero crossing occurs. The position of the peak of -dM/dln(t) in figure 4.12 could be used as a definition of coercivity, but its position will depend upon the measurement time (Sharrock 1990).

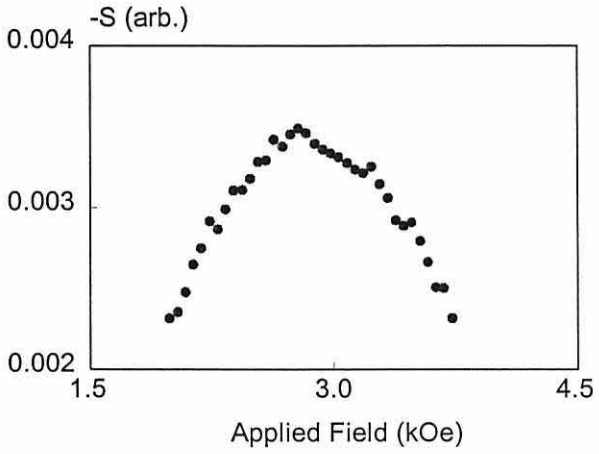

Figure 4.12 Variation of magnetic viscosity with applied field.

Using the theory described in §2.5.2.2, the fluctuation field H_f, and the activation volume of reversal υ, can be obtained from the equations,

$$H_f = \frac{S}{\chi_{irr}} \quad \text{and} \quad H_f = \frac{kT}{\upsilon M_s\left(1 - H / H_K\right)} \tag{4.2}$$

where the fluctuation field represents the effect of thermal energy on the magnetisation of the sample, and is determined from figures 4.12 and 4.9(b). The activation volume describes the volume of magnetic material which reverses coherently, and has been determined using H_K = 6.5kOe (Igaki, et al. 1998) and M_s = 1500 emu cm^{-3} consistent with the thin oxide layer present and manufacturers data (Morales, et al. 1998). Using equation 4.2, the fluctuation field and activation volume as a function of field are shown in figures 4.13(a) and 4.13(b) respectively.

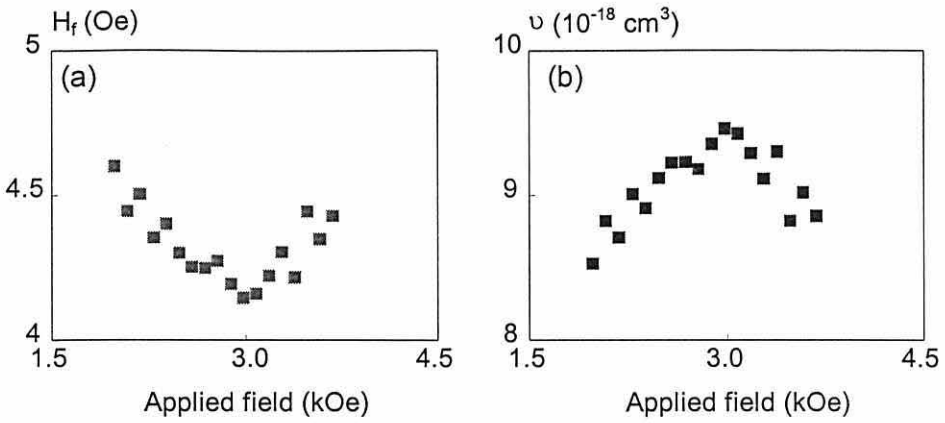

Figure 4.13 (a) Fluctuation field and (b) activation volume of pigment with applied field.

From figure 4.13(a), it is clear that a broad minimum of fluctuation field H_f is observed around the coercivity, in agreement with theoretical (Coverdale, et al. 1990) and experimental studies (de Witte, et al. 1993). Although, for compacted pigments of elongated particles, the morphology of the particles may present a larger H_f due to the switching process nucleating at the ends of the particle where demagnetising fields are stronger (Morales, et al. 1995). Clearly from figure 4.13(b), the activation volume is also not independent of the applied field. Physically, this arises from the fact that the energy barrier to reversal is lowered by the applied field, and consequently larger particles may become involved in the time dependence process (de Witte, et al. 1990).

The peak of the activation volume occurs at approximately 9.4×10^{-18} cm^3. Accordingly, this activation volume of reversal can be related to the physical particle volume from TEM analysis, allowing an observation of the crystallite nature of the particles to be undertaken, as discussed presently in §4.6.1.5. Consequently, a study of the magnetisation reversal mechanisms occurring in the particles can be achieved.

4.6.1.5 TEM Analysis

Information regarding the dimensions and size distribution of the magnetic pigment used in this study can be investigated through Transmission Electron Microscopy (TEM). TEM sample grids were prepared from a highly dilute pigment and water suspension. Specifically, a small amount of pigment was dissolved in approximately 20ml of water in an ultrasonic bath for 10 minutes, before coating the grids. The copper

TEM grids, evaporated with a layer of carbon to reduce static electricity build-up, were carefully drawn through a single bead of the suspension placed upon dental wax, before subsequent drying with a tissue. Microscope observations were made using a Philips™ EM301 TEM, an example of which is shown in figure 4.14.

Figure 4.14 is a false greyscale image which was obtained by allocating different shades of grey to the of the original monochrome image. In this way, various features are more easily identified, for instance the surface passivation layer around the particles can be clearly noticed due to the different diffraction condition of the oxide. Dark and light zones are observed inside some of the particles which suggests that the particles consist of several crystallites. The best example of this can be seen in the particle in the upper right-hand portion of the figure.

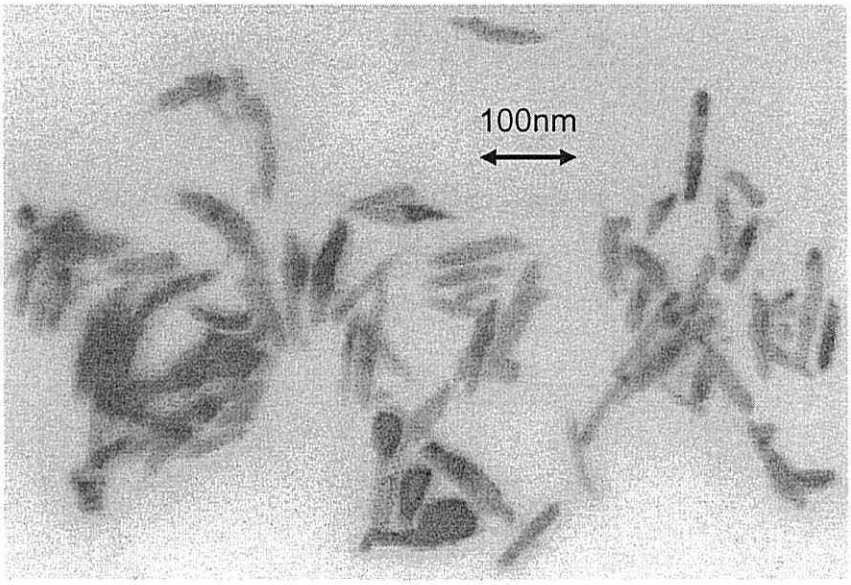

Figure 4.14 False greysacle TEM image of the magnetic pigment.

The crystallite nature of the particles is further confirmed by determination of the size distribution using a Zeiss™ particle size analyser which uses an equivalent circle technique. The procedure involves matching the length of an individual particle from the TEM micrograph to an equivalent circle provided by an illuminated iris, which is logged in 1 of 48 measurement units or bins. The particle size analyser has been calibrated so that each bin corresponds to a established length, and by using the correct scale for the image, it is possible to obtain a size distribution.

Consistent with studies of thin film media (Jones, et al. 1999), the measured distribution of particle lengths which has been fitted by a lognormal function of the form

$$f(L)\,dL = \frac{1}{\left(\sqrt{2\pi}\right)\sigma L}\exp\left[\frac{\left((\ln L)-\mu\right)^2}{2\sigma^2}\right]dL \qquad (4.3)$$

where L is the particle length, σ is the standard deviation of ln(L) with μ the mean value. Figure 4.15 shows the lognormal fit to the data, the median value of the distribution of particle lengths D_m, given by $D_m = e^{\mu}$, was found to be 94nm, with a standard deviation of 18nm. However, it must be noted that the orientation of the particles to the TEM grid can significantly influence the estimation of the size distribution. A true assessment of particle size can only be made if the particle length lies parallel to both the grid and electron beam, which from figure 4.14 is the case for the bulk of particles. Accordingly, for the particles studied with an axial ratio of 6:1, the physical volume was calculated to be 4.8×10^{-17} cm^3.

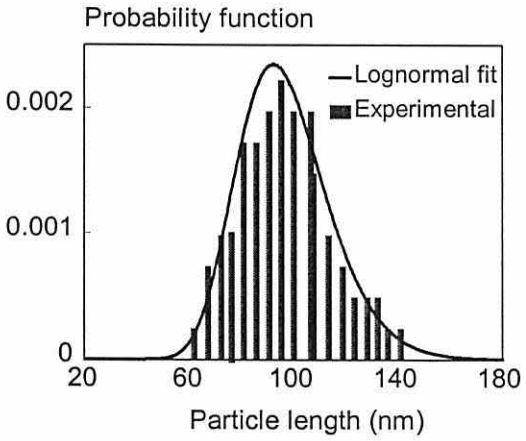

Figure 4.15 Particle length distribution fitted with lognormal function for MP pigment.

By comparison with the activation volume measured in §4.6.1.4, this suggests that there are between 4 and 5 crystallites within each particle, in agreement with figure 4.14. These results are indicative of incoherent magnetisation reversal in the particles, which may account for a lower than expected coercivity (Chantrell, et al. 1992) and broad switching field distribution (Morales, et al. 1998) as observed in figure 4.8(b).

4.6.2 Dispersion Response to Pulsed Magnetic Fields

The magnetic pigment studied in §4.6.1 was now used to prepare two dispersion samples using the procedure described in §4.6. The only difference between the formulations was that one of the dispersing agents was not included in sample #2, leading to a poorer dispersion. In order to examine the real-time response of the dispersions to pulsed magnetic fields, the output signal from the integrator stage is monitored using a Tektronix™ TDS640 digitising oscilloscope connected to a PC through an IEEE 488 interface bus. Figure 4.16 shows the dynamic magnetisation response of (a) dispersion #1 and (b) dispersion #2 to a 1200 Oe pulsed magnetic field of 100μs duration.

The response of the well-dispersed sample #1 to this particular magnetic field pulse shows that there is a pronounced change in the magnetisation, even though the pulsed field is less than that required for Néel reversal as shown in figure 4.8(b). The most probable explanation for this phenomenon is that the particles have undergone a physical rotation into the field direction. This is a somewhat surprising result, as it was previously thought that measurements of this type, over such small timescales, would effectively 'freeze' the mechanical orientation of the particles and allow only the Néel reversal of the dispersion to be tracked, as indicated in figure 4.4 (Hancock, et al. 1996).

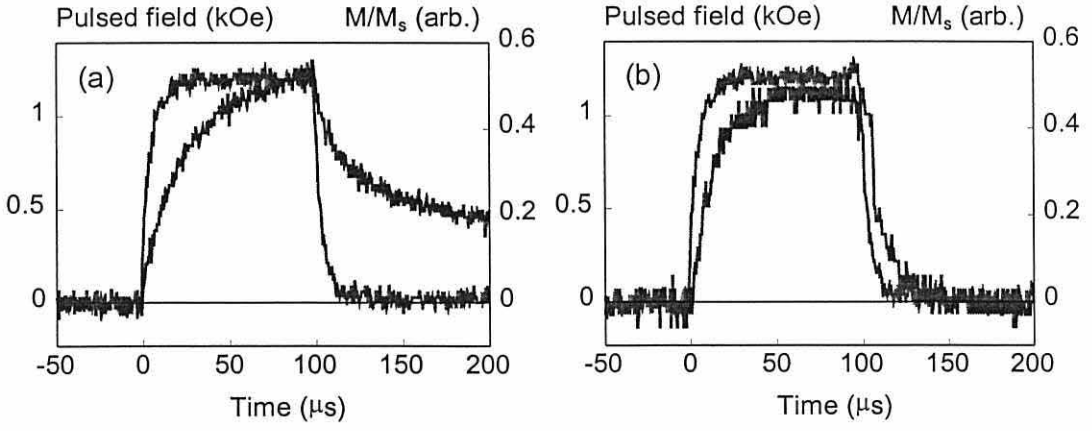

Figure 4.16 Dispersion (a) #1 and (b) #2 response to a 1200 Oe pulsed field of 100μs duration after one hour of milling.

The evidence for mechanical orientation of the particles in sample #1 is substantiated by the magnitude of the remanence. If the increase in magnetisation during the field pulse (i.e. 0→100μs) were due solely to reversible rather than

irreversible changes, the magnetisation beyond the 100μs point would very rapidly relax and return to zero in a few microseconds. This is clearly the case for the poorly dispersed sample #2, figure 4.16(b), as the mechanical torque on the aggregates is too small to allow physical rotation. Further confirmation of the mechanical orientation of dispersed particles is given in figure 4.17. The magnetisation response of (a) sample #1 and (b) sample #2 to a saturating field pulse of 4750 Oe and 100μs duration is presented.

The response of the well-dispersed sample #1 (a) exhibits three distinct magnetisation processes. During the growth of the pulsed field, there is an observed lag and deformation of the response which may be due to distortion of flocculates and networks as they acquire a net moment (Greaves, et al. 1996a). For the duration of the field pulse, a combination of mechanical orientation and Néel reversal is tracked as the field pulse is of sufficient magnitude to switch the particles and agglomerates, in agreement with (Bogardus, et al. 1975). The combination of particle rotation and Néel switching is confirmed as the value of the remanence is slightly greater than the expected value of 0.5 for a system with randomly orientated easy axes (Stoner and Wohlfarth 1948). During relaxation, after the field pulse is removed, mechanical orientation is observed as the principal reversal mechanism.

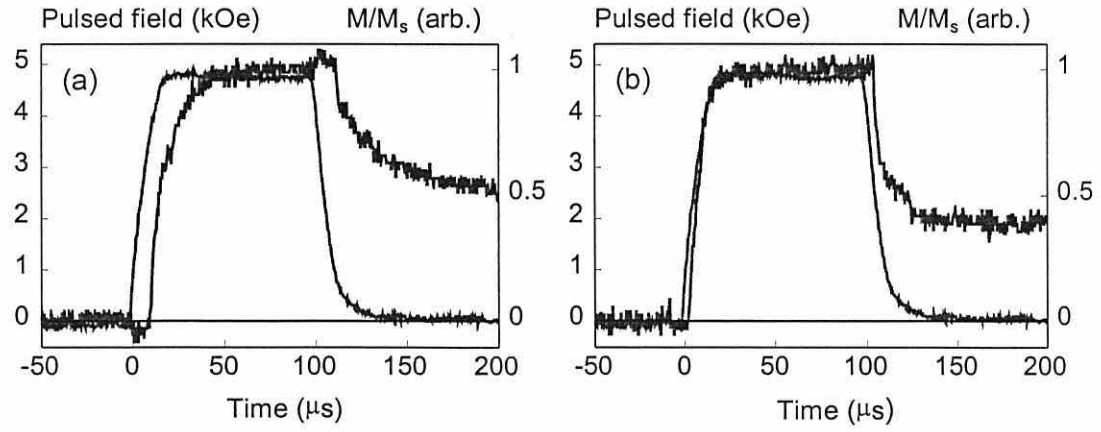

Figure 4.17 Dispersion (a) #1 and (b) #2 response to a 4750 Oe pulsed field of 100μs duration after one hour of milling.

The poorly dispersed sample #2 (b) is characterised by predominately Néel reversal as the magnetisation closely follows the field pulse profile (Greaves, et al. 1997). Although, there is evidence of particle rotation during relaxation, with a more

gradual decay noted between approximately 110μs and 130μs. Further evidence for Néel reversal is given as the value of the remanence is below 0.5 indicating that the pulsed field is not fully saturating the dispersion, in agreement with figure 4.8(b). The distinct difference between the reversal mechanisms of the dispersions is further confirmed by studies of dispersion relaxation as discussed presently in §4.6.2.1, and pulsed remanence measurements presented in §4.6.4.

4.6.2.1 Relaxation Characteristics

Figure 4.18 shows the magnetisation relaxation of dispersions #1 and #2 after the removal of a 3680 Oe pulsed field of 100μs duration after eight hours of milling. The red trace represents a first order exponential fit to the experimental decay using a non-linear least squares Levenberg-Marquardt algorithm.

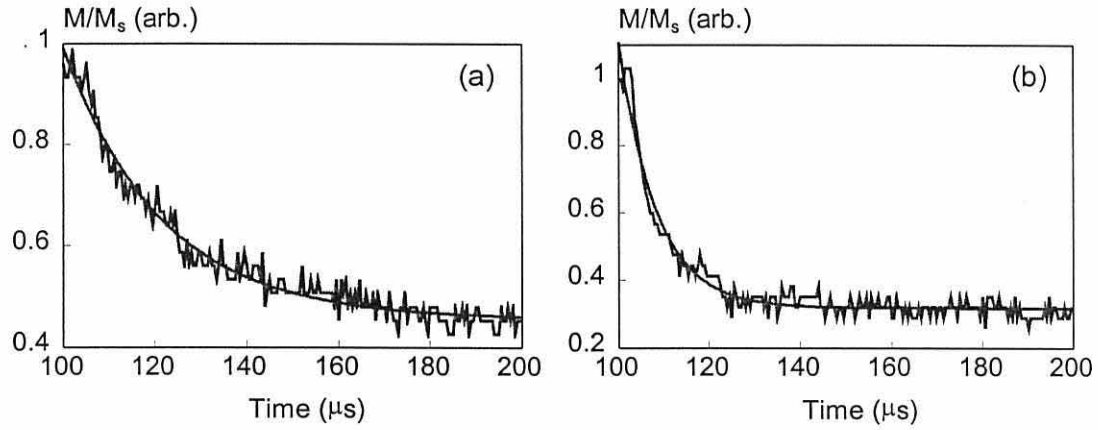

Figure 4.18 Sample (a) #1 and (b) #2 relaxation after the removal of a 100μs duration 3680 Oe pulsed field after 8 hours of milling.

From figure 4.18, the step change in field causes the magnetisation to approach its new value at a rate which decays exponentially with time, as indicated in equation 4.4,

$$m(t) = m(0)\exp\left(\frac{-t}{\tau}\right) \tag{4.4}$$

where m(0) is the initial magnetisation before removal of the field and m(t) is the magnetisation at any time t. τ is a relaxation time which describes how rapidly the

magnetisation approaches its final value. For a pulsed field of 3680 Oe, the relaxation coefficient τ of the dispersion will incorporate a combination of Arrhenius-Néel relaxation, as described in §2.5.2, and Brownian motion relaxation τ_B (Debye 1929),

$$\tau_B = \frac{3V\eta}{kT} \tag{4.5}$$

where V is the particle volume, η is the carrier viscosity, and the product kT is the thermal energy. The exponential form of the Arrhenius-Néel law generally leads to a shorter relaxation time than that obtained from equation 4.5. The transition from dominant Néel to dominant Brownian relaxation depends on the particle volume (Popplewell, et al. 1990), and hence dispersion quality. As a result, a longer relaxation time would tend to indicate a dispersion consisting of well-dispersed particles, in agreement with sample #1, figure 4.18(a). The poorly dispersed sample #2 displays a much shorter relaxation, indicating predominately Néel reversal (b).

The measured relaxation time is the time taken for the magnetisation to fall to 36.8% of its original value from the fit to the experimental data, which for sample #1 was found to be 22.15μs, and for sample #2 10.15μs, as presented in table 4.3.

Sample	$\tau_{3680\ Oe}$ (μs)	η (cp)
#1 1 hour	14.31	36
#1 4 hour	20.96	34
#1 8 hour	22.15	34
#2 1 hour	9.48	48
#2 8 hour	10.15	34

Table 4.3 Relaxation times and milling viscosity of dispersion samples.

From table 4.3, the relaxation time of both dispersions is seen to increase with milling consistent with the break up of structures. It is worth reiterating at this stage that the relaxation of the dispersion magnetisation for both samples #1 and #2 is achieved through a combination of Néel reversal and particle rotation, and accordingly the measured relaxation time serves purely as an indication of the predominate reversal

mechanism present. Similarly, this is the case for further pulsed field studies presented in §4.6.3 and §4.6.4.

4.6.3 Variation of Pulse Width

Note: For results presented in §4.6.3 and §4.6.4, the markers represent actual data points, whilst the connecting lines are included only as a guide to the eye.

Using the technique described in §4.5.1, figure 4.19 shows a series of pulsed remanence curves for dispersion #1 as a function of pulsed field duration (80, 100 and 127μs) and field magnitude (0 → 4750 Oe). The data was obtained by normalising the remanent magnetisation resulting from each pulse with respect to the maximum magnetisation obtained following a 4750 Oe pulsed field of the same duration. The resulting curves are therefore analogous to the IRM curve of figure 4.8(a). However, it must be noted that in figure 4.19, the remanence curve changes are due to both mechanical and Néel reversal effects, whereas in figure 4.8(a) the magnetisation changes are due to Néel reversal only.

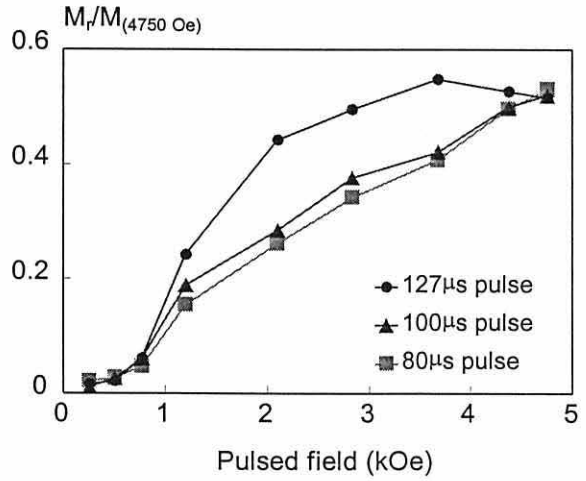

Figure 4.19 Pulsed IRM curves performed at various pulse duration for dispersion #1 after one hour of milling.

From figure 4.19, the value of the remanence is around the Stoner-Wohlfarth value for a system with randomly oriented easy axes, as described in §2.4.1. It is also

clear that the relative magnetisation is greater for the longer duration pulses of the same pulsed field magnitude. This observation is probably associated with the visco-elastic nature of the dispersion microstructure and the relative ease and timescale over which the well-dispersed particles can rotate in the binder/solvent medium. This may also be attributed to the effect of sweep-rate on coercivity, where increasingly larger fields are required to reverse media at higher frequencies, as described in §2.5.4.

4.6.4 Pulsed Quality Assessment

Results have also been obtained to determine the potential of this measurement technique in assessing magnetic particle dispersion and orientation quality. Figure 4.20 shows the pulsed magnetic field measurements for the two different formulations after one and eight hours of continuous horizontal bead milling, as a function of applied magnetic field and for a constant pulsed field duration of 100μs. The data shows marked differences in the mechanical and Néel reversal characteristics of these dispersions. In dispersion #1 the onset of mechanical rotation in fields lower than that for the onset of Néel reversal implies that a greater fraction of the magnetic particles are free to rotate into the applied field direction. The ratio of mechanical to Néel orientation is also greater for the eight hour milled sample of dispersion #1 compared with the one hour milled sample of the same dispersion.

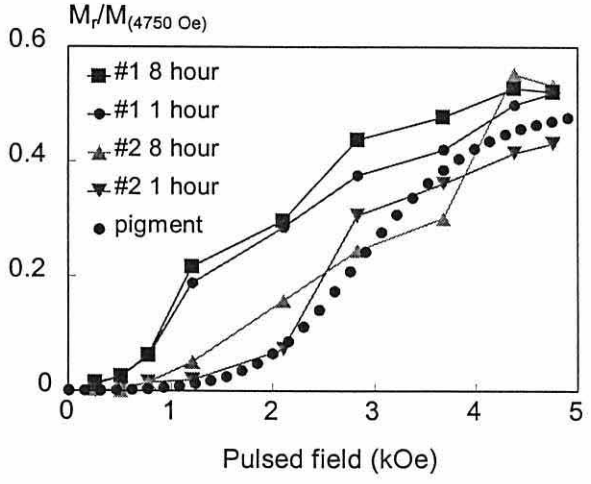

Figure 4.20 Pulsed IRM response to a pulsed field of 100μs duration for dispersions #1 and #2 at various milling times.

By comparison, the results for dispersion #2 show significantly less mechanical rotation and the reversal process would appear to be dominated by Néel reversal. Evidence for a relative increase in particle rotation as a function of dispersion milling time for this dispersion are less conclusive. Of course some mechanical rotation occurs in sample #2 leading to an M_r/M_s value greater than 0.5 as expected for the exclusively Néel switching case. This is visualised more readily by the inclusion of the dry pigment IRM, from figure 4.8(a), normalised to 0.5.

A similar study has been undertaken at the various stages of milling and letdown for sample #1 for a constant pulse width of 100μs, as shown in figure 4.21. The data shows that as the aggregates and structures are broken down with milling, the particles are more easily aligned into the applied field direction in fields lower than that required for the onset of Néel reversal. The results for the letdown samples of 30% and 22% solids ratio reveal the mechanical orientation is enhanced by viscosity changes, allowing a greater proportion of the particles to rotate. Clearly, as the magnetic fraction is decreased, the signal detected is also reduced, which is exhibited as increased noise in the letdown responses.

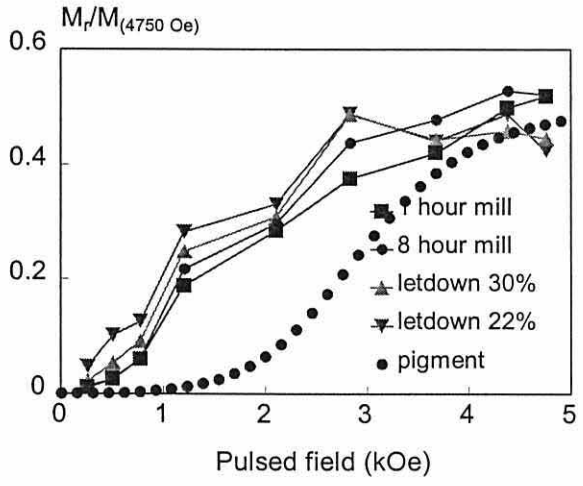

Figure 4.21 Pulsed IRM response to a pulsed field of 100μs duration for dispersion #1 at various stages of milling and letdown.

4.6.5 Characterisation of Coated Tapes

The marked difference in the mechanical and Néel reversal characteristics of dispersions #1 and #2, as described in §4.6.2 and §4.6.4, is confirmed by bulk magnetic

measurements of simple hand-spread coatings taken during milling. The hand-spreads were produced by depositing approximately 10ml of the dispersion onto a 6" wide PET substrate, which is pulled through a knife-blade coater and a 1kOe orienting magnet prior to being allowed to dry in a 400 Oe drying field. The portion of the web dried in the solenoid is identified, and all magnetic measurements are performed on this specific section of the resulting media. A series of hysteresis loops were then measured as a function of milling, as indicated in figure 4.22.

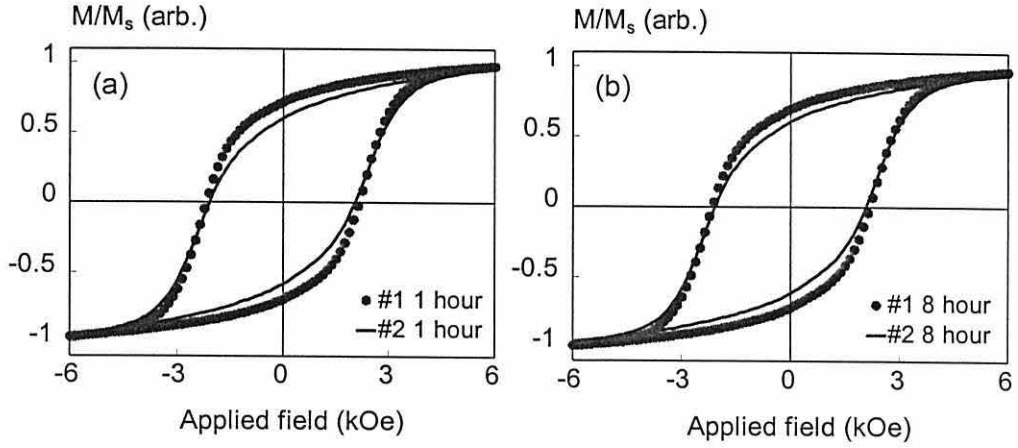

Figure 4.22 Hysteresis loops performed after (a) one and (b) eight hours of continuous bead milling.

For a system of uniaxial single domain particles, tape squareness indicates the degree of alignment of the particles in the tape. It is clear from figure 4.22 that the tape produced from dispersion #1 has a higher squareness and coercivity. This can be explained in terms of the Stoner-Wohlfarth model for an assembly of uniaxial single domain particles, in which the critical field required for switching depends on the orientation of the applied field to the easy axis, as described in §2.4.1. It is also interesting to note that dispersion #1 is not significantly improved with milling, in fact from table 4.4, the squareness drops from 0.703 after one hour of milling to 0.700 after eight hours. The poorly dispersed sample #2 is to some extent recovered during milling, and as agglomerates are broken down, the squareness is increased from 0.591 to 0.608. A similar effect was also noted by (Veitch 1996), who found that for two MP dispersions of contrasting quality, the change produced by 10 hours of milling is much less than the initial difference between the dispersions. This is also consistent with the

pulsed remanence curve shown in figure 4.20, which for sample #2 reveals a relative increase in particle rotation with milling time.

The effects of mechanical orientation can be visualised more easily through examination of differentiated isothermal remanent magnetisation curves. Remanence curves are used for the characterisation of recording media as they measure purely irreversible magnetisation changes. Figure 4.23 shows differentiated IRM curves for samples #1 and #2 as a function of milling. As discussed in §2.6.2.3, the differential of magnetisation with respect to applied field gives an accurate measure of the switching field distribution.

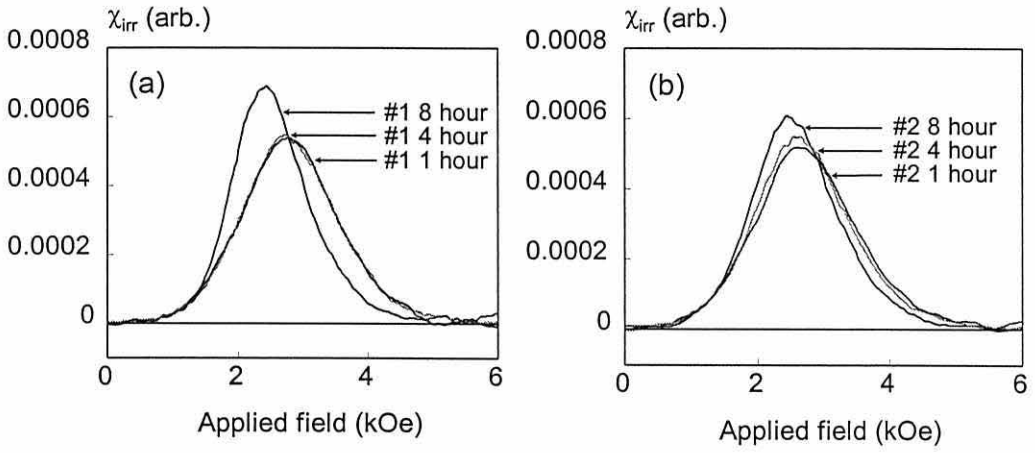

Figure 4.23 Irreversible susceptibility curves for (a) sample #1 and (b) sample #2 as a function of milling.

In figure 4.23, the general trend shows a narrowing of the switching field distribution as the dispersion is milled, consistent with the break up of agglomerates and increased alignment. A measure of this may be obtained by determining the full width at half maximum (FWHM) of the switching distribution, as shown in table 4.4. The values of the FWHM decrease steadily with continuous bead milling, markedly so for both dispersions after 8 hours. From figures 4.23(a) and 4.23(b), it is also observed that the peak of the irreversible susceptibility curve occurs at lower fields with mill duration. Although slight changes in tape squareness are observed for both samples, the reduction in remanent coercivity must be associated with the separation of agglomerates and structures.

The data shown in table 4.4 confirms the improved magnetic and surface characteristics of dispersion #1 compared to sample #2. The measurement of the reflectance was performed using a Rhopoint™ Novo-Gloss 45° glossmeter, with the coating viscosity monitored using a cone and plate viscometer, as described in §4.4.3.

Sample	H_c (Oe)	M_r/M_s	1-S*	FWHM (Oe)	°Reflectance	Coating η (cp)
#1 1 hour	2163	0.703	0.386	1640	90	36
#1 4 hour	2173	0.697	0.393	1650		34
#1 8 hour	2158	0.700	0.397	1340	102	34
#2 1 hour	2059	0.591	0.491	1680	33	48
#2 4 hour	2086	0.613	0.479	1620		36
#2 8 hour	2065	0.608	0.481	1480	93	34

Table 4.4 Properties of the hand-spread tapes.

From table 4.4, smaller 1-S* values for sample #1 indicate a narrower switching field distribution, and hence narrower bit transitions at higher recording densities, as discussed in §2.6.2.1. Equally, it is clear that the state of the dispersion is such that the well-dispersed particles in sample #1 can orientate more readily to an alignment field during coating, in agreement with pulsed field measurements described previously in §4.6.2, §4.6.3 and §4.6.4. The poorly dispersed sample #2 cannot react to small pulsed and DC fields, consequently Néel switching is the predominant reversal mechanism. As a result, mechanical orientation is the critical reversal mechanism for obtaining good particle orientation in the final coated tape.

4.6.6 Concluding Remarks

From the results presented in this chapter, it has been shown that pulsed field studies allow differences in chemical formulation and dispersion quality to be monitored. The assessment of the quality of dispersions is of great importance in the tape manufacturing industry, as poor dispersions are often only detected after coating, resulting in a high volume of wastage. Pulsed field techniques applied in a manufacturing environment may facilitate increased production yield whilst reducing both production time and media variation. This is especially important for the development of future metal

particle media which will have to be manufactured to even tighter tolerances (Veitch, et al. 1999).

Principally, this study has found that mechanical orientation can occur in high quality MP dispersions when the duration of the pulsed field is less than 100μs. Consequently, for well-dispersed systems, particle rotation has been identified as the critical reversal mechanism for obtaining good particle orientation in the final coated product. In contrast, poorly dispersed systems cannot react and rotate to modest pulsed fields, hence Néel switching is the predominant reversal mechanism. The marked difference in the mechanical and Néel reversal characteristics of the dispersion samples has been confirmed in the resulting bulk magnetic measurements of hand-spread coatings taken during the milling process. Publications derived from this study are included in Appendix A (Prichard, et al. 1998).

References

Aharoni, A., *J. Appl. Phys.* **57**, 4702-4705 (1985).

Anthore, R., Gauthier, S., Martinet, A., Petipas, C., *IEEE Trans. Magn.* **16**, 197-202 (1980).

Balkenende, A. R., *J. Magn. Magn. Mater.* **129**, 393-409 (1994).

Bate, G., *Ferromagnetic materials: a handbook on the properties of magnetically ordered substances*. E. P. Wohlfarth, Ed. (Amsterdam: North-Holland, 1980), vol. II.

Bogardus, E. H., Scranton, R., Thompson, D. A., *IEEE Trans. Magn.* **11**, 1364-1366 (1975).

Chantrell, R. W., O'Grady, K., *J. Phys. D: Appl. Phys.* **25**, 1-23 (1992).

Chu, B., Xu, R., Dinapoli, A., *J. Colloid Interface Sci.* **116**, 182-195 (1987).

Coverdale, G. N., Chantrell, R. W., Hart, A., Parker, D., *J. Magn. Magn. Mater.* **120**, 210-212 (1993).

Coverdale, G. N., et al., *J. Magn. Magn. Mater.* **188**, 41-51 (1998).

Coverdale, G. N., Chantrell, R. W., O'Grady, K., *J. Magn. Magn. Mater.* **83**, 442-444 (1990).

Dasgupta, S., *IEEE Trans. Magn.* **20**, 7-12 (1984).

de Witte, A. M., O'Grady, K., Chantrell, R. W., *J. Magn. Magn. Mater.* **120**, 187-189 (1993).

de Witte, A. M., O'Grady, K., Coverdale, G. N., Chantrell, R. W., *J. Magn. Magn. Mater.* **88**, 183-193 (1990).

Debye, P., *Polar Molecules* (The Chemical Catalog Company, New York, 1929).

Deymier, P. A., Jung, C., Raghavan, S., *J. Appl. Phys.* **75**, 5571-5573 (1994).

el-Hilo, M., O'Grady, K., Chantrell, R. W., Dickson, D. P. E., *J. Magn. Magn. Mater.* **123**, 30-34 (1993).

Fisher, R. D., Davis, L. P., Cutler, R. A., *IEEE Trans. Magn.* **18**, 1098-1100 (1982).

Gaunt, P., *J. Appl. Phys.* **59**, 4129-4132 (1986).

Greaves[c], S. J., Hancock, C. P., O'Grady, K., Lane, A. M., *IEEE Trans. Magn.* **32**, 4040-4042 (1996).

Greaves, S. J., Hancock, C. P., O'Grady, K., Lane, A. M., *J. Magn. Soc. Japan* **21**, 241-244 (1997).

Greaves[a], S. J., O'Grady, K., *J. Magn. Magn. Mater.* **155**, 120-122 (1996).

Greaves[b], S. J., O'Grady, K., Lane, A. M., *IEEE Trans. Magn.* **32**, 4046-4048 (1996).

Gunal, Y., Visscher, P. B., *IEEE Trans. Magn.* **32**, 4049-4051 (1996).

Hancock, C. P., PhD, University of Wales (1995).

Hancock, C. P., Greaves, S. J., O'Grady, K., Williams, R. G., Owens, A. R., *IEEE Trans. Magn.* **32**, 4037-4039 (1996).

Igaki, M., Nagamori, H., Shimatsu, T., Takahashi, M., *J. Magn. Magn. Mater.* **183**, 209-219 (1998).

Jakusch, H., *Magnetic recording*. C. D. Mee, E. D. Daniel, Eds. (McGraw-Hill, Inc., 1987), vol. 1: Technology.

Janak, J. F., *Relaxation in magnetic resonance*. C. P. Poole, H. A. Farach, Eds. (Academic Press, 1971).

Jones, G. R., Jackson, M., O'Grady, K., *J. Magn. Magn. Mater.* **193**, 75-78 (1999).

Jung, C., Raghavan, S., Mathur, M. C. A., *IEEE Trans. Magn.* **28**, 2371-2373 (1992).

Jung, C., Raghavan, S., Mathur, M. C. A., *IEEE Trans. Magn.* **29**, 3643-3645 (1993).

Kelly, P. E., O'Grady, K., Mayo, P. I., Chantrell, R. W., *IEEE Trans. Magn.* **25**, 3881-3883 (1989).

Kisomoto, M., Nakazumi, T., Otani, N., Sueyoshi, T., *IEEE Trans. Magn.* **27**, 4645-4647 (1991).

Kuin, P. N., *IEEE Trans. Magn.* **23**, 97-99 (1987).

Kwon, T. M., Jhon, M. S., Karis, T. E., *IEEE Trans. Instrum. Meas.* **41**, 10-16 (1992).

Mathur, M. C. A., Raghavan, S., Jung, C., *Adv. Info. Storage Syst.* **1**, 337-351 (1991).

Mayo, P. I., et al., *IEEE Trans. Magn.* **26**, 228-230 (1990).

Mayo[a], P. I., O'Grady, K., *IEEE Trans. Magn.* **29**, 3640-3642 (1993).

Mayo, P. I., O'Grady, K., Hobby, P. C., *IEEE Trans. Magn.* **28**, 2374-2376 (1992).

Mayo[b], P. I., et al., *J. Magn. Magn. Mater.* **128**, 191-203 (1993).

McCary, R. O., *IEEE Trans. Magn.* **7**, 4-16 (1971).

Mee, C. D., Daniel, E. D., *Magnetic recording* (McGraw-Hill, Inc., 1987), vol. 1: Technology.

Morales, M. P., el-Hilo, M., O'Grady, K., *J. Magn. Magn. Mater.* **140-144**, 2211-2212 (1995).

Morales, M. P., et al., *J. Magn. Magn. Mater.* **190**, 357-370 (1998).

O'Grady, K., Chantrell, R. W., Popplewell, J., Charles, S. W., *IEEE Trans. Magn.* **17**, 2943-2945 (1981).

O'Grady, K., Gilson, R. G., Hobby, P. C., *J. Magn. Magn. Mater.* **95**, 341-355 (1991).

Okamoto, K., Okazaki, Y., Nagai, N., Uedaira, S., *J. Magn. Magn. Mater.* **155**, 60-66 (1996).

Popplewell, J., Rosensweig, R. E., Johnston, R. J., *IEEE Trans. Magn.* **26**, 1852-1854 (1990).

Potanin, A. A., Shrauti, S. M., Arnold, D. W., Lane, A. M., *J. Appl. Phys.* **81**, 3821-3823 (1997).

Prichard, L. S., Mayo, P. I., O'Grady, K., *IEEE Trans. Magn.* **34**, 1684-1686 (1998).

Salem, A. J., Fuller, G. G., *J. Colloid Interface Sci.* **108**, 149-157 (1985).

Scholten[a], P. C., Felius, J. A. P., *J. Magn. Magn. Mater.* **85**, 107-113 (1990).

Scholten[b], P. C., Felius, J. A. P., Slob, C., *IEEE Trans. Magn.* **26**, 72-74 (1990).

Shah, M. J., Cuka, G. M., Karis, T. E., *IEEE Trans. Instrum. Meas.* **41**, 3-9 (1992).

Sharrock, M. P., *IEEE Trans. Magn.* **26**, 193-197 (1990).

Smith, T. L., Bruce, C. A., *J. Colloid Interface Sci.* **72**, 13-26 (1979).

Sollis, P. M., et al., *J. Magn. Magn. Mater.* **120**, 94-96 (1993).

Sollis, P. M., et al., *IEEE Trans. Magn.* **28**, 2695-2697 (1992).

Spratt, G. W. D., Bissell, P. R., Chantrell, R. W., *IEEE Trans. Magn.* **23**, 186-188 (1987).

Spratt, G. W. D., Bissell, P. R., Chantrell, R. W., Wohlfarth, E. P., *J. Magn. Magn. Mater.* **75**, 309-318 (1988).

Stoner, E. C., Wohlfarth, E. P., *Proc. R. Soc. (London)* **A240**, 599-642 (1948).

Street, R., Woolley, J. C., *Proc. Phys. Soc.* **A62**, 562-574 (1949).

Sumiya, K. S., Watataini, F., Hayama, F., Nakamae, K., Matsumoto, T., *J. Magn. Magn. Mater.* **31**, 937-938 (1983).

Swoboda, T. J., et al., *J. Appl. Phys.* **32**, 374S-375S (1961).

Uren, S., Walker, M., O'Grady, K., Chantrell, R. W., *IEEE Trans. Magn.* **24**, 1808-1810 (1988).

Veitch, R. J., *IEEE Trans. Magn.* **32**, 4028-4033 (1996).

Veitch, R. J., Ilmer, A., Lenz, W., Richter, V., *J. Magn. Magn. Mater.* **193**, 279-283 (1999).

Veitch, R. J., Richter, H. J., Poganiuch, P., Jakusch, H., Schwab, E., *IEEE Trans. Magn.* **30**, 4074-4076 (1994).

Wohlfarth, E. P., *J. Appl. Phys.* **29**, 595-596 (1958).

Chapter
5

Nanosecond Pulse Techniques

5.1 Introduction

In recent years, the mechanism of thermally activated switching has been of considerable interest to the magnetic storage industry because of the large difference between the timescales of the recording process and the required storage stability (Sharrock 1994). Today, the need for higher storage densities has led to the development of metal particle pigment formulations with a small particle size, where thermal activation is significant. Correspondingly, over short timescales, substantial increases in remanent coercivity have been observed (Doyle, et al. 1993) (Veitch, et al. 1994) and (Hancock, et al. 1996). An understanding of the switching speed limitation of recording media is of fundamental interest to the scientific community, and may be performed by measuring the remanent coercivity of the medium as the duration of the magnetic field is dramatically reduced.

This chapter details the development of the various techniques used to produce nanosecond duration pulsed magnetic fields inside a microstrip transmission line, of which the magnetic sample forms a part. Essentially, the pulse forming network consists of a short length of coaxial line charged to some high potential. The energy stored in the line is transferred into the matched microstrip line (§5.5) on closing a HV rated switch; which may comprise of a mercury-wetted relay (§5.3) or pressurised nitrogen spark gap switch (§5.4). Propagation of a pulse along the microstrip line causes an electromagnetic wave to be transmitted, the transverse components of which are used to impulse magnetise the sample. Using this technique, studies of the high

speed switching properties of advanced metal particle recording media have been undertaken, and are described in §6.

5.2 High Voltage Pulse Technology

Many of the pioneering developments in high power pulse generation were published in the years shortly after the Second World War; principally due to the sensitive nature of the research. The interested reader is referred to an excellent review of the operation of various high power switches by (Burkes, et al. 1979). Approaches utilising gas ignitrons (Cummings 1963), thyratrons (Weiner, et al. 1980), Marx generators (Richley 1987), avalanche transistors (Fulkerson, et al. 1994), power MOSFETs (Baker, et al. 1994) and drift step recovery diodes (Focia, et al. 1996) have produced kV pulses with rise times of less than 1ns. Unfortunately, example pulses are often ill-defined, or the techniques are complex in nature and do not allow for simple instrument duplication.

Previously, studies of low coercivity γ-Fe_2O_3 and CrO_2 media have been performed using a charged 50Ω coaxial line connected to a mercury wetted reed relay and microstrip line (Hancock, et al. 1996). This instrument is capable of producing well-defined single-shot voltage pulses in excess of 1kV with pulse widths between 0.7ns and 250ns, having rise times of less than 500ps. Termination of the voltage pulse in the 50Ω microstrip line allowed pulsed fields of up to 450 Oe to be generated.

Although preliminary studies of advanced metal particle media have been performed using the mercury wetted relay generator (Prichard, et al. 1999a), the field produced by the instrument is not of sufficient magnitude to switch all of the particles, and consequently a DC bias field supplied from an electromagnet is used to assist the pulsed magnetic field. Consequently, a new pulse generator has been developed based around a pressurised nitrogen spark gap switch, as part of a delay line, which is capable of producing well-defined voltage pulses of over 3kV in a 50Ω environment. The pulse width is adjustable from 7ns to 56ns, with rise times of under 3ns. Details of this instrument are presented in (Prichard 1999), and described in §5.4. Various techniques have also been investigated in §5.4.4 which may be capable of sharpening the edge times of a high voltage pulse, and as a result reduce the overall pulse width. Consequently, a matched 50Ω ferrite pulse sharpener similar to that described by (Seddon, et al. 1988) and (Bolton, et al. 1994) has been developed.

5.3 Mercury Wetted Relay Generator

This particular class of pulse generator was first proposed by (Garwin 1950) who described an instrument capable of producing pulses with rise and fall times of 200ps, at a repetition rate of 120Hz. Pulses of over 100V could have a width varied between 0.5ns and 1μs by altering the length of the coaxial pulse forming line from 5cm to 100m, in a similar manner to the instrument developed by (Hancock, et al. 1997). Essentially, the generator consists of a short open-ended section of coaxial line charged to some potential V. On closing the mercury wetted reed relay, a rectangular pulse of energy with amplitude V/2 and duration twice the electrical length of the pulse forming line is transferred to the matched load. Clearly, special care must be taken to ensure that the characteristics of the relay are closely matched to those of the pulse forming line, in order to avoid attenuated replicas of the main pulse being reflected back into the line, as discussed in §5.3.2.

5.3.1 Generator Theory

In principle, a charged lossless coaxial transmission line will give rise to a rectangular pulse of energy if it is connected through an ideal switch to an output impedance that is equal to the characteristic impedance of the line (Glasoe, et al. 1948). The width of the pulse is therefore proportional to the length of the coaxial line. This is illustrated in figure 5.1, where a voltage source V_S is used to charge up the line through a series resistor R_S. The line is connected through an ideal switch to the load Z_L. For the purpose of analysis, the physical coaxial line length L_α and the effective increase in length due to the switch L_β are combined and denoted by L_γ. To produce a pulse, the charged line is discharged into the load impedance Z_L by means of closing the switch.

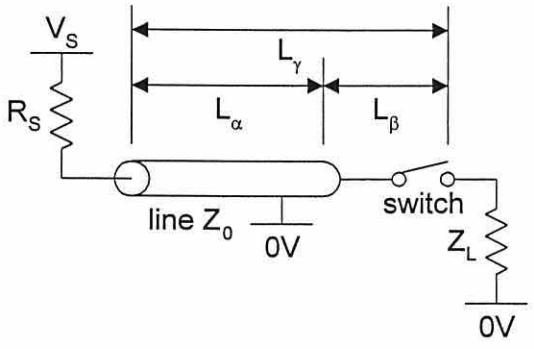

Figure 5.1 Coaxial pulse forming network.

The total pulse width T_{tot} can be calculated from equation 5.1, where it is shown to be dependent upon the coaxial line length, including the 50Ω switch L_γ, and also the characteristic inductance L_0 and capacitance C_0 of the coaxial line.

$$T_{tot} = 2L_\gamma \sqrt{L_0 C_0} \tag{5.1}$$

If the coaxial line and switch are matched to the load and there are no attenuated reflections, the pulse current i(t) is given by

$$i(t) = \frac{V_S}{Z_0 + Z_L} \tag{5.2}$$

and the voltage supplied at the load V_L is given by the equation

$$V_L = \frac{Z_L}{Z_0 + Z_L} V_S \tag{5.3}$$

Consequently, for a system where the characteristic impedance of the load (Z_L = 50Ω) is designed to match the characteristic impedance of the pulse forming line (Z_0 = 50Ω), the load voltage V_L is given by $V_S/2$, and the pulse current i(t) in this case will be $V_S/100$.

5.3.2 Practical Design

The circuit diagram showing the design of the practical pulse generator is given in figure 5.2. In contrast with figure 5.1, the charging resistor R_S and the HV supply V_S are connected at the switch end of the line. This is because for illustrative purposes, it is often easier to visualise pulse propagation by having the supply at the opposite end of the switch, although practically, it is difficult to construct the generator in this way as changing the delay line length becomes more involved. The DC high voltage was supplied from a brandenburg™ PU2707 0–15kV unit, through a 3MΩ charging resistor which has a voltage rating of 10kV. The pulse forming lines were manufactured from 50Ω URM43 coaxial cable which has a breakdown rating of $21kV_{DC}$ and gives a delay

of around 5ns m^{-1}. The length of the coaxial delay lines varied between 10cm and 20m; with the open circuit end of each delay line sealed using an epoxy resin adhesive. Furthermore, the outer braid was trimmed back approximately 5mm from the end of the cable to prevent flashover. High voltage PET100 connectors were used to connect the HV supply, coaxial delay lines and microstrip load to the reed relay.

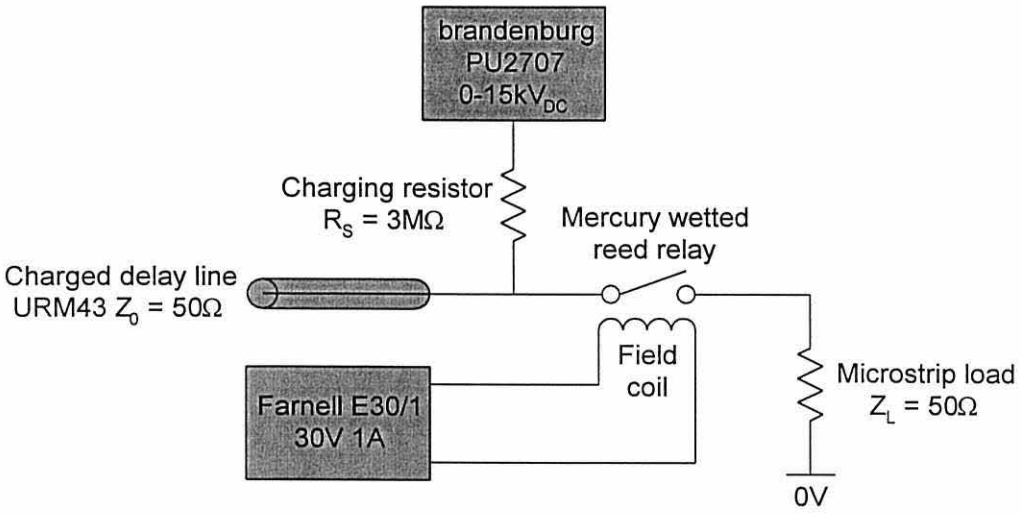

Figure 5.2 Practical design of mercury wetted relay pulse generator.

The 3kV rated mercury wetted relay, supplied by Pickering Electronics Limited, is similar to the relay described by (Garwin 1950), where an external magnetic field forces the flexible ferromagnetic contact onto the fixed contact, thus closing the switch. As shown in figure 5.3, the hermetically sealed contacts are continuously wet with mercury by capillary action to bridge mechanical chatter. In order to minimise discontinuities, the geometry of the switch assembly must be matched to 50Ω. Consequently, the relay was mounted in a brass housing with dimensions chosen in such a way that the characteristic impedance approximates to that of a 50Ω coaxial line incorporating an ideal switch, as discussed by (Hancock 1995). In a similar manner, this procedure is described for the spark gap switch in §5.4.2.

The construction of the mercury wetted reed relay is detailed in figure 5.3, where the closing coil consists of 2000 turns of 42SWG enamelled wire.

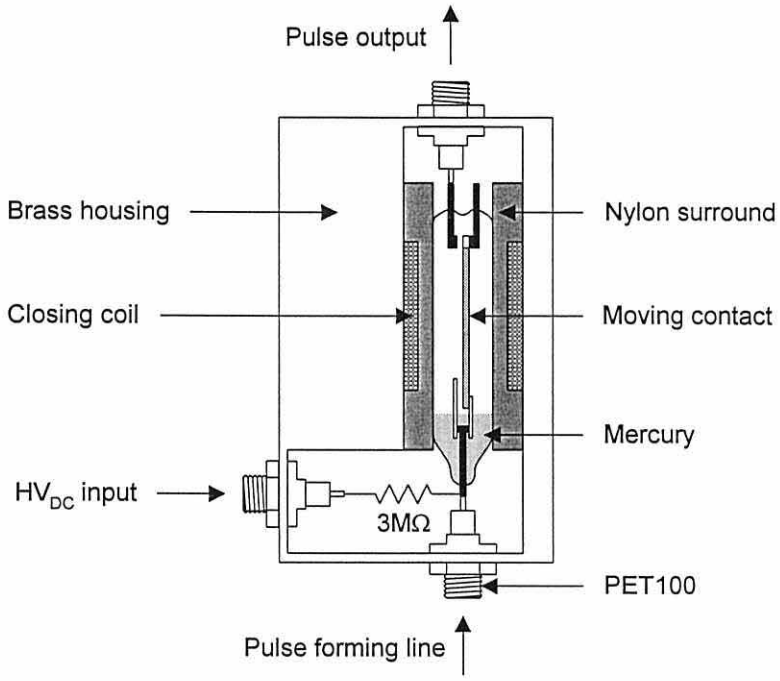

Figure 5.3 Construction of the mercury wetted reed relay.

5.3.3 Generator Characterisation

Pulse measurements were carried out to ensure that the output pulses do not suffer from excessive pulse overshoot and that there are no reflections of the main pulse when the output is terminated with a 50Ω load. The output voltage pulses produced by the generator were measured for various pulse forming delay line lengths. The pulses were obtained from the 50Ω input of a Tektronix™ TDS640 500MHz digitising oscilloscope. Two Barth™ 142-NMFP 20dB high voltage attenuators[1] and a conventional 20dB type 'N' microwave attenuator were coupled to provide 60dB of attenuation to the input channel of the oscilloscope. Consequently, the measured voltage pulses presented in §5.3.3.1 are a factor of 1000 down on the actual values. Furthermore, the bandwidth of the oscilloscope becomes an issue when the edge speed of the signal approaches the rise time of the instrument, which is around 700ps for the 500MHz TDS640 (Tektronix 1998). The actual rise time of the signal RT_{sig} in relation to inherent rise time of the oscilloscope RT_{scope} is approximated by (Tektronix 1998)

$$RT_{meas} = \sqrt{RT_{scope}^{\,2} + RT_{probe}^{\,2} + RT_{sig}^{\,2}} \tag{5.4}$$

[1] Barth Electronics Inc., 1300 Wyoming Street, Boulder City, NV 89005, USA.

where RT_{probe} is the rise time of the probe and RT_{meas} is the rise time measured on the oscilloscope.

5.3.3.1 Sample Field Pulses

On closing the mercury wetted relay with 10cm of coaxial delay line connected at the switch end of the line, the measured pulse at the 50Ω input of the oscilloscope is shown in figure 5.4.

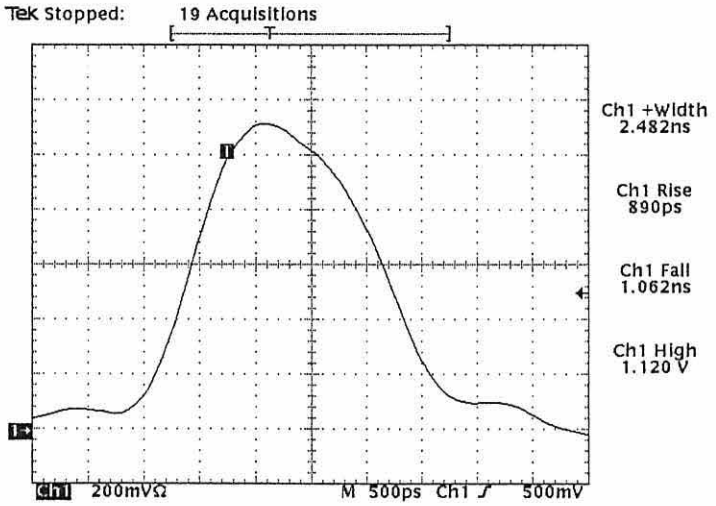

Figure 5.4 10cm coaxial delay line output *(200V per vertical division)*.

With the high voltage supply fixed at 2.3kV, the amplitude of the measured pulse is 1.12kV and the calculated pulse current is 22.4A. From figure 5.4, it is clearly seen that the edges of the pulse are somewhat rounded, which is possibly due to the fact that the Tektronix™ TDS640 oscilloscope has insufficient bandwidth to capture the signal. This particular oscilloscope captures data every 500ps and then implements a sin(x)/x interpolation between the sampled data. The effect of this algorithm on signals with fast edge times is the introduction of overshoot, undershoot and rounding into the measured response (Tektronix 1998).

The measured output pulse with 20cm of coaxial delay line attached is shown in figure 5.5. With a similar appearance to the response of the 10cm pulse forming line shown in figure 5.4, the observed pulse edges are not particularly sharp, with a resulting peak load voltage of 1.08kV at the supply potential of 2.3kV.

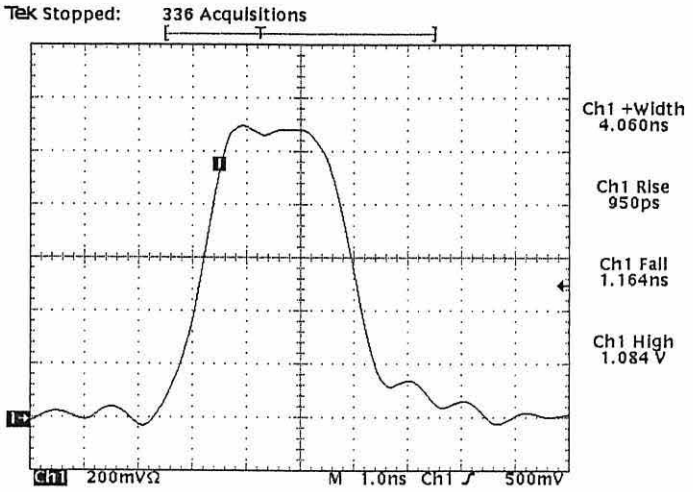

Figure 5.5 20cm coaxial delay line output *(200V per vertical division)*.

Figure 5.6 shows the response of the mercury wetted relay with 1m of pulse forming line connected to the supply. The pulse has a well-defined rectangular shape and is reasonably free from ringing and overshoot. The magnitude of the pulse is 1.12kV with a corrected pulse width of 11.4ns. The corrected rise and fall times of the pulse are 580ps and 970ps respectively, as shown in table 5.1 (§5.3.3.2).

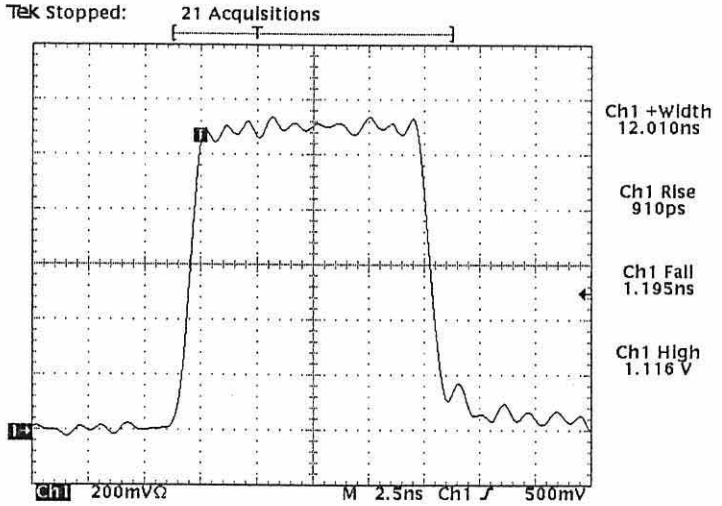

Figure 5.6 1m coaxial delay line output *(200V per vertical division)*.

During testing the timescale was increased to 10ns/div, 25ns/div and 50ns/div to establish whether there were any pulse reflections in the system. It was found in all cases, that the pulses were reasonably free from replicas, either positive or negative, of the main pulse, confirming that the generator is well-matched to 50Ω. Consequently,

figure 5.7 shows a 21.6A 3.5ns pulse from a 20cm coaxial delay line over an extended timescale of 50ns/div.

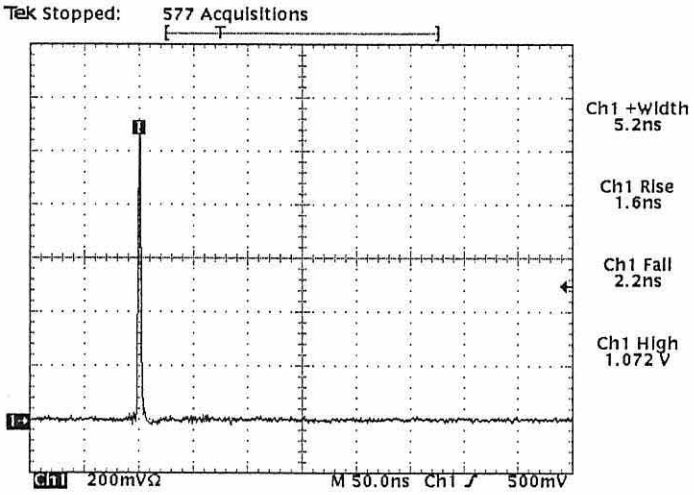

Figure 5.7 21.6A pulse over an extended timescale *(200V per vertical division)*.

5.3.3.2 Generator Specification

The characteristics of the corrected pulses measured from the 50Ω input of the oscilloscope are summarised in table 5.1. It can be clearly seen that each of the pulse widths is greater than the corresponding electrical length of the pulse forming line, as described in equation 5.1. Consequently, the average value for this additional delay due to the mercury relay, the parameter L_β in figure 5.1, was found to be around 950ps.

Delay line length (cm)	10	20	100	400
Corrected rise time (ps)	550	640	580	740
Corrected fall time (ps)	800	930	970	8960
Corrected pulse width (ns)	1.86	3.51	11.44	50.01
Supply voltage V_S (kV)	2.30	2.30	2.30	2.30
Load voltage V_L (kV)	1.12	1.08	1.12	1.12
Pulse current (A)	22.4	21.6	22.4	22.4

Table 5.1 50Ω impedance pulse characteristics for the mercury wetted relay.

As detailed in §5.5, propagation of a current pulse in a 50Ω microstrip line allows pulsed magnetic fields of over 650 Oe to be produced. Using short duration pulses, studies of the switching speed limitation of advanced metal particle media have been performed. The results obtained using the mercury wetted relay are presented in

§6, with publications derived from the work included in Appendix A (Prichard, et al. 1999a).

5.4 Spark Gap Switch

As discussed in §5.2, the pulsed magnetic field produced by the mercury wetted relay is not of sufficient magnitude to switch high coercivity metal particle recording media. Therefore, a pressurised nitrogen (N_2) spark gap switch has been developed which allows single-shot voltage pulses of over 3kV to be generated in the 50Ω microstrip load. Spark gaps are among the most widely used switches in pulsed power applications. They can cover an impressive range of voltages, currents, power transfer and repetition rates (Burkes, et al. 1979), although only a limited range of spark gaps are available commercially considering the wide range of applications and requirements.

Typical applications of spark gap switches include driving the antenna of ultrawideband radar systems (Taylor 1995), triggering optical shutters (Subhash, et al. 1984) and lasers (Golnabi 1992), particle accelerators (Birx, et al. 1982), pollution control (Penetrante 1993), surface elemental analysis (Van Patten, et al. 1996) and medical applications (Boyer, et al. 1998), along with missile and nuclear weapon technologies. More recently, for studies of high speed magnetic switching, Doyle and his co-workers have developed a pressurised N_2 spark gap switch under the direction of Dr. Jon Barth (Stinnett, et al. 1998). This simple device is similar to the spark gap presented in this study and detailed in (Prichard 1999).

5.4.1 Generator Theory

Essentially, the pressurised spark gap switch directly replaces the mercury wetted relay described in §5.3, to switch the energy stored in the delay line into the matched load. The design of the spark gap developed in this work is based upon the pioneering studies of high pressure spark gaps performed by (Fletcher 1949). The main difference between the spark gap developed by Fletcher and the one presented in this study is the process of triggering the gap. In Fletcher's arrangement the pulse generator is triggered by applying a voltage pulse to a third intermediate electrode of the main spark gap. The triggered spark gap is particularly suited for repetition rated operation, and several additional techniques may be employed to initiate the main anode to cathode discharge,

e.g. thermionic emission (Broadbent, et al. 1955), mechanically triggered (Palmer, et al. 1971), UV illumination (Aranchuk, et al. 1982) and laser triggered (Kimura, et al. 1988). However, in the simple design presented here for single-shot operation, the spark gap is made to breakdown by overvolting the dielectric separating the current carrying electrodes. The design of the pressurised N_2 spark gap switch is shown in figure 5.8.

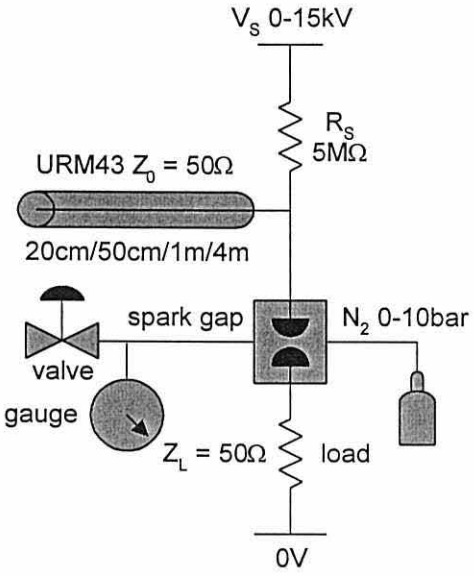

Figure 5.8 Schematic diagram of pressurised N_2 spark gap switch pulse generator.

The spark gap is overvolted by reducing the pressure in the spark chamber to a critical level determined by Paschen's Law, which for a uniform system (Paschen 1889)

$$V_b = \frac{Bpd}{\ln\left[\frac{Apd}{\ln(1/\gamma)}\right]} \tag{5.5}$$

where A, B and γ are functions of the gas. The product pd is given by the gap pressure and distance respectively. Consequently, the breakdown voltage of the gap V_b is a function of pd alone. In order to initiate a spark, the spark chamber is first pressurised with N_2 with the gap width fixed, hence the breakdown voltage of the spark gap can be determined. If the delay line is charged to a potential V_S, and the pressure in the chamber reduced, when $V_b = V_S$ the gap will breakdown and the switch is closed. The

charge stored in the line is now delivered into the microstrip load. As the breakdown process is achieved by the avalanche of ionised gas molecules, a higher gas pressure exhibits a greater density of charge carriers, and hence faster rise times.

The mechanism of gaseous breakdown is thoroughly reviewed by (Cobine 1958), following the pioneering investigations of (Townsend 1900). Townsend's description of breakdown considers a gas between two electrodes; the charge carriers which exist in the gap are electrons from field emission and also gaseous ions. When a voltage is first applied, the current increases slowly as the charge carriers move through the gas with a drift velocity determined by their mobility. As the potential is steadily increased, the electrons and ions are accelerated to very high kinetic energies before colliding with other particles. At a critical potential, the kinetic energies of the particles are sufficient to ionise secondary charge carriers (both electrons and ions) from collisions between gas molecules. An avalanche process now occurs as these secondary particles are accelerated by the high field which produces more cascades of secondary particles. Consequently, the current in the gap very rapidly increases, and a visible spark is observed as the excited ions return to the ground state. This is a self-sustaining breakdown which depends on the discharge path and the nature of the electric circuit. Obviously, at higher gas pressures the mean free path between collisions is considerably reduced, hence the avalanche process proceeds rapidly.

5.4.2 Practical Design

The design of the pressurised N_2 spark gap switch is shown in figure 5.9. The dimensions of the inner and outer conductors, along with the electrodes are chosen in such a way that the wave impedance of the coaxial line formed is 50Ω. The characteristic impedance Z_0 of the assembly may be calculated from (Weiner 1982)

$$Z_0 = \frac{138}{\sqrt{\varepsilon_r}} \log_{10} \frac{b}{a} \qquad (5.6)$$

where a and b are the inner and outer radii of the conductors respectively, ε_r is the relative permittivity of the dielectric, which in this case is 4.0 at 10^6Hz for the glass

filled nylon insulator[1], and 1.0006 for nitrogen gas[1]. The insulator was also chosen for its high dielectric strength >45kVmm^{-1} and good mechanical properties. Using equation 5.6, the 50Ω geometric structure was designed with a = 8.0mm and b = 42.5mm, as indicated in figure 5.9. The majority of the other components in the switch were manufactured from brass, mainly due to the ease with which elements may be machined, and superior conduction losses over other suitable materials, such as aluminium.

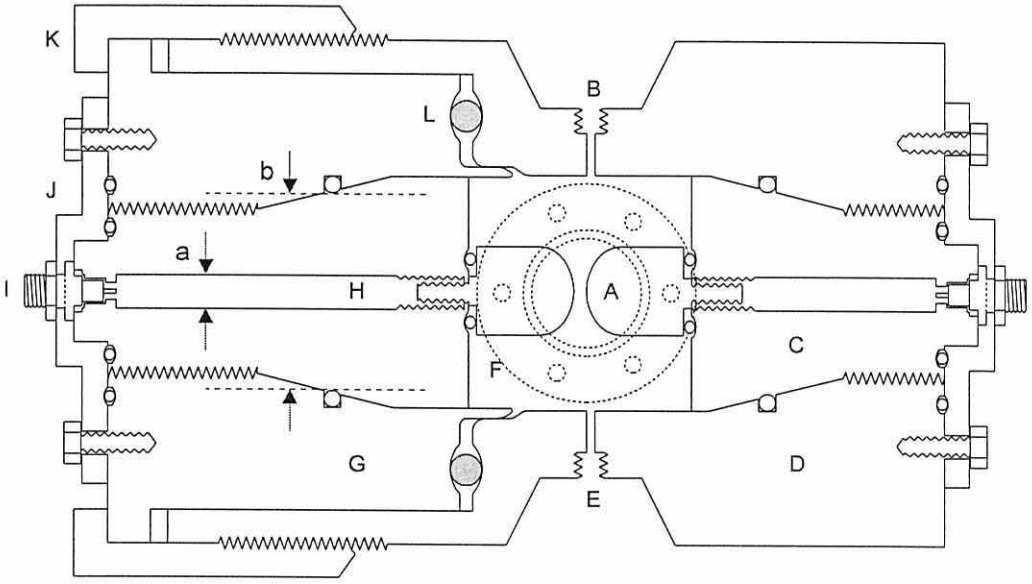

Figure 5.9 Construction of spark gap switch A. spark electrodes B. N_2 inlet C. insulator D. main housing E. N_2 outlet F. spark chamber G. moving piston H. inner conductor I. PET100 connector J. pressure end cap K. gap adjuster L. main 'O' ring seal.

To address the problem of electrode erosion, the hemispherical electrodes were likewise constructed from brass, but with tungsten tips. Comprehensive studies of electrode erosion rates in high energy spark gaps have revealed large scale melting and pitting of brass electrodes after only 2000 pulse discharges (Donaldson, et al. 1984) and (Donaldson, et al. 1986). In a high power electrical discharge, as discussed in §5.4.1, high speed streams of ionised vapour are produced in the space adjacent to the electrode surface. As these streams pass between the electrodes, regions of the spark are thought to be superheated (above 4×10^4K) and upon impact with the opposite electrode produce macroscopic surface damage. In order to reduce erosion, low atomic weight

[1] *Handbook of chemistry and physics* Weast, R. C., Ed. (CRC Press. ed.70th, 1989)

electrodes such as graphite and copper tungsten exhibit good performance. For the hemispherical tungsten-tipped electrodes described in this study, no visible pitting or dendrites were observed, even after at least 3000 pulse discharges.

To facilitate changing the gap distance and hence breakdown voltage, the gap was made adjustable by turning an knurled collet onto a moving piston which is forced against an 'O' ring seal. The gap distance can be readily checked using a feeler gauge through an inspection port. Additionally, in order to improve the pressure rating of the spark gap, the insulator and housing are slightly tapered to connect positively (this taper has been exaggerated in figure 5.9 for visualisation purposes only). The physical size of the spark gap housing is 12cm in diameter and 22cm in length.

A reliable connection between the URM43 coaxial cable and the PET100 connector is crucial when manufacturing high voltage rated cables. In order to maintain the voltage rating it is very important to force the cable right into the back of the connector, not leaving any voids. Silicone grease was then used as a packing element around the pin and the end of the URM43 cable dielectric. In this form, the pulse delay lines and interconnecting coaxial cables were repeatedly able to withstand both DC and pulsed voltages over 6kV.

As detailed in §5.4.1, the spark gap is made to breakdown by overvolting a gaseous dielectric separating the electrodes. A variety of gases have been utilised for spark breakdown, e.g. nitrogen (Fletcher 1949), hydrogen (Aleksandrin, et al. 1976), sulphur hexafluoride (SF_6) (MacGregor, et al. 1993), air (Tou, et al. 1993) and vacuum (Osmokrovic, et al. 1996). Generally, the mobility of charge carriers is increased for smaller and lighter gas species, which produces a faster ionisation process. However, hydrogen is obviously extremely flammable and SF_6 decomposes into a carcinogen after a high energy discharge[1]. Consequently, although operating the gap with these particular gases may produce moderate improvements, they are clearly unsuitable for our limited laboratory resources. The primary benefit of nitrogen over air is the higher relative breakdown strength, $V_{nitrogen}/V_{air} = 1.15$ (Orgler 1900), which permits a shorter gap at a higher pressure. In this configuration, the actual ion transport time across the gap is reduced, and the accelerating force from the field gradient is increased, which correspondingly produces faster rise times.

[1] David Pacholok, Creative Electronics Consultants™, personal communication, 1999.

With nitrogen selected as the gaseous dielectric, the breakdown voltage as a function of gap distance and pressure may be calculated directly from equation 5.5 for a parallel plate system, as shown in figure 5.10. The gas parameters A, B and γ were obtained from (Cobine 1958), assuming an ambient temperature of 20°C. Clearly, the geometric shape of the hemispherical electrodes will tend to concentrate the electric field, and effectively decrease the breakdown voltage (Van Planck 1938). However, using this approximation, it is evident that a broad range of pulse magnitudes are available using a spark gap designed to withstand nitrogen pressures up to 10bar, whilst maintaining variable gap distances between 0.05mm and 0.5mm.

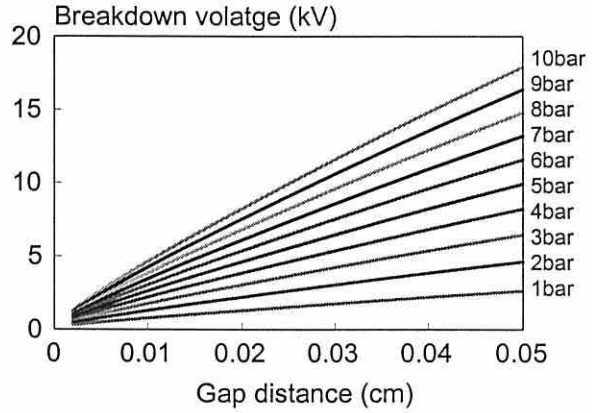

Figure 5.10 Breakdown voltage for parallel plate electrodes as a function of gap distance and nitrogen pressure at 20°C.

5.4.3 Generator Characterisation

Voltage pulses were obtained from the 50Ω input of a Tektronix™ TDS640 500MHz digitising oscilloscope, as described in §5.3.3. In order to reduce the energy to a safely measurable level, two Barth™ 142-NMFP 20dB high voltage attenuators and a conventional 20dB type 'N' microwave attenuator were coupled to provide 60dB of attenuation to the input channel of the oscilloscope. The high voltage attenuators are designed and tested to withstand 5kV over 60ns, and reduce the voltage to a level which any reasonable quality microwave attenuator may easily withstand.

In order to ensure reliable measurements, resistance logging similar to that described by (Richner, et al. 1991) was regularly performed. Using a Fluke® 8062A digital multimeter, the input impedance of each port was recorded to predict partial failure following an overvoltage or pulse width condition. Breakdown of these

components may be determined by a measured increase of input impedance greater than almost 0.25%, or 0.125Ω in a 50Ω system (Richner, et al. 1991).

5.4.3.1 Sample Pulses

Figure 5.11 shows a measured pulse at the 50Ω input of the Tektronix™ TDS640 oscilloscope from the spark gap switch with 1m of pulse forming line connected. The high voltage brandenburg™ PU2707 supply was set to 6kV, with the gap fixed at 0.3mm, and a nitrogen pressure of 4bar.

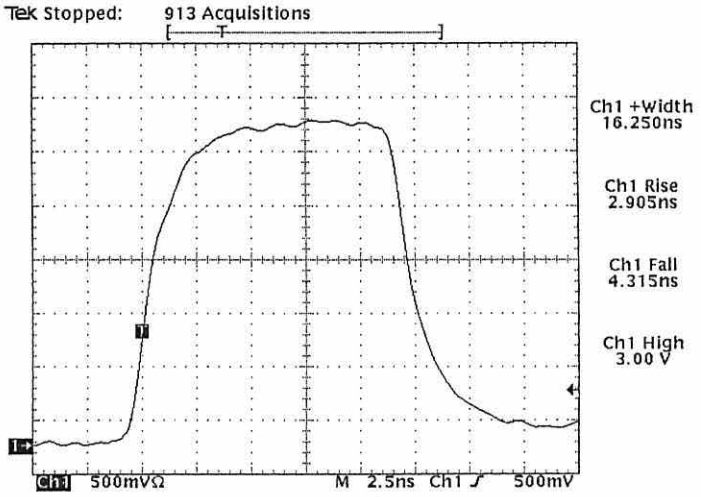

Figure 5.11 1m coaxial delay line output *(500V per vertical division)*.

The measured output pulse has a well-defined rectangular shape which is reasonably free from ringing and overshoot with an amplitude of 3kV and a pulse width of 16.2ns. The corrected rise and fall times of the pulse are 2.8ns and 4.2ns respectively, as shown in table 5.2 (§5.4.3.2). The pulse current can be estimated to a reasonable degree of accuracy to be 60A ± 1.

Figure 5.12 shows the response of the spark gap with 20cm of delay line connected. The high voltage supply was set to 5.2kV, with the gap fixed at 0.25mm, and a nitrogen pressure of 4bar. The magnitude of the pulse is over 2kV, with a pulse width of under 7ns. An interesting feature of this pulse is observed on the rising edge, which appears to be a two-stage process. This may be due to the minor mismatch attributed to the length of the transmission line containing the hemispherical electrodes. The effect is not significant, as the length of the mismatched section is small compared

to the overall system, and is illustrated by the slight increase in rise time. Similarly, under close examination, the same feature can be observed in the rising edge of the pulse shown in figure 5.13.

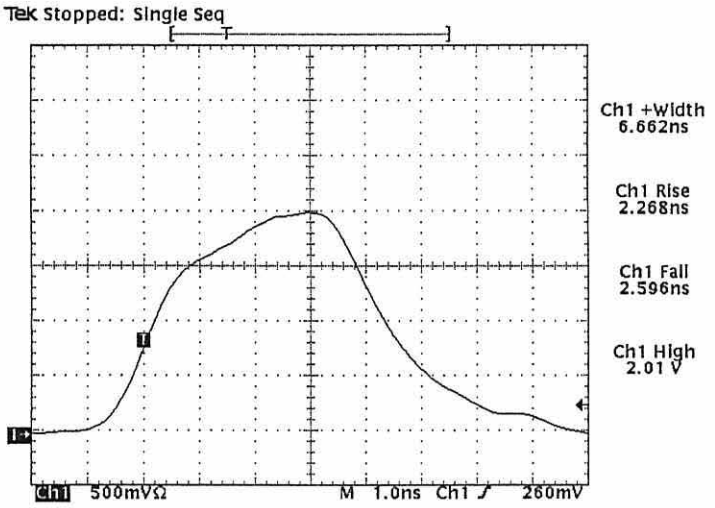

Figure 5.12 20cm coaxial delay line output *(500V per vertical division).*

The measured output pulse with 4m of pulse forming line attached is shown in figure 5.13. As with figure 5.12, the high voltage supply was fixed at 5.2kV, with the gap set at 0.25mm for a nitrogen pressure of 4bar.

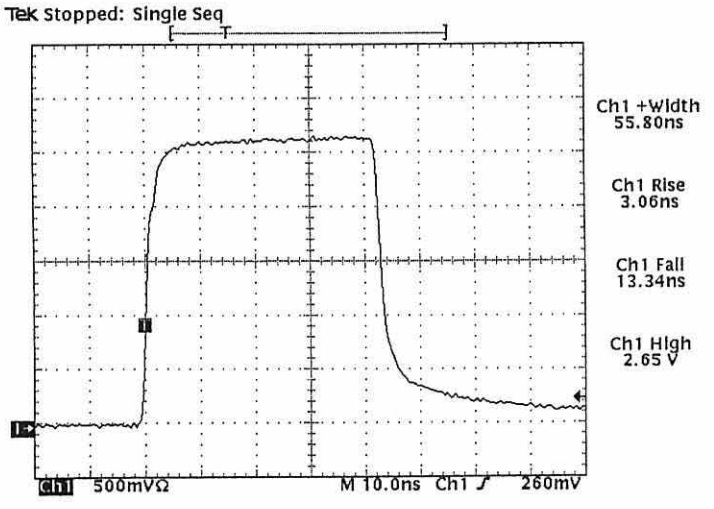

Figure 5.13 4m coaxial delay line output *(500V per vertical division).*

The magnitude of the pulse obtained is 2.65kV, with a pulse width of 56ns. The response is characterised by a fast rise time of around 3ns, together with a more gradual

fall of 13ns. Again, the pulse has a well-defined rectangular shape, and is free from overshoot and oscillations.

During testing the timescale was increased to 10ns/div, 25ns/div and 50ns/div to establish whether there were any pulse reflections in the system. It was found in all cases, that the pulses were reasonably free from replicas, either positive or negative, of the main pulse, confirming that the generator is well-matched to 50Ω. Figure 5.14 shows a 2.85kV 16ns pulse from a 1m coaxial delay line over a timebase of 25ns/div. Clearly, a slight negative overshoot of under 4% is observed at the end of the pulse, which is most likely attributed to the minor mismatch of the hemispherical electrodes.

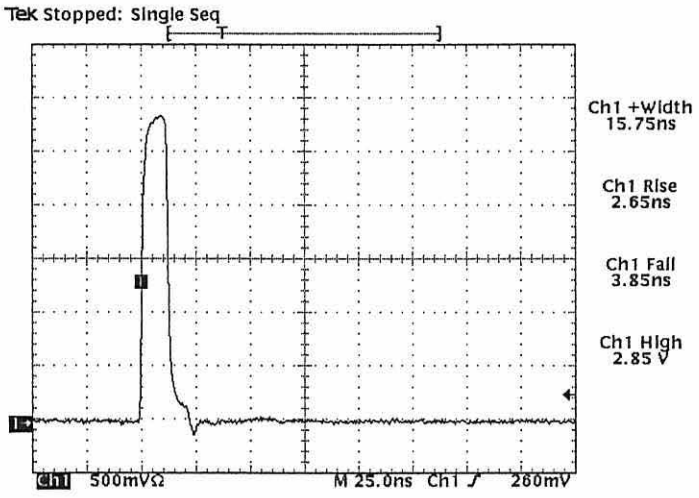

Figure 5.14 57A pulse over an extended timescale *(500V per vertical division)*.

In order to study the effect of the mismatch at the spark gap electrodes, the propagation of an electromagnetic wave may be resolved at the interface of a mismatched section of transmission line. As discussed in §5.3.1, with the pulse forming line charged to potential V, a spark causes a +V/2 pulse to go forward in the direction of the load, and a –V/2 pulse to go backwards towards the delay line. Reflection and transmission processes then occur at the interface between the impedance of the mismatched hemispherical electrodes Z_E, and the impedance of the load Z_L and pulse forming line Z_0. The voltage reflection coefficients towards the load ρ, and in the direction of the pulse delay line ρ' are given by (Chen 1995).

$$\rho = \frac{2Z_L}{Z_L + Z_E} \quad \text{and} \quad \rho' = \frac{Z_E - Z_0}{Z_E + Z_0} \tag{5.7}$$

The propagation time τ through an effective section of mismatched transmission line L is given by $\tau = L / C$, where C is the phase velocity of the electromagnetic pulse. To illustrate the effect, if the characteristic impedance of the mismatched spark electrodes is estimated to be 100Ω, the voltage reflection coefficients may be obtained from equation 5.7, which in this case gives $\rho = 2/3$ and $\rho' = 1/3$. Assuming a step input function, the reflection and transmission processes at the interface are shown in figure 5.15(a), with the associated voltage developed at the load illustrated in figure 5.15(b).

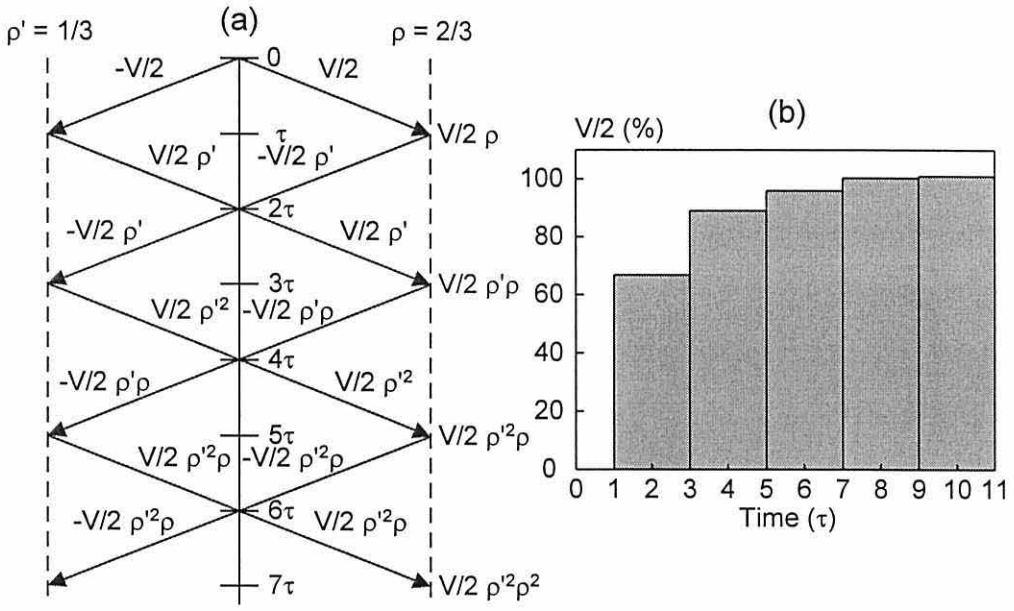

Figure 5.15 (a) Reflection and transmission of an electromagnetic pulse at the impedance interface and (b) the associated voltage developed at the load.

From figure 5.15, it is evident that a short section of mismatched transmission line will tend to lengthen the rise time of an incident pulse. Specifically, the mismatched impedance ratio and the actual length of the mismatched section determine the rise time of the pulse, which may partially account for the shape of the measured pulses observed in figures 5.11, 5.12 and 5.13.

5.4.3.2 Generator Specification

The characteristics of the corrected spark gap pulses from the 50Ω input of the oscilloscope are summarised in table 5.2. All of the pulses were obtained with the high voltage supply set at 6kV, with the gap fixed at 0.3mm and a nitrogen pressure of 4bar. Similar to the mercury wetted relay, it is apparent that each of the pulse widths is greater than the corresponding electrical length of the pulse forming line, as described in equation 5.1. Consequently, the average value for this additional delay due to the spark gap switch, the parameter L_β in figure 5.1, was estimated to be around 4.9ns. This is considerably larger than the observed value for the mercury relay, although this may be expected for a larger structure with a higher inductance and capacitance per unit length.

Delay line length (cm)	20	50	100	400
Corrected rise time (ns)	2.29	2.79	2.82	2.97
Corrected fall time (ns)	2.78	3.22	4.31	13.02
Corrected pulse width (ns)	6.60	10.56	16.15	55.75
Supply voltage V_S (kV)	6.00	6.00	6.00	6.00
Load voltage V_L (kV)	2.27	2.96	3.00	3.01
Pulse current (A)	45.4	59.2	60.0	60.2

Table 5.2 50Ω impedance pulse characteristics for the spark gap switch.

The dependence of the pulse rise time on the nitrogen pressure in the spark chamber is shown in figure 5.16. The pulses were obtained by varying the gap distance and pressure accordingly, so that the magnitude of the measured output pulse is 2.5kV. Each pulse was obtained with 1m of delay line connected.

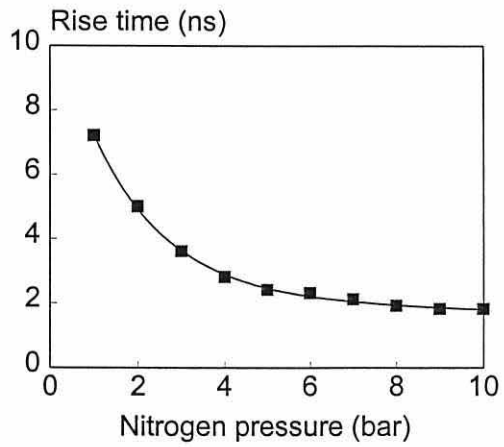

Figure 5.16 Corrected pulse rise time as a function of nitrogen pressure.

From figure 5.16, it is evident that the rise time of a pulse decreases as the nitrogen pressure increases. Obviously, simple kinetic theory implies that at higher gas pressures the mean free path between collisions is considerably reduced, as discussed in §5.4.1.

Using the pressurised N_2 spark gap switch developed in §5.4, pulsed magnetic fields of over 1.8kOe may be generated in the 50Ω microstrip line, as discussed in §5.5. Details of the spark gap switch are similarly described in (Prichard 1999), with measurements obtained from this instrument presented in §6 and also included in Appendix A (Prichard, et al. 1999b).

5.4.4 Pulse Sharpening

In recent years, the need for both higher storage densities and data transfer rates has led to the development of metal particle pigments with a small physical size, where thermal activation is significant (Veitch, et al. 1994). To illustrate, a modern tape drive running at $20ms^{-1}$ and recording 4kfc mm^{-1} would have a bit length of around 15ns and a write head flux rise time of 6ns. As outlined in §5.4, the shortest available pulse from the spark gap switch is just under 7ns in duration, marginally narrower than the 8ns duration pulse reported by (Stinnett, et al. 1998). In order to probe magnetisation reversal over even shorter timescales, various techniques have been investigated which may be capable of sharpening the edge times of a high voltage pulse, and as a result reduce the overall pulse width.

The technique of positioning a secondary pulse sharpening gap after the main spark gap was first described by (Fletcher 1949). In order to utilise the rapid breakdown of a very narrow high pressure secondary gap, it is necessary to isolate it from the main gap. This may be achieved by including a sufficiently long transmission line between the two gaps to prevent reflections, as shown in figure 5.17, after (Fletcher 1949).

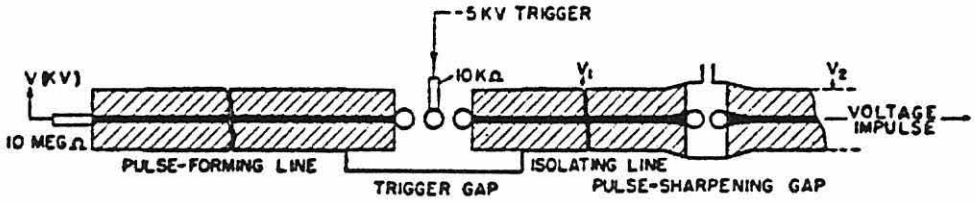

Figure 5.17 Triggered spark gap and secondary sharpening gap.

With Fletcher's arrangement, a 15kV pulse from the triggered gap establishes a large overvoltage on a secondary 0.025mm 150bar nitrogen gap. This gap breaks down very rapidly causing the rise time of the pulse to be sharpened from 20ns to under 1ns. Using this approach, similar pulse improvements have been reported by (Usov, et al. 1968) (Kukhta, et al. 1976) and (Aranchuk, et al. 1982).

A further method of increasing the rise time of a thyratron or spark gap pulse is to use a ferrite pulse sharpener similar to that developed by (Seddon, et al. 1988) and (Bolton, et al. 1994). These devices consist of a coaxial transmission line with a dielectric composed of a ferrite compound. Propagation of an electromagnetic wave down the coaxial sharpening line causes reflection and dispersion of the leading edge of the pulse by the ferrite, which produces a corresponding reduction in rise time. Using this approach, pulse sharpening of 10kV pulses with rise times of under 2ns have been reported by (Weiner, et al. 1981), improved to around 300ps for 70kV pulses by (Seddon, et al. 1988) and finally 60ps 20kV pulses outlined by (Dolan, et al. 1997). This technique is particularly attractive; utilising the high frequency properties of magnetic materials to in turn measure the high frequency properties of magnetic materials. The design and development of a ferrite sharpener under the guidance of Dr. John Dolan[1] is described in §5.4.4.1.

Other techniques employing stub tuners were briefly investigated. The basic principle involves filtering the unwanted frequency components of the propagating pulse using a short section of transmission line which presents a pure reactance at that particular frequency (Edwards 1992). This may be implemented using a coaxial tuner (Jessop 1983) or a monolithic microwave integrated circuit MMIC (Ishii 1989). For pioneering studies of microstrip filters, the interested reader is referred to (Cohn 1958), (Matthaei 1960) and (Kompa, et al. 1980).

5.4.4.1 Ferrite-Loaded Coaxial Line

Of the pulse sharpening techniques described in §5.4.4, the ferrite-loaded coaxial line appeared to offer the greatest improvements. As a result, a matched 50Ω ferrite

[1] Electrical Engineering Division, Cardiff School of Engineering, University of Wales Cardiff, East Building, Newport Road, Cardiff, CF2 IXH, UK.

sharpener was developed, with sample pulses shown presently in §5.4.4.2. The principle of operation may be described from figure 5.18, after (Dolan, et al. 1995).

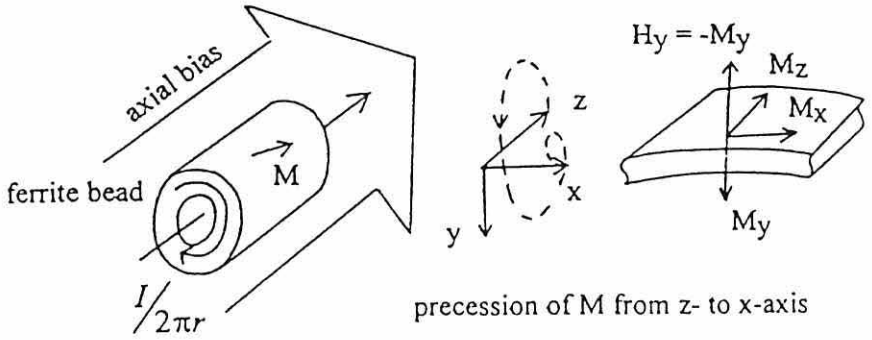

Figure 5.18 Principle of operation of a ferrite-loaded coaxial line.

The pulse sharpener shown in figure 5.18 consists of a coaxial transmission line structure containing a ferrite dielectric. The central conductor of the coaxial line passes through the ferrite bead, with the axial field along the z axis supplied by a solenoid. With the magnetisation vector initially aligned along the z direction, the pulse current produces a circumferential $I/2\pi r$ field which rotates the magnetisation towards this new field. The trajectory of M with H develops a transient radial (y axis) component directed out of the ferrite surface giving rise to a demagnetisation field component H_y (§2.3.2) and also induced surface currents in opposition to the flux. The net demagnetisation field is dominant over both the axial and circumferential field components, and has a major effect in accelerating the rate at which the magnetisation becomes aligned with the new net field. Since a ferrite has a finite relaxation time (§2.5.2), a 'shock front' now develops at the leading edge of the propagating pulse, the rise time of which is determined by the magnitude of the input pulse and the ferrite switching coefficients (Bolton, et al. 1994).

The design of the ferrite-loaded coaxial line is shown in figure 5.19. The ferrite beads and heatshrink sleeving form the dielectric of a coaxial structure matched to a 50Ω environment using equation 5.6, as discussed in §5.4.2.

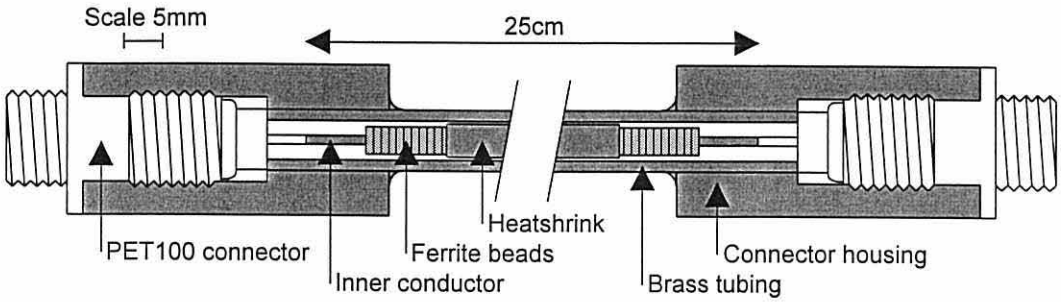

Figure 5.19 Cross sectional view of the ferrite-loaded coaxial line.

The relative permittivity of the NiZn beads is quoted as 12.0[1], together with 2.1 for the polyolefin heatshrink sleeving[2]. Subsequently, a 50Ω geometric structure may be achieved with an inner conductor diameter of 1.2mm, and an outer return conductor diameter of 3.9mm, as illustrated in figure 5.19. At this particular pulse voltage and grade of ferrite, the optimum length of line was found to be 25cm (Dolan, et al. 1997). The axial bias illustrated in figure 5.18, was supplied from a solenoid developed in our laboratories by Dr. Andrew Goodman which allows homogenous fields of up to 500 Oe to be produced over an effective length of 30cm.

The particular grade of NiZn ferrite is Philips™ 4A11. Previously, when arranged as a pulse sharpener, this material has introduced a significant reduction in pulse rise time (Dolan, et al. 1997). Notably, it has a high saturation magnetisation $4\pi M_s$ of 3.5kG and a low coercivity of less than 0.4Oe at room temperature[1]. The ferrite is commercially available as a toroid[3] with an inner and outer diameter of 1.5mm and 2.5mm respectively, and a length of 1.0mm.

5.4.4.2 Sample Voltage Pulses

Figure 5.20 shows a measured pulse at the 50Ω input of the Tektronix™ TDS640 oscilloscope taken directly from the spark gap switch with 20cm of pulse forming line connected. The high voltage brandenburg™ PU2707 supply was set to 4kV, with the gap fixed at 0.25mm, for a lower nitrogen pressure of 2bar.

[1] Soft ferrites data handbook MA01, Philips Components™ Limited, 1998.
[2] *Handbook of chemistry and physics* Weast, R. C., Ed. (CRC Press. ed.70th, 1989)
[3] A small quantity of these particular beads were kindly supplied by Hawnt Electronics Limited, Firswood Road, Garretts Green, Birminghan, B33 0TQ, UK.

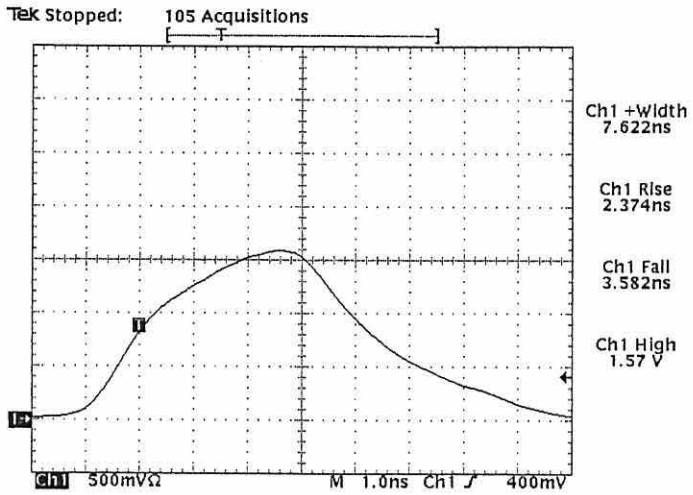

Figure 5.20 20cm coaxial delay line output *(500V per vertical division)*.

The magnitude of the measured output pulse is 1.57kV, with a pulse width of over 7.6ns. The rise and fall times of the pulse are 2.4ns and 3.6ns respectively. Figure 5.21 shows the effect of including the matched ferrite pulse sharpener after the spark gap switch. In agreement with (Dolan, et al. 1995), the optimum axial field supplied from the solenoid was fixed at 300 Oe.

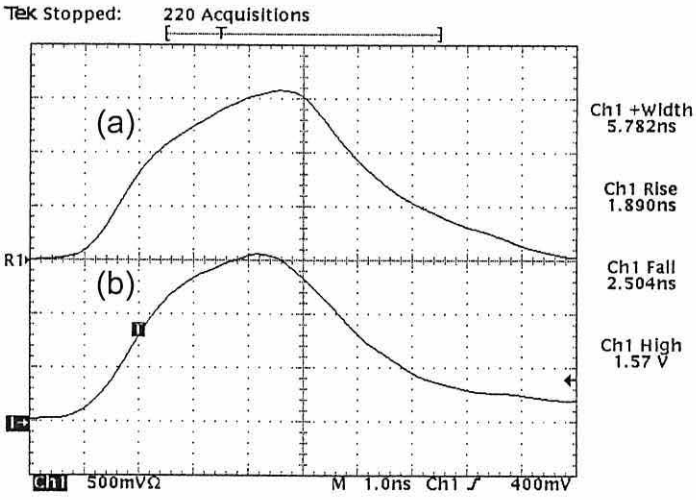

Figure 5.21 (a) Measured pulse from the spark gap switch, along with (b) sharpened pulse from the ferrite-loaded coaxial line *(500V per vertical division)*.

From figure 5.21, it is evident that the ferrite pulse sharpener produces a marginal improvement in pulse shape. The rise time of the pulse is reduced to under 1.8ns, with a subsequent reduction in overall pulse width to 5.8ns. Nevertheless, the

performance of the pulse sharpener is significantly inferior to that reported by (Seddon, et al. 1988) and (Dolan, et al. 1997). Further evidence of the limited performance of the ferrite pulse sharpener is shown in figure 5.22.

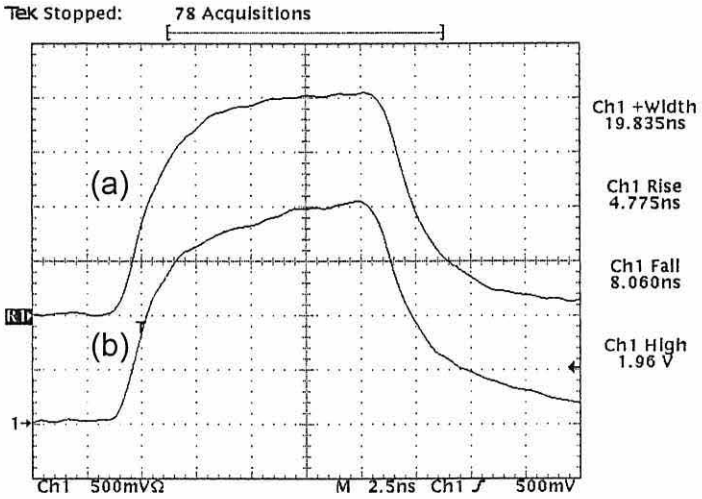

Figure 5.22 (a) Measured pulse from the spark gap switch, along with (b) sharpened pulse from the ferrite-loaded coaxial line *(500V per vertical division)*.

Figure 5.22 shows pulses at the 50Ω input of the oscilloscope taken from the spark gap switch with 1m of pulse forming line connected. Along with figure 5.21, the high voltage supply was fixed at 4kV, with the gap set at 0.2mm for a nitrogen pressure of 2bar. Considering the lower gas pressure, the observed pulse from the spark gap switch (a) has a characteristic rise time of under 5.0ns. Similarly, the pulse obtained from the 300 Oe axially biased ferrite-loaded coaxial line (b) does not display significant pulse steepening, with a marginally improved rise time of under 4.8ns. Putting aside problems of corona discharge in the line and connectors, the problem appeared to be more fundamental.

The pulse steepening effect corresponds to the switching time of the ferrite and the consequent development of an electromagnetic shock wave (Dolan, et al. 1997). If the ferrite is simply biased to a point on the hysteresis loop, the switching time is essentially the magnetisation reversal time. For the case of axial bias, the switching time may be accounted for in terms of coherent precession of the magnetisation vector from its initial axial alignment towards the final circumferential alignment. The shock

wave rise time is defined by the combination of pulsed and static magnetic field components (Dolan 1993).

Solution of the Landau-Lifshitz-Gilbert gyromagnetic equation in the time domain (§2.5.5) shows that the precessional switching time is reduced as the pulse amplitude is increased. The basic assumption made in the design presented in this study is that the value of the damping factor α_d is determined solely by the magnitude of the bias field. In most gyromagnetic devices, the axial bias field is the dominant field component and this assumption would be reasonable. However, for ferrite-loaded coaxial lines in axially biased mode, the damping factor varies with the pulse field amplitude, in addition to the bias field[1]. Essentially, as the pulse amplitude is reduced, the damping factor increases (Gyorgy 1957), which leads to a much slower switching time than is expected.

These results indicate that, for a given size of ferrite bead, there is a definite lower limit on the pulse amplitude below which the axially biased mode becomes ineffective. Unfortunately, for the limited range of pulse amplitudes available in this study, the corresponding pulse steepening effect is small.

5.5 Microstrip Structure

As mentioned briefly in §5.1, the energy stored in the pulse forming line is transferred into a matched microstrip load on closing a high voltage switch. Propagation of a short duration pulse along the microstrip line causes an electromagnetic wave to be transmitted, the transverse magnetic components of which are used to impulse magnetise the sample. However, consideration of the electromagnetic fields associated with a microstrip line is somewhat compounded by the effect of the inhomogeneous dielectric interface which modifies the mode of propagation, as discussed in §5.5.1.

This section outlines the development of a matched 50Ω microstrip line, of which the magnetic sample under investigation forms a part. Due to the popularity of microstrip transmission lines in planar microwave technology, several standard texts have been consulted (Howe Jr 1974) (Gupta, et al. 1979) (Hoffmann 1987) (Ishii 1989) and (Edwards 1992).

[1] John Dolan, University of Wales Cardiff, personal communication, 1999.

5.5.1 Microstrip Technology

A microstrip is a two conductor transmission line having a general geometric structure illustrated in figure 5.23. Specifically, a narrow conducting strip is separated from the ground plane by a thin dielectric sheet (Wu 1957).

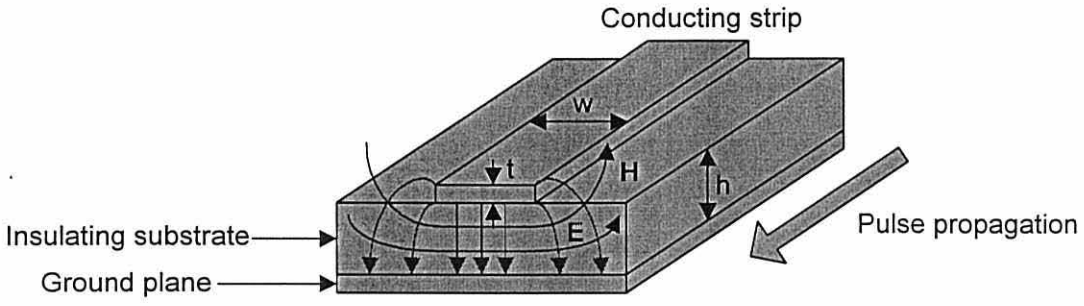

Figure 5.23 Geometric structure of a microstrip line.

The introduction of the microstrip transmission line in the 1950s has now practically replaced conventional microwave coaxial and waveguide technologies. Historically, the microstrip line evolved from the triplate stripline which consisted of an inner conductor enclosed on either side by ground plane. Moreover, with the advent of photolithography, the microstrip became increasingly favoured for the intensifying demands of microwave integrated circuits (MIC), and more recently monolithic microwave integrated circuits (MMIC). With MMIC technology, transmission lines along with other electronic components such as resistors, capacitors, diodes and transistors may be manufactured monolithically on a single substrate (Ishii 1989).

Conceptually, a microstrip structure may be visualised using the parallel wire transmission line of (Lecher 1890). Figure 5.24 shows the development of the microstrip line from a parallel wire line, with a cross sectional view of the electric and magnetic field distribution, after (Gupta, et al. 1979). The transformation from (a) to (b) is essentially a change in conductor geometry, whereas from (b) to (c) involves placing a conducting sheet at the plane of symmetry. The final microstrip configuration (d) is obtained by inserting a thin dielectric substrate between the two conductors. The introduction of the dielectric effectively multiplies the flux in the region bounded by the microstrip and ground plane, along with providing mechanical support for the circuit (Hoffmann 1987). However, the dielectric medium of the transmission line becomes

inhomogeneous, and a microstrip structure cannot support a pure transverse electromagnetic mode (TEM) of propagation, as detailed in §5.5.1.1 and §5.5.1.2.

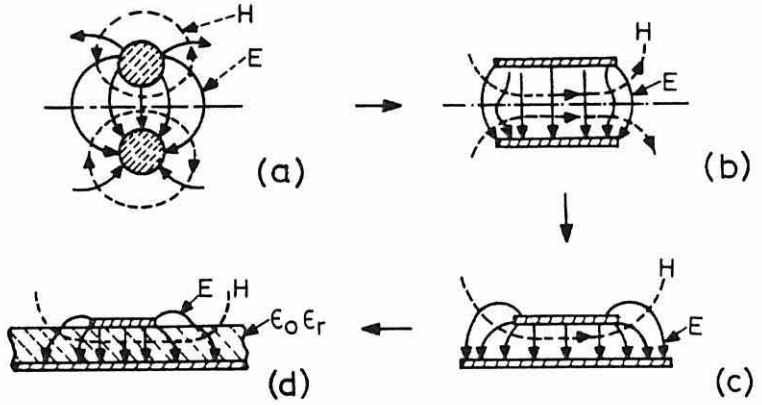

Figure 5.24 Development of the microstrip line from a parallel wire transmission line.

Historically, dynamic magnetisation studies involving microstrip lines were first performed by (Kakuno, et al. 1973). In this investigation, magnetisation reversal in NiFeCo thin films was detected optically using the Kerr effect through a window in the ground plane of the stripline. A single pulse of energy was delivered into the microstrip line on closing a mercury wetted relay, similar to that described in §5.3. More recently, a modified approach using an optically triggered microstrip line has been utilised to study fast magnetic phenomena in a wide variety of systems; the interested reader is referred to (Freeman 1994) and (Hicken, et al. 1999).

As a precursor to recent studies of high frequency magnetisation reversal in recording media, the speed limited performance of magnetic tapes has been reported as early as 1974 (Thornley, et al. 1974). In this investigation, a series of commercial tapes were studied using a continuous microstrip recording system, in which a DC erased tape was passed under a microstrip line in order to rapidly switch the magnetisation. The effect of the field pulse duration was then measured with a read head to give an estimation of the switching time (Thornley 1975).

5.5.1.1 Pure Transverse Electromagnetic Mode

Pure transverse electromagnetic mode (TEM) will occur on a transmission line which consists of two electrodes separated by an entire cross section of homogeneous dielectric (Hoffmann 1987). Consequently, the pure TEM mode is commonly excited in

coaxial lines and triplate structures. TEM modes are distinguished by having no electric and magnetic field components in the direction of wave propagation, and with only longitudinal currents flowing in the electrodes, the E and H components lie entirely in the transverse plane. As the potential difference between the two electrodes is independent of the path, the pure TEM line is characterised by a unique characteristic impedance and phase velocity, both of which are independent of frequency.

5.5.1.2 Quasi-Transverse Electromagnetic Mode

A microstrip structure cannot support a pure TEM mode of propagation as the area containing the fields consists of inhomogeneous dielectric, as indicated in figure 5.23. Propagation of an electromagnetic wave along a microstrip line therefore supports a quasi-TEM mode, as the wave velocity in air is faster than in the dielectric substrate. Consequently, parts of the propagating wave have different velocities and cannot produce a single transmission mode (Hoffmann 1987). However, as two isolated electrodes are present (as opposed to a waveguide), the quasi-TEM mode is a special type of hybrid wave in which the transverse field components dominate. The lower the frequency, then the closer the wave propagation approaches pure TEM. An approximate static analysis of quasi-TEM lines at low frequencies, below 3GHz (Ishii 1989), is described in §5.5.2.1. This approach takes account of the dominance of the TEM mode, and ignores the longitudinal field components to obtain a frequency independent value for the characteristic impedance and phase velocity.

5.5.2 Microstrip Geometry

Planar technology implies that the characteristics of a microstrip line may be controlled in a single plane. As a result, the width of a microstrip line on a dielectric substrate may be adjusted to control the characteristic impedance, so that it closely matches that of the 50Ω switch assembly. In the previous study of low coercivity γ-Fe_2O_3 and CrO_2 media (Hancock 1995), a microstrip line was constructed which developed a magnetic field of 22 OeA^{-1}, as detailed in §5.5.3. Therefore, for the maximum available current pulse of 22A from the mercury wetted relay, a pulsed field of around 450 Oe was generated. Details of the design of this microstrip line are outlined in (Hancock, et al. 1996).

Although preliminary studies of advanced metal particle media have been performed using this particular microstrip line (Prichard, et al. 1999a), the magnetic field produced is not of sufficient magnitude to switch all of the particles. Consequently, in order to obtain a larger current density and hence an enhanced magnetic field, a narrower microstrip line has been developed, similar to that described by (He, et al. 1995). In order to maintain the required 50Ω matching impedance, the geometry of this narrower microstrip line has been altered by using a substantially thinner dielectric substrate. Of course, the insertion of a magnetic tape sample between the substrate and ground plane will also influence the geometry of the microstrip, as shown in figure 5.25. Modifying the geometry of the microstrip line has led to an increased field calibration of 30 OeA^{-1}, with the design procedure outlined in §5.5.2.1.

The particular dielectric material favoured in this study was Kapton® polyimide. This homogeneous material has a high dielectric strength of up to 195kV mm^{-1}, together with excellent wave conducting properties[1]. A sheet of Pyralux® LF laminate with a 35μm layer of copper on one side was kindly provided by DuPont® Electronic Materials. Copper is diamagnetic, therefore it retains no remanent magnetisation after the removal of the field pulse. The thickness of both the Kapton® substrate and the acrylic adhesive layer is 25μm, as shown schematically in figure 5.25. The thickness of the magnetic coatings under investigation are typically around 18μm.

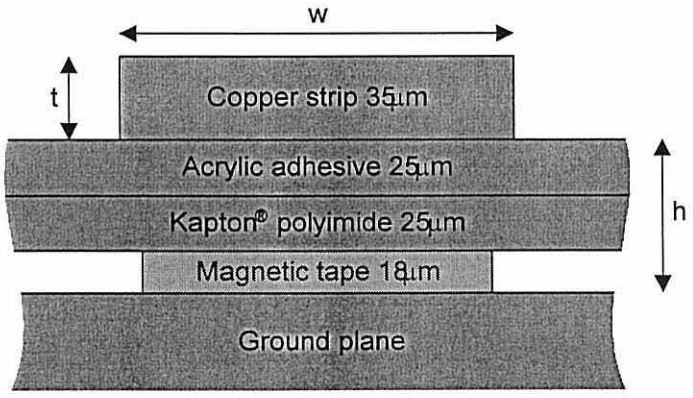

Figure 5.25 Cross sectional view of the microstrip line.

[1] Pyralux® LF flexible composites datasheet, DuPont® Electronic Materials, 1995.

5.5.2.1 Line Impedance Calculations

Exact equations for microstrip circuit parameters do not exist due to the inhomogeneous dielectric interface. However, functional approximations have been derived by a number of workers (Wheeler 1965) (Gunston, et al. 1969) and (Bahl, et al. 1977). Using the assumption that the microstrip line has no dielectric and that the thickness of line is zero, (Wheeler 1977) revealed that over the entire range $0 < w/h < \infty$, the line width w may be calculated with an error of less than 1% using equation 5.8

$$\frac{w}{h} = \frac{8\sqrt{\exp(Z_0/30) - 1 + (\pi^2/4)}}{\left[\exp(Z_0/30) - 1\right]} \tag{5.8}$$

where Z_0 is the characteristic impedance of the line. The parameter h is the separation between the microstrip line and ground plane, as shown in figure 5.25. To ensure that the geometry of the microstrip line is well-matched to 50Ω, the line width was found to be 329.4μm. Similarly, (Hilberg 1971) derived a practical approximation with an error of less than 0.6% for all microstrip lines with $Z_0 < 132\Omega$, such that

$$\frac{w}{h} = \frac{2}{\pi}\left[\frac{60\pi^2}{Z_0} - \ln(2) - \ln\left\{\frac{60\pi^2}{Z_0} - \ln(2)\right\} - 1\right] \tag{5.9}$$

Using equation 5.9, the line width of a 50Ω microstrip line was calculated as 334.9μm.

For a practical microstrip line of finite thickness t, fringing fields will occur at the vertical edges of the conducting strip. This effectively increases the apparent line width and suggests that the characteristic impedance Z_0 will decrease (Ishii 1989). To preserve the desired 50Ω environment, (Wheeler 1977) showed that the line width may be corrected using a broadening factor Δw which accounts for the additional stray field at the edges of the microstrip line, given by

$$\Delta w = \frac{t}{\pi} \ln \frac{4\exp}{\sqrt{(t/h)^2 + \left\{\frac{1/\pi}{(w/t) + 1.10}\right\}^2}} \tag{5.10}$$

For the microstrip line described by equation 5.9, the width correction factor Δw was found to be 33.9μm. Consequently, a 301.0μm wide microstrip line was manufactured via wet etching and secured in a housing, the design of which is outlined in figure 5.26.

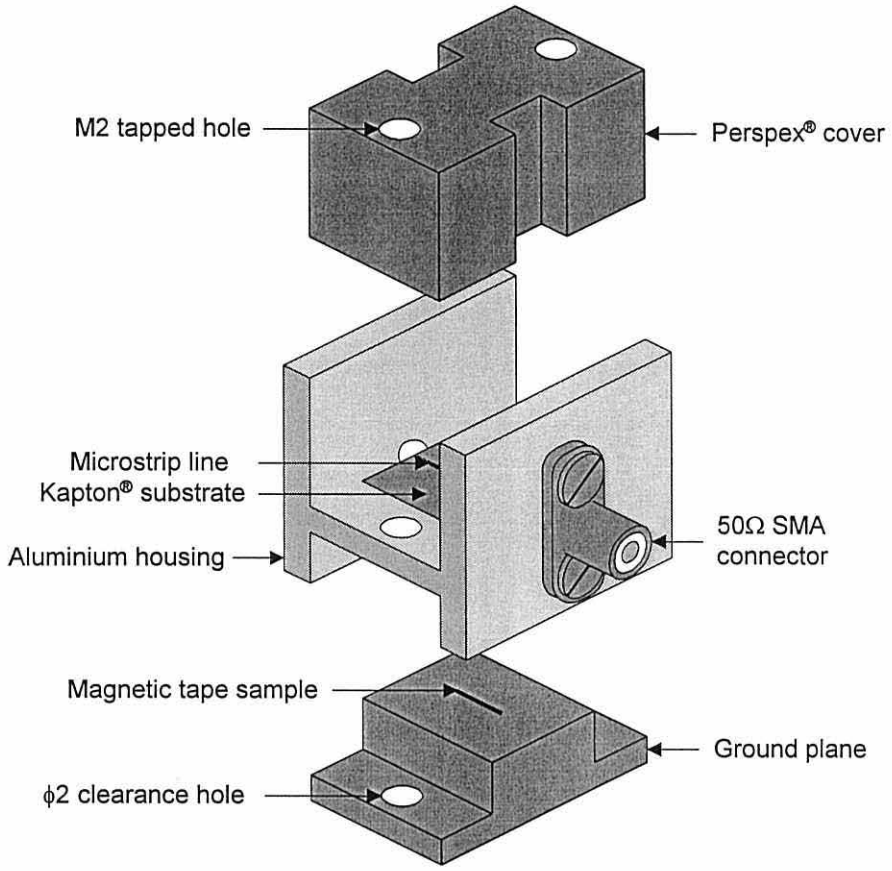

Figure 5.26 Microstrip line housing.

The design of the aluminium housing shown in figure 5.26 allows the magnetic tape sample to be easily inserted between the microstrip line and removable ground plane. In order to secure the sample firmly in position, the microstrip line is clamped between the Perspex® block and ground plane. To avoid attenuated replicas of the main pulse being reflected back along the microstrip line, a 50Ω SMA plug termination was connected at end of the line.

5.5.3 Magnetic Field under the Microstrip

As discussed in §5.5, propagation of a short duration pulse along the microstrip line causes an electromagnetic wave to be transmitted. However, the magnitude of the transverse magnetic field components H_y are not easily resolved. Using the assumption

that the microstrip line has an electric and magnetic field distribution similar to that shown in figure 5.24, both (Thornley, et al. 1974) and (Doyle, et al. 1993) estimated the magnetic field using equation 5.11, from earlier studies by (Kakuno, et al. 1973).

$$H_y = \frac{8000}{w} I_z \tan^{-1}\left(\frac{w}{2h}\right) \tag{5.11}$$

In order to obtain a larger current density and hence an enhanced magnetic field, the narrower microstrip line described in §5.5.2 has led to an increased field calibration of over 30 OeA^{-1}. Therefore, for the maximum available current pulse I_z of 60A from the spark gap switch, a pulsed field of around 1.8kOe is produced.

5.6 Concluding Remarks

This chapter has detailed the design and development of the various techniques used to produce nanosecond duration pulsed magnetic fields inside a microstrip transmission line, of which the magnetic sample forms a part. Using these techniques, studies of the high speed switching properties of advanced metal particle recording media have been undertaken, and described in §6. Publications derived from the work are included in Appendix A. Photographs of the mercury reed relay, microstrip line and ferrite pulse sharpener are shown in figure 5.27. A photograph of the pressurised nitrogen spark gap switch is shown in figure 5.28.

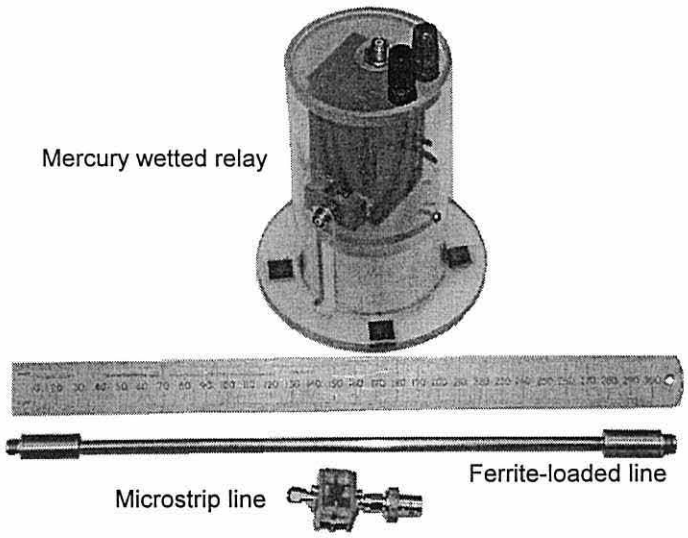

5.27 Photograph of the mercury relay, microstrip line and ferrite-loaded coaxial line.

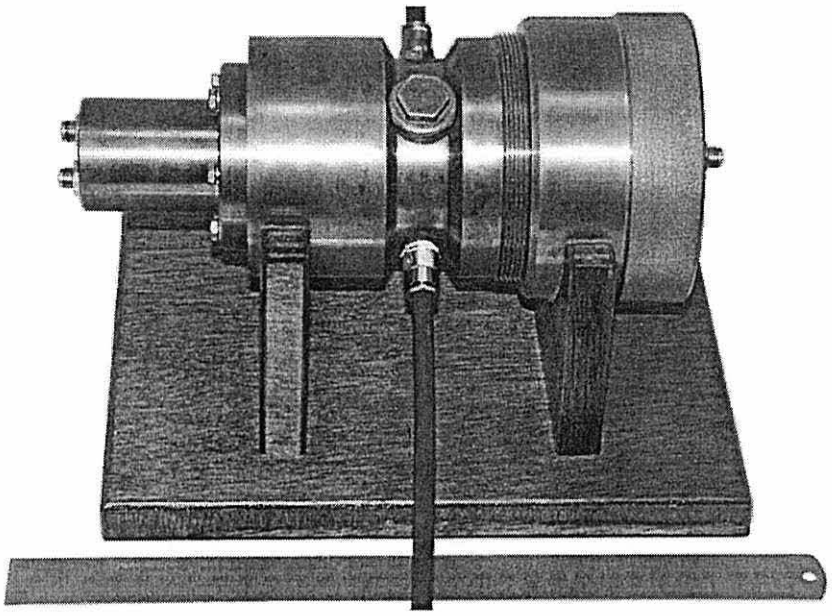

5.28 Photograph of the pressurised nitrogen spark gap switch.

References

Aleksandrin, A. I., Samodelov, I. S., *translated from Prib. Tekh. Eksp.* **4**, 142-144 (1976).

Aranchuk, L. E., Dorokhin, L. A., Znatnov, E. V., Tulupov, M. V., Tsafrin, V. Y., *translated from Prib. Tekh. Eksp.* **5**, 138-140 (1982).

Bahl, I. J., Trivedi, D. K., *Microwaves* **16**, 174-182 (1977).

Baker, R. J., Ward, S. T., *Electron. Lett.* **30**, 1634-1635 (1994).

Birx, D. L., Cook, E. G., Reginato, L. L., Schmidt, J. A., Smith, M. W., "The application of magnetic pulse compression to the grid system of the ETA/ATA accelerator", 15th Power Modulator Symposium, Baltimore, Maryland, 10-14 (IEEE, 1982).

Bolton, H. R., et al., "Investigations into sub-ns pulse generation using ferrite-loaded coaxial lines", Advisory Group for Aerospace Research and Development, Ottawa, 1-9 (NATO, 1994).

Boyer, C. N., Holland, G. E., Seely, J. F., *Rev. Sci. Instrum.* **69**, 2524-2530 (1998).

Broadbent, T. E., Wood, J. K., *Brit. J. Appl. Phys.* **6**, 368-370 (1955).

Burkes, T. R., Craig, J. P., Hagler, M. O., Kristiansen, M., Portnoy, W. M., *IEEE Trans. Electron Devices* **26**, 1401-1411 (1979).

Chen, W., *The circuits and filters handbook* (CRC Press, ed. 1st, 1995).

Cobine, J. D., *Gaseous conductors, theory and engineering applications* (Dover Publications, Inc., 1958).

Cohn, S. B., *IEEE Trans. Microwave Theory Tech.* **MTT-6**, 223-231 (1958).

Cummings, D. B., *IEEE Trans. Comm. Electron.* **68**, 514-523 (1963).

Dolan, J. E., *IEE Proc.-Sci. Meas. Technol.* **140**, 294-298 (1993).

Dolan, J. E., Bolton, H. R., Shapland, A. J., *Electron. Lett.* **33**, 2049-2050 (1997).

Dolan, J. E., Bolton, H. R., Shapland, A. J., "Modelling of pulse sharpening effects in ferrite-loaded coaxial lines", International Symposium on Nonlinear Electromagnetic Systems, Cardiff (IOS Press, 1995).

Donaldson, A. L., Hagler, M. O., Kristiansen, M., Jackson, G., Hatfield, L., *IEEE Trans. Plasma Sci.* **12**, 28-38 (1984).

Donaldson, A. L., et al., *IEEE Trans. Magn.* **22**, 1441-1447 (1986).

Doyle, W. D., He, L., Flanders, P. J., *IEEE Trans. Magn.* **29**, 3634-3636 (1993).

Edwards, T. C., *Foundations for microstrip circuit design* (John Wiley and Sons, ed. 2nd, 1992).

Fletcher, R. C., *Rev. Sci. Instrum.* **20**, 861-869 (1949).

Focia, R. J., Schamiloglu, E., Fleddermann, C. B., *Rev. Sci. Instrum.* **67**, 2626-2629 (1996).

Freeman, M. R., *J. Appl. Phys.* **75**, 6194-6198 (1994).

Fulkerson, E. S., Booth, R., "Design of reliable high voltage avalanche transistor pulsers", 21st International Power Modulator Symposium, Costa Mesa, California (IEEE, 1994).

Garwin, R. L., *Rev. Sci. Instrum.* **21**, 903-904 (1950).

Glasoe, G. N., Lebacqz, J. V., *Pulse generators* (McGraw-Hill Book Company, Inc., 1948).

Golnabi, H., *Rev. Sci. Instrum.* **63**, 5804-5805 (1992).

Gunston, M. A. R., Weale, J. R., *Electron. Lett.* **5**, 697-698 (1969).

Gupta, K. C., Garg, R., Bahl, I. J., *Microstrip lines and slotlines* (Artech House, Inc., 1979).

Gyorgy, E. M., *J. Appl. Phys.* **28**, 1011-1015 (1957).

Hancock, C. P., PhD, University of Wales (1995).

Hancock, C. P., O'Grady, K., el-Hilo, M., *J. Phys. D: Appl. Phys.* **29**, 2343-2351 (1996).

Hancock, C. P., Owens, A. R., O'Grady, K., *IEE Proc.-Sci. Meas. Technol.* **144**, 229-233 (1997).

He, L., Wang, D., Doyle, W. D., *IEEE Trans. Magn.* **31**, 2892-2894 (1995).

Hicken, R. J., Wu, J., *J. Appl. Phys.* **85**, 4580-4582 (1999).

Hilberg, W., *Archiv fuer Elektrotechnik* **54**, 200-205 (1971).

Hoffmann, R. K., *Handbook of microwave integrated circuits* (Artech House, Inc., 1987).

Howe Jr, H., *Stripline circuit design* (Artech House, Inc., 1974).

Ishii, T. K., *Microwave engineering* (Harcourt Brace Jovanovich, ed. 2nd, 1989).

Jessop, G. R., *VHF/UHF manual* (Royal Society of Great Britain, ed. 4th, 1983).

Kakuno, K., Gondo, Y., *Journal of the Physical Society of Japan* **35**, 1292-1296 (1973).

Kimura, W. D., Kushner, M. J., Seamans, J. F., *J. Appl. Phys.* **63**, 1882-1888 (1988).

Kompa, G., Mehran, R., *The Radio and Electronic Engineer* **50**, 54-58 (1980).

Kukhta, V. R., et al., *translated from Prib. Tekh. Eksp.* **6**, 1670-1673 (1976).

Lecher, E., *Annalen der Physik* **41**, 850-870 (1890).

MacGregor, S. J., Tuema, F. A., Turnbull, S. M., Farish, O., *J. Phys. D: Appl. Phys.* **26**, 954-958 (1993).

Matthaei, G. L., *IEEE Trans. Microwave Theory Tech.* **MTT-8**, 580-593 (1960).

Orgler, A., *Annalen der Physik* **1**, 159-174 (1900).

Osmokrovic, P., Arsic, N., Lazarevic, Z., Kartalovic, N., *IEEE Trans. on Power Delivery* **11**, 858-864 (1996).

Palmer, A. W., House, H., *J. Phys. E: Sci. Instrum.* **4**, 115-118 (1971).

Paschen, F., *Annalen der Physik* **37**, 69 (1889).

Penetrante, B. M., "Pollution control applications of pulsed power technology", 9th IEEE International Pulsed Power Conference, Albuquerque, New Mexico, 1-5 (IEEE, 1993).

Prichard, L. S., "Development of a nanosecond spark gap pulse generator", S. Iezekiel, Ed., PREP'99 Conference, UMIST, Manchester, 238-241 (IEEE, 1999).

Prichard[a], L. S., O'Grady, K., *J. Magn. Magn. Mater.* **193**, 220-223 (1999).

Prichard[b], L. S., O'Grady, K., *IEEE Trans. Magn.* **35**, 2784-2786 (1999).

Richley, E. A., *Elect. Wire. World* **93**, 519-523 (1987).

Richner, J. R., Askin, T. O., "How to know when you've been zapped, or practical techniques for selecting a reliable attenuator for use in high voltage pulse measurements" (Barth Electronics Inc., 1300 Wyoming Street, Boulder City, Nevada 89005., 1991).

Seddon, N., Thornton, E., *Rev. Sci. Instrum.* **59**, 2497-2498 (1988).

Sharrock, M. P., *J. Appl. Phys.* **76**, 6413-6418 (1994).

Stinnett, S. M., Doyle, W. D., Flanders, P. J., Dawson, C., *IEEE Trans. Magn.* **34**, 1828-1833 (1998).

Subhash, N., Sathianandan, K., *J. Phys. E: Sci. Instrum.* **17** (1984).

Taylor, J. D., *Introduction to ultra-wideband radar systems* (CRC Press, 1995).

Tektronix, "Application note: effects of bandwidth on transient information" *http://www.tek.com/Measurement/App_Notes/dpo/bwtransient/eng/* (1998).

Thornley, R. F. M., *IEEE Trans. Magn.* **11**, 1197-1199 (1975).

Thornley, R. F. M., Williams, J. A., *IBM J. Res. Develop.* , 576-578 (1974).

Tou, T. Y., et al., *IEEE Trans. Plasma Sci.* **21**, 696-700 (1993).

Townsend, J. S., *Nature* **62**, 340-341 (1900).

Usov, Y. P., Sterligov, A. G., *translated from Prib. Tekh. Eksp.* **2**, 123-125 (1968).

Van Patten, P. G., Noll, J. D., Myrick, M. L., Li, C. R., Sudarshan, T. S., *J. Phys. Chem.* **100**, 3646-3651 (1996).

Van Planck, D. W., *AIEE Trans.* **57**, 45 (1938).

Veitch, R. J., Richter, H. J., Poganiuch, P., Jakusch, H., Schwab, E., *IEEE Trans. Magn.* **30**, 4074-4076 (1994).

Weiner, K., *The UHF compendium* (Verlag Rudolf Schmidt, 1982).

Weiner, M., Beattie, W., "Generation of nanosecond pulses with a thyratron switch", 14th Pulse Power Modulator Symposium, Orlando, Florida, 179-182 (IEEE, 1980).

Weiner, M., Silber, L., *IEEE Trans. Magn.* **17**, 1472-1477 (1981).

Wheeler, H. A., *IEEE Trans. Microwave Theory Tech.* **MTT-25**, 631-647 (1977).

Wheeler, H. A., *IEEE Trans. Microwave Theory Tech.* **MTT-13**, 172-185 (1965).

Wu, T. T., *J. Appl. Phys.* **28**, 299-302 (1957).

Chapter
6

High Speed Switching in Metal Particle Recording Media

6.1 Introduction

The speed limited performance of magnetic tapes has been reported as early as 1974 (Thornley, et al. 1974). In recent years, the need for both higher storage densities and data transfer rates has led to the development of metal particle pigment formulations with a small physical size, where thermal activation is significant. For example, a modern tape drive running at $20ms^{-1}$ and recording $4kfcmm^{-1}$ would have a bit length of around 15ns and a write head flux rise time of 6ns. Correspondingly, over these short timescales, substantial increases in remanent coercivity have been observed (Doyle, et al. 1993) (Veitch, et al. 1994) and (Hancock, et al. 1996). As a result, the characterisation of these advanced particulate materials to find their switching speed limits is of fundamental scientific and commercial interest, as highlighted in recent investigations (Stinnett, et al. 1998a) (Stinnett, et al. 1999) and publications derived from this study (Prichard, et al. 1999a) (Prichard, et al. 1999b) included in Appendix A.

In this chapter, the switching characteristics of a series of five metal particle tape samples are examined over a wide range of timescales. Pulsed field measurements are performed as DC demagnetisation (DCD) curves which closely resemble the digital recording process. As the behaviour of recording media is strongly dependent on the timescale of the reversal process (Néel 1949), this provokes conflicting requirements for writing and storage coercivities. Consequently, in order to relate high frequency

recording properties to archival storage stability, the results are compared with recent models of magnetisation reversal (Sharrock, et al. 1981) (el-Hilo, et al. 1992).

6.2 Sample Characterisation

A series of metal particle (MP) tape samples have been studied using pulsed and swept DC fields. The samples were produced by the industrial collaborators in this project, Imation Corporation, MN[1]. The first four samples were prepared from the same magnetic pigment to form a dispersion with a solids ratio of 40% by weight. The acicular magnetic particles had an average length of 150nm, with an aspect ratio of 9:1, and a SSA of $50m^2\ g^{-1}$. The dispersion was composed of a proprietary formulation of binders, dispersants, lubricants and head cleaning agents. The formulations were initially premixed at high solids ratio in a double planetary mixer before being transferred to a high shear recirculating bead mill, similar to that described in §4.3.2. After milling, the dispersion was subsequently letdown to approximately 25% solids and coated as a single layer using a fully automated coater. During coating, changes in the speed of the polyester web and the initial viscosity of the coated formulation were varied, so that a series of tape samples were produced with an increasing degree of particle orientation. The samples are typical of media used in high speed digital tape systems, such as the Imation Travan™ linear cartridge.

The fifth tape sample was prepared from a very small pigment, with an average particle length of only 65nm. With the trend to ever smaller particles for advanced recording media (Richter, et al. 1995), thermally activated switching becomes more significant as the thermal limit to data density is approached (Sharrock 1994). The classical explanation is that very small particles are easier to switch since the energy barrier to reversal is assumed to be proportional to the total particle volume (Néel 1953).

This section details the basic magnetic characterisation of the samples using a variety of measurement techniques, as described in §2.6. Conventional bulk magnetic measurements including basic hysteretic information, along with studies of the switching behaviour determined by remanence curves are presented. The well-established δM technique has been used to study the nature of interactions and there

[1] Data Storage and Information Management, Imation Corporation, Discovery-2D-37, 1 Imation Place, Oakdale, MN 55128-3414, USA.

effect on reversal. Measurements of the time dependence of magnetisation were performed using the method detailed in §2.5.2.1, and as a result, the activation volume of reversal may be determined allowing an observation of the sub-crystallite nature of the particles to be obtained.

6.2.1 Basic Magnetic Characterisation

All of the magnetic measurements reported in §6.2 were performed using a PMC MicroMag™ 2900 alternating gradient force magnetometer. The hysteresis loops of the five samples, measured in the coating direction, are shown in figure 6.1. The measurements were performed at a linear sweep-rate of 511 Oe s^{-1}.

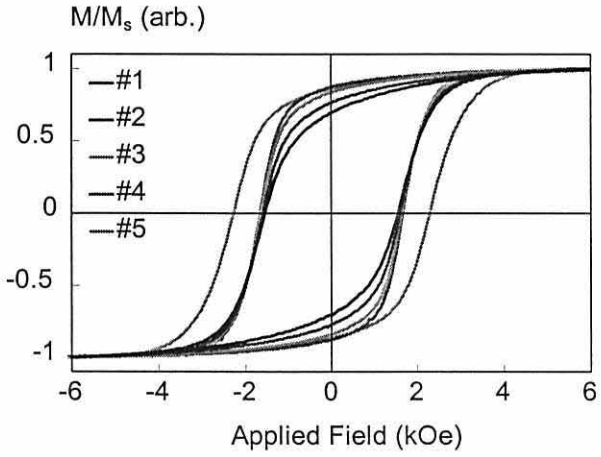

Figure 6.1 Hysteresis loops for samples #1 to #5.

As discussed in §2.6.2.1, the basic characteristics obtained from the hysteresis loops in figure 6.1, are shown in table 6.1.

Sample	#1	#2	#3	#4	#5
H_c (kOe)	1.55	1.60	1.64	1.66	2.29
M_r/M_s [a]	0.70	0.77	0.83	0.88	0.86
M_r (memu cm^{-2})[b]	36.9	40.7	44.2	46.5	33.9
1-S*	0.501	0.420	0.356	0.333	0.360

[a] M_s = M at 10kOe [b] Measurement performed using a PAR 4500 VSM

Table 6.1 Hysteresis loop properties of the tape samples.

From figure 6.1, the increase in tape squareness M_r/M_s from 0.70 for sample #1 to 0.88 for sample #4 is clearly evident. The smaller particle sample #5 has a loop

squareness of 0.86. In particulate recording media, one of the more desirable magnetic properties is that of high tape squareness (Chantrell, et al. 1992). For acicular metal particles with uniaxial magnetisation, squareness gives an indication of the magnetic texture, i.e. the degree of alignment of the particles easy axes. In terms of recording properties, the signal to noise ratio of textured systems is enhanced due to the narrower switching field distribution (Köster 1984) which gives sharper transitions between recorded bits (Williams, et al. 1971), as detailed in §2.6.2.3. Although, a corresponding increase in time dependent behaviour has also been observed (Uren, et al. 1989).

From table 6.1, it is clear that the coercivity increases with sample texture. This may be explained from Stoner-Wohlfarth theory for uniaxial single domain particles (Stoner and Wohlfarth 1948), as described in §2.4.1. These workers predicted that an increase in coercivity accompanies the alignment of an isolated particle into the applied field direction. The behaviour of an assembly of non-interacting uniaxial particles is simply the summation of the behaviour of each individual particle. As a result, for well aligned media, the switching field will be narrow. For poorly textured media, each of the particles will switch at its own coercivity to give broadened switching field distribution, as confirmed by the (1-S*) values in table 6.1.

6.2.2 Remanence Curves

Remanence curves, unlike hysteresis loops, measure only irreversible changes in magnetisation (O'Grady 1990). The two principal remanence curves considered in this study were measured as a function of magnetising and demagnetising field. As discussed in §2.6.2.2, the isothermal remanence $M_r(H)$ is obtained after the application and removal of an increasing applied field, with the sample initially demagnetised. The DCD remanence $M_d(H)$ is measured from the saturation remanent state by the application of increasing demagnetising fields. Figure 6.2 shows the measured IRM and DCD remanence curves for the four samples prepared from the same magnetic pigment.

For the IRM curve in figure 6.2(a), the sample demagnetisation was achieved through the application of a slowly decreasing 50Hz field supplied by a LDJ Electronics Incorporated™ 7000H loop tracer. For the remanence curves presented in figure 6.2, it is evident that a wide range of switching fields are present. Previous studies have shown that a wide distribution of switching fields may result in thermal loss of data for

the low coercivity particles and lead to significant overwrite problems caused by the high coercivity particles (Bertram 1986) and (Flanders and Sharrock 1987). Investigations by (Morales, et al. 1999) have shown that the formation of sub-crystallites within the particles may account for the broadened range of switching fields, in addition to effects of the particle size distribution and angular dependence of the coercivity. The crystallites are most likely formed during the hydrogen reduction process; nucleating at the ends of the original oxide particle (Morales, et al. 1998). An observation of the crystallite nature of the particles is described in §6.2.4, from a comparison of the activation volume of reversal and the physical particle volume determined from TEM analysis.

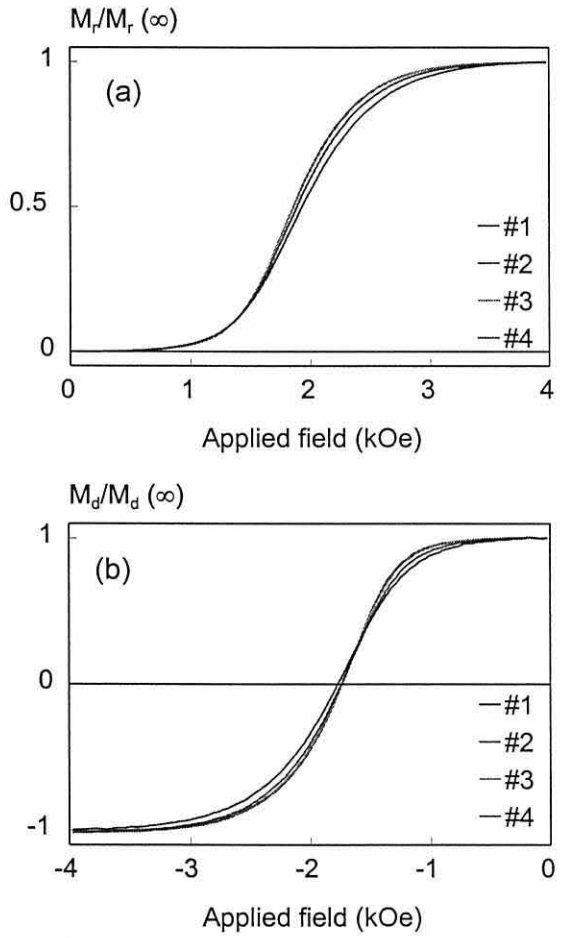

Figure 6.2 (a) Isothermal remanent magnetisation and (b) DC demagnetisation curves obtained for samples #1 to #4.

As detailed in §2.6.2.3, the irreversible susceptibility $\chi_{irr}(H)$ is obtained from the differential of the principal remanence curves, as shown in figure 6.3.

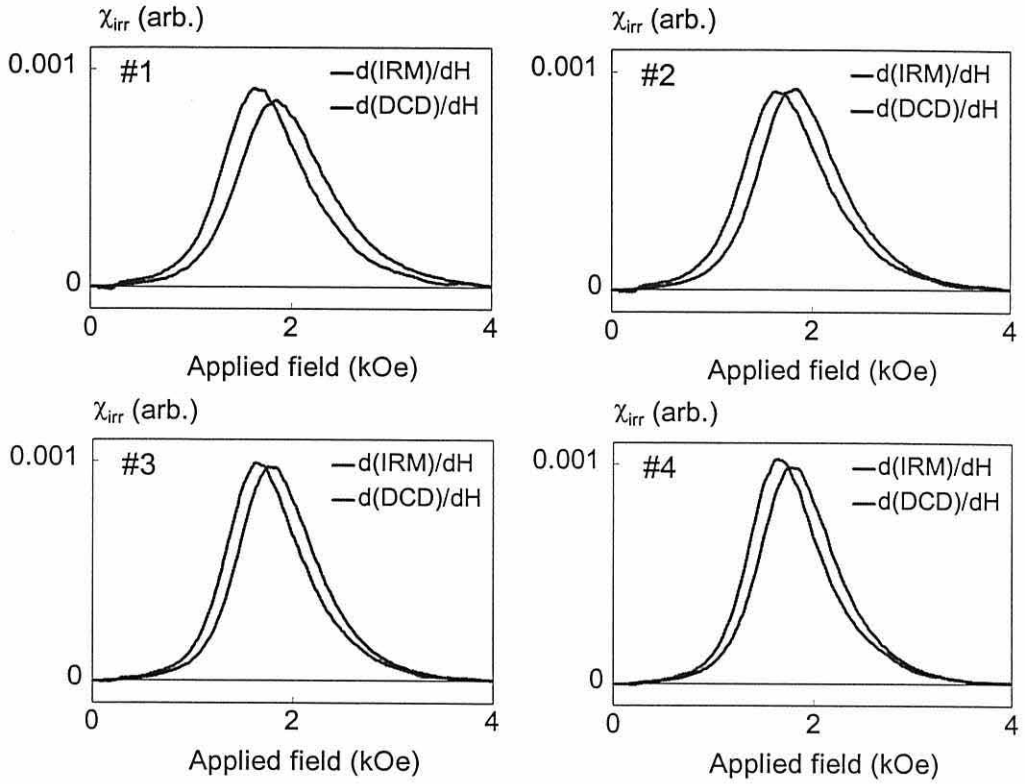

Figure 6.3 Irreversible susceptibility curves for tape samples #1 through #4.

Irreversible susceptibility curves provide a measure of the switching field distribution (Chantrell, et al. 1992), as the process by which remanence is acquired is related to the energy barrier distribution of the system (O'Grady, et al. 1992). Accordingly, the switching field distributions of the four tape samples were obtained by normalising the area under the irreversible susceptibility curves to unity, as indicated in figure 6.3.

Comparison of each pair of differentiated remanence curves shown in figure 6.3, indicates that for all samples the differentiated IRM curve is displaced to higher fields relative to the DCD curve. In the absence of interactions, (Wohlfarth 1958) demonstrated that the differentials of both the IRM and DCD curves would be identical, as discussed in §2.6.2.4. Consequently, this observation is indicative of demagnetising dipolar interactions between the particles, which indicate that it is easier for the system to be demagnetised rather than magnetised, in agreement with (Mayo, et al. 1991). In addition, it is also evident that as the particle orientation increases, the shape and lateral position of the differentiated remanence curves become successively closer, which would seem to suggest that the level of demagnetising interaction decreases with increasing magnetic texture.

From figures 6.2 and 6.3, parameters obtained from the remanence curves are summarised in table 6.2. As defined in §2.6.2.2, the remanent coercivity H_{cr}' of the IRM curve is the field at half of the level of the saturation remanence. The remanent coercivity H_{cr} of the DCD curve is the field required to reduce the magnetisation to zero.

Sample	#1	#2	#3	#4	#5
H_{cr}' (Oe)	1935	1890	1860	1860	2580
H_{cr} (Oe)	1785	1750	1745	1740	2410
$FWHM_{IRM}$ (Oe)	1055	960	900	880	1340
$FWHM_{DCD}$ (Oe)	975	950	875	840	1260

Table 6.2 Remanence parameters for the tape samples.

For samples #1 through #4, there is a general narrowing of the irreversible susceptibility curves with particle orientation in both IRM and DCD measurements. However, there is a more pronounced narrowing of the switching field distribution which originates from the IRM curve. This arises since reversal from the DC saturated state always begins from a micromagnetic configuration in which the majority of the moments are aligned parallel, which leads to reversal largely in unison and hence a narrower SFD with less influence of texture. However, for the IRM case, which originates from a demagnetised state, the initial configuration is that of flux closure which is not well defined. Hence, there can be many starting conditions leading generally to a wider SFD. Under these circumstances, the influence of texture becomes more significant as it reduces the possible initial configurations. Thus, the effect of texture on $\chi_{irr}(H)$ from the IRM curve is greater. Furthermore, the significant reduction in remanent coercivity H_{cr}' with increasing magnetic texture may be an indication of increased cooperative switching between the more aligned particles (Mayo, et al. 1991).

Consistent with other traditional acicular particulate systems (Spratt, et al. 1988) and (Mayo, et al. 1990), the smaller particle sample #5 also exhibits demagnetising interactions between the particles, with the differentiated IRM curve displaced to higher fields relative to the DCD curve. This high coercivity sample is typical of a tape medium for future high-density recording. Since the energy barrier in materials with dominant shape anisotropy depends on the square of the magnetisation, as shown in equation 2.8, extremely small stable particles of iron-cobalt have been reported by

(Richter, et al. 1995) (Hisano, et al. 1998) and (Morales, et al. 1998). For other recent developments in all aspects of MP technology, the interested reader is referred to (Okamoto, et al. 1999) and (Veitch, et al. 1999).

6.2.3 δM Studies

Interaction effects have been studied using the δM technique. As discussed in §2.6.2.4, the δM curve is determined from a comparison of the two principal remanence curves. A plot of δM(H) shows the effective magnitude of the interactions at various fields as the magnetisation reversal occurs (Kelly, et al. 1989), which is shown for all samples in figure 6.4.

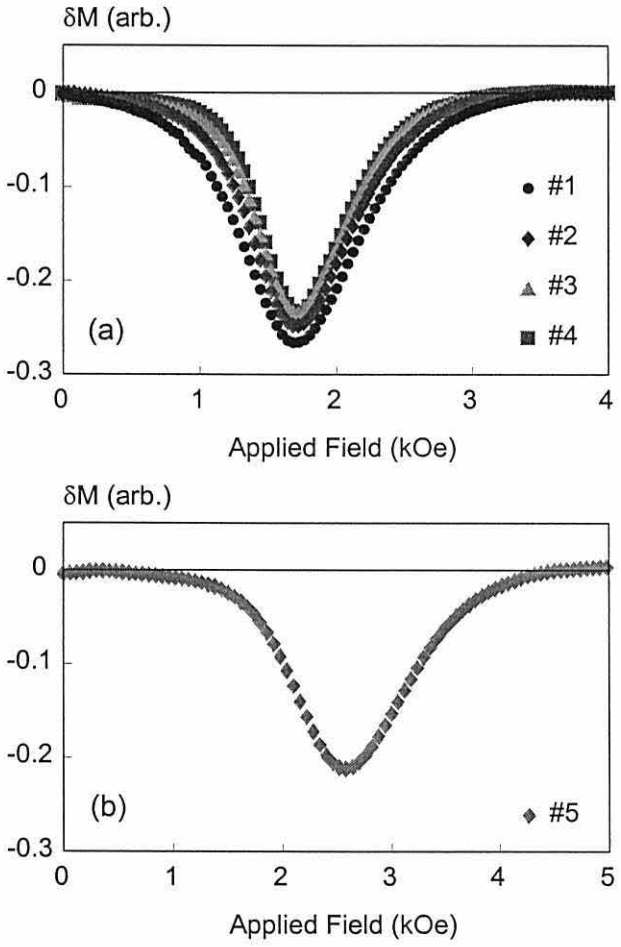

Figure 6.4 Comparison of δM curves for all tape samples.

As with all acicular particulate systems, a negative δM parameter is observed over the entire field range, indicating that the interactions serve to favour the demagnetised state (O'Grady, et al. 1992). From figure 6.4(a), it is clear that the level of

interaction decreases with particle orientation. Physically, the local magnetic field from dipolar interactions between the more aligned particles tends to hinder magnetisation reversal (Bottoni, et al. 1992).

Dipolar coupling occurs in all particulate media as a result of the demagnetising field from one particle influencing the environment of the other particles, as outlined in §2.5.6. The demagnetising effect of dipolar interactions tends to lead to flux closure configurations, thereby stabilising the demagnetised state, with the vast majority of particles reversed in lower than expected fields (Spratt, et al. 1988). Similarly, the results presented here are in agreement with simulations of fine particles using a Monte Carlo approach (el-Hilo, et al. 1996) and (Chantrell, et al. 1996). These workers found that dipolar interactions tend to decrease both the coercivity and remanence, and increase the temperature above which the magnetisation will become superparamagnetic.

6.2.4 Time Dependence Studies

Measurements of the time dependence of magnetisation were made using the method detailed by (Stoner and Wohlfarth 1948) and interpreted according to the framework of (Gaunt 1986). Specifically, data is obtained in the second and third quadrants of the hysteresis loop by first saturating the sample in first quadrant, and then applying a constant negative field to the sample. For all five samples with a wide distribution of energy barriers, a quasi linear variation of magnetisation with ln(t) was observed, as shown in figure 6.5 for sample #1.

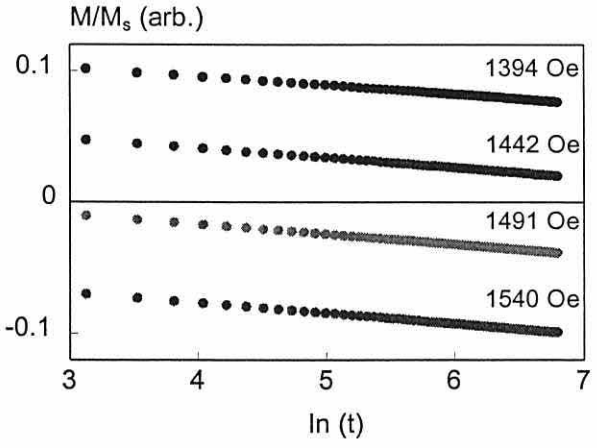

Figure 6.5 Variation of magnetisation with time at fields around the coercivity.

Using the procedure described in §2.5.2, the fluctuation field H_f and activation volume υ of all five samples are shown in figure 6.6. The activation volume describes the volume of magnetic material which reverses coherently, and was calculated using a saturation magnetisation M_s = 1500 emu cm^{-3} which is consistent with the thin oxide layer present (Morales, et al. 1998).

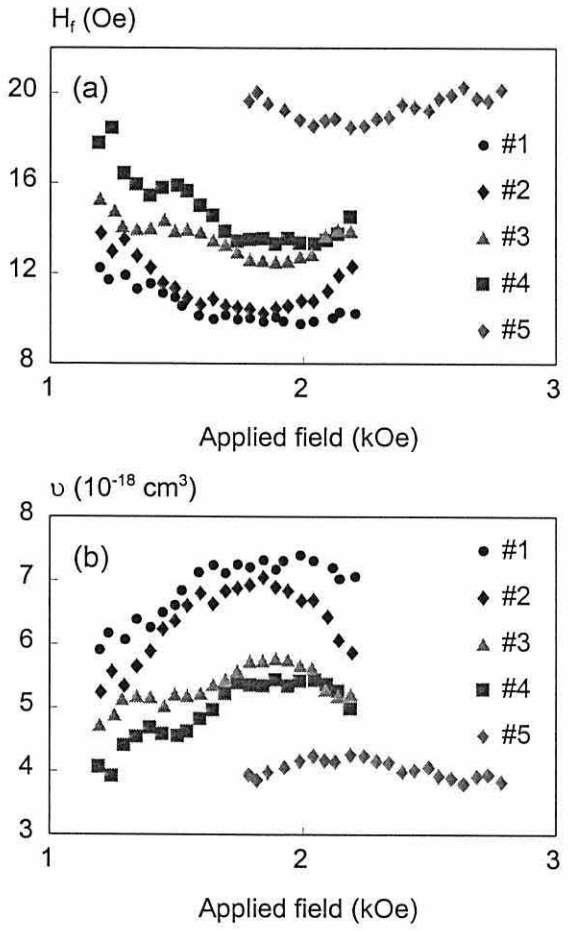

Figure 6.6 (a) Fluctuation fields and (b) activation volumes for all samples.

From figure 6.6(a), it is evident that for each sample the fluctuation field exhibits a broad minimum around the coercivity, in agreement with previous studies of particulate media (de Witte, et al. 1993). As the fluctuation field represents the effects of thermal energy on the magnetisation of the sample (Néel 1951), it appears that increasingly aligned media are more susceptible to the effects of thermal activation. This is in agreement with similar studies of γ-Fe_2O_3 recording media (Uren, et al. 1989). These workers suggested that since time dependence effects are related to the distribution of

energy barriers in the system, it follows that they are related in some way to the irreversible susceptibility and hence the magnetic viscosity.

Figure 6.6(b) shows the measured activation volumes at fields around the coercivity. For the four tape samples prepared from the same magnetic pigment, the data indicates that increasing the degree of particle orientation essentially reduces the activation volume. From comparison with TEM images, the activation volume is between 3 and 4 times smaller than the physical volume. This would indicate the existence of about 3 to 4 crystallites per particle, with magnetisation reversal occurring through incoherent rotation. The apparent decrease in activation volume with orientation may be due to changing dipolar interactions between aligned particles (Morales, et al. 1995), as discussed in §6.2.3.

Interestingly, sample #5 has an activation volume which is only marginally smaller than that determined for samples #1 through #4. Furthermore, the measured activation volume is comparable to the physical particle volume obtained from TEM analysis, which suggests that reversal is achieved through a somewhat more coherent mechanism, i.e. a single domain particle. In essence, although produced from distinctly different sized pigments, the tape samples under investigation do appear to consist of sub-crystallites of similar volume. Empirically, (Veitch, et al. 1994) found that thermal activation was related to the size of the crystallographic sub-units within the particle. Consequently, very small particles can be less susceptible to thermal effects than larger ones (Stinnett, et al. 1998), as investigated in the remaining sections of this chapter. The parameters obtained from time dependence studies are summarised in table 6.3.

Sample	#1	#2	#3	#4	#5
H_f (Oe)	10.0	10.5	12.5	13.4	18.9
υ (10^{-18} cm^3)	7.2	6.9	5.8	5.4	4.2
V_{phys} (10^{-18} cm^3)[a]	22.1	22.1	22.1	22.1	4.4
V_{phys}/υ	3.0	3.2	3.8	4.1	1.1

[a] Calculated from TEM images

Table 6.3 Parameters obtained from time dependence measurements.

6.3 Low Frequency Sweep-rate Measurements

At any finite temperature, an irreversible change in magnetisation occurs when an applied field reduces the effective height of an energy barrier under the assistance of

thermal energy, as discussed in §2.5.2. Therefore, magnetisation reversal depends not only on the strength of the magnetic field, but also the length of time the field is applied (Sharrock, et al. 1981). One further manifestation of time dependence in recording media is the sweep-rate dependence of coercivity (el-Hilo, et al. 1992), where the coercivity relevant to the writing process, which takes place on nanosecond timescales, may be considerably higher than that required for archival storage, where stability is required for years. The measurements presented in this section are performed as DCD curves which closely resemble the digital recording process, and it is assumed that the remanent coercivity behaves in a similar manner to the coercivity (He, et al. 1995).

The variation in remanent coercivity with sweep-rate was measured initially using the AGFM, as detailed in §6.3.1. It was ensured that the field step between magnetisation measurements was constant for all sweep-rates. Furthermore, the time constant was kept as short as possible, which provides a quasi continuous field sweep (O'Grady, et al. 1993). Measurements over microsecond timescales were performed using the pulsed field magnetometer described in §3 which is capable of generating field pulses up to 4.7kOe, with variable widths between 25μs to 130μs.

6.3.1 Alternating Gradient Force Magnetometer Results

The variation in remanent coercivity with sweep-rate R for samples #1 and #4 is shown in figure 6.7. The measurements were performed as DC demagnetisation (DCD) curves over a wide range of sweep-rates using a PMC MicroMag™ 2900 alternating gradient force magnetometer. As discussed in §6.3, it was ensured that the field step between magnetisation measurements was kept constant at 10 Oe, along with the minimal setting of the time constant at 10ms in order to secure a near continuous field sweep.

Figure 6.7 indicates how magnetisation reversal proceeds at relatively slow field sweeps. Clearly, the remanent coercivity increases as a function of sweep-rate, as reversal depends not only on the strength of the magnetic field, but also the length of time the field is applied (Néel 1949), as detailed in §2.5.2. Furthermore, it is clear that the most aligned sample #4 exhibits a significant rate of increase in remanent coercivity. Assuming that the remanent coercivity behaves logarithmically over these limited timescales (Oseroff, et al. 1987), sample #1 shows a remanent coercivity increase of almost 0.75% per decade, whereas sample #4 exhibits an increase in remanent

coercivity of over 0.95% per decade. Consequently, it appears that increasingly textured media are more susceptible to the effects of thermal agitation, in agreement with the results presented in §6.2.4.

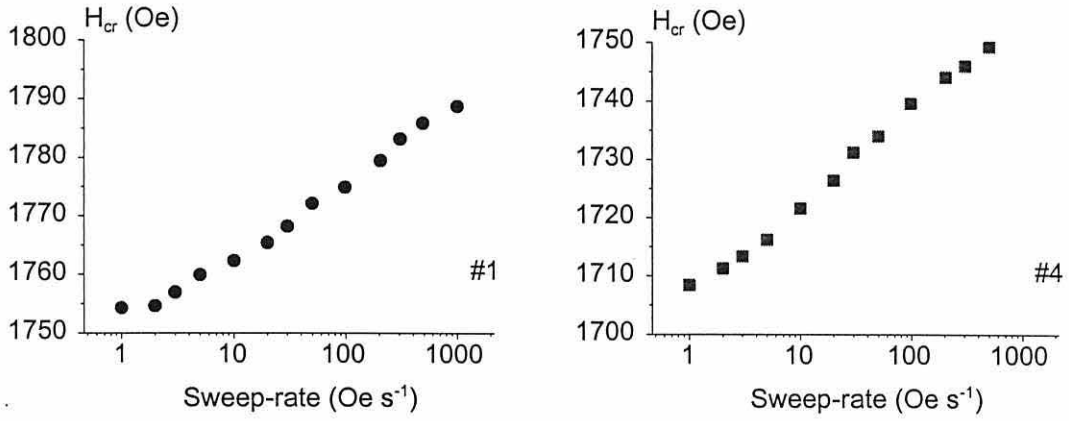

Figure 6.7 Measured variation in remanent coercivity as a function of sweep-rate.

Using the theory developed by (el-Hilo, et al. 1992) and (de Witte, et al. 1993), the value of the mean anisotropy field H_K may be estimated from figure 6.7. This approach is particularly useful, as the remanent coercivity at infinite frequency approaches that of the anisotropy field (Néel 1949), and provides an estimate of the head field required to write high frequency transitions on the samples.

The sweep-rate dependence of the remanent coercivity may be expressed as a logarithmic power series, as described in equation 6.1 (el-Hilo, et al. 1992). This relation is obtained from the expansion of equation 2.43, as outlined in §2.5.4. The resultant variation in remanent coercivity involves errors of less than 2% for values of sweep-rate up to 10^6 Oe s^{-1}, such that

$$H_c(R) = A_0 + A_1 \ln(R / R_0) + A_2 \left[\ln(R / R_0)^2\right] + \ldots \tag{6.1}$$

where R_0 is the initial value of the sweep-rate. The constants A_0, A_1 and A_2 are given by

$$A_0 = \left[1 - \sqrt{\ln(C) / \alpha_m}\right] H_K \tag{6.2}$$

$$A_1 = H_K / 2\sqrt{\alpha_m \ln(C)} \tag{6.3}$$

$$A_2 = H_K / 8\sqrt{\alpha_m}\left[\ln(C)\right]^{3/2} \tag{6.4}$$

where $\alpha_m = K_u V_m/kT$ and $C = f_0 H_K/2\alpha_m R_0$. Figure 6.8 shows the measured variation in remanent coercivity for samples #1 and #4 fitted with a second order polynomial of the form given in equation 6.1. Using expressions for A_0 and A_1, the value of the anisotropy field may be determined from

$$H_K = A_0 + 2A_1 \ln\left(\left[\frac{kT}{2\pi M_s V_m}\right]^{1/2} \frac{\gamma_0}{R_0} H_K^{3/2}\right) \tag{6.5}$$

where the gyromagnetic ratio γ_0 is -1.76×10^7 s^{-1} Oe^{-1}. Equation 6.5 contains only two unknowns: the median particle volume and the saturation magnetisation. However, in order to optimise the fit, the median particle volume may be substituted by the activation volume υ (de Witte, et al. 1993), as detailed in §6.2.4. Specific coefficients involved in the calculation of the anisotropy field are included in table 6.4.

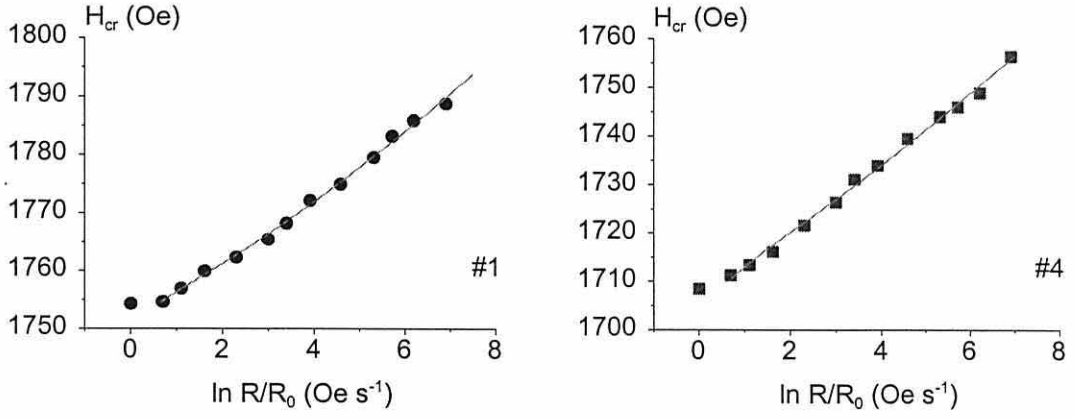

Figure 6.8 Calculated variation in remanent coercivity as a function of sweep-rate.

Parameter	M_r/M_s	M_s (emu cm^{-3})	υ (10^{-18}cm^3)	A_0 (Oe)	A_1 (Oe)	H_K (Oe)
#1	0.70	1500	7.2	1756.3	2.79	1910
#4	0.88	1500	5.4	1712.9	5.53	2020

Table 6.4 Characterisation and fitting parameters for samples #1 and #4.

Table 6.4 indicates that the calculated effective anisotropy field H_K for the more aligned sample #4 is notably higher than for sample #1, in agreement with Stoner-Wohlfarth theory of uniaxial single domain particles, as described in §2.4.1. Consequently, using a similar approach to (Sharrock, et al. 1981), the sweep-rate dependence of the remanent coercivity may be used to predict the head field required to write high frequency transitions on media. Clearly, whilst it may not be entirely appropriate to infer high speed properties from these measurements, this technique provides a useful estimate with which to compare measurements over short timescales. Additionally, it is not affected by the uncertainties involved in comparing pulsed and swept measurement systems.

Interestingly, the values of H_K are somewhat below that expected from the closure point of the hysteresis loop, but are probably an effective average for the system which contains a relatively wide distribution of switching fields arising from either the distribution of the anisotropy constant or more likely the distribution of sub-crystallites (Morales, et al. 1999). This is confirmed in a recent experimental study of anisotropy field distributions in a similar series of progressively aligned metal particle tape samples (Jones, et al. 2000), as included in Appendix A.

6.3.2 Dispersion Pulsed Field Magnetometer Results

In order to study switching characteristics over a wide range of frequencies, pulsed field measurements were performed using the solenoid-based magnetometer developed to monitor the reversal processes of metal particle dispersions (Prichard, et al. 1998). As discussed in §3, this instrument is capable of generating field pulses up to 4.7kOe, with variable widths between 25μs and 130μs. A typical 40μs duration pulsed field with a magnitude of over 2.1kOe is shown in figure 6.9. In assigning an appropriate sweep-rate to the pulse, a triangular pulse shape is assumed with a constant slope both rising and falling, similar to that described by (Shimatsu, et al. 1999). To illustrate, the sweep-rate of the field pulse displayed in figure 6.9 is approximately 0.85×10^8 Oe s^{-1}. Intriguingly, measurements over microsecond timescales, which are somewhere between those available from a hysteresis loop tracer and those observed during the writing process, are distinctly different from those timescales arising through standard measurements or archival storage, as indicated schematically in figure 2.10.

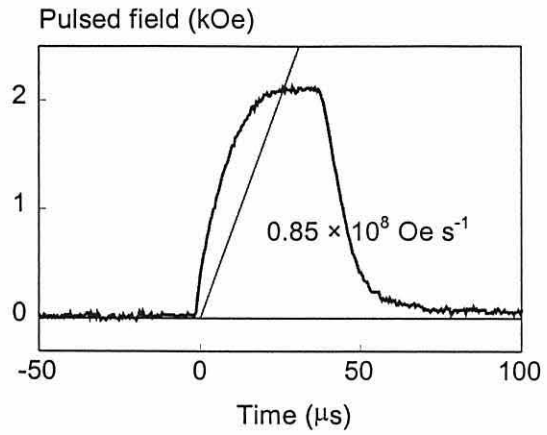

Figure 6.9 Typical magnetic field pulse obtained from the dispersion magnetometer, together with its corresponding sweep-rate.

Accordingly, whilst it may not be entirely appropriate to compare pulsed and swept measurement systems, novel characterisation techniques are essential to optimise future head and media design, as recently highlighted in studies of FePt thin films over similar timescales (Shimatsu, et al. 1999). Figure 6.10 shows the measured variation in remanent coercivity with sweep-rate for samples #1 and #4, including additional pulsed fields of 40μs and 100μs duration. As a guide to the eye, the data is fitted with a simple second order polynomial.

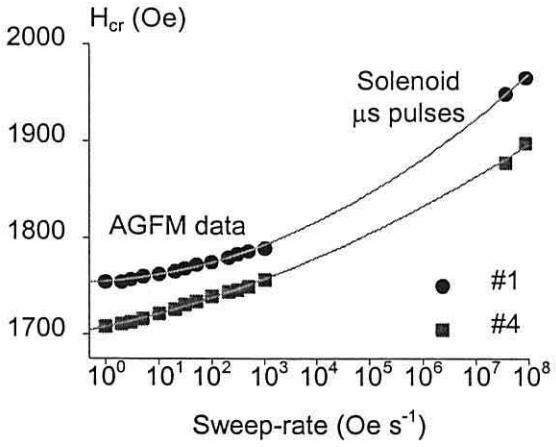

Figure 6.10 Measured variation in remanent coercivity as a function of sweep-rate.

Figure 6.10 indicates how magnetisation reversal proceeds as the field sweep increases. As suggested in §6.3.1, the most aligned sample #4 displays a much steeper variation in remanent coercivity over longer timescales. The implications of this are

that transitions written on increasingly textured systems are more likely to suffer thermal demagnetisation, which promotes conflicting requirements in terms of recording performance (Bertram 1986) and media durability (Okamoto, et al. 1999). Of course, over these timescales the mechanism of thermally activated switching is effectively described using the Arrhenius-Néel formulation, as given in equation 2.25.

In this classic study, (Néel 1949) proposed that thermal fluctuations can assist an external field to overcome an anisotropic energy barrier. Accordingly, in a system of uniaxial single domain particles, increasing the degree of texture is found to increase both the mean effective anisotropy field (Stoner and Wohlfarth 1948) and anisotropy constant (Luborsky 1961), as outlined in §2.3.1. However, the results presented in §6.2.4 indicate that the effective sub-crystallite volume is significantly reduced as the particle orientation increases, and, since both the anisotropy constant and switching volume occur in the exponent of equation 2.25, these parameters strongly influence the switching process.

Referring again to figure 6.10, it is apparent that the poorly aligned sample #1 displays a steeper variation in remanent coercivity as the field sweep increases. This is a somewhat surprising observation, as the results obtained from both conventional time dependence studies (§6.2.4) and relatively slow field sweeps (§6.3.1) indicate that, over these timescales, it is increasingly textured media which are more susceptible to the effects of thermal agitation. This may be explained, at least in part, by considering the switching behaviour of an interacting uniaxial dipole pair, which forms the simplest possible micromagnetic system (Bertram, et al. 1970). This system was further extended by (Lyberatos, et al. 1993) to simulate the effect of thermal agitation on the mode of magnetisation reversal.

In terms of these simulations, it is interesting to consider the case in which the bond angle between the particles is parallel to the applied field, with the easy axes oriented in the same direction. In the absence of thermal agitation, the symmetric fanning mode of reversal does not occur, as essentially there is zero torque acting on the magnetic moments. Consequently, the moments always reverse simultaneously to a parallel state. The introduction of thermal fluctuations in a weakly interacting system tends to break the symmetry of the arrangement, which leads to nucleation of the

fanning mode at the correct field. Therefore, the concept of thermal activation may be seen as being an intrinsic part of the reversal process (Chantrell, et al. 1998).

In terms of magnetic recording, the effect of thermal activation on the relaxation time τ of an interacting system is significant. As discussed in §2.5.2, the relaxation time of reversal may be defined as the average switching time as given by the Arrhenius-Néel law in equation 2.25. By substituting a value for the energy barrier into equation 2.25, (Lyberatos, et al. 1993) calculated relaxation times in order to obtain an estimate of the attempt frequency f_0. In agreement with (Brown 1963), the attempt frequency was found to increase for low values of temperature and reverse field. However, a strong dependence of the attempt frequency on the level of interaction was also observed. Specifically, an increase in dipolar interaction results in a reduction of the attempt frequency, and a consequent increase in the relaxation time. The implications of this, extended to magnetic recording, are that a larger increase in coercivity with frequency would be observed than is predicted from the Arrhenius-Néel formalism. Therefore, this is consistent with the results presented in figures 6.4(a) and 6.10, from which it is clear that the effects of the interaction, i.e. less flux closure, decreases with particle orientation, and a steeper variation in remanent coercivity is measured as the field sweep increases.

6.4 Nanosecond Pulsed Field Studies

The characterisation of advanced particulate materials to find their switching limits is of fundamental scientific and commercial interest. In recent years, the need for both higher storage densities and data transfer rates has led to the development of metal particle pigment formulations with a small physical size, where thermal activation is significant. For example, a modern tape drive running at $20ms^{-1}$ and recording $4kfcmm^{-1}$ would have a bit length of around 15ns and a write head flux rise time of 6ns, whilst the internal demagnetising fields act over the duration of the desired storage, which may be several years. Conventional laboratory methods cannot easily investigate switching behaviour over this extended timescale, although in recent years pulsed field measurements have begun to probe nanosecond reversal (Doyle, et al. 1993) (Hancock, et al. 1996). With future recording systems requiring data to be written at near nanosecond duration, this

raises an interesting question: how fast can the magnetisation in magnetic recording media be switched?

Recent attempts to answer this question have been made using picosecond pulsed field studies (Back, et al. 1998) (Back, et al. 1999). Generating field pulses using finely focused relativistic electron bunches at the Stanford Linear Accelerator Center, these workers found that ultrafast magnetic field pulses as short as 2ps were able to reverse the magnetisation of CoPt thin films. Applying the pulsed field perpendicular to the magnetisation exerts maximum torque on the spins, and reversal can be triggered in fields as low as 2.3kOe. Of course over these extremely short timescales, the behaviour of the moments is governed by the dynamics of the atomic spins, which is described by the Landau-Lifshitz-Gilbert gyromagnetic equation, as outlined in §2.5.5. The magnetic information was imaged using spin-resolved scanning electron microscopy (Allenspach 1994).

Further techniques such as optical pump-probe spectroscopy have been used to observe picosecond timescale spin dynamics in ferromagnetic thin films (Freeman 1994). Using this approach, an optically triggered transient magnetic field is propagated past the sample under study, perturbing the spin system, with the subsequent evolution of the spin system monitored through its interaction with a time delayed optical probe beam. The non-resonant nature of this experimental technique allows parameters such as the damping factor α_d to be determined accurately (Hicken, et al. 1999).

As a precursor to recent studies of nanosecond magnetisation reversal in recording media, the speed limited performance of magnetic tapes has been reported as early as 1974 (Thornley, et al. 1974). In this investigation, a series of commercial tapes were studied using a continuous microstrip recording system, in which a DC erased tape was passed under a microstrip line in order to rapidly switch the magnetisation. The effect of the field pulse duration was then measured with a read head to give an estimate of the switching time (Thornley 1975). Subsequent pulsed field investigations have been performed on a wide range of particulate recording media (Doyle, et al. 1993) (He, et al. 1996) (Hancock, et al. 1996) (Stinnett, et al. 1998a) and publications derived from this study (Prichard, et al. 1999a) (Prichard, et al. 1999b) included in Appendix A. However, in recent years, the emphasis of these microstrip line studies has shifted to thin film media (Stinnett, et al. 1998b) (Doyle, et al. 1998), where a current trend of

40% annual growth in data transfer rates prevails, and sub-nanosecond recording may be required in two to three years (Klaassen, et al. 1998).

Very recently, spinstand measurements of the time dependence of the remanent coercivity have been reported (Richter, et al. 1998). The basis for this measurement technique involves using the reverse DC erased noise as an indicator for the remanent coercivity (Bertram, et al. 1986). Specifically, after saturating a band of tracks in one direction, an increasing DC field is then applied in the reverse direction. As this reverse field is increased, the broadband medium noise exhibits a broad maximum around the remanent coercivity. Pulse duration may be varied by altering the linear velocity and gap length, or by subjecting the recording medium to many such field pulses rather than just one. As outlined by (el-Hilo, et al. 1993) (Lewis, et al. 1993), this 'reptation' process can be traced directly to magnetic viscosity. Using this approach, experimental data has been obtained over timescales close to the actual writing process, down to 5ns, in order to analyse the stability of recorded transitions (Richter, et al. 1999). For further developments concerning spinstand measurements and thermal stability, the interested reader is referred to an excellent review by (Weller, et al. 1999).

6.4.1 Mercury Wetted Relay Measurements

High speed switching measurements were initially performed using a charged 50Ω coaxial line connected to a mercury wetted relay and microstrip line. This instrument is capable of producing extremely well-defined single-shot voltage pulses in excess of 1kV with pulse widths between 0.7ns and 250ns, having rise times of less than 500ps. Termination of the voltage pulse in the 50Ω microstrip line allows pulsed fields of up to 450 Oe to be generated. Consequently, in order to allow measurements to be achieved over a full switching range, a DC bias field is used to assist the pulsed field. Details of this instrument have been described by (Hancock, et al. 1997), and outlined in §5.3.

Pulsed field measurements are performed as DC demagnetisation (DCD) curves which closely resemble the digital recording process, and are similar to those described by (Doyle, et al. 1993). The sample is initially saturated positively in the coating direction of the tape with a field of 5kOe in a PAR 155 vibrating sample magnetometer, before being subject to a DC bias and pulsed field in the opposite direction. The tape is then returned to the VSM, and the remanent magnetisation M_d measured. To complete

the measurement, the sample is saturated with a field of 5kOe in the negative direction, so that the change in magnetisation can be determined. The magnitude of the opposing pulsed and biased field are repeatedly increased to create a DCD curve. The remanent coercivity H_{cr} is then defined as the field required to reduce the remanent magnetisation to zero, as discussed in §2.6.2.2.

Figure 6.11(a) shows a series of pulsed DC demagnetisation curves obtained for the poorly aligned sample #1. The measurements were performed for pulse widths of 1.8ns, 5.8ns and 10.9ns duration. The quasi-DC measurement was achieved by retaining the sample in the reversed DC bias field for a period of 5s, before measuring the remanent magnetisation M_d. The effect of sweep-rate on the remanent coercivity is clearly demonstrated as the pulsed curves are shifted to the right of the DC response. This effect is particularly marked for the 1.8ns pulse. The corresponding switching field distributions (SFD) are shown in figure 6.11(b), which are calculated from the differential (dM_d/dH) of the DCD curve, as described in §2.6.2.3. It is evident that the peak of the differential decreases as the pulse width is reduced. An observed broadening of the SFD is also noted, the full width at half maximum of which has been found to increase with decreasing pulse width, in agreement with (He, et al. 1996).

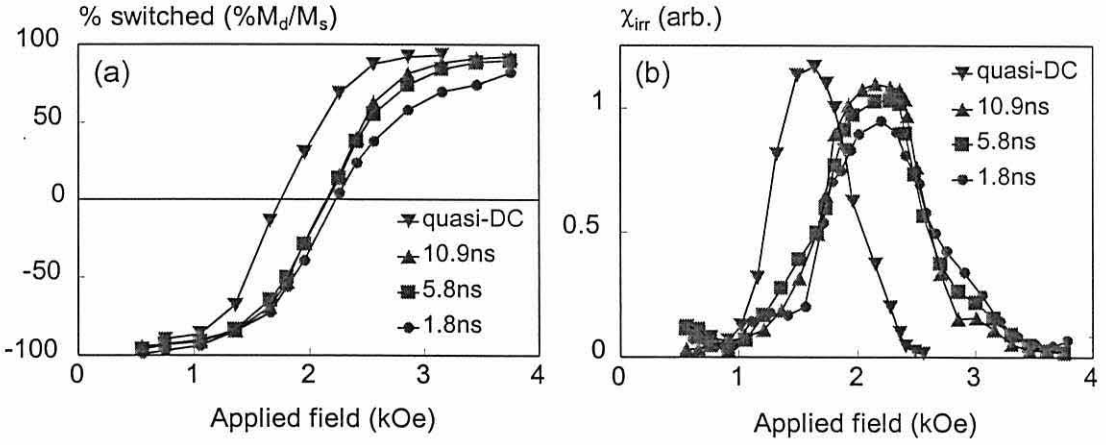

Figure 6.11 (a) Pulsed DC demagnetisation curves measured using the mercury wetted relay, together with their appropriate (b) switching field distributions.

The implications of figures 6.11(a) and 6.11(b) are that, as well as the larger head field required to write at higher frequencies, the output signal recovered from the tape is also reduced. This observation may be explained in terms of the model proposed

by (Néel 1951), which suggests that the effect of thermal agitation can be characterised by an internal fluctuation field H_f, as discussed in §2.5.2.1. For an assembly of identical uniaxial particles, it is straightforward to show that (Gaunt 1986)

$$H_f = \frac{kT}{\upsilon M_s\left(1 - H / H_K\right)} \tag{6.6}$$

where υ is the activation volume (Wohlfarth 1984), as determined in §2.5.2.2. Clearly, equation 6.6 indicates that the fluctuation field is independent of time, which has been verified experimentally for γ-Fe_2O_3 media (Hancock, et al. 1996) and CrO_2 tape (Stinnett, et al. 1999). These workers found that over timescales greater than 10ns, the shape of the irreversible susceptibility curve does not change, although significant variations in remanent coercivity occur. However, for field pulses under 10ns, in the region where precessional dynamics of the atomic spins become important, a distinct broadening of the irreversible susceptibility curve is apparent, similar to that shown in figure 6.11(b). Therefore, this strongly suggests that the onset of gyromagnetic switching tends to increase the switching time of the high coercivity particles relative to those with a lower coercivity (Stinnett, et al. 1999).

Figure 6.12 shows the measured variation in remanent coercivity with sweep-rate for the smaller particle sample #5. These results indicate how magnetisation reversal proceeds over a wide range of field sweeps, and includes both AGFM and solenoid pulsed field data, which span some ten orders of magnitude. For the shortest pulse duration of 1.8ns, the remanent coercivity is increased to around 1.31 times the value of the DC level, as shown in table 6.5.

From table 6.5, it is clear that sample #5 experiences only a marginal increase in high speed remanent coercivity over the much larger sized pigment used to prepare samples #1 through #4. Although produced from distinctly different sized particles, the tape samples under investigation do appear to consist of crystallites of similar volume, as discussed in §6.2.4. Empirically, (Veitch, et al. 1994) found that thermally activated reversal is better explained in terms of the activation volume as opposed to the physical particle volume. Consequently, very small particles can be less susceptible to the

effects of thermal activation than larger ones (Stinnett, et al. 1998), similar to that observed in table 6.5.

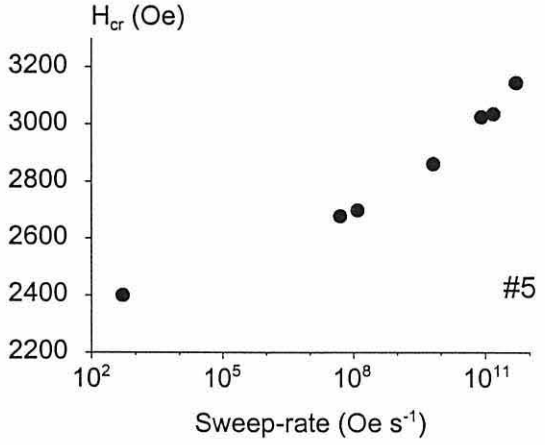

Figure 6.12 Measured variation in remanent coercivity as a function of sweep-rate.

Sample	#1	#2	#3	#4	#5
H_c (kOe)[a]	1.55	1.60	1.64	1.66	2.29
υ (10^{-18} cm^3)[b]	7.2	6.9	5.8	5.4	4.2
H_{cr}(1.8ns)/H_{cr}(5s)	1.30	1.15	1.26	1.29	1.31
H_{cr}(10.9ns)/H_{cr}(5s)	1.24	1.18	1.23	1.21	1.26

[a] Measured at a sweep-rate of 511 Oe s^{-1} [b] §6.2.4

Table 6.5 Parameters obtained from mercury wetted relay measurements.

Unfortunately, no correlation between particle orientation and the high speed switching properties was identified, although this is subject to further investigation in §6.4.2. Furthermore, in order to relate high frequency recording properties to archival storage stability, the experimental results reported in this section are compared with recent models of magnetisation reversal (Sharrock, et al. 1981) (el-Hilo, et al. 1992), as described in §6.5.

6.4.2 Spark Gap Switch Measurements

Although useful information regarding the high speed properties of metal particle media was revealed by the results presented in §6.4.1 and (Prichard, et al. 1999a), the field produced by the mercury wetted relay was not of sufficient magnitude to switch all of the particles, and consequently a DC bias field supplied from an electromagnet was used

to assist the pulsed field. Although the magnitude of the DC bias has been found to be negligible (He, et al. 1996), the samples were further investigated using the pulse generator which is based around a pressurised nitrogen spark gap switch. Pulsed magnetic fields of up to 1.8kOe can be produced having widths between 7ns and 56ns. Details of this instrument have been described by (Prichard 1999), and outlined in §5.4.

Figure 6.13 shows a series of pulsed DC demagnetisation curves obtained for the set of four tape samples prepared from the same magnetic pigment. In order to enhance the sensitivity of the measurement, the effect of the field pulse was determined using a PMC MicroMag™ 2900 alternating gradient force magnetometer, which has revealed a correlation between particle orientation and high speed switching properties. As expected, substantial increases in remanent coercivity are observed as the pulse width decreases. Furthermore, it is evident that for the shortest pulse duration of 7ns, the remanent coercivity is found to increase with orientation for all four samples, as indicated in table 6.6. Indeed, the most aligned sample #4 exhibits a very large rate of increase in remanent coercivity at the shortest pulse widths. The implications of this are that larger head fields are required to write high frequency transitions on more aligned media. This is in agreement with recent spinstand measurements (Richter, et al. 1999) and simulations (Hannay, et al. 1999) of increasingly textured thin film media. Likewise, very recent simulations of advanced metal particle media have revealed a rapid increase in dynamic coercivity in the nanosecond regime, which is made steeper both by increased orientation and dipolar interactions (Coverdale, et al. 2000).

The origin of this dramatic rate of increase in remanent coercivity with increasing particle alignment is complex, and is subject to further investigation in §6.5. Clearly, for timescales greater than a few nanoseconds, the mechanism of thermally activated switching is effectively described using the Arrhenius-Néel formulation. For relatively slow field sweeps, the results presented in §6.3.1 indicate that increasing the degree of particle alignment effectively diminishes the height of the energy barrier since the activation volume is reduced through decreasing interactions. This results in reducing both the switching time and the field at which reversal proceeds, similar to that observed in figure 6.7. As field sweep increases, the results presented in §6.3.2 suggest that the inverse is observed. Specifically, decreasing the degree of particle orientation tends to increase the level of stable configurations, which results in a reduction of the

attempt frequency, and a consequent increase in relaxation time (Lyberatos, et al. 1993). The implications of this, over these timescales, are that a larger increase in coercivity with frequency would be observed than is predicted from the Arrhenius-Néel law, similar to that shown in figure 6.10.

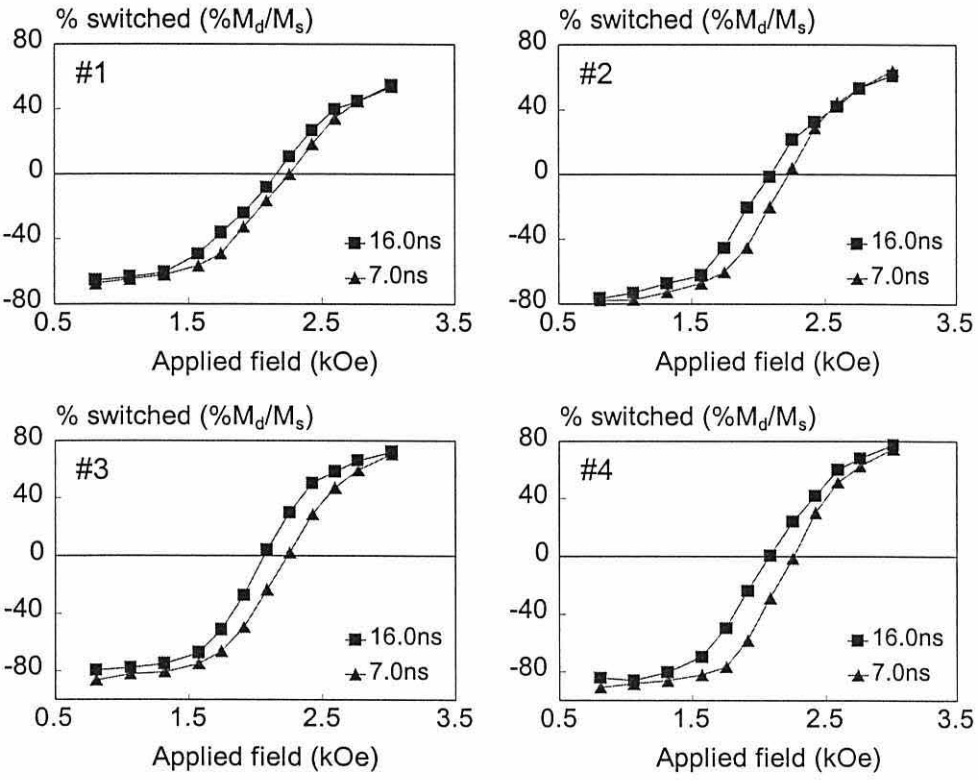

Figure 6.13 Pulsed DC demagnetisation curves obtained for samples #1 through #4.

Sample	#1	#2	#3	#4	#5
H_c (kOe)[a]	1.55	1.60	1.64	1.66	2.29
M_r/M_s[ab]	0.70	0.77	0.83	0.88	0.86
H_{cr}(7.0ns)/H_{cr}(5s)	1.22	1.20	1.19	1.20	1.19
H_{cr}(16.0ns)/H_{cr}(5s)	1.27	1.28	1.29	1.30	1.29

[a] Measured at a sweep-rate of 511 Oe s^{-1} [b] §6.2.1 M_s = M at 10kOe

Table 6.6 Parameters obtained from nitrogen spark gap switch measurements.

However, as the timescale of the reversal process approach the nanosecond time regime, it is well known that phenomena influenced by gyromagnetic effects, in addition to thermal ones, become significant (Doyle, et al. 1993). The same mechanisms which allow the magnetisation to dissipate energy through the lattice, also allow the thermal energy in the lattice to couple to the magnetisation and raise its energy. Consequently, when changes in magnetic energy are relatively slow or the

activation volume is small, thermally activated reversal will dominate. However, when the magnetic energy changes are relatively fast or the sub-crystallite volume is large, gyromagnetic switching tends to dominate (He, et al. 1996). Additionally, studies by (Yu, et al. 1994) have suggested that the reversal mechanism in acicular particles becomes more coherent at the onset of gyromagnetic switching, which tends to increase both the switching time and the switching field of these high coercivity particles (Stinnett, et al. 1999). The implications of this, are that at nanosecond timescales, textured media exhibit a larger increase in coercivity than is predicted from the Arrhenius-Néel formalism, similar to that observed in figure 6.13. The correlation between particle orientation and high speed switching is discussed further in §6.5.

6.5 Theoretical Considerations

Coercivity measurements of recording media over short timescales have been reported as early as 1974 (Thornley, et al. 1974). However, these measurements are difficult to perform, which has led to the development of the thermal switching model of (Sharrock, et al. 1981). With this semi-empirical model, the coercivity may be measured over two appreciably different and convenient timescales, using standard techniques, to predict the coercivity over many orders of magnitude; an approach popularised by (Doyle, et al. 1998). The Arrhenius-Néel relaxation gives rise to a time variation of the coercivity $H_c(t)$ that may be described by Sharrock's Law, as outlined in §2.5.3, such that

$$H_c(t) = H_K\left(1-\left[\frac{kT}{K_u V}\ln\left(\frac{f_0 t}{0.693}\right)\right]^{1/2}\right) \tag{6.7}$$

where K_u is the anisotropy constant, V is the switching volume and the product kT is the thermal energy. The parameter f_0 is the attempt frequency which represents the number of fluctuations per second of the magnetisation vector around its mean position.

Furthermore, a micromagnetic model describing the time dependence of magnetisation in terms of the sweep-rate dependence of coercivity $H_c(R)$ was derived explicitly by (el-Hilo, et al. 1992), and may be written as equation 6.8. To obtain a good fit, the median particle volume V_m may be substituted by the activation volume υ.

$$H_c(R) = H_K\left(1-\left[\frac{kT}{K_u V_m}\ln\left(\frac{f_0 H_K kT}{2K_u V_m}\frac{1}{R}\right)\right]^{1/2}\right) \tag{6.8}$$

This variation which depends on physical parameters, produces a well-defined behaviour of coercivity with sweep-rate. In a similar approach to that described in equation 6.7, fitting the relation to experimental data may be used to accurately determine parameters such as the mean anisotropy field, anisotropy constant and switching volume.

6.5.1 Thermal Switching Model

The variation in high speed remanent coercivity for the smaller particle sample #5, shown in figure 6.12, was fitted to the thermal switching model described by equation 6.7. Clearly, the advantage of this approach which defines a time variation of coercivity, obviates any uncertainties which may arise in assigning a pulse width to an appropriate sweep-rate, as shown in figure 6.14.

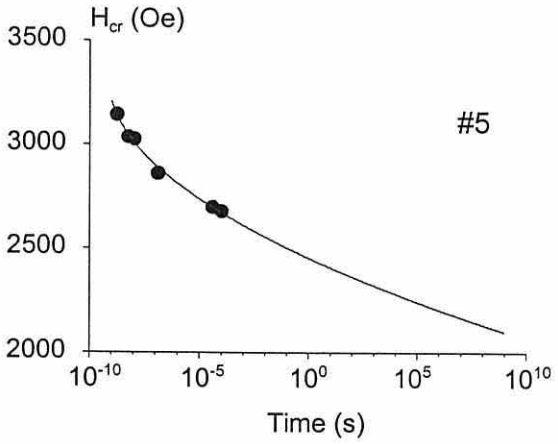

Figure 6.14 Predicted time variation in remanent coercivity for sample #5.

Figure 6.14 demonstrates the effectiveness of this model, as equation 6.7 is used together with pulsed field measurements to predict the coercivity of the sample over some eighteen orders of magnitude. The predicted values of remanent coercivity are in excellent agreement with the experimental high speed measurements, with the switching volume V substituted in this study by the measured activation volume υ, which was

found to be 4.2×10^{-18} cm^3. Other parameters obtained from the fit to the data include the anisotropy field H_K = 3320 Oe, and anisotropy constant $K_u = 2.96 \times 10^6$ erg cm^{-3}. These values give a resulting value for the saturation magnetisation M_s ($H_K = 1.8K_u/M_s$) of 1600 emu cm^{-3}, which is consistent with the thin oxide layer present and manufacturers data (Morales, et al. 1998), as included in Appendix A. The value of the attempt frequency was set at 10^9Hz, following the studies of (Brown 1959).

Although archival storage stability will be further addressed in §6.5.4, it is interesting to note that figure 6.14 predicts a 10ns writing coercivity of 3010 Oe and a 10 year storage coercivity (3×10^8s) of 2130 Oe. Obviously, the storage coercivity must be of sufficient magnitude to provide long-term stability against transition broadening or other forms of signal degradation (Sharrock 1990), and may be characterised by the thermal stability factor K_uV/kT. Using the fit to the experimental data obtained from equation 6.7, the value obtained for sample #5, with an average particle length of only 65nm, was 304. Setting a stability criterion of 100 for this factor (Sharrock 1994) would suggest that particle volumes could be reduced by 1/3 if the values of K_u and H_K were maintained. Of course, this would necessitate significant improvements in crystallinity, but does imply that further advances can be made in pigment technology before the thermal limit to data density is approached. Incidentally, the volume of these particles would not be significantly larger than volumes predicted for unstable superparamagnetic behaviour in iron particles; 1.0×10^{-18} cm^3 (Bean, et al. 1959).

Figure 6.15 shows the variation in high speed remanent coercivity for tape samples #1 and #4, fitted to equation 6.7. As discussed in §6.4.2, it is evident that the most aligned sample #4 exhibits a very large rate of increase in remanent coercivity at the shortest pulse widths. The fit to the data was achieved using values of H_K = 2450 Oe and $K_u = 1.53 \times 10^6$ erg cm^{-3} for sample #1, together with $K_u = 1.57 \times 10^6$ erg cm^{-3} and H_K = 2460 Oe and for sample #4. However, it is clear from figure 6.15 that the fit to the experimental data is poor, markedly so for the most aligned sample #4.

The most probable explanation for the poor fit of Sharrock's Law to the high speed data of sample #4, is that increasingly textured media appear more likely to be influenced by gyromagnetic effects in the nanosecond regime, similar to that observed in figure 6.15. Furthermore, since equation 6.7 is based upon the mechanism of thermally activated reversal, the larger increase in remanent coercivity displayed by

sample #4 may be evidence of the breakdown of the Arrhenius-Néel formalism. However, despite uncertainties in assigning an appropriate sweep-rate to a pulse width, the el-Hilo micromagnetic model exhibits a much improved fit, as described in §6.5.2.

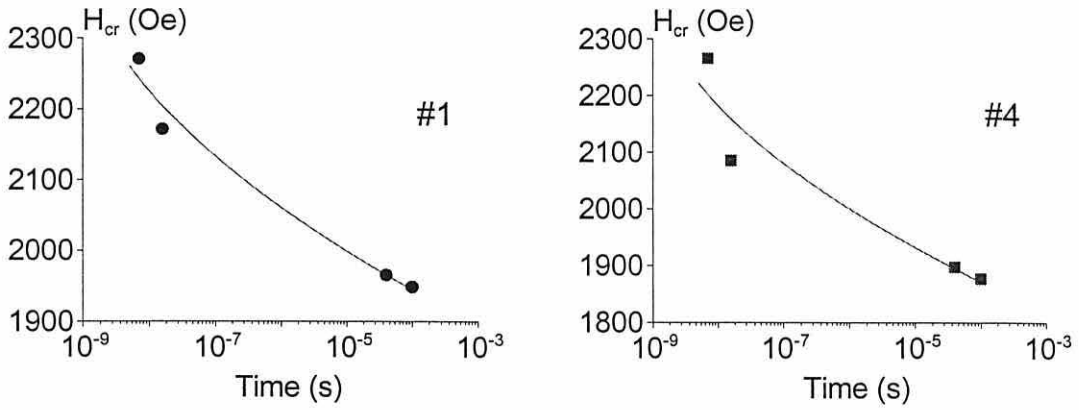

Figure 6.15 Predicted time variation in remanent coercivity for samples #1 and #4.

6.5.2 el-Hilo Model

In comparison with §6.5.1, the variation in high speed remanent coercivity for the smaller particle sample #5, was fitted to the el-Hilo model described by equation 6.8.

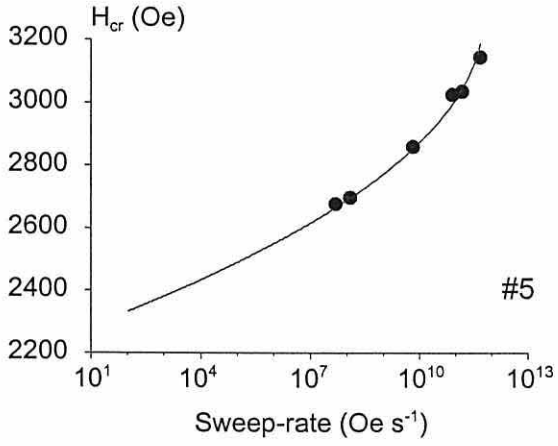

Figure 6.16 Predicted variation in remanent coercivity as a function of sweep-rate.

The predicted values of remanent coercivity are in excellent agreement with the experimental high speed measurements, with the median particle volume V_m substituted in this study by the activation volume. Parameters obtained from the fit to the data include H_K = 3270 Oe and $K_u = 2.64 \times 10^6$ erg cm^{-3}, using a value of 10^{11}Hz for the

attempt frequency. The resulting figure obtained for the thermal stability factor K_uV_m/kT is 271, which is in reasonable agreement with that predicted from Sharrock's Law. Furthermore, inasmuch as sample #5 is representative of advanced media, having an average particle length of only 65nm, the values obtained for the stability factor are consistent with other recent studies of particulate media (Suzuki 1999) (Sharrock 1999). The fitting parameters involved in the characterisation of sample #5 are summarised in table 6.7.

Coefficient	f_0 (Hz)	H_K (Oe)	K_u (10^6 erg cm^{-3})	K_uV/kT[cd]
Sharrock's Law[a]	10^9	3320	2.96	304
el-Hilo model[b]	10^{11}	3270	2.64	271

[a] §2.5.3 [b] §2.5.4 [c] Assuming $V = 4.2 \times 10^{-18}$ cm^3 [d] At room temperature

Table 6.7 Characterisation and fitting parameters for sample #5.

Table 6.7 indicates that the values of H_K are somewhat below that expected from the closure point of the hysteresis loop, as shown in figure 6.1, but are probably an effective average for the system which contains a relatively wide distribution of switching fields arising from either the distribution of the anisotropy constant or more likely the distribution of crystallographic sub-units within the particle (Morales, et al. 1999). This is confirmed in a recent experimental study of the determination of anisotropy field distributions in a similar series of progressively aligned metal particle tape samples (Jones, et al. 2000), as included in Appendix A.

To obtain an acceptable fit to the experimental data, large differences in attempt frequency are noted in table 6.7. This is possibly due to the uncertainties involved in comparing pulsed and swept measurement systems. Essentially, the attempt frequency represents the number of fluctuations per second of the magnetisation vector around its mean position, and lies in the range 10^9Hz (Brown 1959) to 10^{12}Hz (Gaunt 1986). Therefore, the attempt frequency determines the shortest times to which both models are applicable. For the data shown in figure 6.16, a triangular pulse shape is assumed with a constant sweep-rate both rising and falling, as shown schematically in figure 6.9. However, according to (Flanders and Sharrock 1987), the effective timescale of the measurement is related to the sweep-rate R through equation 6.9,

$$t = H_K\left[\ln\left(f_0 t\right)\right]^{1/2}\left(kT / K_u V\right) / R \tag{6.9}$$

which gives a sweep-rate which is roughly two orders of magnitude smaller than that obtained assuming a triangular pulse[1]. Clearly, the effect of shifting the sweep-rate to higher values also necessitates an appropriate increase in attempt frequency. However, results are often found to be relatively insensitive to the value chosen for the attempt frequency (Sharrock 1994), similar to that observed in table 6.7.

Figure 6.17 shows the measured variation in remanent coercivity with sweep-rate for samples #1 and #4, fitted with equation 6.8. As discussed in §6.4.2, it is apparent that the most aligned sample #4 exhibits a considerable rate of increase in remanent coercivity at the shortest pulse widths, which may be explained in terms of the transition to gyromagnetic switching (Doyle, et al. 1993).

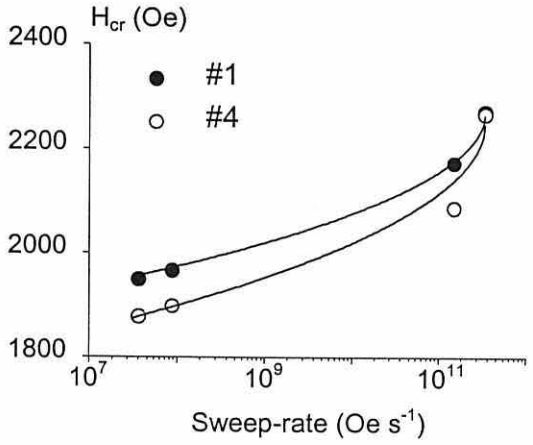

Figure 6.17 Predicted variation in remanent coercivity as a function of sweep-rate for tape samples #1 and #4.

The predicted values of remanent coercivity are in excellent agreement with the high speed measurements for the poorly aligned sample #1. The fit to this data was achieved using values of H_K = 2250 Oe and $K_u = 2.47 \times 10^6$ erg cm^{-3}. However, for the more aligned sample #4, a poorer fit to the data is evident using values of H_K = 2270 Oe and $K_u = 2.64 \times 10^6$ erg cm^{-3}. Likewise, an adequate fit to the experimental data cannot be

[1] Michael Sharrock, Imation Corporation, MN, personal communication, 1999.

obtained when AGFM results are included due to the uncertainties in assigning an appropriate sweep-rate to a pulse width when comparing pulsed and swept systems.

The implications of figure 6.17 are clear; the change in remanent coercivity for sample #1 is most likely thermal in origin (Néel 1949). This is in agreement with the thermal decay measurements presented in §6.2.4, in which the poorly aligned sample #1 presents a smaller fluctuation field due to the changing interparticle interactions (Morales, et al. 1995). For the most aligned sample #4, the local magnetic field from the dipolar interaction tends to hinder magnetisation reversal (Bottoni, et al. 1992), and a higher field is required for reversal over short timescales. The steeper variation in remanent coercivity of sample #4 cannot be resolved by the micromagnetic el-Hilo model, and may be indicative of the onset of precessional effects (Stinnett, et al. 1999) or a sudden change in the mode of reversal (He, et al. 1995). The relationship between particle orientation and high speed switching properties is also shown in table 6.8. Since the high speed remanent coercivity is found to increase with alignment for all samples, the corresponding fit to the data reveals a consequent reduction in the thermal stability ratio $K_u V_m/kT$.

Sample	#1	#2	#3	#4
M_r/M_s[a]	0.70	0.77	0.83	0.88
H_K (Oe)	2250	2260	2270	2270
V_m (10^{-18} cm^3)[b]	7.2	6.9	5.8	5.4
K_u (10^6 erg cm^{-3})	2.47	2.34	2.51	2.64
$K_u V_m/kT$[c]	431	394	352	343

[a] §6.2.1 M_s = M at 10kOe [b] §6.2.4 [c] At room temperature

Table 6.8 Characterisation and fitting parameters for samples #1 through #4.

6.5.3 Inclusion of Low Frequency Results

Figure 6.18 shows the measured variation in remanent coercivity over a wide range of frequencies for samples #1 and #4. Similar to that described in §6.5.2, the el-Hilo model is fitted to the experimental data, which includes slowly swept AGFM results (§6.3.1), solenoid-based microsecond measurements (§6.3.2) and nanosecond timescale studies from the spark gap switch (§6.4.2). The specific coefficients involved in the fit were obtained from the high speed data *only*, that is those parameters defined in table 6.8.

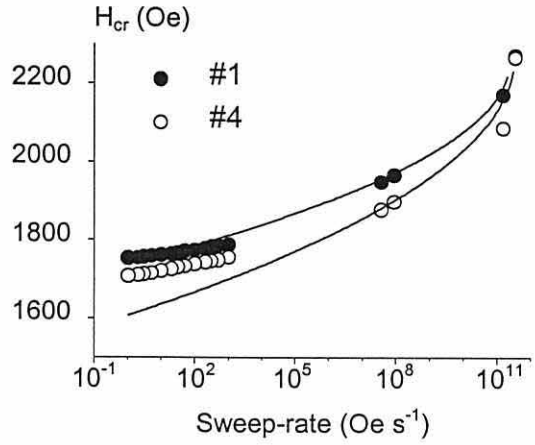

Figure 6.18 Predicted variation in remanent coercivity as a function of sweep-rate for tape samples #1 and #4.

It is apparent from figure 6.18, that a reasonable fit to the poorly aligned tape sample #1 is achieved over a wide range of sweep-rates, which correspond to both writing and long measurement times. However, the fit to the most aligned sample #4 suffers significant departures at low field sweeps. Although there are uncertainties in assigning an appropriate sweep-rate to a pulse timescale, as suggested in §6.5.2, it appears that the poor fit to sample #4 is indicative of the limitations of this thermal model to map the reversal of samples which are dominated by precessional switching at high frequencies. Conversely, in agreement with the results presented in §6.5.1 and §6.5.2, the poorly aligned sample #1 appears to be dominated by thermally activated reversal over the entire range.

In addition, using a similar approach to (Sharrock, et al. 1981), the sweep-rate dependence of the remanent coercivity was used to predict the head field required to write high frequency transitions on tape samples #1 and #4. Specifically, the el-Hilo model was fitted to both AGFM and solenoid pulsed field data *only*, as shown originally in figure 6.15. Clearly, whilst it may not be entirely appropriate to infer high speed properties from these measurements, this technique provides a useful estimation with which to compare measurements over short timescales. As before, figure 6.19 indicates that the poorly aligned sample #1 is dominated by thermal switching, inasmuch as a reasonable fit to the data is observed with H_K = 2270 Oe and $K_u = 2.60 \times 10^6$ erg cm^{-3}. These values give an acceptable thermal stability ratio K_uV_m/kT of 457.

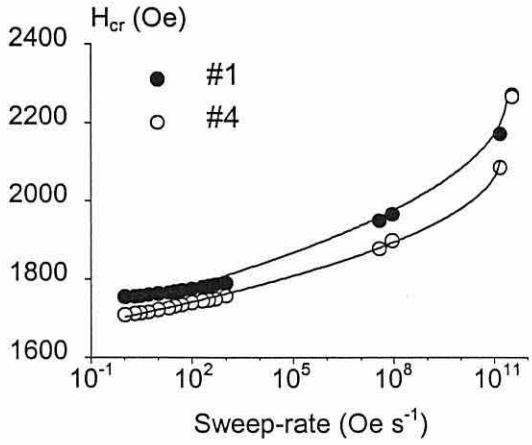

Figure 6.19 Predicted variation in remanent coercivity as a function of sweep-rate for tape samples #1 and #4.

Unsurprisingly, the fit to the most aligned sample #4 is found to deviate at high frequencies, as equation 6.8 artificially limits the remanent coercivity over timescales which approach the nanosecond regime. The coefficients involved in the fit to the data are given by $H_K = 2110$ Oe and $K_u = 5.49 \times 10^6$ erg cm^{-3}. This affirms the limitations of this approach for samples which appear to be dominated by gyromagnetic switching over short timescales.

6.5.4 Long Term Archival Observations

The fundamental requirements of a recording medium are that it retains a magnetisation signal of adequate intensity and transition density for the desired storage time (Bertram 1986). Furthermore, the medium must be adequately resistant to spurious external demagnetisation fields, but not be too difficult to overwrite or erase (Sharrock 1990). Since the behaviour of recording media is strongly dependent on the timescale of the reversal process (Néel 1949), this provides conflicting requirements for writing and storage coercivities. Having a storage coercivity significantly below the writing coercivity is not necessarily a source of difficulty, indeed it is characteristic of smaller particles which present an enhanced signal to noise. Of course, the practical capabilities of available recording transducers limit the writing coercivity, whereas the signal intensity recovered from the media is constrained by the storage coercivity. The ratio

between the writing and storage coercivities is characterised by the thermal stability factor K_uV/kT, as discussed in §2.5.

The utilisation of the switching models developed by (Sharrock, et al. 1981) and (el-Hilo, et al. 1992) have been well documented in this study. To illustrate, figure 6.20 indicates the variation in remanent coercivity for the smaller particle sample #5. As mentioned in §6.5.2, this sample is representative of advanced development media, having an average particle length of only 65nm. From Sharrock's Law, the predicted variation in remanent coercivity is in excellent agreement with the experimental data over a wide range of timescales, as indicated by curve (a). This is characterised by a thermal stability factor of 304, as described in table 6.7.

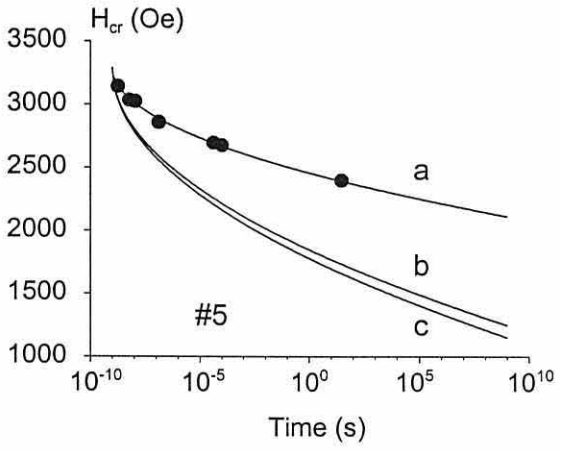

Figure 6.20 Predicted time variation in remanent coercivity for sample #5.

The expected result of reducing the sub-crystallite volume by a factor of three is illustrated in curve (b). This has the effect of reducing the stability ratio to around the suggested limit of 100 (Sharrock 1994), if the values of K_u and H_K are maintained. It is interesting to note that curve (b) predicts a 10ns writing coercivity of 2810 Oe, along with a 10 year storage coercivity (3×10^8s) of 1280 Oe. Consequently, the storage coercivity is only around 46% of the writing coercivity, which is at the very limit of thermal stability. Additionally, curve (c) shows the predicted remanent coercivity for this new system, with the ambient temperature elevated from 21°C (298K) to 40°C (317K). This value is consistent with the observed operating temperatures in modern high speed tape drives. Clearly, thermal fluctuations assist the external field to overcome the anisotropic energy barrier (Néel 1949), which results in the apparent

reduction of remanent coercivity. Specifically, the small increase of ambient temperature to 40°C, corresponds to a reduction in the predicted 10 year storage coercivity of approximately 100 Oe.

6.6 Concluding Remarks

The switching characteristics of a series of five metal particle tape samples have been studied over a wide range of timescales. These measurements reveal that the remanent coercivity in the nanosecond regime is generally around 30% higher than the value at the DC level. Furthermore, a distinct broadening of the switching field distribution can also be observed at high frequencies. The implications of this are that, as well as the larger head field required to write high frequency transitions, the output signal recovered from the tape is also reduced. In agreement with (Veitch, et al. 1994), thermally activated reversal is better explained in terms of the sub-crystallite or activation volume as opposed to the physical particle volume. Consequently, very small particles can appear less susceptible to the effects of thermal activation than larger ones.

The results presented in this chapter have also revealed a correlation between the degree of particle orientation in the tape and high speed reversal properties. The origins of this effect are complex, and are related at different timescales to the sub-crystallite or activation volume, particle interactions and phenomena influenced by gyromagnetic effects. The implications of this are that larger head fields are required to write high frequency transitions on increasingly textured systems. Clearly, this promotes conflicting requirements in terms of recording performance (Bertram 1986) and media durability (Okamoto, et al. 1999). Therefore, for certain applications, e.g. helical scan, in common with recent recording measurements of advanced metal particle media (Jackson, et al. 1999), it may be that a high degree of texturing is not of such critical importance.

Additionally, in order to relate high frequency recording properties to archival storage, the results have been compared with recent models of magnetisation reversal (Sharrock, et al. 1981) (el-Hilo, et al. 1992). By fitting these models to the experimental data, parameters such as the mean anisotropy field and anisotropy constant may be accurately determined. Consequently, the ratio K_uV/kT, which is commonly cited as a measure of magnetic stability, has been found to lie in the range 271 to 457. Setting a

stability criterion of 100 for this factor (Sharrock 1994), suggests that particle volumes could be reduced by between 1/3 and 1/4 if the values of K_u and H_K were maintained. Certainly, this would necessitate significant improvements in crystallinity, but does imply that further advances in pigment technology can be made before the thermal limit to data density is approached. Incidentally, the volume of these particles would not be significantly larger than volumes predicted for unstable superparamagnetic behaviour in iron particles.

The series of publications derived from this study are included in Appendix A (Prichard 1999) (Prichard, et al. 1999a) (Prichard, et al. 1999b).

References

Allenspach, R., *J. Magn. Magn. Mater.* **129**, 160-185 (1994).

Back, C. H., et al., *Science* **285**, 864-867 (1999).

Back, C. H., et al., *Phys. Rev. Lett.* **81**, 3251-3254 (1998).

Bean, C. P., Livingston, J. D., *J. Appl. Phys.* **30**, 120S-129S (1959).

Bertram, H. N., *Proc. IEEE* **74**, 1494-1511 (1986).

Bertram, H. N., Hallamasek, K., Madrid, M., *IEEE Trans. Magn.* **22**, 247-252 (1986).

Bertram, H. N., Mallinson, J. C., *J. Appl. Phys.* **41**, 1102-1104 (1970).

Bottoni, G., Candolfo, D., Cecchetti, A., Masoli, F., *J. Magn. Magn. Mater.* **116**, 285-290 (1992).

Brown, W. F., *J. Appl. Phys.* **30**, 130S-132S (1959).

Brown, W. F., *Phys. Rev.* **130**, 1677 (1963).

Chantrell, R. W., Coverdale, G. N., el-Hilo, M., O'Grady, K., *J. Magn. Magn. Mater.* **158**, 250-255 (1996).

Chantrell, R. W., Hannay, J. D., Wongsam, M., Lyberatos, A., *IEEE Trans. Magn.* **34**, 349-354 (1998).

Chantrell, R. W., O'Grady, K., *J. Phys. D: Appl. Phys.* **25**, 1-23 (1992).

Coverdale, G. N., Chantrell, R. W., *Paper HE-10, Intermag 2000, Toronto* (2000).

de Witte, A. M., el-Hilo, M., O'Grady, K., Chantrell, R. W., *J. Magn. Magn. Mater.* **120**, 184-186 (1993).

Doyle, W. D., He, L., Flanders, P. J., *IEEE Trans. Magn.* **29**, 3634-3636 (1993).

Doyle, W. D., Stinnett, S. M., Dawson, C., He, L., *J. Magn. Soc. Japan* **22**, 91-106 (1998).

el-Hilo, M., de Witte, A. M., O'Grady, K., Chantrell, R. W., *J. Magn. Magn. Mater.* **117**, L307-L310 (1992).

el-Hilo, M., O'Grady, K., Chantrell, R. W., "Modelling of interaction effects in fine particle systems", D. P. E. Dickson, S. A. Walton, Eds., 2nd International Workshop on Fine Particle Magnetism, University of Wales, Bangor (1996).

el-Hilo, M., O'Grady, K., Chantrell, R. W., *J. Appl. Phys.* **73**, 6653-6655 (1993).

Flanders, P. J., Sharrock, M. P., *J. Appl. Phys.* **62**, 2918-2928 (1987).

Freeman, M. R., *J. Appl. Phys.* **75**, 6194-6198 (1994).

Gaunt, P., *J. Appl. Phys.* **59**, 4129-4132 (1986).

Hancock, C. P., O'Grady, K., el-Hilo, M., *J. Phys. D: Appl. Phys.* **29**, 2343-2351 (1996).

Hancock, C. P., Owens, A. R., O'Grady, K., *IEE Proc.-Sci. Meas. Technol.* **144**, 229-233 (1997).

Hannay, J. D., Chantrell, R. W., Richter, H. J., *J. Appl. Phys.* **85**, 5012-5014 (1999).

He, L., Doyle, W. D., Varga, L., Fujiwara, H., Flanders, P. J., *J. Magn. Magn. Mater.* **155**, 6-12 (1996).

He, L., Wang, D., Doyle, W. D., *IEEE Trans. Magn.* **31**, 2892-2894 (1995).

Hicken, R. J., Wu, J., *J. Appl. Phys.* **85**, 4580-4582 (1999).

Hisano, S., Saito, K., *J. Magn. Magn. Mater.* **190**, 371-381 (1998).

Jackson, M., Sinclair, G., O'Grady, K., *J. Appl. Phys.* **85**, 5540-5542 (1999).

Jones, G. R., Prichard, L. S., Hutchings, J. A., Laidler, H., O'Grady, K., *J. Appl. Phys.* , Paper DA-12, 44th MMM Conference, San Jose (2000).

Kelly, P. E., O'Grady, K., Mayo, P. I., Chantrell, R. W., *IEEE Trans. Magn.* **25**, 3881-3883 (1989).

Klaassen, K. B., Hirko, R. G., Contreras, J. T., *IEEE Trans. Magn.* **34**, 1822-1827 (1998).

Köster, E., *IEEE Trans. Magn.* **20**, 81-83 (1984).

Lewis, V. G., Mayo, P. I., O'Grady, K., *J. Appl. Phys.* **73**, 6656-6658 (1993).

Luborsky, F. E., *J. Appl. Phys.* **32**, 171S-183S (1961).

Lyberatos, A., Chantrell, R. W., *J. Appl. Phys.* **73**, 6501-6503 (1993).

Mayo, P. I., Erkkila, R. M., Bradbury, A., Chantrell, R. W., *IEEE Trans. Magn.* **26**, 1894-1896 (1990).

Mayo, P. I., et al., *J. Magn. Magn. Mater.* **95**, 109-117 (1991).

Morales, M. P., el-Hilo, M., O'Grady, K., *J. Magn. Magn. Mater.* **140-144**, 2211-2212 (1995).

Morales, M. P., et al., *J. Magn. Magn. Mater.* **193**, 314-317 (1999).

Morales, M. P., et al., *J. Magn. Magn. Mater.* **190**, 357-370 (1998).

Néel, L., *J. Phys. Rad.* **12**, 339-351 (1951).

Néel, L., *Ann. Géophys.* **5**, 99-136 (1949).

Néel, L., *Rev. Mod. Phys.* **25**, 293-296 (1953).

O'Grady, K., *IEEE Trans. Magn.* **26**, 1870-1875 (1990).

O'Grady, K., Chantrell, R. W., in *Studies of magnetic properties of fine particles and their relevance to materials science* J. L. Dormann, D. Fiorani, Eds. (Elsevier Science Publishers, 1992) pp. 93-102.

O'Grady, K., Lewis, V. G., Dickson, D. P. E., *J. Appl. Phys.* **73**, 5608-5613 (1993).

Okamoto, K., et al., *J. Magn. Magn. Mater.* **193**, 378-383 (1999).

Oseroff, S. B., Franks, D., Tobin, V. M., Schultz, S., *IEEE Trans. Magn.* **23**, 2871-2873 (1987).

Prichard, L. S., "Development of a nanosecond spark gap pulse generator", S. Iezekiel, Ed., PREP'99 Conference, UMIST, Manchester, 238-241 (IEEE, 1999).

Prichard, L. S., Mayo, P. I., O'Grady, K., *IEEE Trans. Magn.* **34**, 1684-1686 (1998).

Prichard[a], L. S., O'Grady, K., *J. Magn. Magn. Mater.* **193**, 220-223 (1999).

Prichard[b], L. S., O'Grady, K., *IEEE Trans. Magn.* **35**, 2784-2786 (1999).

Richter, H. J., Ranjan, R. Y., *J. Magn. Magn. Mater.* **193**, 213-219 (1999).

Richter, H. J., Veitch, R. J., *IEEE Trans. Magn.* **31**, 2883-2888 (1995).

Richter, H. J., Wu, S. Z., Malmhall, R., *IEEE Trans. Magn.* **34**, 1540-1542 (1998).

Sharrock, M. P., *IEEE Trans. Magn.* **35**, 4414-4422 (1999).

Sharrock, M. P., *J. Appl. Phys.* **76**, 6413-6418 (1994).

Sharrock, M. P., *IEEE Trans. Magn.* **26**, 193-197 (1990).

Sharrock, M. P., McKinney, J. T., *IEEE Trans. Magn.* **17**, 3020-3022 (1981).

Shimatsu, T., Lodder, J. C., Sugita, Y., Nakamura, Y., *IEEE Trans. Magn.* **35**, 2697-2699 (1999).

Spratt, G. W. D., Bissell, P. R., Chantrell, R. W., Wohlfarth, E. P., *J. Magn. Magn. Mater.* **75**, 309-318 (1988).

Stinnett, S. M., Doyle, W. D., *IEEE Trans. Magn.* **34**, 1681-1683 (1998).

Stinnett, S. M., Doyle, W. D., Flanders, P. J., Dawson, C., *IEEE Trans. Magn.* **34**, 1828-1833 (1998).

Stinnett, S. M., Doyle, W. D., Koshkina, O., Zhang, L., *J. Appl. Phys.* **85**, 5009-5011 (1999).

Stoner, E. C., Wohlfarth, E. P., *Proc. R. Soc. (London)* **A240**, 599-642 (1948).

Suzuki, T., *J. Magn. Magn. Mater.* **193**, 374-377 (1999).

Thornley, R. F. M., *IEEE Trans. Magn.* **11**, 1197-1199 (1975).

Thornley, R. F. M., Williams, J. A., *IBM J. Res. Develop.* , 576-578 (1974).

Uren, S., O'Grady, K., Chantrell, R. W., Popplewell, J., *IEEE Trans. Magn.* **25**, 3656-3658 (1989).

Veitch, R. J., Ilmer, A., Lenz, W., Richter, V., *J. Magn. Magn. Mater.* **193**, 279-283 (1999).

Veitch, R. J., Richter, H. J., Poganiuch, P., Jakusch, H., Schwab, E., *IEEE Trans. Magn.* **30**, 4074-4076 (1994).

Weller, D., Moser, A., *IEEE Trans. Magn.* **35**, 4423-4439 (1999).

Williams, M. L., Comstock, R. L., *17th AIP Conf. Proc.* **5**, 738-742 (1971).

Wohlfarth, E. P., *J. Phys. F: Met. Phys.* **14**, L155-L159 (1984).

Wohlfarth, E. P., *J. Appl. Phys.* **29**, 595-596 (1958).

Yu, Y., Harrell, J. W., *IEEE Trans. Magn.* **30**, 4083-4085 (1994).

Chapter 7

Conclusions and Further Work

7.1 Discussion of Work

This investigation has detailed the development of two pulsed field magnetometers which allow novel measurements of particulate recording media to be performed. The samples studied are indicative of advanced metal particle recording media which are currently utilised for high density data storage applications, such as Imation Travan™ linear tape.

The first part of this investigation concerned the characterisation of metal particle dispersions using microsecond duration pulsed magnetic fields. It is well known that the most critical stage in the production of particulate media is the preparation of a homogenous and stable pigment dispersion (Mathur, et al. 1991). However, the magnetic characterisation of a dispersion is often difficult to interpret as the application of a DC magnetic field alters the microstructure (O'Grady, et al. 1991). Conversely, if the dispersion is rapidly changed using a pulsed field of short duration, this may be used to give an indication of the state of the microstructure without having to make allowances for field induced aggregation of particles and is the basis for this study.

The magnetometer developed in this investigation is an extension to previous work, in which an instrument capable of producing fields of up to 1270 Oe allowed low coercivity dispersions to be studied in a similar manner (Hancock 1995). However, the field produced by the magnetometer was not of sufficient magnitude to switch higher

coercivity metal particles. Accordingly, particular emphasis has been placed on improvements in terms of field amplitude and homogeneity.

Specifically, a magnetometer has been developed which consists of a MOSFET pulse generator which produces well-defined current pulses of over 125A, with selectable pulse widths between 25μs and 130μs. The current pulse is driven into a small field coil assembly, the geometry of which is such that a magnetic field of over 4.7kOe is generated, with symmetrical rise and fall times of around 15μs. This short duration magnetic field impulse magnetises the wet dispersion sample, while an anti-phase sense coil and integrator stage process the magnetisation of the sample under the field pulse. The output is monitored using a 500MHz digitising storage oscilloscope, allowing the dynamic magnetisation response to the applied pulsed field to be viewed in real-time.

Proving studies performed with this instrument have somewhat surprisingly revealed that mechanical orientation can occur in high quality metal particle dispersions when the duration of the pulsed field is less than 100μs. Consequently, for well dispersed systems, particle rotation has been identified as the critical reversal mechanism for obtaining good particle orientation in the final coated product. In contrast, poorly dispersed systems cannot react and rotate to modest pulsed fields, hence Néel switching is the predominant reversal mechanism. The marked difference in the mechanical and Néel reversal characteristics of the dispersion samples have been confirmed in the resulting bulk magnetic measurements of hand-spread coatings taken during the milling process (Prichard, et al. 1998). Happily, this instrument is continually proving to be a useful addition to the laboratory, see for instance (Blackwell, et al. 2000).

The second part of this investigation concerned the highly topical issue of high speed reversal in particulate media. In recent years, the mechanism of thermally activated switching has been of considerable interest to the magnetic storage industry because of the large difference between the timescales of the recording process and the required storage stability (Sharrock 1994). With future recording systems requiring data to be written at near nanosecond duration, this raises an interesting question: how fast can the magnetisation in magnetic recording media be switched? Since conventional

laboratory methods cannot easily resolve switching behaviour in this time regime, novel pulsed field techniques have been developed to probe nanosecond reversal.

The second magnetometer developed in this investigation is again an extension to previous work, in which an instrument capable of producing nanosecond duration pulsed fields of up to 450 Oe was described (Hancock 1995). Similarly, the field produced by the magnetometer was not of sufficient magnitude to switch high coercivity metal particle media. Consequently, a 50Ω pressurised nitrogen spark gap switch has been developed capable of producing well-defined single-shot voltage pulses of over 3kV. The pulse width is adjustable from 7ns to 56ns, with rise times of under 3ns. The magnetometer consists of a charged coaxial line connected through the spark gap to an improved 50Ω microstrip structure, the geometry of which allows pulsed magnetic fields to be produced with a maximum amplitude of 1.8kOe (Prichard 1999).

Proving studies using this instrument have been performed on a series of five advanced metal particle tape samples. These measurements reveal that the remanent coercivity in the nanosecond regime is around 1.3 times the value of the DC level. Furthermore, a distinct broadening of the switching field distribution can also be observed at high frequencies. The implications of this are that, as well as the larger head field required to write high frequency transitions, the output signal recovered from the tape is also reduced. Interestingly, thermally activated reversal may be better explained in terms of the crystallographic sub-unit volume as opposed to the physical particle volume, and as such, very small particles can appear less susceptible to the effects of thermal activation than larger ones (Prichard, et al. 1999a).

Furthermore, these pulsed field studies have revealed a correlation between the degree of particle orientation in the tape and high speed reversal properties. The origins of this effect are complex, and are related at different timescales to the crystallite or activation volume, particle interactions and phenomena influenced by gyromagnetic effects. The implications of this are that larger head fields are required to write high frequency transitions on increasingly textured systems (Prichard, et al. 1999b). Clearly, this promotes conflicting requirements in terms of recording performance (Bertram 1986) and media durability (Okamoto, et al. 1999).

In order to relate high speed properties to archival storage, the results have been compared with recent models of reversal (Sharrock, et al. 1981) (el-Hilo, et al. 1992).

By fitting these models to the experimental data, a prediction of the remanent coercivity over many orders of magnitude may be obtained, and parameters such as the mean anisotropy field and anisotropy constant may be accurately determined. However, for samples which appear to be dominated by precessional dynamics, both models are unable to map the reversal at high frequencies, and theoretical approaches using the deterministic Landau-Lifshitz-Gilbert equation of motion may seem more appropriate (Chantrell, et al. 1998).

Finally, the thermal stability factor K_uV/kT, which is commonly cited as a measure of magnetic stability, has been found to lie in the range 271 to 457 for all samples. Setting a stability criterion of 100 for this ratio (Sharrock 1994) suggests that particle volumes could be reduced by between 1/3 and 1/4 if the values of K_u and H_K are maintained. Certainly, this would necessitate significant improvements in crystallinity, but does imply that further advances in pigment technology can be made before the thermal limit to data density is approached. Incidentally, the volume of these particles would not be significantly larger than volumes predicted for unstable superparamagnetic behaviour in iron particles.

7.2 Future Work

In recent years, the phenomenal increase in rigid disk capacity has been achieved astoundingly quickly, even by the standards of the IT industry. To illustrate, it is hard to imagine a personal computer being supplied with a 10MB hard disk, yet that was standard of an IBM PC of the mid 1980s. Less than eight years ago, an entry level PC had a 100MB hard disk. Today, an equivalent machine is supplied with 12GB of storage. Likewise, data transfer rates have risen dramatically: a modern rigid disk recording 200kbpi whilst revolving at 15000 rpm has a corresponding bit cell length of only 2ns (Sharrock 1999). Clearly, it is appropriate at this time to enquire where the likely fundamental limitations of this form of recording media lie. Unfortunately, in order to perform measurements of high speed reversal on rigid disk media, four separate issues will need to be considered.

Firstly, in order to probe magnetisation reversal over timescales even shorter than the bit cell length mentioned above, significant improvements to the present system need to be envisaged. Currently, the shortest available pulse from the spark gap switch

is just under 7ns in duration, marginally narrower than the 8ns duration pulse reported by (Stinnett, et al. 1998). Various techniques have been briefly evaluated in this study which may be capable of sharpening the edge times of a high voltage pulse, and as a result, reduce the overall pulse width. These include, positioning a high pressure secondary gap after the main spark gap (Fletcher 1949), filtering the unwanted components of the propagating pulse by employing a stub tuner (Edwards 1992), or most promisingly, utilising a ferrite pulse sharpener (Seddon, et al. 1988). The fact that only a very limited pulse steepening effect was encountered using the latter approach in this investigation, should not detract from what may be possible; 20kV pulses having rise times below 60ps (Dolan, et al. 1997).

The second issue that needs to be addressed if measurements of high speed reversal in rigid disk media are to be realised, is one of pulsed field amplitude. Current state-of-the-art 12Gbits/in^2 rigid disk media possess a coercivity of around 3.5 kOe (Weller, et al. 1999), which is significantly greater than the 1.8kOe maximum pulse available from the spark gap switch. Clearly, substantial increases in pulse voltage, and hence magnetic field, need to be developed. Currently, the output voltage of the spark gap is limited to 3kV, which is predominately due to electrical breakdown of the PET100 coaxial connectors. Significant improvements could be quite easily gained by changing over to 10kV rated HN connectors, remembering that the interface to the spark gap should maintain a 50Ω wave impedance. Of the other HV techniques identified which may give improvements whilst preserving pulse edge times, the most promising candidates include drift step recovery diodes (Focia, et al. 1996) and avalanche transistors (Fulkerson, et al. 1994) (Klaassen, et al. 1999).

The third problem which needs to be considered, is that of detecting the fraction of the grains that switch under the pulsed field. It is well known that for an equivalently sized sample of rigid disk media, the magnetisation signal associated with it is dramatically smaller than for particulate media. Consequently, the continued use of AGFM to measure the remanent magnetisation is likely to be problematic. Another approach, favoured by (Doyle, et al. 1998), is to measure the switched fraction by placing a Hall probe in close proximity to the microstrip line. However, the problem with both of these techniques, is that they are static measurements of the remanent state. They provide no information about the dynamics of the reversal process, and in

particular whether the magnetisation continues to precess after the removal of the field. Experiments to observe this are critically important, as precessional effects become more apparent at the highest frequencies. Recently, such methods for detecting the dynamic response of the magnetisation have been developed. The interested reader is referred to: spin-resolved scanning electron microscopy (Allenspach 1994), magneto-optic Kerr effect (Freeman 1994) (Siegmann, et al. 1995) (Hiebert, et al. 1997), spin-polarised tunneling (Koch, et al. 1998) and inductive probing (Silva, et al. 1999).

Finally, there are significant practical problems to be overcome in actually performing the experiment. For a tape sample, the thickness of both the web and coating are known to a reasonable precision. Since the sample under investigation forms part of the matched microstrip line, a small deviation in sample thickness is likely to cause attenuated replicas of the main pulse being reflected back into the line. Clearly, the increased thickness of a rigid disk sample is such that the current density, and hence magnetic field under the microstrip line, would be dramatically reduced. Doyle and his co-workers overcome this problem by breaking the media into tiny fragments. These fragments are then examined under an optical microscope for candidates of the approximate dimensions, before accurately determining the thickness of the sample using a profilometer (Stinnett, et al. 1998). Of course, this then creates problems associated with determining the orientation of anisotropic samples.

On a final note, the reader may be interested to learn that a substantial research grant has recently been allocated to this laboratory to study high speed magnetisation reversal in rigid disk media. To resolve the difficulties in measuring the switched fraction, a combined pulsed field and magneto-optic Kerr effect system is planned, whereby the sensing of the magnetisation can be performed almost simultaneously. Of course, this would necessitate stabilised optics to allow for the measurement of absolute values of magnetisation, similar to that described by (Hiebert, et al. 1997). It is also envisaged that experimental data will be provided for comparison with the widely recognised theoretical model of (Chantrell, et al. 1998), in order to relate thermal activation to the fundamental media parameters associated with high speed coercivity. It is also anticipated that studies of perpendicular rigid disk media may be undertaken, since it is broadly recognised that longitudinal media will cease to provide the gains demanded for densities over 50Gbits/in^2, and as such, perpendicular media is

increasingly seen as the only viable option for future ultrahigh density storage applications.

References

Allenspach, R., *J. Magn. Magn. Mater.* **129**, 160-185 (1994).

Bertram, H. N., *Proc. IEEE* **74**, 1494-1511 (1986).

Blackwell, J. J., Hutchings, J. A., O'Grady, K., *Paper HE-05, Intermag 2000, Toronto* (2000).

Chantrell, R. W., Hannay, J. D., Wongsam, M., Schrefl, T., Richter, H. J., *IEEE Trans. Magn.* **34**, 1839-1844 (1998).

Dolan, J. E., Bolton, H. R., Shapland, A. J., *Electron. Lett.* **33**, 2049-2050 (1997).

Doyle, W. D., Stinnett, S. M., Dawson, C., He, L., *J. Magn. Soc. Japan* **22**, 91-106 (1998).

Edwards, T. C., *Foundations for microstrip circuit design* (John Wiley and Sons, ed. 2nd, 1992).

el-Hilo, M., de Witte, A. M., O'Grady, K., Chantrell, R. W., *J. Magn. Magn. Mater.* **117**, L307-L310 (1992).

Fletcher, R. C., *Rev. Sci. Instrum.* **20**, 861-869 (1949).

Focia, R. J., Schamiloglu, E., Fleddermann, C. B., *Rev. Sci. Instrum.* **67**, 2626-2629 (1996).

Freeman, M. R., *J. Appl. Phys.* **75**, 6194-6198 (1994).

Fulkerson, E. S., Booth, R., "Design of reliable high voltage avalanche transistor pulsers", 21st International Power Modulator Symposium, Costa Mesa, California (IEEE, 1994).

Hancock, C. P., PhD, University of Wales (1995).

Hiebert, W. K., Stankiewicz, A., Freeman, M. R., *Phys. Rev. Lett.* **79**, 1134-1137 (1997).

Klaassen, K. B., Van Peppen, J. C. L., *IEEE Trans. Magn.* **35**, 625-631 (1999).

Koch, R. H., et al., *Phys. Rev. Lett.* **81**, 4512-4515 (1998).

Mathur, M. C. A., Raghavan, S., Jung, C., *Adv. Info. Storage Syst.* **1**, 337-351 (1991).

O'Grady, K., Gilson, R. G., Hobby, P. C., *J. Magn. Magn. Mater.* **95**, 341-355 (1991).

Okamoto, K., et al., *J. Magn. Magn. Mater.* **193**, 378-383 (1999).

Prichard, L. S., "Development of a nanosecond spark gap pulse generator", S. Iezekiel, Ed., PREP'99 Conference, UMIST, Manchester, 238-241 (IEEE, 1999).

Prichard, L. S., Mayo, P. I., O'Grady, K., *IEEE Trans. Magn.* **34**, 1684-1686 (1998).

Prichard[a], L. S., O'Grady, K., *J. Magn. Magn. Mater.* **193**, 220-223 (1999).

Prichard[b], L. S., O'Grady, K., *IEEE Trans. Magn.* **35**, 2784-2786 (1999).

Seddon, N., Thornton, E., *Rev. Sci. Instrum.* **59**, 2497-2498 (1988).

Sharrock, M. P., *IEEE Trans. Magn.* **35**, 4414-4422 (1999).

Sharrock, M. P., *J. Appl. Phys.* **76**, 6413-6418 (1994).

Sharrock, M. P., McKinney, J. T., *IEEE Trans. Magn.* **17**, 3020-3022 (1981).

Siegmann, H. C., et al., *J. Magn. Magn. Mater.* **151**, L8-L12 (1995).

Silva, T. J., Lee, C. S., Crawford, T. M., Rogers, C. T., *J. Appl. Phys.* **85**, 7849-7862 (1999).

Stinnett, S. M., Doyle, W. D., Flanders, P. J., Dawson, C., *IEEE Trans. Magn.* **34**, 1828-1833 (1998).

Weller, D., Moser, A., *IEEE Trans. Magn.* **35**, 4423-4439 (1999).